Selective Oxidation of Methane into Methanol using Sub-nanometre Copper Clusters: A Computational Study

PhD degree on Sustainable Chemistry

Mario Gallego Rodríguez

Director: Dra. Mercedes Boronat Zaragoza

Valencia, Mayo de 2024

INSTITUTO DE TECNOLOGÍA QUÍMICA
EXCELENCIA SEVERO OCHOA
CSIC
UNIVERSITAT POLITÈCNICA DE VALÈNCIA

Beyond the Sky

Agradecimientos

"Caminante no hay camino, se hace camino al andar"

Antonio Machado

A lo largo de estos intensos años, he tenido la suerte de emprender un intenso viaje en el mundo de la investigación junto a personas que a partir de ahora llevaré conmigo. Aquel niño que una vez quedaba fascinado por cómo de la nada, las cosas más increíbles podían ocurrir y que soñaba con dedicarse a investigar todavía está presente, alimentando esa curiosidad que hace que los que amamos esta ciencia queramos dedicarnos en cuerpo y alma para mejorar las vidas de las personas y para hacer de este mundo un lugar mejor.

Si hay algo que he vuelto a descubrir en estos 4 años y medio en los que hemos sufrido las consecuencias de una pandemia global es que el límite solo está en nuestra imaginación y en nuestra capacidad de explotar nuestro potencial a través del trabajo tanto físico como mental. Espero que esta pequeña y humilde contribución pueda servir para luchar contra el cambio climático para así preservar lo que considero que es una de las cosas más valiosas de este mundo, nuestra conexión sinergética con la naturaleza.

Tengo mucho por lo que agradecer en este viaje, y primeramente me gustaría empezar con la persona que me ha guiado de forma incansable

durante todo este tiempo, mi directora, la Dra. Mercedes Boronat Zaragoza. Me ha demostrado lo que significa ser un profesional de la investigación no solamente por sus enseñanzas, sino por su entereza, por su dedicación, por su persona. Solo con observarla he podido aprender muchísimo y espero algún día alcanzar el ejemplo que ella ha sido para mí. Por esto y por mucho más, gracias de corazón. También me gustaría agradecer al Dr. Avelino Corma por su contribución al proyecto con sus ideas y las discusiones científicas realizadas a lo largo de esta etapa.

No puedo olvidarme de mis compañeros con los que he compartido cientos de momentos tanto en la oficina como fuera de la misma: Nacho Tirado, Dr. Pau Ferri, Dr. Reisel Millán, Dra. Alechania Mitsurini, Dr. Santiago León, Dr. Germán Sastre, Omer Faruk, Pablo García, Sara Karimi, Miguel Ródenas y Álvaro Royo. Gracias por el excelente ambiente de trabajo, por vuestro compañerismo y por las charlas distendidas e interesantes que siempre hemos tenido en los descansos. En especial, me gustaría agradecer a los doctores Pau y Reisel por su inestimable ayuda cada vez que les he preguntado algo y por darme ese empujón que necesitaba al principio del doctorado en el momento más difícil.

Esto no hubiera sido posible si no fuera por el apoyo de mis padres, Jose Antonio y Cipriana. Ellos me enseñaron que las oportunidades solo se consiguen con esfuerzo, tesón y valentía, y que es tan importante trabajar como descansar para volver a conectar con uno mismo y no perderse en un mar de estrés, dudas y monotonía. También me enseñaron la importancia de apoyarte en los demás para lograr objetivos que de otra forma serían inalcanzables, ya que lo importante no es tanto el resultado sino el camino y los amigos que te impulsan a conseguir tu meta. Como mención especial, debo agradecer a mi abuela María por ser mi confidente y ofrecerme siempre su tiempo para charlar, pequeños momentos sencillos que nunca olvidaré.

También me gustaría agradecer a mis amigos por todo el apoyo emocional que me han dado durante todos estos años: Pablo Sánchez,

por sacarme siempre una sonrisa en los momentos más inesperados; Jose María Márquez, por escucharme cuando más lo necesitaba; Iván Murillo, por hacerme desconectar de la rutina; Javier Martín, por tus consejos sobre la búsqueda de oportunidades; y Jorge Tomás, por tus locas historias.

Por último y no menos importante, me gustaría agradecer a la que, sin duda alguna, ha sido mi pilar y mi sustento en esta última etapa, mi compañera de vida Ana. Gracias por tu apoyo en los momentos más críticos, gracias por esos paseos por la playa, por los ánimos durante el proceso de escritura, por los pequeños detalles del día a día, por las tardes de sofá y manta y por los que sin duda son de los mejores momentos de mi vida. Espero poder seguir caminando a tu lado y seguir ampliando nuestro número de experiencias juntos, ya que este mundo es mejor cuando sé que estás en él.

Ha llegado el momento de que dibuje mi propio camino de la única manera en que es posible, caminando. Gracias desde el fondo de mi corazón.

Este trabajo ha sido posible gracias al Instituto de Tecnología Química (ITQ), el cual me proporcionó la beca predoctoral (PRE2018-083547) que me permitió desarrollar esta tesis doctoral en el programa Severo Ochoa (SEV-2016-0683). También quiero agradecer a la Red Española de Supercomputación (RES), y al Centro de Cálculo de la Universitat de València por brindarme los recursos computacionales y a la Unión Europea y al Gobierno de España por la financiación para realizar este trabajo a través de los proyectos MAT2017-82288-C2-1-P (AEI/ UE), MCIN PID2020-112590GB-C21, CEX2021-001230-S y TED2021-130739B-I00 (MCIN/AEI/FEDER, UE)

Mario Gallego Rodríguez

Valencia, a 28 de Mayo de 2024

Contents

Agradecimientos .....

Contents .....

Glossary .....

Chapter 1 Introduction 1

1.1 Catalysis 2

1.2 Heterogeneous Catalysis 10

1.2.1 Steps 11

1.2.1.1 Mechanistic Insights 13

1.2.2 Solid Catalysts 14

1.2.2.1 Crystal Lattices 14

1.3 Zeolites and Zeotypes 17

1.3.1 Zeolites 17

1.3.2 Zeotypes 22

1.4 Metal Clusters and the Sub-nanometre realm 25

1.4.1 The beginning of Cluster Science 25

1.4.2 Metal Clusters: Definition & Properties 27

1.5 Brief history of Methane-to-Methanol chemical reaction 31

Chapter 2 Computational Chemistry: Theoretical background and Methodology 43

2.1 Computational Chemistry: A theoretical field of science 44

2.2 The Schrödinger equation 46

2.3 The settlement of Density Functional Theory (DFT) 52

2.3.1 Kohn-Sham self-consistent method 55

2.3.2 The quest to find the best approximation to the exchange-correlation functional 59

2.3.2.1 Local-density Approximation (LDA) 60

2.3.2.2 Generalized Gradient Approximation (GGA) 61
2.3.2.3 Meta-GGAs and Hybrid Functionals 62
2.3.2.4 The inclusion of dispersion forces in DFT 63
2.4 Basis Sets 66
2.4.1 Atom-centred Basis Sets 66
2.4.2 Reciprocal Space and Planewaves 67
2.4.3 Solutions to the use of Planewaves: Pseudopotentials and the Projector Augmented-wave method (PAW) 71
2.5 Potential Energy Surface (PES) 74
2.6 The Vienna Ab-initio Simulation Package (VASP) 76
2.6.1 Minimum States 76
2.6.2 Transition States 76
2.6.3 Vibrational Analysis 78
2.6.4 Free energy 80
2.6.5 Charge Analysis 82
2.6.6 Reaction Kinetics 84
2.7 Models 85
2.7.1 Periodic Models 86
Chapter 3 Selective Oxidation of Methane to Methanol with Molecular O_2 using Sub-nanometre Copper Clusters 91
3.1 Introduction 92
3.2 O_2 dissociation over Cu_n clusters 95
3.3 Methane Oxidation on 2D and 3D Cu_5 Clusters 104
3.4 Methane Oxidation on Cu_7 clusters 118
3.5 Discussion for both Langmuir-Hinshelwood and Eley-Rideal pathways in Cu_n clusters 129
3.5.1 Cu_5 clusters 130
3.5.2 Cu_7 clusters 135
3.6 Conclusions 142
3.7 Appendix 144

Chapter 4 Selective Oxidation of Methane into Methanol over Cun Clusters supported within CHA 153
4.1 Introduction 154
4.2 O_2 dissociation over Cu_n-CHA clusters 157
4.2.1 Confined Cu_n Clusters 157
4.2.2 O_2 adsorption on supported Cu_n Clusters 160
4.2.3 O_2 dissociation on supported Cu_n Clusters 166
4.2.4 Successive dissociation of multiple O_2 molecules on supported Cu_n clusters 171
4.2.4.1 Cu_5 clusters 171
4.2.4.2 Cu_7 clusters 177
4.3 CH_4 activation over Cu_5-CHA-2Al clusters 184
4.4 Competing Processes in Cu_5 clusters 193
4.5 CH_4 activation over Cu_7-CHA-2Al clusters 200
4.6 Competing processes in Cu_7 clusters 208
4.7 Discussion of the selective oxidation of methane into methanol over Cu_n-2Al-CHA 213
4.8 Conclusions 220
4.9 Appendix 222
Chapter 5 Alternative Zeotype Systems for the selective partial oxidation of methane into methanol 231
5.1 Introduction 232
5.2 O_2 dissociation over Cu_5-zeotype clusters 234
5.2.1 AlPO & SAPO systems 234
5.2.2 MeAPO systems 239
5.3 CH_4 activation over Cu_5-2O zeotype systems 246
5.3.1 SAPO system 246
5.3.2 ZnAPO System 249
5.3.3 FeAPO System 251
5.3.4 MgAPO System 253

5.3.5 TiAPO System 255
5.3.6 ZrAPO System 257
5.3.7 SnAPO System 259
5.3.8 Brief discussion of the CH_4 activation on Cu_5-2O-zeotype systems 261
5.4 Successive dissociation of O_2 molecules over Cu_5-TiAPO systems 263
5.5 CH_4 activation over Cu_5-3O TiAPO systems 267
5.6 Competitive Processes on Cu_5-2O TiAPO system 270
5.7 Conclusions 272
5.8 Appendix 274
Chapter 6 Conclusions 279
Summary 285
Resumen 291
Resum 297
List of Publications 303
References 305

Glossary

ΔG	Gibbs Reaction Energy
AlPO	Aluminophosphate
BAS	Brönsted Acid Site
BJ	Becke-Johnson
BO	Born-Oppenheimer
CHA	Chabazite
DFPT	Density Functional Perturbation Theory
DFT	Density Functional Theory
DFT-D	Dispersion-Corrected Density Functional Theory
DME	Dimethyl Ether
E	Electronic Energy
ER	Eley-Rideal
Erel	Relative Electronic Energy
G	Gibbs Free Energy
Gact	Gibbs Activation Energy
Gads	Gibbs Adsorption Energy
GGA	Generalized Gradient Approximation
Grel	Relative Gibbs Energy
GTO	Gaussian-Type Orbitals
HF	Hartree-Fock
HK	Hohenberg-Kohn
HOMO	Highest Occupied Molecular Orbital

IPCC	Intergovernmental Panel on Climate Change
IUPAC	International Union of Pure and Applied Chemistry
IZA	International Zeolite Association
kJ/mol	Kilojoules per mole
KS	Kohn-Sham
LAS	Lewis Acid Sites
LBFGS	Limited-memory Broyden-Fletcher-Goldfarb-Shanno
LDA	Local density Approximation
LH	Langmuir-Hinshelwood
LPG	Liquified Petroleum Gas
LUMO	Lowest Unoccupied Molecular Orbital
MeAPO	Metal-substituted Aluminophosphate
MEP	Minimum Energy Pathway
MMO	Methane Monooxygenase
MP	Møller-Plesset
MR	Member ring
MTM	Methane to Methanol
NP	Nanoparticles
PAW	Projector-Augmented Wave
PBC	Periodic Boundary Conditions
PBE	Perdew-Burke-Ernzernhof
PES	Potential Energy Surface
POM	Partial Oxidation of Methane
q	Total Atomic Charge
QM	Quantum Mechanics

QTAIM	Quantum Theory of Atoms in Molecules
SAPO	Silicoaluminophosphate
SBU	Secondary Building Unit
SCF	Self-Consistent Field
STO	Slater-Type Orbitals
TF	Thomas-Fermi
TS	Transition State
VASP	Vienna Ab-initio Simulation Package
vdW	Van-der-Waals

Chapter 1
Introduction

The present dissertation collects our research efforts to comprehend and unravel one of the most challenging reactions in the contemporary context, the partial oxidation of methane into methanol.

First and foremost, the very basic fundamentals of this thesis will be explained. What is catalysis, how many types of catalysis are and what is the role of green chemistry in all of this.

Secondly, a concise overview of the systems that have been used throughout the entire study will be detailed. For this purpose, sub-nanometre metal clusters, in other words, aggregates of only a few metal atoms with a particle size smaller than 1 nm, have been selected.

Lastly, the reasons that conduct us to undertake this project will be explained: Why this reaction is so important in the period we live in, what are its implications, why this reaction is not already solved, what is the solution we have proposed and what are its advantages in comparison to the other ones investigated and reported in the literature.

1.1 Catalysis

Catalysis is the chemical phenomenon in which the reaction rate of a chemical reaction is altered by a substance called catalyst. The name was coined by Berzelius in 1835, when he realised that a number of isolated observations might be proved in terms of what he called "catalytic power",[1–3] although the first known use of inorganic catalysts dates back to the 16th century, when Cordus used sulfuric acid to catalyse the conversion of alcohol to ether.[4] With the passage of time, the understanding of this concept was finally understood, first by Ostwald and Sabatier in the early 20th century, proving that catalysts do not change the equilibrium of a chemical reaction[5,6], and subsequently by Rideal and Taylor, who expounded on the different known concepts up to that period.[7]

In the chemical reaction scheme, the function of the catalyst is completely different from the reagent. A reagent is consumed during the reaction to be transformed into the product whereas a catalyst plays a support role in the chemical reaction, weakening the internal bonds of a reactant, thereby facilitating its interaction with other chemicals, or orienting the particles to get more successful collisions, and ultimately, enabling the chemical reaction, remaining unchanged at the end. An interesting point to mention is that this is an idealisation of the process, since many catalysts undergo an irreversible change because of several chemical interactions, in other words, the catalyst deactivates.

But how can a catalyst achieve this? To answer this question, let us have a look at the picture below:

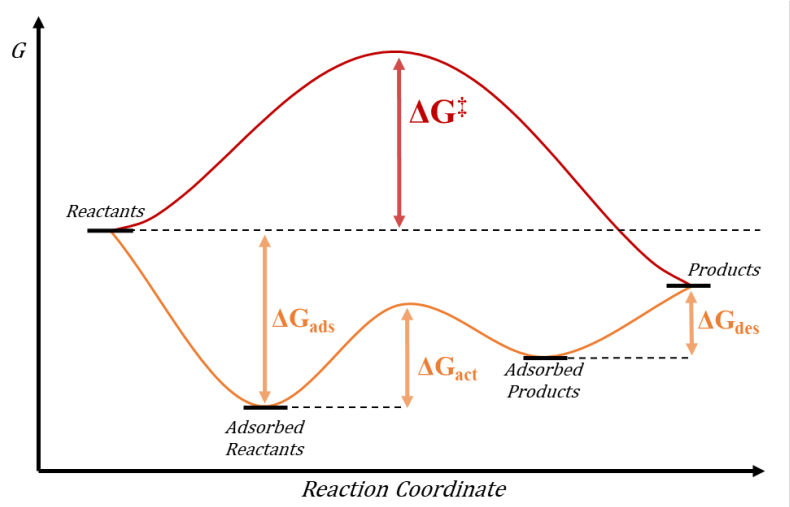

Figure 1.1 - General reaction scheme of a catalysed and a non-catalysed chemical reaction. Dark red line depicts the non-catalysed reaction and orange line depicts the different steps of a catalysed reaction. $\Delta G^{\ddagger}$ is the Gibbs free energy for the non-catalysed transition state and ΔG_{ads}, ΔG_{act} and ΔG_{des} represent the Gibbs free energies for the adsorption, activation, and desorption steps, respectively.

The Gibbs free energy[8] is a state function that relates enthalpy, a thermodynamic property that measures the thermal energy of a chemical system, and entropy, a magnitude that describes the degree of disorder of a system, meaning the number of possible microstates in which a system can be arranged in thermodynamic equilibrium, marking how spontaneous a chemical reaction is, in other words, the evolution of a chemical system.[9,10] A state function means that the value of a thermodynamic property depends only on the nature and state of the initial reactants and final products, and not on the reaction intermediate steps that have been taking place to carry out the transformation. This means that if the Gibbs free energy of a chemical reaction decreases as the reaction proceeds, then the reaction will spontaneously transform reagents into products. The equation below depicts the Gibbs free energy calculation (1.1):

Where ΔG is the Gibbs free energy change, ΔH is the enthalpy change, T is the temperature and ΔS is the entropy change.

$$\Delta G = \Delta H - T\Delta S \tag{1.1}$$

According to figure 1.1, $\Delta G^{\ddagger}$ is the difference between the highest point in the non-catalysed reaction path and the Gibbs free energy of the reactants, which determines the activation barrier of the system, the energy required to perform the chemical reaction. In this high point, a "transition state" (TS) is formed, a high-energy complex proposed by Eyring and by Evans and Polanyi in 1935 in which the reactants are interacting just before turning into products.[11–13]. Contributions of Marcelin, Kohnstamm, Scheffer and Brandsma related the equilibrium constant "K" with the Gibbs free energy[13] (1.2):

$$\Delta G^0 = -RT \ln K \tag{1.2}$$

Where ΔG^0 is the standard Gibbs free energy, R is the gas constant, T is the temperature and K the equilibrium constant. Decomposing equation (1.2) to get the rate constant as van't Hoff did conducts to the Eyring–Polanyi equation (1.3):

$$k = \kappa \frac{k_B T}{h} e^{-\Delta G^{\ddagger}/RT} \tag{1.3}$$

And this formula can also be expressed like (1.4):

$$k = \kappa \frac{k_B T}{h} e^{\Delta S^{\ddagger}/R} e^{-\Delta H^{\ddagger}/RT} \tag{1.4}$$

Where k is the rate constant, κ is the transmission coefficient (which is usually 1), k_B is the Boltzmann constant, h is the Planck constant, T is the temperature, R is the gas constant and $\Delta S^{\ddagger}$ and $\Delta H^{\ddagger}$ are the entropy change and the enthalpy change between the transition state and the reactants respectively. Therefore, this formula can explain the kinetics of chemical reactions and the important implications of the transition state in chemistry.

Catalysts possess particular properties that determine their influence in the chemical reaction: *Activity*, *selectivity* and *stability*.

The *activity* of a catalyst measures the magnitude of the alteration in the reaction rate of a chemical reaction. In simpler terms, lower activation barriers conduct to better activities. However, this modification does not have to be positive in all cases, in fact, catalysts may have positive impact on specific reactions and negative impact on others. When a catalyst hinders a chemical process, then it is called inhibitor.

Selectivity is perceptible when a chemical reaction undergoes multiple chemical reaction paths at the same time that generate dissimilar products. In this case, a catalyst with good selectivity is able to direct the chemical reaction to certain reaction pathways to produce only the desirable product. This functionality is absolutely important for chemical reactions with high risks of forming different product mixes and for industrial processes, since selectivity can determine the feasibility of an entire process.

Stability is also a very important feature that is related to how many catalytic cycles a catalyst can withstand under the reaction conditions before experiencing poisoning or deactivation. This is a very good descriptor in industrial processes to discard different catalyst proposals. As a general rule, catalysts with great stability are more robust, reliable and easily implemented in industry for commercial processes.

But how can a catalyst be poisoned in a catalysed process? To answer this question, we need to talk about *active sites*.

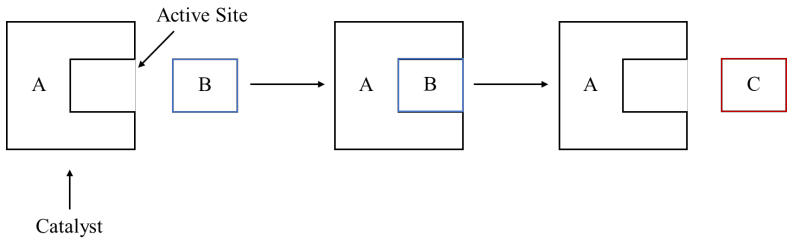

Figure 1.2 - Simple scheme of the role of an active site A in a catalytic reaction, where reactant B adsorbs on the active site to be transformed into product C.

Active sites are the nuclear part of catalysts in which the catalysed reaction occurs. This new concept was introduced by Taylor in 1925, postulating that the entire surface of a catalyst is not responsible of the overall activity.[14] Normally, a catalyst with multiple active sites has its activity increased, but having this is not always convenient, considering that each active site may have different activity, selectivity, and stability against a specific chemical reaction, so increasing the number of a distinct active site is generally the most accepted approach.

However, there is a physical limit in which a catalyst cannot produce more products because all the active sites of the catalyst have been occupied by the reactants and the velocity of the reaction reach a peak. This phenomenon is called saturation, and it is depicted in figure 1.3:

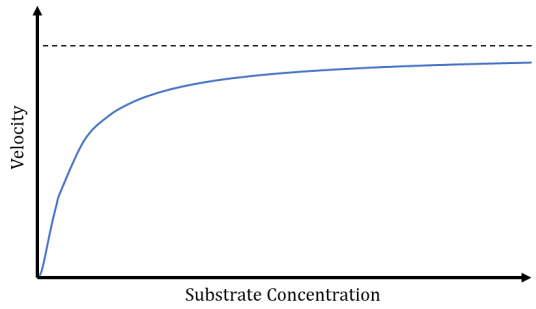

Figure 1.3 - General Scheme of catalyst poisoning due to the saturation of active sites.

Additionally, there may be other reasons for the deactivation of the catalytic reaction like catalyst modification, migration-coalescence[15] or sintering.[16]

With all of this in mind, it is natural to think how important catalysts are for the entire chemical industry.[17,18] From petrochemistry[19,20] to pharmaceutical industry,[21–23] polymer industry,[24,25] fine chemistry,[26–28] commodity chemical industry[29] and so on and so forth, around 85-90 % of chemicals require catalysis at some production point.[30] The use of catalysts is essential because it leads to faster, greener and more energy-efficient chemical reactions that make possible commercial products, becoming a crucial pillar of chemistry that represents a one step forward for the human civilization.

As a wide subject area, catalysis encompass different disciplines, but green chemistry stands out as one of the most emerging fields in chemistry in the last 20 years. It combines the protection of the environment with chemical processes that seek energy efficiency to the very fabric of existence, atoms, becoming a cornerstone in the fight against global warming.[31–35]

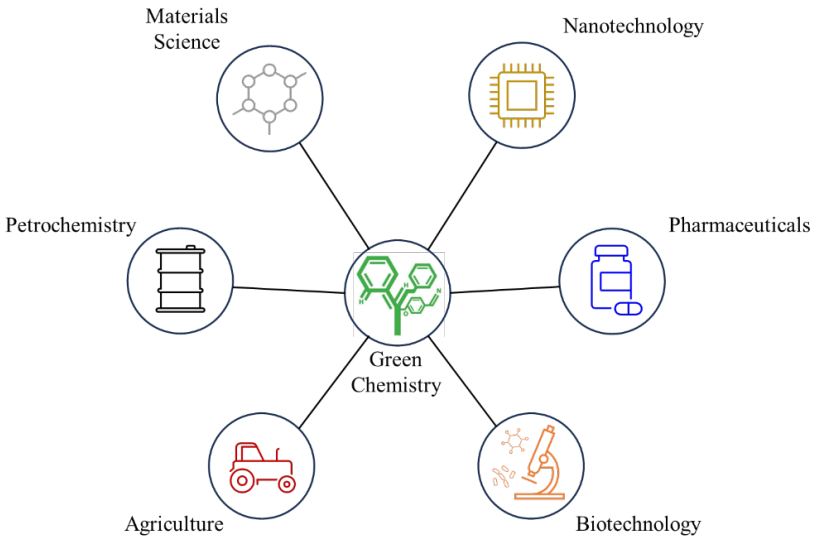

Figure 1.4 - Scheme with the main fields of science related to Green Chemistry.

In this discipline, twelve principles were settled on 1998 to encourage chemical industry and governments to pursue a more sustainable and greener world:

1. Prevent Waste
2. Atom Economy
3. Less hazardous synthesis
4. Design benign chemicals
5. Benign solvents & auxiliaries
6. Design for energy efficiency
7. Use of renewable feedstocks
8. Reduce derivatives
9. Catalysis
10. Design for degradation
11. Real-time analysis for pollution prevention
12. Inherently benign chemistry for accident prevention

In this way, the use of catalysis supports the fulfilment of the generic Green Chemistry principles, specifically numbers 1, 2, 5, 6, 8, 9 and 12. Hence, following the principles of green chemistry, this dissertation is in the way to uncover a green catalyst able to perform the methane-to-methanol reaction. In the coming chapters, different approaches will be discussed.

1.2 Heterogeneous Catalysis

There are three big groups of catalysts that comprehend the entire discipline:

On the one hand, we have *homogeneous catalysis*. In this subfield, the reactants and the catalyst remain in the same phase, principally liquid state in almost 90 % of the cases. This subject area stands out for its mass transport, activity, and selectivity. Normally, a organometallic complex is responsible for the catalysed reaction.[36,37]

On the other hand, we have *heterogeneous catalysis*, the kind of catalyst in which this thesis is based on. In this subcategory, the reagents and the catalyst are in a different state of matter, generally liquid or gas for reagents and solid for catalysts. This field of knowledge stands out for its applications in the chemical industry and the easier recovery of the catalyst.[38,39]

Lastly, we have *biocatalysis*. This field of study is so special that it is only focused on biological processes that maintain life with the use of enzymes, super specific biological catalysts that have evolved with the passage of centuries, millenniums, and aeons to specialise in particular chemical reactions achieving superb results in activity and selectivity. Nevertheless, this catalyst class is very sensitive to the reaction conditions and change them entail from worse activity or selectivity to the total deactivation of the enzyme. That is one of the reasons why enzymes are difficult to implement in industrial processes.[40]

Having introduced all types of catalysts, we will focus our efforts on heterogeneous catalysis, and the possibilities of this field in our research project.

In the vast majority of cases, heterogeneous catalysis takes place at the surface of a solid catalyst, although catalysed reactions can also be performed in the internal surface, in other words, in the micropores and channels of the catalyst. Mesoporous or amorphous materials are the great example of this.[41] Therefore, heterogeneous catalyst can be considered as the nexus between condensed-matter physics and chemistry.[42]

1.2.1 Steps

A heterogeneous catalytic reaction is comprised of four different steps: *Diffusion*, *adsorption*, *reaction*, and *desorption*.[43,44] Considering a hypothetic chemical reaction in equation (1.5) where A and B are the reactants, C is the catalyst and D is the final product, figure 1.5 illustrates a general scheme of a heterogeneous catalytic reaction.

$$A + B \xrightarrow{C} D \tag{1.5}$$

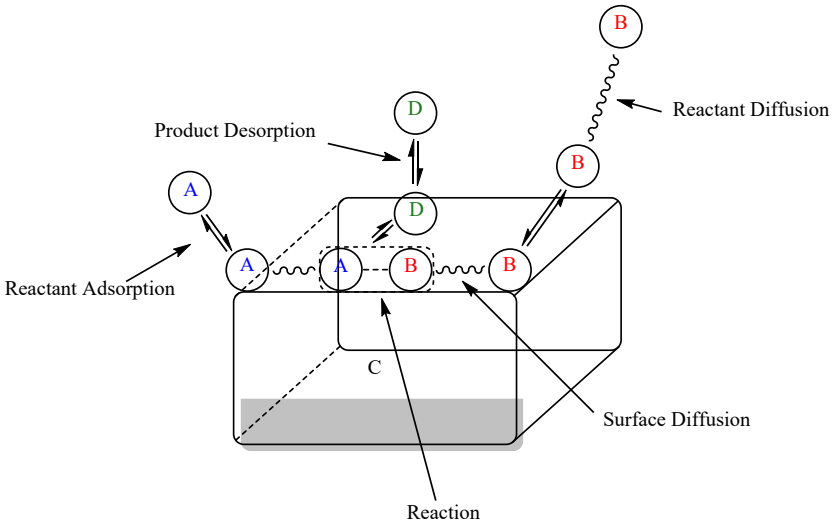

Figure 1.5 – General scheme of a heterogeneous catalytic reaction.

In the *diffusion* step, mass transport is happening, and the reactants are in the process of reaching or leaving the adsorbent, that is, the catalyst. Depending on the catalyst structure, the size and concentration of the reactants and the polarity of the adsorbent, diffusion is modulated as desired, affecting the residence time of reactants and products, and so the intermediates and by-products of the chemical reaction.

Next is the *adsorption* step.[45] It is defined as the process in which the reactants form a complex with the catalytic active site. When the reactant is adsorbed on the catalyst surface is called adsorbate. Depending on the adsorption energy, the residence time of the reactant on the catalyst internal or external surface will be shorter or longer, meaning high adsorption energies imply longer residence times and vice versa. This is crucial for the catalyst activity, as Balandin described using volcano plot relations between reaction rates and adsorption energies.[46]

There are two adsorption modes: On the one hand is *physisorption*, in which weak interactions between the catalyst and the reagent occur, and it is distinguished by its reversibility, fast and non-dissociative processes with the possibility of adsorbate multilayers. This kind of interactions range from Van der Waals forces to hydrogen bonding and does not change the electron density distribution of both the adsorbate and the adsorbent. In addition, the enthalpy adsorption remains in the range of 5-40 $KJ \cdot mol^{-1}$, relying upon the polarities involved with the adsorbates.

On the other hand, is *chemisorption*, an irreversible process that occurs when stronger interactions due to chemical forces like covalent and ionic bonds are entailed, formation and rupture of bonds included. Consequently, the electron density can be arranged in diverse forms, with the unique possibility of monolayers on the catalyst surface. The distinctiveness of this process provokes high adsorption enthalpies which may vary between 40 and 800 $KJ \cdot mol^{-1}$. Furthermore, the adsorption process can proceed through a dissociative or non-dissociative path.

In the *reaction* step, the reagents must overcome an activation barrier based on the transition state stability to yield the product. Furthermore, it can also be altered by the stability of the previous intermediate. Once finished, the product of the chemical reaction is formed. To achieve greater activities, optimisation of geometric, electronic and support parameters is required.

The *desorption* step comprises the last step in heterogeneous catalysis. The product abandons the catalyst active site, and it is diffused away from the catalytic system. Depending on the stability of the anchored product to the catalyst surface, the desorption energy will be higher or lower. It is for this reason that catalysts must be reactive to facilitate bond breakage and at the same time they need to be unstable to not form a very stable complex that promotes permanent product adsorption, thereby poisoning the catalyst.

1.2.1.1 Mechanistic Insights

Different mechanisms have been proposed for explaining different heterogeneous catalysed reactions. The first proposed mechanism was detailed by Langmuir first in 1918[47,48] and polished by Hinshelwood in 1926,[49] in which they posed a pathway to transform reactants into products on the catalyst surface. In detail, both reactants are chemisorbed on the catalyst, and then, the catalytic chemical reaction occurs. Taking into account again equation (1.5), figure 1.6 depicts a general scheme of this type of mechanism:

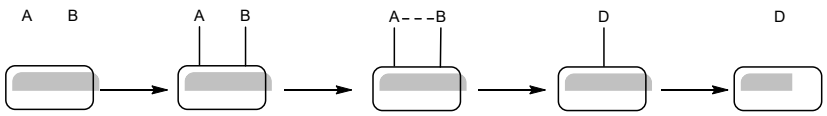

Figure 1.6 - General Scheme of a Langmuir-Hinshelwood type mechanism.

Later on in 1939[50–52], Eley and Rideal uncovered a new mechanism directly related to gas species, in which chemisorbed and physisorbed species react to form chemicals. This is the well-known Eley-Rideal mechanism, which differs from Langmuir-Hinshelwood in the way the reactants interact with the catalyst. Figure 1.7 illustrates a general scheme:

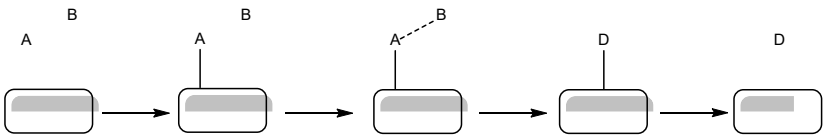

Figure 1.7 – General Scheme of an Eley-Rideal type mechanism.

1.2.2 Solid Catalysts

Overall, heterogeneous catalysis uses solid catalysts to undergo chemical reactions, but in this description, a lot of different materials can belong to this category. To understand what makes a good solid catalyst, the fundamentals of solid catalysts will be described.

1.2.2.1 Crystal Lattices

Crystalline solids are materials with a periodic arrangement of atoms defined by the unit cell (Figure 1.8), which is the smallest building block that once repeated in the translational axes, draws the entire crystal structure, reflecting the symmetries that define the characteristics of the material. The repetition of the unit cell forming an array of atoms in where each atom has the same surrounding environment is called the crystal lattice.[53]

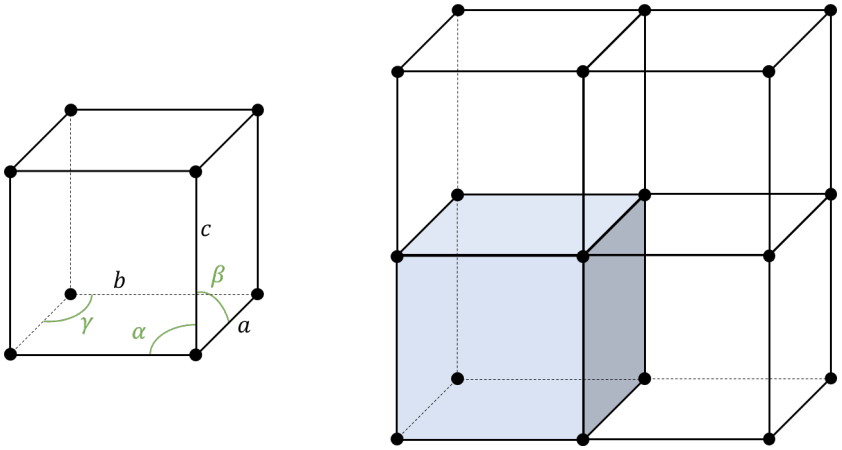

Figure 1.8 - General Scheme of a Unit Cell and a crystal lattice. *a*, *b,* and *c* are the translational vectors and α, β and γ are the angles between the planes formed by these vectors. Lattice points do not represent atoms, but places in space that are indistinguishable from each other.

In order to measure the lengths of the edges of a unit cell and the angles between them, lattice parameters are used. These parameters are indicated by the translation vectors (*a, b,* and *c*), and the angles between these vectors (α, β and γ), referring to the three vertices *bc*, *ac* and *ab* respectively.

Crystalline materials must be consistent with the translational periodicity, allowing only 32 point groups in this state of matter, also referred to as crystal classes. Among these, only 14 arithmetic crystal lattices are found in 3D materials, also known as *Bravais lattices*, which can be also divided into 7 lattice systems (Figure 1.9).

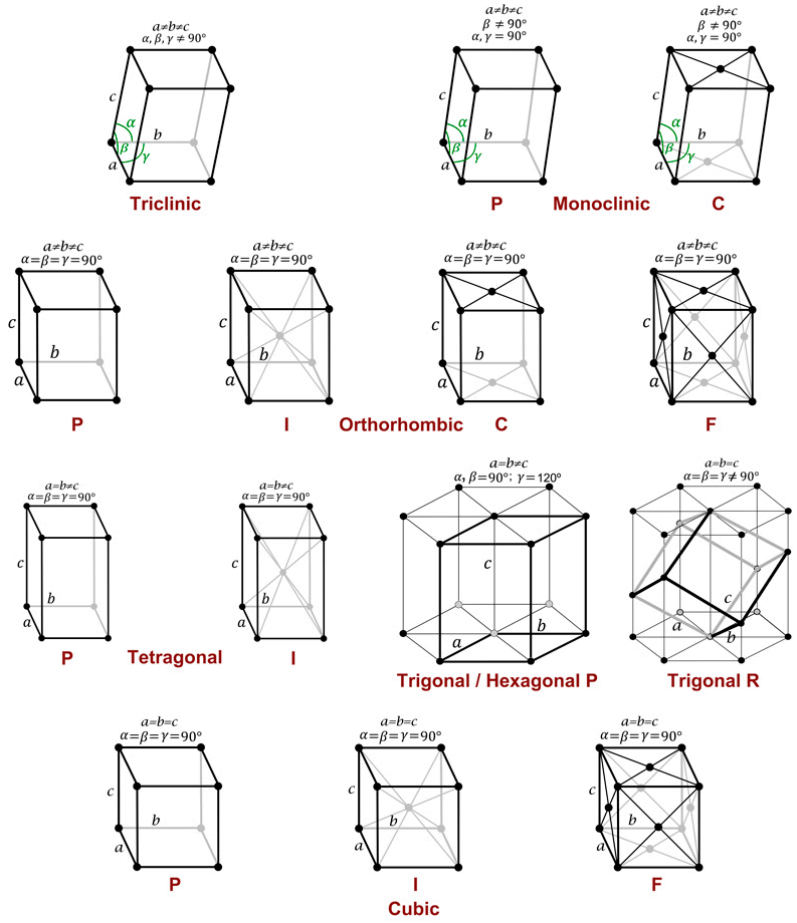

Figure 1.9 - Bravais Lattice Systems – From "CSIC crystallography"[54] by Martínez-Ripoll.

To identify the different directions [*hkl*] and planes of a crystal lattice (*hkl*), Miller indexes[53,55] are used. They can also be used to point out the planes in which certain molecules are adsorbed on the catalyst. However, it is difficult to obtain or synthesise pure crystals of our desired material in the real world, since the reaction conditions and other fluctuations can provoke the appearance of crystal defects and other inhomogeneities. But with the correct tools and a good perspective, chemists can take advantage of that to enhance the reactivity of the catalyst to new levels.[56]

1.3 Zeolites and Zeotypes

1.3.1 Zeolites

Zeolites are a high-efficient solid catalyst class made of linked tetrahedra consisting of silicates or aluminates, $[SiO_4]^{4-}$ and $[AlO_4]^{5-}$, that can be found in nature through volcanic activity[57] or synthesised in a laboratory.[58,59] These tetrahedra shape the framework of zeolites into a versatile microporous material with excellent hydrothermal stability,[60,61] high surface area,[60,62,63] nest effects,[64–66] well-defined acid and basic sites[67,68] with channels, cages and cavities of molecular dimensions[61,69,70] that range from 3 to 15 Å (See figure 1.10 as an example).

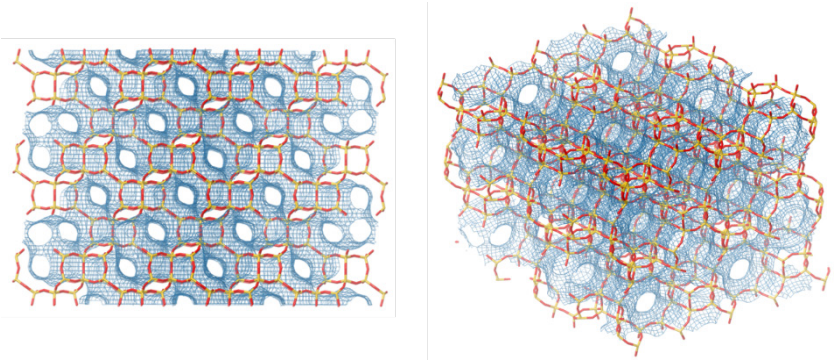

Figure 1.10 - Channels and Cavities of the Chabazite Zeolite from two different perspectives extracted from the IZA database.[71]

The origin of the word "zeolite" comes from the composition of two Greek words, "ζέω" (zéō), which means boil and "λίθος" (líthos), which means stone, meaning boiling stone, a direct reference to the experiment performed by the Swedish mineralogist Axel Fredik Cronstedt in 1756, who observed steam when these silicate minerals were undergone to heating on a borax bead.[72,73] Thus, the structure of pores and cavities that make zeolites unique were revealed, showing that these cavities can be filled with water molecules and extra-framework metal-exchanged cations, in which the latter regulate not

only the electrical neutrality of the framework to compensate each alumina tetrahedron with residual charges of "*-1*", but also the affinity between adsorbates and adsorbents with its impact on the separation properties;[74,75] acidity, controlling the amount and strength of Brönsted (BAS) and Lewis acid sites (LAS), and therefore the catalytic activity, since the original charge-compensating cations like acidic protons or Na^+ can be replaced by other more interesting ones for our desired reaction.[76–78]

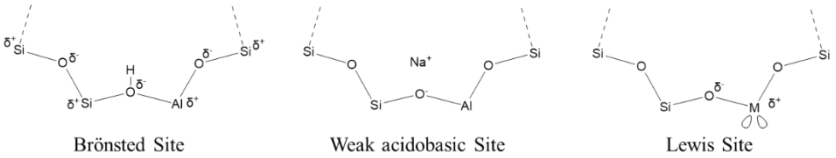

Figure 1.11 - General depiction of the different acid-basic sites in zeolites.

Overall, artificial zeolites are synthesised employing numerous methodologies under hydrothermal conditions at temperatures fluctuating from 100 to 200 ºC,[68,79–84] to produce precise topologies. Additionally, there are more factors involved in zeolite synthesis, like Al-distribution. According to the Loewenstein's rule,[85] Al–O–Al moieties in aluminosilicate crystalline materials are forbidden because of their intrinsic instability. Generally, this is true for the majority of zeolites, even though there are exceptions under specific conditions, like Si/Al ratios near one, or H-zeolites, because Al clustering is sensitive to the type of counterion used for charge compensation more than the framework structure.[86–88] These facts are crucial for the design of zeolite synthesis.

A zeolite framework can be break down in several building units[89–92]: Basic building unit (BBU), Secondary building unit (SBU), Periodic building unit (PerBU), Composite building unit (CBU), Constituting composite building unit (cCBU) and fundamental building unit (FBU). Principally, the most representative ones are SBUs and CBUs, since are

the most frequently encountered (See figure 1.12 running the gamut of SBUs). The basic building units are composed of the TO_4 tetrahedra, from which the rest of the groups are built. For more details, check the review from Yi Li and Jihong Yu.[91]

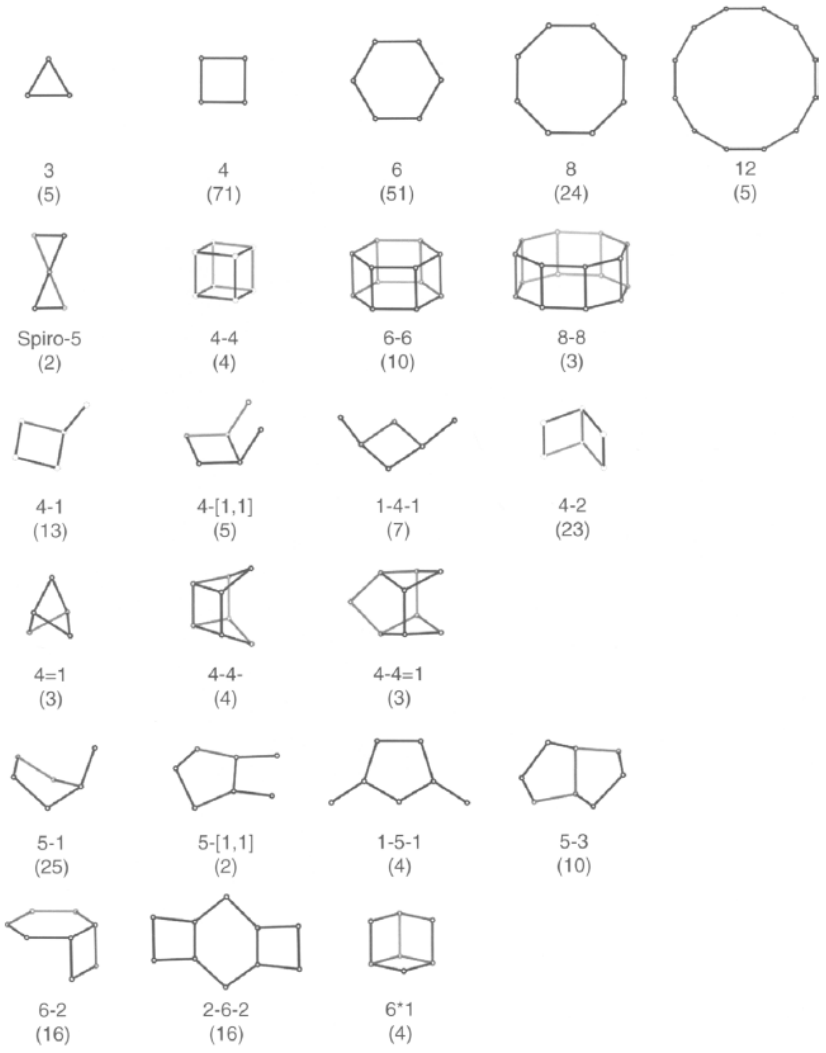

Figure 1.12 - Secondary Building Units (SBUs) and their Symbols. The number in parenthesis describes the frequency of occurrence. Extracted from the Atlas of Zeolite Framework Types, 6th Edition.[93]

These building units are formed by rings, which are cycles of T and O atoms that are not the sum of a few shorter cycles. To denominate the different types of rings, the established nomenclature states that a *n*-ring is made of *n* T atoms and *n* O atoms. These rings range from 3-member rings (3MR) to 4, 8, 12, 18 and so on and so forth, and are one if not the most important zeolite feature because of its involvement in pore size, therefore regulating the chemical reactions that can be carried out, acting as molecular sieves controlling the mass transport of the different molecules (See figure 1.13 picturing different examples of n-rings that can be found in several zeolite systems).

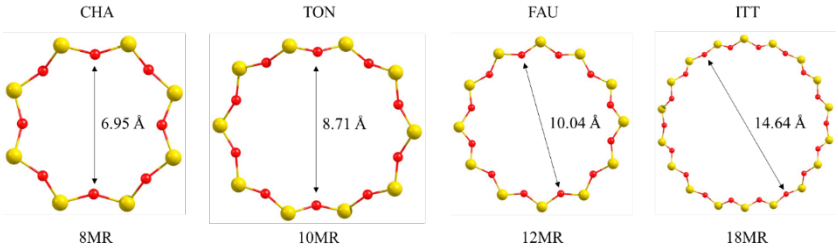

Figure 1.13 - Rings and Pore diameters of various zeolite frameworks. Measures given by the IZA database.[71]

Depending on the zeolite framework formed with the combination of the different building units, they are classified with a code made of 3 capital letters following the rules of the IZA Structure Commission (IZA-SC). However, to be included in the database, each new uncovered zeolite framework must be characterised. For further details of these framework types, consult the entitled *Atlas of Zeolite Framework Types*.[93] In this dissertation, CHA topology has been selected to be thoroughly studied with an increasing amount of Al atoms in the zeolite framework to know the role of these acid sites in the methane-to-methanol (MTM) reaction (§2.7.1).

Another classification of zeolites corresponds to the dimensionality. Generally, zeolites are defined as three-dimensional (3D) materials, but recently, bidimensional (2D) or layered zeolites are emerging as a new field of study.[94–96] They are microporous materials characterised by

their stacked sheets with attributes that can be tailored at nanoscale. Among them are strong acidic sites, interlayer porosity expansion, high surface area and modulated mass transport. We find good examples in pillared, delaminated and hierarchically assembled zeolitic materials in the literature.[97–99]

To enhance the catalytic properties of zeolites, the introduction of Al atoms and the isomorphous incorporation of distinctive metal atoms to the zeolite structure to create BAS, LAS or redox active sites can be regulated by the synthesis method, attending to the Si/Al ratio we are searching for.[100,101] Thanks to that, it is possible to incorporate and encapsulate metal atoms in the zeolite framework, creating metal-containing zeolites and metal-exchanged zeolites, respectively.[102] Later on, an enumeration of the intrinsic properties of the selected catalyst family, the origin of their catalytic properties (§1.4.2) and the current strategies to perform the studied chemical reaction in this dissertation will be discussed (§1.5).

Hitherto, the structural diversity of zeolitic frameworks reach to 256, all of them validated by the International Zeolite Association (IZA).[92] Amongst the recognisable zeolite types, 67 correspond to natural zeolites.[103]

Once the basic concepts of zeolites have been introduced, let us dive into a new class of zeolitic derivative materials, zeotypes, which share several features with zeolites and possess distinctive qualities.

1.3.2 Zeotypes

Zeotypes are crystalline microporous oxides with zeolite functionalities that diverge from zeolites in chemical composition, in light of zeolites being limited to pure silica and silicoaluminate materials, whilst zeotypes encompass different family materials like aluminophosphates (AlPOs),[104,105] silicoaluminophosphates (SAPOs)[106–109] or metal-substituted aluminophosphates (MeAPOs), with metals such as Fe, Mg, Ti, Zn, Sn, etc. being part of the framework.[105,110–114] Figure 1.14 shows examples of each zeotype and details the possible substitutions to form SAPOs and MeAPOs from AlPOs.

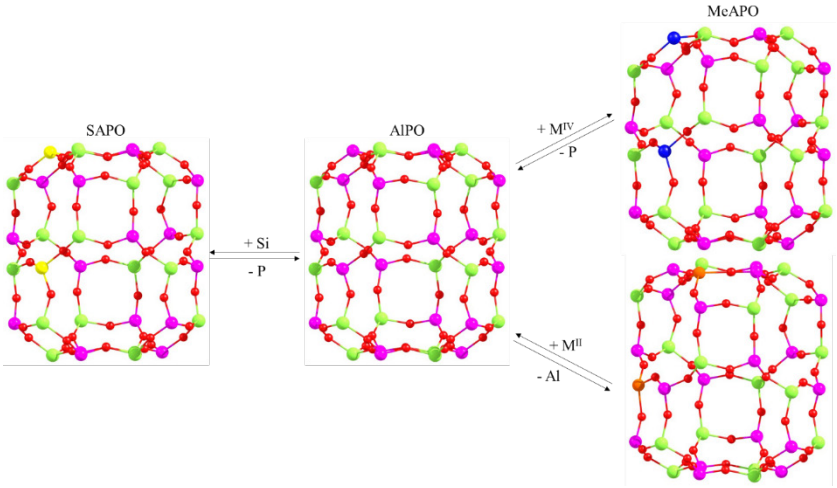

Figure 1.14 – Illustrations of an AlPO zeotype, and SAPO and MeAPO zeotypes formed by isomorphous substitution, respectively, referred to the CHA topology. Al, O, P, Si, tetravalent metal (M^{IV}) and divalent metal (M^{II}) atoms are labelled as green, red, purple, yellow, dark blue and orange, respectively.

Regarding AlPOs, they possess a neutral framework composed of AlO_4 and PO_4 tetrahedra with an absence of acidic and basic properties, but framework P^{5+} cations bestow structural flexibility, translated into a better diffusion, and their ionic character not only provides better

hydrophilicity but permits the isomorphous substitution of metal ions, creating subfamilies of aluminophosphates in the process. However, AlPOs are sensitive to water. There are evidences showing hydrolysis of these materials at circa 323 and 473 K, promoted by the presence of Na^+ and NH_4^+, which limit the use of these zeotypes.[115] The principal applications of these materials are for adsorption, gas separation and host-guest chemistry.[116–120]

To introduce catalytic activity in AlPOs, Si^{4+} cations are normally incorporated in the place of P^{5+}, giving shape to SAPOs, creating Brönsted acid sites in the case of using protons as the compensating cation and Lewis acid sites if transition metals are used, belonging to the zeotype framework, enhancing its applications in heterogeneous catalysis.

Besides, these isostructural materials introduce high chemical as well as thermal stability in comparison with AlPOs, introducing new catalytic properties and redox activity.[121–126] Likewise, this family can also integrate other metal atoms by substituting Al atoms for divalent metals to generate novel reactivity (MeAPSOs).[127]

Nevertheless, the introduction of silicon atoms to AlPOs could create silicon islands,[128] which do not add new catalytic sites, but contribute to an improved thermal stability,[129] increased hydrophobicity,[130] and the tuning of the acidic acid sites beyond these isolated silicon tetrahedra, in other words, silicon islands can control the acidity of SAPO materials.[131] Apart from SAPOs use as zeolite membranes,[132,133] there are several instances about their catalytic properties compiled in the literature.[134–138]

But this is not the only way to promote AlPO's catalytic activity. The addition of transition metals to the AlPO framework generates MeAPOs, zeotypes that combine the flexibility of AlPOs with the incorporation of heteroatoms boosting Brönsted and Lewis

acidity,[114,139,140] but especially redox activity, since these materials make easier the incorporation of transition metals with different oxidation states thanks to its framework made of PO_4^{3-} and AlO_4^{5-} tetrahedra.[105,111,141–143]

With the fundamentals of catalysis, zeolites and zeotypes explained, next the catalyst model that has been used throughout the entire dissertation will be expounded, stressing its peculiarities, unique morphology, and their uses in heterogeneous catalysis. Let us introduce metal and sub-nanometre clusters.

1.4 Metal Clusters and the Sub-nanometre realm

When a material enters in the sub-nanometre scale, its catalytic properties may change in a completely new fashion, acquiring catalytic behaviours that would be impossible otherwise. The next sections describe the development of cluster science, what metal clusters and sub-nanometre metal clusters are, and their distinctive characteristics.

1.4.1 The beginning of Cluster Science

Cluster science possess its roots in 1857, when Faraday accidentally uncovered the first metallic colloid, ruby gold, trying to unravel the optical properties of gold,[144] even though ruby gold had been used for centuries to make stained-coloured glass by the Romans in the 4th century, the Venetians in the 16th century, or to make distinctive colours like "Purple of Cassius" in the 17th century.[145]. This is not the only use that nanoparticles have had in ancient history going unnoticed. Lately, Cardell and Guerra discovered that gold nanoparticles are the responsible for a purple colour in the medieval Muslim "La Alhambra" monument due to a natural electrochemical corrosion-based reaction.[146] Even there are registers about dyed marble using gold particles in the archives of Ashurbanipal, which dates back to 6400 BCE.[147]

However, it was not until the 1960s when nanoscience experienced a significant surge. In that time, the use of IR spectroscopy to characterise molecules was consolidated,[148,149] Cotton stated in a seminar the first definition of "metal atom cluster",[150] and the development of techniques including nozzle beams and mass spectrometry[151–154] expanded the field to the next level with innovative approaches that could not be previously carry out, showing that in terms of properties, clusters differ from metal bulks.[155–162]

Once again, in the 1980s, with the revelation that catalytic reactions may be sensitive to the nanostructure of the material,[163] another

revolution came to the fore. The mature of supersonic expansion and beam techniques[164,165] coupled with the emergence of ultrahigh vacuum techniques such as Scanning Tunnelling Microscopy (STM)[166,167] or Atomic Force Microscopy (AFM)[168] through Scanning probe microscopes (SPM),[169] brought about that cluster science could be perfected with new discoveries and applications on the field, heterogeneous catalysis included.[170–177]

Precisely, it is in this area in which metal clusters open the gates of knowledge to the discovery of new and tailored green catalysts, catalysts that could not have imagined in the past, with promising attributes depending on their size, shape and charge.[178–184]

To delve into the details of metal clusters, the next section describes metal clusters, with a stress in sub-nanometric metal clusters and their special qualities.

1.4.2 Metal Clusters: Definition & Properties

According to the International Union of Pure and Applied Chemistry (IUPAC), a metal cluster is a number of metal centres grouped close together which can have direct metal bonding interactions or interactions through a bridging ligand but are not necessarily held together by these interactions.[185]

Depending on the number of atoms that these conglomerates possess, they can range from a few atoms to 20000, but most clusters with catalytic potential have a diameter smaller than 2 nm that bases their reactivity on a very high surface-to-volume ratio, quantum confinement at reduced sizes and unique geometric and electronic structures.[161,181,183,186–191]

In comparison with nanoparticles (NPs), clusters encompass well-defined structures normally less of 2 nm , whereas nanoparticles are referred to particles of any shape between the range of 1 and 100 nm with less precise characterization.[192] Considering the cluster and nanoparticle definitions above might be mistakenly misinterpreted by the readers, to avoid confusion with the terminology, this dissertation will treat these terms differently. First, for better understanding and simplicity, the terms clusters and nanoclusters will act as synonyms, and nanoparticles will be particles above the limit of 2 nm. Figure 1.15 illustrates a complete image of this.

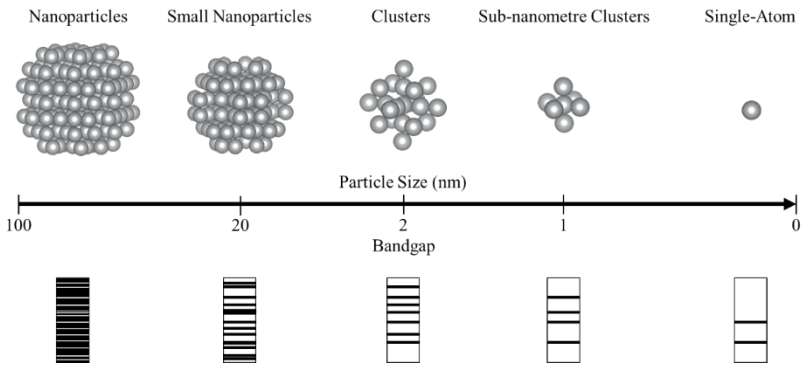

Figure 1.15 - Geometric and electronic structures of Nanoparticles, Small Nanoparticles, Clusters, Sub-nanometre Clusters and Single Atoms.

Due to metal clusters' tiny size, they can be considered as the bridge between homogeneous and heterogeneous catalysis, as they typically exhibit properties from both subject areas, having caught the utmost attention and interest of scientists as a result.[192,193]

Taking this into account, it is clear that nanoclusters attain exotic properties when they enter in the sub-nanometre realm (< 1 nm). At this scale, quantum confinement effects cause the electrons to be distributed in discrete electronic states with a non-null HOMO-LUMO gap (See figure 1.15), making them more similar to molecules than to bulk metals, and so, acquiring a non-metallic character.[194]

A change in electronic structure implies changes in their optical properties. Normally, noble metal NPs below 20 nm show a strong light adsorption attributable to the collective oscillation of the electrons in the metal conduction gap, this is the so called surface plasmonic resonance (SPR),[195] which can be observed at the UV-Vis (UV-Visible) range. However, in the case of clusters, this adsorption band is no longer observed, and the UV-Vis spectrum is transformed into a molecular-like absorption spectrum with thin peaks as cause of the discretisation of the energy bands in the conduction band with the appearance of

larger HOMO-LUMO gaps as the particle size decreases, displaying fluorescence and semiconductor behaviour.[196,197] This phenomenon can be exploited for synthesising and characterising tailored materials with specific wavelength emissions adjusting the atom metal, size, and ligands of the nanocluster, becoming promisingly useful as biosensors.[198] Examples in gold, silver and copper nanoclusters among others are found in the literature.[199–201]

To explain this electronic behaviour, we must go back to the 1980s. In this time, there was controversy about the elucidation of stability patterns in mass spectroscopy experiments due to "magic numbers": represented invariant discontinuities in otherwise smooth trends in cluster abundance versus size over a wide range of experimental conditions.[202] To solve that, Knight et al. proposed in 1984 the jellium model to offer an explanation to the stability of sodium clusters with larger intensity in the mass spectra.[170,203] Under this model, it is assumed that the positive charge of all ions within the cluster is uniformly distributed over a sphere of the cluster's size, which in the case of the most abundant sodium clusters would correspond to closed-shell electronic configurations, revealing the concept of magic clusters, in which a metal cluster of specific size with larger frontier orbitals is more stable than other configurations.[204] As a consequence of that, these clusters may resemble the behaviour of isolated atoms, like Al_{13}, which presents halogen-like properties similar to chlorine.[205–207] This fact led to the concept of "Superatom", a cluster acting as a stable unit in some ways analogous to an atom, which Jenna, Khanna and Castleman discussed profoundly proposing a 3D periodic table in which these superatoms could be adapted, with tailored properties mimicking different elements depending on the atomicity and the electronic structure.[161,208,209]

Bearing this in mind, the electronic configuration also has consequences in terms of cluster geometry, shape and stability.[190,210–212] To achieve stabilisation, clusters maximise the metal-metal interactions by overlapping their d orbitals, which produce more compact structures and a minimisation of the potential energy surface (PES) (§2.5). This is accomplished in combination with the hybridisation of the ns and (n-

1)d orbitals induced by the relativistic contraction of the ns and np orbitals and the relativistic expansion of the (n-1)d orbitals, which is more pronounced for the heavier transition metals of the 6th and the elements of the 7th period.[213] This explains why Au_n clusters adopt a 2D structure up to n= 11, 10 and 7 for anionic, neutral and cationic clusters, respectively, in contrast with larger n values, in which 3D structures are preferable. In the case of 2D clusters, the stronger 5d-6s mixing favours the planar structure, whereas for 3D structures, it is possible to maximise the d-d interactions.[214] Therefore, the transition from 2D to 3D structures will vary for each element as a function of the atomicity, the total number of atoms forming a cluster.

In general, a mixed of 2D and 3D morphologies are found with slightly energy differences, like for B_n, Cu_n, Au_n and Pt_n clusters depending on the electronic structures.[215–218] This plays an important role in the catalytic performance as it can tip the scales in favour of specific products or isomers, exhibiting conversion, selectivity and activation energy values that would not be possible with nanoparticles or bulk metals. In simpler terms, the low coordination of the atoms, along with the accessibility of the reactant molecules can create scenarios with enhanced and selective reactivity.[181,219] Naturally, the implications of the structure's shape are essential for the comprehension of the heterogeneous catalysis steps that were formerly described (§1.2.1). Furthermore, it is possible to observe changes in the morphology and shape of the cluster throughout the catalytic reaction. This effect is the so-called fluxionality, and it is fundamental for the understanding of the development of catalytic reactions.[220–222] Lastly, other factors like sintering or migration cannot be forgotten, because they can lead to critical alterations of the stability of a catalytic reaction.[183,223]

All things considered, with the potential of sub-nanometre clusters to revolutionise the current chemistry, an allegation of the motives for undertaking this research project will be next expounded. Let us introduce the historical context of the chemical reaction addressed in this dissertation, along with the motivation to achieve the methane-to-methanol reaction for a greener and sustainable world.

1.5 Brief history of Methane-to-Methanol chemical reaction

Methane is a high symmetry molecule that is well-known for its implications in climate change as the second most anthropogenic greenhouse gas after CO_2,[224,225] reaching a new peak of 1866 ppb in 2023 as stated in the last report of the Intergovernmental Panel on Climate Change (IPCC).[224]

Owing to this concerning data, scientists are seeking new ways to leverage methane. One of the most promising concepts consists of transforming the main component of natural gas into methanol, also known as wood alcohol, a colourless, neutral, and polar liquid at room temperature used as a base material in the chemical industry[226] (See scheme 1.1).

Scheme 1.1 - Methanol Value Chain

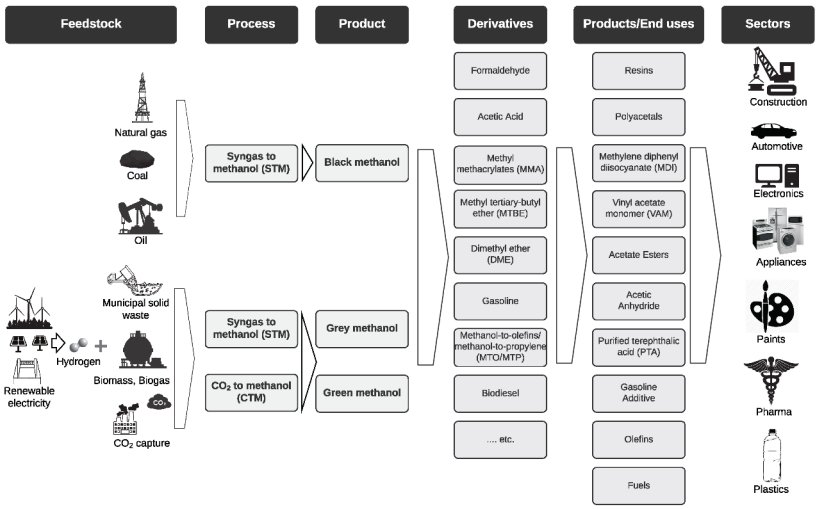

Note. From "A Review of The Methanol Economy The Fuel Cell Route"[227] by Simon Araya, S.; Liso, V.; Cui, X.; Li, N.; Zhu, J.; Sahlin,

S.L.; Jensen, S.H.; Nielsen, M.P.; Kær, S.K. A Review of The Methanol Economy: The Fuel Cell Route. Energies **2020**, 13, 596.

Methanol is also used as a fuel additive, and can be used as fuel in adapted motors.[226] Hence, scientists are doing research on this area for biofuel production,[228,229] given that by comparison with gasoline, methanol releases less toxic compounds and possesses a higher storage stability.[230,231] Another methanol usage is connected to the substitution of petroleum in the chemical synthesis industry.[232] Not only provides a convenient long-term storage solution to enhance renewable energy source penetration but also contributes to a more sustainable chemical industry by reducing its dependence on fossil fuels. In addition, methanol is involved in numerous key processes in sectors like Automotive, Electronics, Plastics, Pharma and so on[233] (See scheme 1.1).

In this fossil fuel transition era, the centralisation of all energetic vectors into zero-carbon processes, particularly the use of green hydrogen along other technologies,[234,235] is crucial for rerouting fossil fuels to alternative applications in industry, applying the principles of green chemistry.[31,32] This poses a solution that does our share for creating innovative sustainable energetic vectors, and therefore, to mitigate the effects of global warming. That is our cause to fight for a greener world for our future generations.

The current processes applied in industry entail expensive indirect routes with high-extreme temperatures ranging from 500 to 1200 ºC and pressures able to reach 30 bar.[236–241] In a few words, these routes consist of turning methane into syngas, a mixture of CO and H_2, and then convert it to several types of chemicals, methanol included. In order to transform methane into syngas, distinct technologies have been developed: Steam reforming[242–246], dry reforming[242,245,247–253] and even partial oxidation[254–259] using the concepts of catalysis described before (§1.1), but all of them requires harsh conditions or excessive reactant consumption. Nonetheless, they continue to be used at industrial scale as they are economically viable at large scale.[260] In contrast, catalytic processes permit a wide variety of other routes, like direct routes, in

which methane is converted through a catalytic process into the desired product in less steps, being superior to indirect routes in regard to resources, sustainability and reaction conditions.[241] When these processes are optimised, the situation will change for the entire industry, hence all the efforts have been channelled to make feasible direct routes for the MTM process.

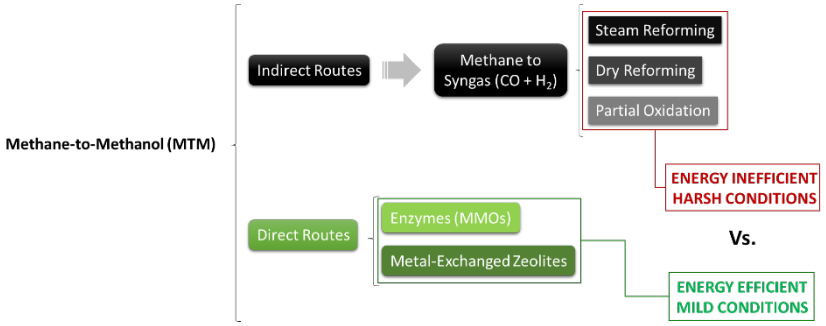

Figure 1.16 - Possible paths for the transformation of methane into methanol.

However, current direct methanol production from methane is scarcely effective. Several reviews have reported that high methane conversions conduct to trivial methanol selectivity and vice versa, which makes this reaction rather inviable for industry for both stepwise and continuous processes,[261–264] primarily attributable to the higher reactivity of methanol compared to methane, and thus, to the overoxidation of the alcohol to species like CO_2, CO, formic acid or formaldehyde in minor proportions.[265–269] Moreover, new experiments have confirmed methoxy species and adsorbed molecular methanol as the major products in activated copper and iron zeolites with spectroscopic methods like in situ Fourier transform infrared (FTIR),[270–276] and nuclear magnetic resonance spectroscopy (NMR).[277–279] Curiously, there is an exception for this behaviour in methanol derivatives,[267,268,280,281] with greater methane conversion and selectivity producing methyl bisulphate,[282–286] methyl halides,[287–289] methyl trifluoroacetate,[288,290–293] etc., which are hydrolysed to produce methanol. In other words, protected methanol compounds.

Notwithstanding, these systems are riddled with toxic salts and strong solvents, which rule out this approach from the perspective of green chemistry and the goal of this research. Even so, these catalytic setups are still being investigated to substitute this toxic substances for greener processes.[294–298]

Thermodynamically, it is an arduous task to preserve and isolate methanol as a product in the required harsh conditions to activate methane[254,299,300] while inhibiting overoxidation because the dissociation energy for the C-H bond of methanol is 402.14 ± 0.32 kJ/mol compared to the methane C-H bond dissociation energy of 438.892 ± 0.065 kJ/mol, one of the strongest C-H bonds in nature.[301] As a result, the energy required to break the C-H bond in methanol is 36.752 kJ/mol lower than in methane and 54.322 kJ/mol lower regarding its C-OH bond. Moreover, as a polar molecule, methanol is more prone to adsorb on the catalyst surface and then being more activated for oxidation.

Despite all the inconvenience, various works have confirmed that both homogeneous and heterogeneous catalysis carry out the activation of methane at low temperatures,[302–304] with the enzymatic systems found in methanotrophic bacteria named methane monooxygenases (MMOs) being the most prominent example of methane partial oxidation at mild conditions, becoming a chemical role model for a lot of scientists.[305–309] Albeit these enzymes present excellent results, they cannot be used at great scale caused of excessive economic cost, slow growth rate and low cell density.[310,311]

In order to reproduce this catalytic system for a feasible industrial process, zeolites were selected as good candidates owing to their similar attributes in terms of site isolation, ligand field strength and active site[312] with additional advantages as good thermal and hydrothermal stability, regulable acidity and flexible composition among others[78,313,314] (§1.3).

So far, diverse zeolite systems have been studied to carry out the methane-to-methanol reaction at mild conditions employing molecular oxygen as the principal oxidant agent in the majority of studies because of its availability, cost and green properties.[315,316] Additionally, other studies have experimented with green oxidants such as N_2O,[317–319] hydrogen peroxide[320–322] or water itself[271,323] with interesting results. Theoretically, scientists have often utilised transition metal elements such as Cu and Fe, but also experiment with more exotic choices for this reaction like Pt, Pd, Rh, etc., all of them as cationic species[324–331] although experimental studies mainly achieve methanol production and selectivity for Cu and Fe-zeolites.[332–335] Curiously, recent studies of Moteki et al. based on ZSM-5 point to a CO-assisted process using supported transition metals like Ru.[336,337]

In particular, copper-exchanged zeolites have outclassed other zeolite catalysts as the most relevant zeolite system because of better catalytic performance,[338] the use of molecular oxygen unlike Fe-zeolites,[339,340] easier industrial application[271,341,342] and superior selectivity towards methanol[261,278,343]. Actually, the addition of Cu^{2+} to other zeolites like Fe-ZSM-5 enhance methanol selectivity,[321,344–346] therefore it does not come as a surprise that this specific element is dominating and centring the discussions in academy and industry spheres.

In reference to Cu-zeolites, various active centres have been proposed (See figure 1.17), which may vary depending on Si/Al ratio, zeolite topology and copper loading:[347] monocopper[348–350] $[CuOH]^+$, copper oxide[351] $[CuO]^+$, bis(μ-oxo)dicopper[343,352,353] $[Cu_2O_2]^{2+}$, mono(μ-oxo)dicopper,[317,352–358] $[Cu_2O]^{2+}$, trinuclear copper cluster[359–363] $[Cu_3O_3]^{2+}$, even tetramers and pentamers,[361] $[Cu_4O_4]^{2+}$ and $[Cu_5O_5]^{2+}$ although these ones have not been observed experimentally. Indeed, these active centres share a lot of similarities, specially mono(μ-oxo)dicopper $[Cu_2O]^{2+}$ and the trinuclear cluster $[Cu_3O_3]^{2+}$, in the methane activation mechanism,[326,364–366] and they may be interconverted between each other, so a mix of these active sites may coexist and contribute to methanol conversion at the same time.[367] The principal consensus rules that $[Cu_2O]^{2+}$ exhibits low activation barriers, high reactivity, and ultimately as the main source of methanol, hence if

our research is able to unbalance this equilibrium towards mono(μ-oxo)dicopper sites with higher spin density and lower negative charge on the oxygen atom, we will be closer to a feasible material for industrial applications at low temperatures.

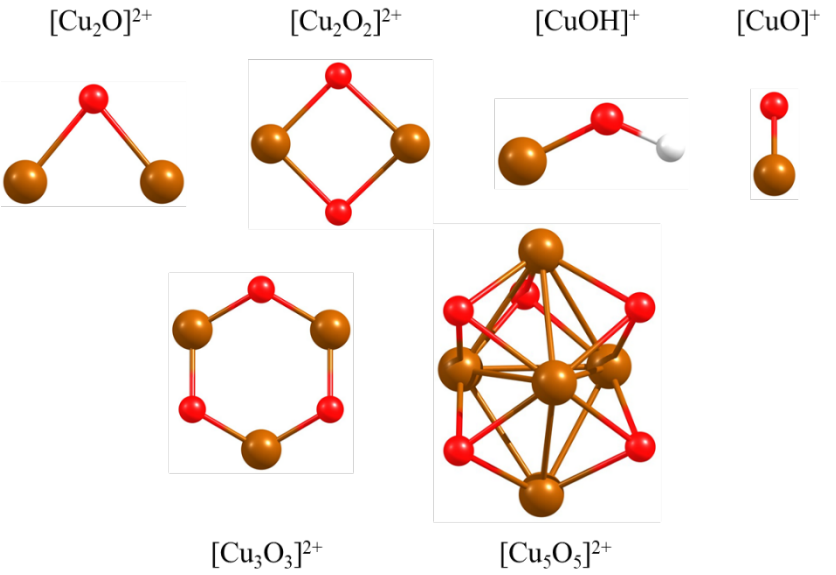

Figure 1.17 - Posed copper active sites for the direct conversion of methane into methanol. Note that $[Cu_5O_5]^{2+}$ has not been found experimentally.

The methane-to-methanol reaction can be resumed in the next steps (Scheme 1.2). The procedure starts at high temperatures to activate the oxidant reactant, oxidising the Cu^{+} atoms to Cu^{2+}, preparing the catalyst for the reaction. Next, high methane and low oxidant partial pressures are applied at lower temperatures to transform methane into methanol and to avoid methane overoxidation. In this step, Cu^{2+} atoms are reduced to Cu^{+} just as the beginning of the reaction. Then, high temperatures are required to regenerate the active centres with the oxidant agent to produce methanol over and over again.[300,368]

Scheme 1.2 - Simplified reaction cycle of the MTM process over Cu-exchanged zeolites.

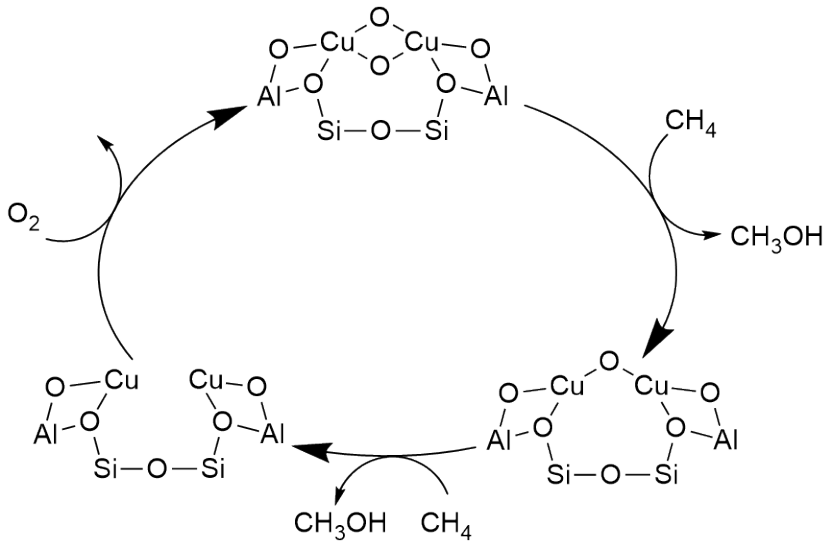

Nevertheless, the regeneration of the catalytic cycle has proven to be challenging when it comes to efficiently re-oxidise the remaining Cu (I) species, since these ones lower methanol selectivity and their accumulation can be used as an overoxidation descriptor.[369] Furthermore, Cu-zeolites are very sensitive to oxidant concentration, provoking that high and medium partial oxidant pressures imply high risks of methanol overoxidation to carbon dioxide. Fortunately, thanks to the dedicated work of scientists, reports in the literature have been found showing methane activations and methanol productions at 200 ^{o}C, thereby addressing these problems.[338,370] Despite this, the search for new catalysts that can enhance the current systems is essential.

In relation to the mechanistic insights, most of the published papers are only focused on the first part of the cycle[364,371–377] and water molecules to desorb methanol from the catalyst surface are needed.[261,264,300,332,378–381]. As far as my knowledge extends, the work presented by Engedahl et al.[382] depicts the most complete image of the MTM process over Cu-exchanged zeolites, Cu-SSZ-13 specifically, but still, they did not

consider supplementary paths and by-products that can be involved throughout the process. In this dissertation, a complete mechanism of the MTM process will be detailed including sub-routes, alternative mechanisms (§1.2.1.1) and the formation of by-products. Let us continue with other zeolite materials with high-impact possibilities to disrupt methane-to-methanol subject area.

Another remarkable zeotype material that has drawn attention in the recent years is the Silicoaluminophosphate (SAPO), as it is possible to dope metal and inorganic non-metal atoms in this material (§1.3.2). Currently, SAPOs have been used in the methanol-to-olefin (MTO) process with superior performance, selectivity, and stability,[109,134,383,384] but direct methane to methanol has barely been explored,[385] a potential subject area to bear in mind.

On the other hand, AlPOs present an electrically neutral lattice, bringing about an absence of acidic and basic activity, but despite this, they possess an ionic character, which facilitate the incorporation of transition metals with various transition states, creating metal-substituted aluminophosphates in the process (MeAPOs) (M: Mg, Zn, Fe, Ti, etc.). The applications of this zeotype are highlighted in the redox catalysis,[386] since as mentioned before (§1.3.2), these transition-metals with the framework flexibility of AlPOs could be beneficial for the MTM process.

Similar to the previous instance, there is no literature involving the use of MeAPOs for the direct methane to methanol reaction, so with these materials and SAPOs, a new state-of-the-art technology can be uncovered to turn methane into methanol, thereby opening up new alternatives for green processes, attending to their unique features mentioned above. SAPOs and MeAPOs will be introduced in chapter 5 as a result of the different results and conclusions described in chapters 3 and 4, expanding the actual limits of the methane to methanol chemical reaction.

Upon thorough examination of the literature, it is worth mentioning that the vast majority of the cited works pertain to positive active sites. However, using cationic species imply a stronger binding with the produced methanol, hampering its desorption, and requiring water assistance,[262,387] so a cationic species does not necessarily have to be the most optimal active site for the reaction.

Interestingly, new works have proposed anionic species as alternative active sites with promising features.[215,387,388] In relation to cationic species, they present weaker CH_3 interaction with the active site after C-H breakage, thereby reducing the possibility of methanol overoxidation and weaker interaction with the produced methanol, which facilitates the desorption step. On the other hand, the activation of C-H bond on anionic systems results more difficult in contrast with cationic systems[389] and the negative charge must be preserved in the metal in order to avoid the methyl radical adsorption. Furthermore, the implementation of these catalytic systems into zeolites, monolayers, composites or any other kind of support remains unclear as of today. This can also be applied to homogeneous catalysis.

However, zeolitic materials based on close-neutral active centres have not been explored. Considering that these catalysts could be nearly as active as cationic species[390] with lower methanol desorption energies and active centre attachment, many of the problems portrayed in the cationic zeolite systems could be overcome, becoming a viable alternative for the MTM process.

Precisely, there is a class of compounds that have captivated scientists for their unique physical and chemical properties, in addition with the ability to tailor these properties at will in a very predictable way: Metal nanoclusters, an aggrupation of metal atoms that possess a wide number of applications, one of them consisting of the catalysis of different chemical reactions with modulated activities depending on the size, shape and charge of the aggregate (§1.4.2). In fact, in the methane-to-methanol process, it has been demonstrated that gold and rhodium nanoclusters have reported methanol and methyl hydroperoxide conversion.[391,392]. In chapter 3 the different approaches to this kind of

catalyst will be explained in detail, and chapter 4 will develop these concepts into a real system.

Taking into account the performance of particulate Methane Monooxygenase (pMMO) at activating methane in dinuclear copper sites at mild conditions, the extensive bibliography about copper-exchanged zeolites, the possibilities of AlPO and MeAPO frameworks for new innovative catalysts, the opportunity to open up a new field of study in relation to close-neutral metallic active centres and the unique properties of metal nanoclusters; sub-nanometre copper clusters have been selected as the main subject matter of this dissertation.

But prior to set forth our research, it is necessary to present the theoretical fundamentals of computational chemistry in which this doctoral thesis is based on. Let us start out by introducing a brief historical context of this field and all the related concepts that conduct us to the results gathered in this dissertation.

Chapter 2 Computational Chemistry: Theoretical background and Methodology

During the course of this chapter, the fundamentals in which computational chemistry is based on, and the consequent models derived from theory will be described.

A brief introduction to computational chemistry is presented. Henceforth, the very basic fundamentals ranging from the Schrödinger equation, crossing Hartree-Fock to Density Functional Theory will be detailed.

Following that, the methodology employed to perform the computational calculations will be introduced. More specifically, the approximations that have been considered and the use of planewaves to describe the catalytic system.

Lastly, the periodic models of the microporous materials used in this study will be detailed.

2.1 Computational Chemistry: A theoretical field of science

Computational chemistry is underpinned in the principles of quantum mechanics (QM) to fully understand the complicated electronic structure and properties of atoms and molecules. This field of science has its roots in the history of quantum theory, when Werner Heisenberg set the first mathematical formulation in 1925 showing a new perspective of the world (*matrix mechanics*),[393] and one year later, Erwin Schrödinger posed his famous equation based on the wave equation (*wave mechanics*),[394] which turned out to be equivalent. Later this year, Max Born proposed the square modulus of the wave function as the probability for finding the particle.[395]

At this time, there was already physicists trying to unravel the mysteries of the quantum world using hand-cranked calculating machines,[396] like Douglas Rayner Hartree, whom will be mentioned in the next section (§2.2).

After the second world war with the development of electronic computers in the 1950s, quantum chemistry took a step forward with the first computational experiments to predict qualitative and quantitative properties of the chemical reality with an astonishing speed compared to former methodologies. Nevertheless, these calculations were prohibitive to the majority of chemists and still, the computational cost required to carry out these experiments was enormous for very simple atoms and molecules.

After the refinement of methods (§2.3.1), approximations (§2.3.2) and algorithms throughout the 1960s and 1970s, the standardisation of these into software packages (§2.6) offered computational feasible alternatives with accurate basis sets (§2.4) to simulate different chemical environments using semi-empirical and ab-initio methods (§2.2).[397–401] Little by little, chemists were approaching to deeper levels of chemical accuracy.

This process continues at the present. As the computational power increases, simulations with hundreds of atoms or more in models (§2.7) are now possible in a couple of days, becoming a solid support or even an alternative to empirical data and experiments. In the future, only the scientific ingenuity will make progress in this theoretical subject area. For a more complete historic perspective of quantum chemistry, please consult these references.[402,403]

Below, a concise and precise resume of the most relevant topics of quantum chemistry in this dissertation will be expounded. Let us start with the cornerstone of quantum chemistry, the Schrödinger equation.

2.2 The Schrödinger equation

In 1926, Erwin Schrödinger established the basics of quantum mechanics with his famous *Schrödinger equation*,[394] which is an alternative mathematical method from Werner Heisenberg's[393] that introduced the notion of the wave function (Ψ), a mathematical concept that defines the state of a system. The time-independent non-relativistic equation is plotted down below (2.1):

$$\hat{H}|\Psi\rangle = E|\Psi\rangle \tag{2.1}$$

Where Ĥ is the Hamiltonian operator, E is the energy of the system and Ψ the wave function. This operator includes the contributions of the potential and kinetic energies (2.2):

$$\hat{H} = \hat{T} + \hat{V} = \hat{T}_n + \hat{T}_e + \hat{V}_{NN} + \hat{V}_{eN} + \hat{V}_{ee} \tag{2.2}$$

Where $\hat{T}_n$ and $\hat{T}_e$ are the kinetic energy for the nuclei and electrons, respectively, and $\hat{V}_{NN}$, $\hat{V}_{eN}$, and $\hat{V}_{ee}$ correspond to the potential energy of all particle pairs interacting with each other, which means nucleus-nucleus, electron-nucleus, and electron-electron, respectively.

The solutions of this equation are eigenvalues that satisfy the discrete electronic levels in the eigenvalue spectrum that are manifested in the atomic orbitals (Figure 2.1). Unfortunately, this equation has only analytic solutions for diatomic molecules like Hydrogen or Helium, because otherwise, the complex differential equations make the wave equation practically unsolvable.

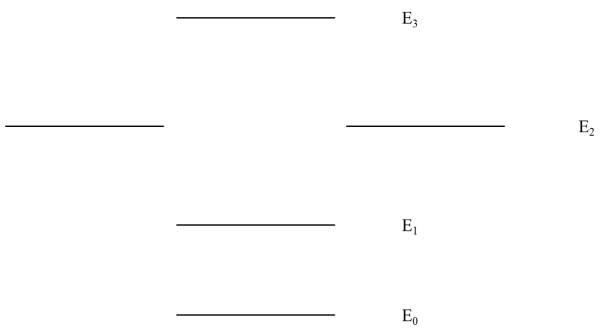

Figure 2.1 - Energy eigenstates associated to discrete eigenvalues in the eigenvalue spectrum. Degenerated levels correspond to linearly independent wave functions with the same eigenvalue.

Knowing that the nuclei are much heavier than electrons (~1836 times heavier), Born and Oppenheimer concluded that from the perspective of electrons, the nuclei are static because their movement is quite slow compared to electrons, and from the point of view of the nuclei, the electrons behave like an electronic cloud that can adiabatically adapt to the motion of the nucleus. Considering this, the term $\widehat{T}_n$ is nullified, and $\widehat{V}_{NN}$ is constant. This is the *Born-Oppenheimer approximation (BO)*,[404] an essential concept that permits the decoupling of the nuclei and electrons motions, giving rise to fundamental concepts of chemistry like the 3D model of a molecule, the structure of a molecule.

Considering this approximation, equation (2.1) can be reformulated in terms of electronic energies to equation (2.3)

$$H_{el}\psi_k(\vec{r};\vec{R}) = E_{el}\psi_k(\vec{r};\vec{R}) \qquad (2.3)$$

Where E_{el} are the electronic eigenvalues, ψ_k are the eigenfunctions and H_{el} is the electronic Hamiltonian (*clamped nuclei Hamiltonian*), which is depicted down below (2.4):

$$H_{el} = -\sum_i \frac{\hbar^2}{2m}\Delta_i + \sum_i \sum_{j>i} \frac{Z_i Z_j e^2}{4\pi\varepsilon_0 |\vec{R}_i - \vec{R}_j|} - \sum_i \sum_j \frac{Z_i e^2}{4\pi\varepsilon_0 |\vec{R}_i - \vec{r}_j|} + \sum_i \sum_{i<j} \frac{e^2}{4\pi\varepsilon_0 |\vec{r}_i - \vec{r}_j|} \qquad (2.4)$$

Where m is the electron mass, $\hbar$ is the reduced Planck constant, Z_i and Z_j are the nuclei charges, e is the electron charge and ε_0 is the vacuum permittivity.

Despite this approximation, the Schrödinger equation is still insoluble for heavier elements and molecules, so at this point, scientists tried to fix this problem with different approaches.

The first successful and accurate approach to the solution of this problem came hand in hand with Douglas Rayner Hartree and Vladimir Fock with the Hartree-Fock method (HF),[405,406] that consists in the minimisation of the mean energy value of the Hamiltonian through self-consistent steps based on the variational principle (2.5) using an approximated antisymmetric wave function composed of N electrons, denoted as the *Slater determinant* (2.6)

$$E = \frac{\langle \Psi | \hat{H} | \Psi \rangle}{\langle \Psi | \Psi \rangle} \tag{2.5}$$

$$\Phi_{SD} = \frac{1}{\sqrt{N!}} \begin{vmatrix} \chi_1(x_1) & \chi_2(x_1) & \cdots & \chi_N(x_1) \\ \chi_1(x_2) & \chi_2(x_2) & \cdots & \chi_N(x_2) \\ \cdots & \cdots & \cdots & \cdots \\ \chi_1(x_N) & \chi_2(x_N) & \cdots & \chi_N(x_N) \end{vmatrix} \tag{2.6}$$

Where χ_i are the orthonormal spin-orbital wavefunctions, x_N includes the coordinates of space and spin, and N are the total electrons of the system.

This mode of expressing the wave function in (2.6) has advantages, since the antisymmetric determinant respect to an interchange of any two electron positions satisfies Pauli's exclusion principle.[407] The minimisation of equation (2.5) in regard to the spin-orbitals defined in equation (2.6) lead to the Hartree-Fock equation (2.7)

$$\hat{f}_i \chi_i = \epsilon_i \chi_i \tag{2.7}$$

Where $\hat{f}_i$ is the one-electron Fock operator, which is defined down below (2.8):

$$\hat{f}_i = -\frac{1}{2}\Delta_i - \sum_{j=1}^{M} \frac{Z_j e^2}{4\pi\varepsilon_0 \vec{r}_{ij}} + V^{HF}(i) \tag{2.8}$$

Where V^{HF} is the Hartree-Fock potential, which represents the mean potential on the electron *i* occasioned by the presence of the remaining N-1 electrons. This potential can be expressed as (2.9):

$$V^{HF}(x_i) = \sum_{j=1}^{N} \left(\hat{J}_j(x_i) - \hat{K}_j(x_i) \right) \tag{2.9}$$

Where $\hat{J}_j$ is the Coulombic spin-orbital Operator, which describes the electrostatic repulsion of the charge distributions and $\hat{K}_j$ is the exchange spin-orbital operator, which is a quantum mechanical effect that only occurs between identical particles. Both operators are calculated as depicted in (2.10) and (2.11):

$$\hat{J}_j(x_1) = \int dx_2 \left|\chi_j(x_2)\right|^2 \vec{r}_{12}^{-1} \tag{2.10}$$

$$\hat{K}_j(x_1)\chi_i(x_1) = \int dx_2 \chi_j^*(x_2) \vec{r}_{12}^{-1} \chi_i(x_2) \tag{2.11}$$

Due to the variational principle, the energy calculated with (2.5) is an upper limit to the true ground energy of the system (See figure 2.2). Therefore, the Hartree-Fock equation is focused on the best set of spin orbitals for the minimisation of this energy to approach as near as possible to the true energy in the ground state by the self-consistent field (SCF) method. This means that in order to minimise the energy of the system, initial guesses of $\hat{J}_j$ and $\hat{K}_j$ operators are taken to build a first set of spin-orbitals to solve the Hartree-Fock equations. Once the eigenvalue equations are solved, new set of spin-orbitals are obtained, and these ones are used to construct again the coulomb and the exchange operators to solve again the Hartree-Fock equations. This process is iteratively done until one condition is satisfied: The input and output orbitals differ less than a threshold value that is previously defined at the beginning. The result of the SCF method is the Hartree-

Fock energy (E_{HF}). The difference between the energy of the ground state level and the energy of the Hartree-Fock is called correlation energy (2.12):

$$E_C^{HF} = E_0 - E_{HF} \tag{2.12}$$

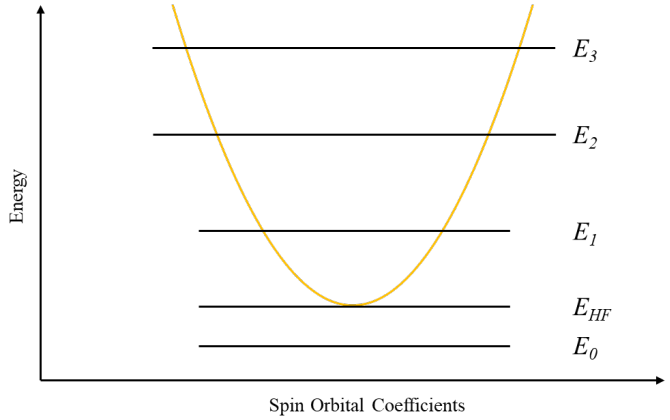

Figure 2.2 - Variational theorem and Hartree-Fock approximation.

In spite of the fact that the HF method has not been employed for the attainment of this dissertation, it has been described for its importance in quantum chemistry in the development of more advanced methods based on it, because it was ahead of its time for being the first method to compute analytically integrals and for reducing the many-electron problem to single-electron problems. Unfortunately, it entails a severe drawback, since it lacks in the description of electron correlations conducting to a poor description of the electronic structure. Furthermore, this method is not able to give an explanation to other problems like bond breaking, as they require multiple determinants to be accurately described. For these reasons, correlation methods (a.k.a. post HF methods) were developed, like configuration interaction (CI), coupled-cluster (CC) or Møller-Plesset (MP) perturbation theory.[408–411]

Apart from post-HF methods, different approaches were derived from HF. On one hand there are ab-initio methods, which compute the fundamental properties of a molecule or material using the first-principle laws of quantum physics without using previous knowledge

or experimental data about the system.[397,398,401] For that motive, as the level of theory progresses, better approximations to the real material or molecule can be performed at the expense of computational cost, obtaining better descriptions of the system.

On the other hand, there are semiempirical methods, which take experimental data or previous results of ab-initio calculations to carry out computations with less demanding computational cost, but less accurate compared to ab-initio methods.[399,400]

Nevertheless, other scientists adopted different points of view. Instead of solving the Schrödinger equation, the system would be characterised by the electron density. This dissertation is founded on the ideas of these scientists that created the Density Functional Theory (DFT), which will be further explained in the section below.

2.3 The settlement of Density Functional Theory (DFT)

The DFT method construct was originated in 1927 just in parallel to Schrödinger discoveries, when Enrico Fermi and Llewellyn Thomas performed independent atomic calculations using the electron density as the main variable instead of the wave function in the forerunner theory called the Thomas-Fermi (TF) theory back then.[412–414] However, this theory was proved to be inefficient in computing the shell structure of atoms, anticipating such things like that all molecules are less stable than their constituent atoms.[415]

It took several decades until 1964 when Pierre Hohenberg and Walter Kohn established the fundamentals of DFT theory in a landmark paper in which they stated that the ground state energy for an electronic system is a functional of the electron density $\rho(r)$ for non-degenerate systems, leading to the theorems of Hohenberg-Kohn (HK).[416] Although these theorems were also expanded to degenerate ground states later.[417,418]

To begin with, $\rho(r)$ is defined as the density of the electron cloud carrying N electrons, and the integration of the whole 3D space results in the number of electrons (2.13):

$$\int \rho(\vec{r}) d\vec{r} = N \tag{2.13}$$

Where *r* represents the volume unit of the system.

Once again, the Hamiltonian is defined as the sum of the potential and kinetic energy (2.2), but this time, the interaction between the nuclei and electrons is expressed through the external potential for N electrons (2.14):

$$\hat{V}_{eN} = \sum_{i=1}^{N} \hat{v}_{ext}(\vec{r}_i) \tag{2.14}$$

Naturally, nuclei are considered fixed, so the potential contribution of the nucleus-nucleus interaction ($\hat{V}_{NN}$) is a constant as stated by the BO approximation (§2.2).

The first theorem dictates that the external potential is uniquely determined by the ground state density ρ_0, in other words, two external potentials cannot express the same ground state electron density. To prove this, the authors used the "*Reductio ad absurdum"* method. For a more comprehensive demonstration, refer to the original paper or the one published by Levy in 1982.[416,419]

The second theorem states that the ground state density can be calculated minimising the energy functional, obeying the variational principle as a corollary. Hence, the exact ground state of the system is the global minimum, and the density which minimise this energy is the exact ground state density.

Unifying equations (2.2) and (2.14), the formula for the ground state energy depending on the electron density is obtained (2.15):

$$E_v(\rho) = \int \hat{v}_{ext}(\vec{r})\rho(\vec{r})\, d\vec{r} + F_{HK}[\rho] \tag{2.15}$$

And for the exact ground state energy (2.16):

$$E_0(\rho_0) = \int \hat{v}_{ext}(\vec{r})\rho_0(\vec{r})\, d\vec{r} + F_{HK}[\rho_0] \tag{2.16}$$

Where $E_0(\rho)$ is the ground state energy, $\hat{v}_{ext}$ is the one-electron external potential operator, ρ_0 is the ground state electron density and $F_{HK}[\rho_0]$ is the Hohenberg-Kohn functional, a universal functional that encompasses the terms of kinetic and potential energy that are not collected in the external potential, which is valid for any number of particles and any external potential (2.17):

$$F_{HK}[\rho_0] = \min_{\Psi \to \rho_0} \langle \Psi | \hat{T} + \hat{V}_{ee} | \Psi \rangle \tag{2.17}$$

To ensure that the minimisation of the density is positive in all space and satisfies equation (2.13), the Lagrange multipliers optimisation method is used by means of an undetermined Lagrange multiplier denoted as μ. Then, the minimisation proceeds as (2.18), giving rise to the Euler–Lagrange variational equation:

$$\frac{\partial[E_v(\rho) - \mu(\int \rho(\vec{r}) - N)]}{\partial\rho(\vec{r})} = 0 \qquad (2.18)$$

Minimising equation (2.18) results in equation (2.19) for the Lagrange multiplier:

$$\mu = \hat{v}_{ext}(\vec{r}) + \frac{\partial F_{HK}[\rho]}{\partial\rho(\vec{r})} \qquad (2.19)$$

Curiously, this Lagrange multiplier could be physically identified as the chemical potential, a thermodynamic concept that denotes the variation of chemical energy of the system respect to the number of moles of a species, in other words, the tendency to chemically react to form new substances, which is very related to the electrons valence shell. Equation (2.20) pictures the thermodynamic formula:

$$\mu = \frac{\partial E}{\partial N} \qquad (2.20)$$

However, discussions regarding the refutation of the physical meaning of this multiplier exist. Other perspectives suggest that this Lagrange multiplier reflects the gauge freedom of the external potential $\hat{v}_{ext}$, or simply an arbitrary constant.[420]

On balance, if we know the ground state density ρ_0, we know the external potential of the system, which implies a fully determined Hamiltonian to obtain the many-body ground state and excited states wave functions Ψ with all the information of the system[421] as a functional of the ground state electron density ρ_0. Thus, all the properties of the system are determined by the ground state density ρ_0 (2.21).

$$\begin{array}{ccc} \hat{v}_{ext}(\vec{r}) & \Longleftarrow & \rho_0(\vec{r}) \\ \Downarrow & & \Uparrow \\ \hat{H}(N, Z_j, \vec{r}_{ij}) & \Rightarrow & \Psi \end{array} \qquad (2.21)$$

This formulation is quite useful in comparison with the HF method, not only is the resolution of the Schrödinger equation avoided, posing as a viable alternative that can be measured experimentally in contrast to the wave function, but also requires less computational cost (n^3) than the HF method (n^4). Furthermore, DFT is computed using 3 spatial variables as compared with 4N variables in the HF method (3N spatial variables and N spin variables).

2.3.1 Kohn-Sham self-consistent method

One of the drawbacks of the HK theorems is that it is not possible to know the Hohenberg-Kohn functional $F_{HK}[\rho]$, in specific, the term for the kinetic energy. For this problem, Walter Kohn and Lu Jeu Sham posed a different alternative to approximate $F_{HK}[\rho]$.[422]

They proposed a fictional system with N non-interacting electrons, wherein the ground state density is the real density for the system with interacting electrons. For that purpose, the independent-electron approximation of kinetic energy is used since this kinetic energy is exactly calculated from the non-interacting Schrödinger wave equation. Subsequently, an unknown exchange-correlation term which includes all the errors associated with the non-interacting system is introduced to approximate the real ground state energy. Thus, the interacting electron system can be calculated from the non-interacting electron system by subjecting the system to an effective potential V_{eff} also known as the Kohn-Sham potential, bringing back the concept of single electronic orbitals from the HF method (§2.2).

In the Kohn-Sham (KS) formulation, the universal functional from the Hohenberg-Kohn theorem is expressed through equation (2.22):

$$F[\rho] = \hat{T}_s[\rho] + \hat{J}[\rho] + \hat{E}_{xc}[\rho] \qquad (2.22)$$

$$J[\rho] = \frac{1}{2}\iint \frac{\rho(\vec{r}_i)\rho(\vec{r}_j)}{\vec{r}_{ij}} d\vec{r}_i d\vec{r}_j \tag{2.23}$$

Where T_s is the kinetic energy of a non-interacting system at a given electron density ρ, J is referred to the classical Hartree (Coulomb) repulsion of the density [Eq. (2.23)] and $\widehat{E}_{xc}$ is the exchange-correlation energy, which represents the non-classical electrostatic interaction energy and the difference between the kinetic energies of the interacting and non-interacting systems. This last term includes all the unknown values of the system.

So, based on equations (2.15) and (2.22), the ground state density formula results in equation (2.25):

$$E_v(\rho) = \int \rho(\vec{r})\hat{v}_{ext}(\vec{r})\, d\vec{r} + \hat{T}_s[\rho] + \frac{1}{2}\iint \frac{\rho(\vec{r}_i)\rho(\vec{r}_j)}{\vec{r}_{ij}} d\vec{r}_i d\vec{r}_j + \hat{E}_{xc}[\rho] \tag{2.24}$$

Using the Euler-Lagrange equation, equation (2.24) can also be expressed as (2.25):

$$\mu = \hat{v}_{eff} + \frac{\partial T_s(\rho)}{\partial \rho} \begin{cases} \hat{v}_{eff} = \hat{v}_c + \hat{v}_{xc} \\ \hat{v}_c = \hat{v}_{ext} + \int \dfrac{\rho(\vec{r}_j)}{|\vec{r}_i - \vec{r}_j|} d\vec{r}_j \\ \hat{v}_{xc} = \dfrac{\partial E_{xc}[\rho]}{\partial \rho(\vec{r})} \end{cases} \tag{2.25}$$

Being $\hat{v}_{eff}$ the effective potential, $\hat{v}_c$ the coulomb potential and $\hat{v}_{xc}$ the exchange-correlation potential.

Therefore, a non-interacting Hamiltonian can be constructed as a sum of one-electron operators, being equal to the true Hamiltonian for a non-interacting reference system (2.26):

$$\hat{\mathcal{H}} = -\frac{1}{2}\sum_{i=1}^{N} \Delta_i + \sum_{i=1}^{N} \hat{v}_{eff}[\rho(\vec{r}_i)] \tag{2.26}$$

In order to derive the Kohn-Sham orbitals from the ground state density, the Kohn-Sham equation, analogous to the HF method, is pictured below (2.27):

$$\hat{f}_{KS}\varphi_i = \epsilon_i\varphi_i \tag{2.27}$$

$$\hat{f}_{KS} = -\frac{1}{2}\Delta + \hat{v}_{eff}[\rho(\vec{r}_i)] \tag{2.28}$$

Where $\hat{f}_{KS}$ is the Kohn-Sham one-electron operator (2.28) and φ_i represents the Kohn-Sham orbitals, in other words, the one-electron eigenfunctions of a many-body system defined by the Slater determinants.

Finally, the new electron density using the new Kohn-Sham orbitals is calculated as equation (2.29):

$$\rho(\vec{r}) = \sum_{i=1}^{N} |\varphi_i(\vec{r})|^2 \tag{2.29}$$

These fundamentals are the principles of the procedure employed in multiple electronic state calculations to compute the total energy of the system and to unravel the physical and chemical properties of a material iteratively through the SCF method. Next, a complete scheme of the process is illustrated:

Scheme 2.1 - Computational flowchart of the Kohn-Sham iteration procedure

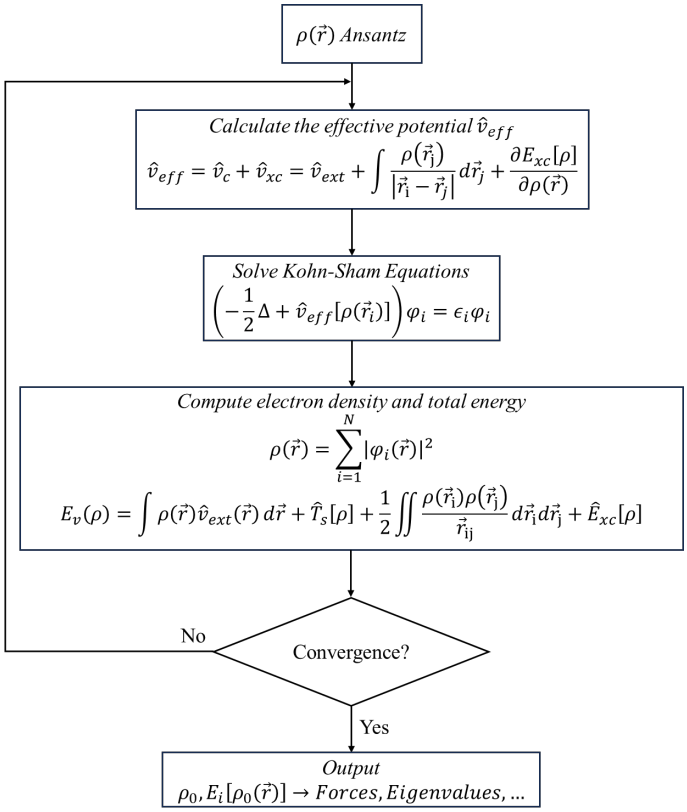

Even though the KS orbitals lack in physical meaning in comparison with HF except for the energy of the highest occupied KS orbital (HOMO), which is in theory equal to the first ionization potential,[423,424] this theory is exact in principle, and addresses the correlation problems posed in the HF method (§2.2) with a reasonable computational cost. Nevertheless, it still presents a main issue, which is related to the analytical form of exchange-correlation functional. The nature of this functional is still unknown and needs good approximations to accurately describe the system and the election of the exchange-correlation approximation to obtain the best results is difficult to predict.

In the next sub-sections, the different exchange-correlation functionals that scientists have proposed to resolve the inherent problems of the Kohn-Sham theory will be discussed.

2.3.2 The quest to find the best approximation to the exchange-correlation functional

With the passage of time, DFT advances have provoked the minimisation of errors in the definition of the exchange-correlation functional, making DFT a very versatile tool. All of these advances are resumed in the Jacob's ladder,[425] an illustration that depicts the levels of sophistication of the different exchange-correlation functionals in search for chemical accuracy to get closer to reality.

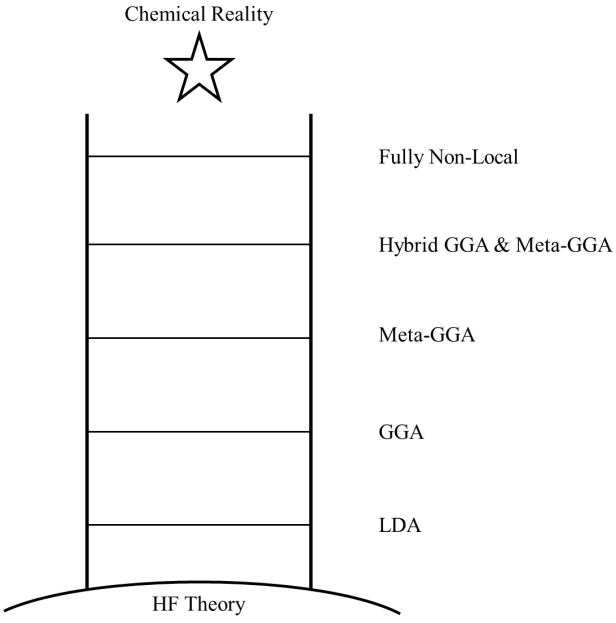

Figure 2.3 - DFT Jacob's Ladder

The steps more relevant to this dissertation will be explained in more detail below.

2.3.2.1 Local-density Approximation (LDA)

The first approximation was suggested by the authors of the Kohn-Sham theory in the same paper they proposed this new paradigm.[422] It is clear that the density distribution in a molecule or material is inhomogeneous, but within a small volume, its homogeneity may be assumed. Thus, everything is decided locally, and the contribution of the exchange-correlation term can be computed as a product of the small volume and the exchange-correlation energy density from the homogeneous gas theory. This is the *Local-density approximation* (LDA) and replaces the exchange-correlation potential at each point by means of a simple homogeneous electron gas model in a box with a density equal to the local density at the point.

The formula to define the exchange-correlation energy is down below (2.30):

$$E_{xc}^{LDA}[\rho] = \int \rho(\vec{r})\varepsilon_{xc}[\rho(\vec{r})]d^3\vec{r} \qquad (2.30)$$

Where $\varepsilon_{xc}[\rho(r)]$ is the exchange-correlation energy of each particle in a uniform electron gas.

Moreover, this term is composed of two extra terms illustrated in equation (2.31):

$$\varepsilon_{xc} = \varepsilon_x[\rho(\vec{r})] + \varepsilon_c[\rho(\vec{r})] \qquad (2.31)$$

$$\varepsilon_x[\rho(\vec{r})] = -\frac{3}{4}\left(\frac{3}{\pi}\right)^{1/3}\rho^{1/3} \qquad (2.32)$$

Where ε_x is the exchange energy, which is extracted from Dirac's work,[426] and ε_c is the correlation energy, which is derived from quantum Monte Carlo simulations.[427,428]

LDA has been successful in determining the electronic energy bands and related physicochemical properties of metals and semiconductors. In fact, it fulfils the sum-rules of the exchange-correlation hole, which is the probability of finding an electron r_j given that there is an electron at r_i, because it generates a reasonable estimation of the spherical average[429,430] and the errors in the exchange and correlation energy densities tend to cancel.

On the other hand, LDA is not rigorous for systems with a high non-uniformity of the electron density. E.g., LDA tends to overestimate metal d-band, semiconductor's band gap, covalent and ionic bonds. In addition, it possesses deficiencies describing hydrogen bonds.

Later on, LSDA was developed, a more accurate exchange-correlation model that considered spin contributions.[428,431]

2.3.2.2 Generalized Gradient Approximation (GGA)

To go beyond of LSDA in the treatment of inhomogeneous electron distributions, Perdew, Becke, Langreth, Lee, and other scientists in the 1980s proposed new approximations that introduce a gradient component ∇_ρ to more properly describe the true electron density.[432–435]

The first implementation was the *gradient-expansion approximation* (GEA), which was already suggested by Kohn and Sham in their original work.[422] The formula for the exchange-correlation is depicted below (2.33):

$$E_{xc}^{GEA}[\rho] = \rho(\vec{r})\varepsilon_{xc}^{LDA}[\rho(\vec{r})]d^3\vec{r}\left[1 + C_{xc}\left(\frac{\vec{\nabla}_{\rho(\vec{r})}}{2k_F(\vec{r})\rho(\vec{r})}\right)^2\right] \quad (2.33)$$

$$k_F(\vec{r}) = [3\pi^2\rho(\vec{r})]^{1/3} \quad (2.34)$$

$$s(\vec{r}) = \frac{\vec{\nabla}_{\rho(\vec{r})}}{2k_F(\vec{r})\rho(\vec{r})} \quad (2.35)$$

Where ε_{xc}^{LDA} is the exchange-correlation of the LDA approximation, C_{xc} is a fitting constant, k_F is the Fermi wave vector (2.34) and $s(\vec{r})$ is a dimensionless quantity (2.35).

Notwithstanding, GEA approximations brought worse results than LDA in real systems and violates the sum-rules,[429,432] so this approximation was ruled out. After the failure of GEA, the *generalized gradient approximation* (GGA) was developed. As in LDA, GGA splits the exchange-correlation energy into two terms for the exchange and correlation energy, respectively, in which the correlation energy is determined through Monte Carlo simulations (2.36):

$$E_{xc}^{GGA}(\rho) = \int f(\rho, \nabla\rho) d\vec{r} = E_X^{GGA} + E_C^{GGA} \qquad (2.36)$$

In general, GGA provides more accurate approximations than LDA with good descriptions of the geometries, frequencies, charge densities and hydrogen bonds, but still provokes deficiencies for weaker interactions and an underestimation of the band gap. Among the different GGA functionals in the literature like PW91[436] or LYP,[434] the PBE functional has been employed in this dissertation.[437] The exchange energy formulation is illustrated in equation (2.37):

$$E_x^{PBE} = -\int \rho(\vec{r})^{4/3} \left[\frac{3}{4}\left(\frac{3}{\pi}\right)^{1/3} + \frac{\mu[s(\vec{r})]^2}{1+\mu[s(\vec{r})]^2/\kappa}\right] d\vec{r} \qquad (2.37)$$

Where μ and κ are fundamental constants with the values 0.21951 and 0.804, respectively.

2.3.2.3 Meta-GGAs and Hybrid Functionals

To add more recent progress in this field, two more exchange-correlation functionals will be expounded. Meta-GGA functionals[438,439] were developed to correct GGA functionals adding the kinetic energy density τ (2.38 & 2.39):

$$E_{xc}^{mGGA}(\rho) = \int f(\rho, \nabla\rho, \tau)d\vec{r} \quad (2.38)$$

$$\tau(\vec{r}) = \sum_{i}^{N} |\nabla\varphi_i(\vec{r})|^2 \quad (2.39)$$

Where φ_i are the self-consistent KS orbitals.

Lastly, hybrid functionals were proposed. This functional family corrects GGA functionals using a mix of Hartree-Fock exchange integral with GGA exchange functionals at a constant ratio based on the adiabatic connection. Two of the most widely known are B3LYP[434,435,440,441] and HSE06.[442,443]

2.3.2.4 The inclusion of dispersion forces in DFT

To provide a complete chemical explanation of a molecule or a material, it is essential to comprehend the weak interactions between atoms and molecules in the long-range. Unfortunately, DFT was unable to accurately predict these because of the non-local nature of these interactions such as the van der Waals forces (vdW), which are systematically underestimated.

In light of the exposed problem, Stefan Grimme et al.[444–446] designed a method to implement dispersion forces in DFT which was coined as DFT-D. It is hinged upon Becke's power-series ansatz from 1997,[447] and is explicitly parameterized by including damped atom-pairwise dispersion corrections of the form $C_6 \cdot R^{-6}$, in which C_6 coefficients are referred to atom pairs.

The old Grimme-D2 method calculates the total energy of the system based on equation (2.40):

$$E_{DFT-D2} = E_{KS-DFT} + E_{disp} \quad (2.40)$$

In which, E_{disp} is an empirical dispersion correction given by equation (2.41):

$$E_{disp} = -s_6 \sum_{A=1}^{N_{at}-1} \sum_{B=A+1}^{N_{at}} \frac{C_6^{AB}}{R_{AB}^6} f_{dmp}(R_{AB}) \qquad (2.41)$$

Where N_{at} is the number of atoms in the system, C_6^{AB} denotes the dispersion coefficient for atom pair AB, s_6 is a global scaling factor that only relies on the standard KS density functional used, R_{AB} is the interatomic distance, and f_{dmp} is the damping function that oscillates between 0 and 1, which is defined in equation (2.42):

$$f_{dmp}(R_{AB}) = \frac{1}{1 + e^{-d(R_{AB}/R_r - 1)}} \qquad (2.42)$$

Where R_r is the sum of atomic vdW radii.

Years later, Grimme himself corrected the method refining the dispersion energy with high dispersion levels and little tweaks to the damping function, giving rise to DFT-D3[446]. However, this method can only be used for the first 94 elements in the periodic table.

In this correction, the DFT-D3 energy, E_{disp} and f_{dmp} take this shape:

$$E_{DFT-D3} = E_{KS-DFT} - E_{disp} \qquad f_{d,n}(r_{AB}) = \frac{s_n}{1 + 6\left(r_{AB}/s_{R,n}R_{0AB}\right)^{-\alpha_n}} \qquad (2.43)$$

$$E_{disp} = E^{(2)} + E^{(3)} \qquad E^{(3)} = \sum_{ABC} f_{d,(3)}(\bar{r}_{ABC})\, E^{ABC} \qquad (2.44)$$

$$E^{(2)} = \sum_{AB} \sum_{n=6,8,10,\ldots} s_n \frac{C_n^{AB}}{r_{AB}^n} f_{d,n}(r_{AB}) \qquad E^{ABC} = \frac{C_9^{ABC}(3\cos\theta_a \cos\theta_b \cos\theta_c + 1)}{(r_{AB}r_{BC}r_{CA})^3} \qquad (2.45)$$

Where C_n^{AB} denotes the averaged (isotropic) nth-order dispersion coefficient, for atom pair AB, r_{AB} is the internuclear distance, E^{ABC} is the leading nonadditive dispersion term for three atoms ABC, $\theta_{a,b,c}$ are

the internal angles of the triangle form by the three atoms and C_9^{ABC} is the triple-dipole constant.

Analogously, the Becke-Johnson (BJ) damping can also be used in this method (2.46):

$$f_{d,n}(r_{AB}) = \frac{s_n r_{AB}^n}{r_{AB}^n + (a_1 R_{0AB} + a_2)^n} \tag{2.46}$$

In the case of this dissertation, Grimme DFT-D2 method and damping function formulated in equation (2.42) have been used to carry out periodic DFT calculations using the Vienna Ab-initio Simulation Package (VASP). For all the calculations, the default parameters of the equations presented above have been used.

2.4 Basis Sets

In quantum chemistry, the wavefunction is constructed as a linear combination of independent basis functions, forming all of them the basis set. Hence, if we were able to use an infinite set of these functions, this mathematical concept could be used to exactly represent the atomic and molecular orbitals for finite systems, and bands for periodic systems. However, it is computationally impossible to do that. In its place, a finite basis set is determined, and the basis functions must be selected to create a well-defined basis set able to reflect the nature of the problem and permit calculations to compute a wide range of properties apart from energy-related ones.

2.4.1 Atom-centred Basis Sets

The first basis set dates back to 1930, when Slater designed an approximation of the wave function with a set of spherical harmonics, known as the Slater-Type Orbitals (STOs)[448] (2.47):

$$\chi_{\zeta,n,l,m}(r,\theta,\varphi) = Nr^{n-1}Y_{l,m}(\theta,\varphi)e^{-\zeta,r} \qquad (2.47)$$

Being r, θ and φ the spherical coordinates, N is a normalisation constant, $Y_{l,m}$ is the spherical harmonic function, ζ is the orbital exponent and n,l and m are the quantum numbers. Nevertheless, these orbitals are computationally difficult.

This problem was solved when in 1950, Samuel Francis Boys introduced the Gaussian-Type Orbitals (GTOs),[449] which are easier to compute (2.48):

$$\chi_{\zeta,i,j,k}(x,y,z) = Nx^i y^j z^k e^{-\zeta r^2} \qquad (2.48)$$

Here, x, y and z are the cartesian components of the distance between the electron and the centre of the GTO. The sum of the powers i, j, k in the angular part of the function defines the angular momentum of the atomic orbital.

By definition, a minimal set is the one that is able to describe the core and valence electrons of an atom. Taking into account that the valence and virtual orbitals are key to describe chemical reactivity and other properties, minimal sets does not permit a precise description of the molecular environment. Furthermore, GTOs does not properly describe the behaviour in the short and long ranges due to the r^2 dependence in equation (2.48) in comparison with STOs.[450]

As a consequence, W. J. Hehre et al. formulated that STOs could be expressed as a linear combination of primitive gaussian functions, defining the contracted Gaussian functions.[451] In this class, the most popular basis is the STO-NG basis, where N is an integer (2.49):

$$\phi_{STO-NG} = \sum_i a_i \varphi_{i,GTO} \qquad (2.49)$$

For which, $\varphi_{i,GTO}$ is referred to a primitive gaussian function whilst ϕ_{STO-NG} is the contracted wavefunction.

To augment the accuracy of the basis set for valence orbitals, split-valence basis sets were developed, including more primitive gaussian functions. For more details, refer to the works of Weigend, Pople, Dunning and more.[452–457]

2.4.2 Reciprocal Space and Planewaves

In (§1.2.2.1), the concepts of unit cell and lattice vector were introduced to define a crystal lattice in the real space. However, in quantum chemistry, another annotation of the space is more useful for periodic solids, the reciprocal space, which is also known as the *k-space* and constitutes the Fourier transform of the real space.

In this mathematical formulation, the space is represented through reciprocal vectors,[458] which are perpendicular to two of the other real space axes, and are defined as (2.50):

$$\vec{a}^* = 2\pi\frac{\vec{b}\times\vec{c}}{\vec{a}\cdot(\vec{b}\times\vec{c})} \qquad \vec{b}^* = 2\pi\frac{\vec{c}\times\vec{a}}{\vec{a}\cdot(\vec{b}\times\vec{c})} \qquad \vec{c}^* = 2\pi\frac{\vec{a}\times\vec{b}}{\vec{a}\cdot(\vec{b}\times\vec{c})} \tag{2.50}$$

Where the denominator is also the volume of the unit cell. These vectors mean that every plane in a real lattice becomes a point in the reciprocal lattice. With these vectors, a translational vector can be constructed (2.51):

$$\vec{G} = k_1\vec{a}^* + k_2\vec{b}^* + k_3\vec{c}^* \tag{2.51}$$

Being k_i the integers used to define planes with the Miller indexes in the real lattice, respectively (*h, k, l)*.

As a result, the primitive unit cell in the reciprocal space is given by the first Brillouin zone, which is the equivalent of a Wigner-Seitz cell in a reciprocal lattice (See figure 2.4). Its boundaries are limited by the Bragg planes and has all the symmetries of the point group of the reciprocal lattice. In the case of this dissertation, the Γ-point has been employed, which is at the centre of the zone.

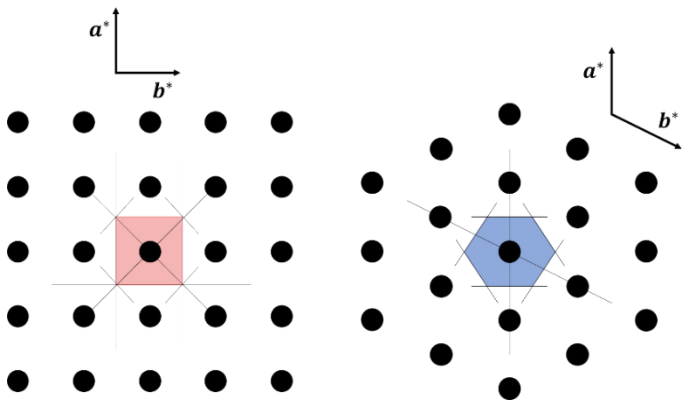

Figure 2.4 – Depiction of the Brillouin Zone in two different 2D-lattice systems

Among the applications of this non-physical space are the simplification of the interpretation of x-ray diffraction patterns and easier calculations of wave propagation in crystals.

All of the mentioned above is quite important for the alternative basis sets used in this dissertation, periodic models. According to Bloch's theorem,[459,460] a wavefunction in a periodic system must fulfil the Born-von Karman boundary conditions or just periodic boundary conditions (PBC), in simpler terms, the eigenfunctions must remain unchanged to reflect the periodical nature of the lattice (2.52).

$$\Psi(r) = \Psi(r+R) \qquad R = n_1\vec{a}_1 + n_2\vec{a}_2 + n_3\vec{a}_3 \qquad (2.52)$$

Where R is a general lattice vector of the unit cell.

For these conditions, there is only one function that satisfies the restrictions in an infinite crystal, and that is the complex exponent, which is a planewave (2.53):

$$PBC\begin{cases} |\Psi(r)|^2 = |\Psi(r+R)|^2 \\ \Psi(r+NR) = C^N \cdot \Psi(r) \rightarrow C = e^{ikr} \\ C^N = 1 \end{cases} \qquad (2.53)$$

Therefore, a periodic wavefunction can be expressed as a product of a periodic function with a planewave of momentum $\hbar k$ based on the symmetry of the lattice (2.54):

$$\Psi_k(r) = e^{ikr}u_k(r) \qquad (2.54)$$

$$u_k(r) = u_k(r+R) = \frac{1}{\sqrt{\Omega}}\sum_{\vec{G}} c_{k,\vec{G}}e^{i\vec{G}r} \qquad (2.55)$$

In these equations, the wavevector k characterises the first Brillouin zone, r is the position vector, and u_k is the lattice periodic function, which is usually expanded on a basis set of planewaves. As you can see, it conducts to the use of the reciprocal lattice vector illustrated in equation (2.51). Ω denotes the volume of the unit cell.

Applying this theorem, the one-electron eigenfunctions of the Kohn-Sham equations can simply be described as planewaves in the reciprocal space by just using the minimum expression of the crystal, which is the first Brillouin zone, sampled by a mesh of *k-points*. To generate the Γ-centred k-point grid, the regular k-point mesh method compiled in VASP has been used.[461]

$$\hat{\mathcal{H}}\Psi_k = E\Psi_k \tag{2.56}$$

Just like the atom-centred basis set, an infinite number of planewaves is required to get an appropriate expansion, but the coefficients $c_{k,\vec{G}}$ depicted in (2.55) with small kinetic energy are more significative than those with high kinetic energies.[462] As such, the planewave basis set can be truncated so only planewaves of less kinetic energy than an energy cut-off count on the calculation (2.57), thereof an infinite basis set is become to a finite basis set.

$$\frac{\hbar^2\left|k+\vec{G}\right|^2}{2m} \leq E_{cut} \tag{2.57}$$

Planewaves possess critical advantages in comparison to atom-centred basis sets.[463] They are simple, universal, orthonormal and does not depend on the position of the atoms in the crystal, as well as the convergence of the system can be easily adjusted modifying E_{cut} and the Fast Fourier Transform (FFT) can be easily implemented to transform the results into the real space. In contrast, the most problematic issue will be described in the next subsection.

2.4.3 Solutions to the use of Planewaves: Pseudopotentials and the Projector Augmented-wave method (PAW)

When you look at the wavefunction, the nodal structure of the core electrons possesses so much complexity that to fully delineate this part, the amount of imperative planewaves is immense considering the importance of this fraction in chemical bonding, which is primarily due to valence electrons. For economising computational cost and obtaining a faithful planewave basis set, pseudopotentials were introduced, approximations that mimic the behaviour of the core electrons upon valence electrons replacing the strong ionic potential in this zone to simplify the electronic calculations.[462,464–467] Beyond the core region, at a core radius r_c, the resulting pseudo-wavefunction and the all-electron wavefunction (which is the same wavefunctions than the Kohn-Sham single particle wavefunction explained in §2.3.1) are indistinguishable.

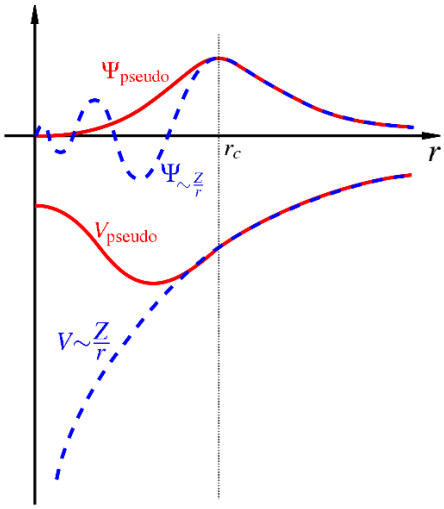

Figure 2.5 - Comparison between the pseudo-wavefunction and the all-electron wavefunction.

Upon this solution, the most widely used pseudopotentials are the ones created by the Stuttgart/Cologne group,[468] the Troullier-Martins pseudopotentials,[469] the ultra-soft pseudopotentials introduced by Vanderbilt,[470–472] and the Projector Augmented-wave proposed by Blöchl,[473,474] which is the one chosen for this dissertation.

Precisely, the PAW formalism is based on the ideas of Vanderbilt[475] and Krogh Andersen[476] to implement all-electron wavefunctions (ψ_n) with smooth pseudopotentials ($\tilde{\psi}_n$) for the valence electrons using a pseudo-wavefunction transformed by the transformation operator $\hat{\mathcal{T}}$ (2.58):

$$|\psi_n\rangle = \hat{\mathcal{T}}|\tilde{\psi}_n\rangle \tag{2.58}$$

To achieve this, PAW uses two grids, a radial one for the region inside the PAW sphere and a regular mesh for the entire unit cell. Subsequently, the partial waves and the projector functions are composed of a radial and an angular part. Therefore, $\hat{\mathcal{T}}$ will only transform the inner augmentation sphere delimited by a core radius, since outside of this region, the true wavefunction is smooth. The transformation operator is defined as (2.59):

$$\hat{\mathcal{T}} = 1 + \sum_a \sum_i \left(|\phi_i^a\rangle - |\tilde{\phi}_i^a\rangle\right)\langle\tilde{p}_i^a| \tag{2.59}$$

Where a denotes an atom index, ϕ_i^a and $\tilde{\phi}_i^a$ are the partial and the smooth partial wave, respectively, and $\tilde{p}_i^a$ is the projector smooth function, which is depicted in (2.60):

$$\langle\tilde{p}_i^a| = \sum_j \left(\{\langle f_k^a|\tilde{\phi}_l^a\rangle\}\right)_{ij}^{-1} \langle f_j^a| \tag{2.60}$$

In which f_j^a is any set of linearly independent functions. By definition, the projector functions will be localised if the functions f_j^a are localised.

In summary, the all-electron wavefunction is expressed as (2.61):

$$\psi_n(r) = \tilde{\psi}_n(r) + \sum_a \sum_i \left(\phi_i^a(r) - \tilde{\phi}_i^a(r)\right) \langle \tilde{p}_i^a | \tilde{\psi}_n \rangle \quad (2.61)$$

In these equations, the partial and smooth wavefunctions are used to expand the sets of all-electron wave-functions, i.e., they are used as atomic specific basis sets.

In spite of being a more demanding method than other pseudopotentials, the PAW approach provides the nodal features of the valence orbitals and the expectation values of all-electron operators with a really high transferability, much more than other pseudopotentials with the accuracy corresponding to the *Full-Potential Linearized Augmented-Planewave* (FLAPW),[477] which is used for benchmarks for DFT calculations in solids.

In conjunction with the PBE functional to express the exchange-correlation energies (§2.3.2.2), this is the methodology that has been used throughout the entire study.

Once explained the computation of energy for a system of N particles using DFT, a key concept in chemistry will be explained, the *potential energy surface* (PES).

2.5 Potential Energy Surface (PES)

In a chemical energy profile, the minimum energy pathway (MEP) is the most optimal route to transform reactants into products. Nevertheless, there are infinite routes to arrive to the same point, and these are represented by the potential energy surface (PES).

The PES is the embodiment of the forces of interaction among atoms, molecules, catalysts, and materials in a chemical reaction. Indeed, the PES serves as valuable source of structural and chemical insights into molecules. Its dimensionality varies based on the number of atom coordinates, which is often simplified by visualising two independent variables with the energy computed with the stated methods above of our particle system using a hypersurface (Figure 2.6).

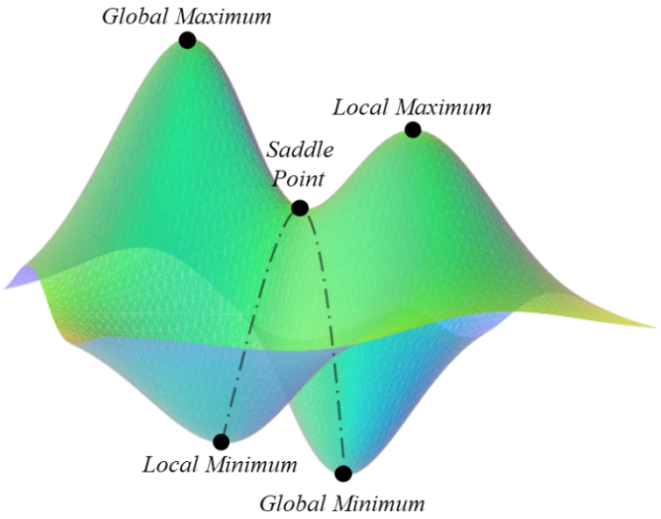

Figure 2.6 - Hypothetical representation of the Potential Energy Surface. The dashed line pictures the minimum energy pathway.

These are the most interesting points on a potential energy surface:

- Global minimum: The most stable conformation at the extremum where the energy is the lowest. A molecule has only one global minimum.

- Local minima: Additional low energy regions of the PES where a change in geometry in any direction yields a higher energy geometry.

- Saddle point: Stationary point between two low energy extrema where there is an increase in energy in all directions except one, and for which the slope (first derivative) of the surface is zero. It depicts the transition state of a chemical reaction.

Therefore, taking into consideration the components of our system, the different stable reactants and products will be localised in the local and global minimums and the transition states for each possible reaction will be situated in the saddle points of the PES. Interestingly, taking a slice of this hypersurface facilitates the extraction of a reaction scheme, like the one depicted in §1.1, figure 1.1.

Finally, a brief description of the simulation package used to run the computational calculations will be presented.

2.6 The Vienna Ab-initio Simulation Package (VASP)

VASP was born in the MIT by the hand of Mike Payne, Jürgen Furthmüller and Georg Kresse later in Vienna as a Fortran 90 program that performs ab-initio computational simulations for atomic scale materials modelling with the objective of predicting their optical, geometric and electronic properties, in simpler terms, the behaviour of a material in a specific chemical environment.[478]

Next, the procedures to calculate the different intermediates and chemical parameters in the reaction coordinate will be detailed.

2.6.1 Minimum States

In (§2.3 and 2.3.1), the DFT fundamentals and the Kohn-Sham method explained how to compute the energy of a system with a specific configuration. To determine electronic ground states, VASP utilises optimisation algorithms whose objective is the convergence of forces and energies to the MEP. In the case of this dissertation, the Limited-memory Broyden-Fletcher-Goldfarb-Shanno (LBFGS),[479,480] compiled within the VTST tools[481] was employed owing to its efficiency. Specifically, the program used a fixed convergence criterion of 10^{-6} eV and an energy cut-off of 600 eV.

2.6.2 Transition States

Comparatively, obtaining a transition state, the saddle point of a PES at the maximum along the MEP, is much more convoluted than a minimum state. Fortunately, in 1999 Graeme Henkelman, Hannes Jónsson et al. developed and improved the dimer method.[482,483]

From an initial guess configuration, this method permits the search of nearby saddle points using a dimer made of two images from the initial conformation that scarcely differs and a unit vector $\widehat{N}$ that is moved across the reaction coordinate. As the dimer is displaced, slightly rotations of the dimer around its axis are performed seeking the minimisation of the dimer energy and the maximisation of the curvature, all of this only using first derivatives of the potential energy, in regard to other methods.[484–486]

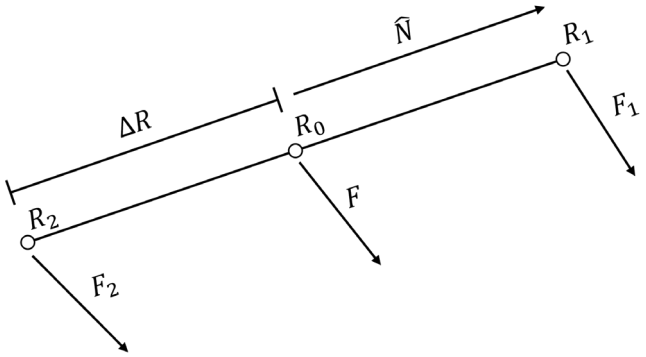

Figure 2.7 - Dimer definition with the corresponding forces acting upon points R.

If the transition state is clear, a MODECAR file that includes the initial direction along the dimer is created to quantify the unit vector. If this file does not include any instructions to get the saddle point, a set of arbitrary vectors will be selected instead.

The curvature of the dimer is calculated according to equation (2.62):

$$C = \frac{(F_2 - F_1) \cdot \widehat{N}}{2\Delta R} = \frac{E - 2E_0}{(\Delta R)^2} \qquad (2.62)$$

Where F_1 and F_2 are forces acting upon 1 and 2, respectively, $\widehat{N}$ is the unit vector, ΔR is the spacing between both images, E is the sum of both images' energy and E_0 is the energy of the midpoint of the dimer.

To evaluate the curvature and ensure the calculation is converging towards a saddle point along the MEP, the curvature must be consistently negative as well as the forces are decreasing until very low values. Furthermore, vibrational analyses are conducted to verify the presence of an imaginary frequency associated with the attained transition state upon convergence (§2.6.3).

To set up the calculation, the conjugate gradient method compiled in the VTST tools,[481] which is the recommended option, was used. As in the minimum states (§2.6.1), a convergence criterion of 10^{-6} eV and an energy cut-off of 600 eV was set.

2.6.3 Vibrational Analysis

To confirm the nature of minimums and transition states after geometry convergence, it is necessary to unravel the vibrational motions of the nuclei enclosed in the nuclear Schrödinger equation (2.63 & 2.64):

$$\hat{H}_n \Psi_n(R) = E_n \Psi_n(R) \tag{2.63}$$

$$\left[-\frac{\hbar^2}{2\mu}\Delta_i + V(R)\right]\psi_n(R) = E_n \psi_n(R) \tag{2.64}$$

For the sake of simplicity, the quantum harmonic oscillator model is used. In a nutshell, in the minimum or maximum of a system, the nuclear potential can be formulated as a *Taylor Series Expansion* approximated to the quadratic term, resulting in a very similar formula than the classical spring potential (2.65):

$$V(R) = \frac{1}{2}\frac{d^2E}{dR}(R - R_0)^2 = \frac{1}{2}k(R - R_0)^2 \tag{2.65}$$

Moreover, the nuclear eigenfunction can be expressed as a product of a gaussian function and a Hermite polynomial (2.66):

$$\psi_n(R) = \frac{1}{\sqrt{2^n n!}}\left(\frac{\mu\omega}{\hbar\pi}\right)^{1/4} e^{-\mu\omega R^2/2\hbar} H_n\left[\left(\frac{\mu\omega}{\hbar}\right)^{1/2} R\right] \qquad (2.66)$$

Resolving the nuclear Schrödinger equation, the quantised vibrational levels are obtained (2.67):

$$E_n = \left(n + \frac{1}{2}\right) h\nu \qquad (2.67)$$

$$\nu = \frac{\omega}{2\pi} = \frac{1}{2\pi}\sqrt{\frac{k}{\mu}} \qquad (2.68)$$

$$\mu = \frac{m_1 m_2}{m_1 + m_2} \qquad (2.69)$$

Being *n* the quantum number, ν the vibrational frequency, ω the angular frequency, *k* the bond force constant and μ the reduced mass.

For systems with more than 2 atoms, the Hessian matrix (second derivate of energy) and the mass-weighted Hessian matrix are computed as shown in (2.70), respectively:

$$H_{ij} = \left[\frac{\partial^2 E}{\partial x_i \partial x_j}\right]_{\{x_i\}_{eq}} \qquad H'_{ij} = \frac{H_{ij}}{\sqrt{m_i m_j}} \qquad (2.70)$$

The resultant eigenvectors and eigenvalues will be the force constants and normal modes, respectively. For minimum states, it will possess 3N-6 positive eigenvalues. For transition states, it will have 3N-7 normal modes and one negative eigenvalue, being this imaginary frequency with its corresponding eigenvector the definitive proof of the saddle point.

VASP possesses 2 ways for the calculation of the vibrational parameters: Finite differences and density functional perturbation theory (DFPT).[487,488] For this dissertation, the latter has been used setting the IBRION parameter to 7 and performing an isolated calculation after geometry convergence.

2.6.4 Free energy

Although in (§1.1) the basic concepts of Gibbs free energy were explained, a more elaborated and precise definition of it is normally used, ruled by statistical mechanics.

In this formalism, the macroscopic thermodynamic properties of a system depend on the number of microstates of the collection of molecules and particles, which constitutes an ensemble. All of them are determined by the partition function (2.71), which summarises the number of microstates accessible to our system in a given ensemble:

$$\mathcal{Z} = \sum_i e^{\frac{\mu N_i - E_i}{k_B T}} \tag{2.71}$$

Therefore, one can derive from equation (2.71) all the thermodynamic properties of the system. For more details, consult references in the literature.[489–491]

The absolute Gibbs free energies of all species are given by (2.72):

$$G = E_{tot} + E_{zpe} + E_{vib} - TS_{vib} \tag{2.72}$$

Where E_{tot} is the electronic energy obtained from the DFT calculation, E_{zpe} is the zero-point energy correction, E_{vib} is the vibrational thermal energy contribution and S_{vib} is the vibrational entropy. The origin of this correction term comes from the fact that, at absolute zero (0 K), nuclei still possess vibrational contributions with their consequential implications in the energy of the system. The zero-point energy is described as follows (2.73):

$$E_{zpe} = \sum_{i=1}^{3N-6} \frac{1}{2} h\upsilon_i \tag{2.73}$$

Respect to the other terms in equation (2.72), the vibrational contributions to the energy and entropy have been calculated according to (2.74 & 2.75), respectively:

$$E_{vib} = R \sum_{i=1}^{3N-6} \frac{h\upsilon_i}{k_B(e^{h\upsilon_i/k_BT} - 1)} \tag{2.74}$$

$$S_{vib} = R \sum_{i=1}^{3N-6} \left[\frac{h\upsilon_i}{k_BT(e^{h\upsilon_i/k_BT} - 1)} - ln\left(1 - e^{h\upsilon_i/k_BT}\right)\right] \tag{2.75}$$

For a more exact Gibbs expression, the translational and rotational contributions of energy and entropy can also be implemented in equation (2.72), giving rise to equation (2.76):

$$G = E_{tot} + E_{zpe} + E_{vib} + E_{rot} + E_{trans} - T(S_{vib} + S_{rot} + S_{trans}) \tag{2.76}$$

The formulae of these new terms are illustrated in equations (2.77, 2.78 & 2.79):

$$E_{rot} = E_{trans} = \frac{3}{2}RT \tag{2.77}$$

$$S_{rot} = R\left\{\left[\sqrt{\frac{\pi I_a I_b I_c}{\sigma}}\left(\frac{2\pi k_B T}{h^3}\right)^{3/2}\right] + \frac{3}{2}\right\} \tag{2.78}$$

$$S_{trans} = R\left\{\ln\left[V\left(\frac{2\pi M k_B T}{h^3}\right)^{3/2}\right] + \frac{3}{2}\right\} \tag{2.79}$$

2.6.5 Charge Analysis

In addition to vibrational and free energy parameters, the charge transfer between the different components of the system is crucial for the understanding of the chemical evolution of the system, giving us hints about the descriptors of a well-performed catalysed reaction.

To compute it, it is resorted to one of the quantum interpretations of chemical bonding described by Richard Bader and his colleagues in 1985, the Quantum Theory of Atoms in Molecules (QTAIM),[492–495] whose principles satisfy Hellmann-Feynman[496,497] and virial theorems.[498] On chemical grounds, a topological mapping of the electron density ρ in terms of the gradients ∇_ρ contains the information that pictures the molecular structure of a system, meaning atoms, bonds, atom charges, electron lone pairs and so on and so forth.

In this model, nuclei are identified as maxima on the ∇_ρ map in which all gradient paths converge, behaving as attractors. This definition leads to the atomic basin concept, which is the region of space in which all gradient paths terminate at a specific attractor. Combining both concepts, an atom is defined as the attractor point enclosed by its atomic basin.

These atoms are connected to each other through saddle points in the interatomic surface with concentrated electron density, defining the network that give rise to the molecule, the molecular graph, providing physical meaning to the chemical bond. The points of the map where the flux of ∇_ρ is nullified are called *critical points*. Likewise, the trajectories connecting paired nuclei through these critical terms are termed *bond paths*.

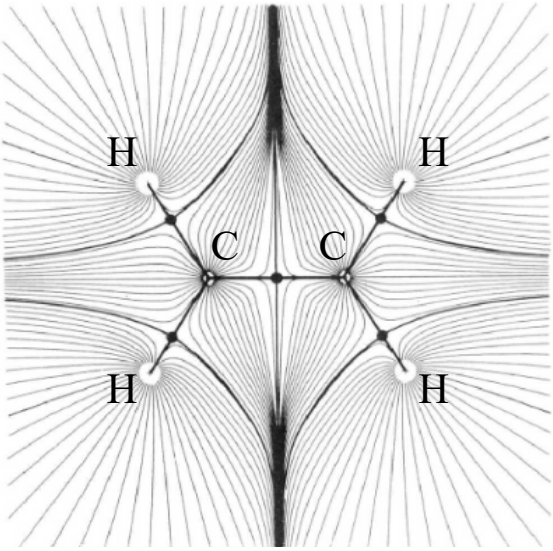

Figure 2.8 - Gradient density map containing the nuclei in C_2H_4. The bond critical points in the interatomic surfaces are depicted as black dots. Adapted with permission from (492) Bader, R. F. W. Atoms in Molecules. Acc. Chem. Res. **1985**, 18 (1), 9–15. https://doi.org/10.1021/ar00109a003. Copyright **1985** American Chemical Society.

Hence, the atomic charge can be calculated as the integral of the electron density contained in the atom. To evaluate it for each atom in the molecule, the *Bader* program was employed.[499]

As a complement, the *Chargemol* program[500,501] was used in chapter 5 to ascertain the atomic charges of Cu_5 within MeAPOs in which the *Bader* program is found to be more limited.

2.6.6 Reaction Kinetics

In order to predict the final product of a chemical reaction, the knowledge of the kinetics of a chemical reaction to discern between the different competitive reactions is essential.

As stated in §1.1, the rate constant k that explains the kinetics of a chemical reaction is extracted from the Eyring–Polanyi equation (1.3):

$$k = \kappa \frac{k_B T}{h} e^{-\Delta G^{\ddagger}/RT} \tag{2.80}$$

In this case, the activation energy terms in $\Delta G^{\ddagger}$ are the ones computed in equation (2.69).

2.7 Models

In order to study a chemical reaction and foresee the evolution of a catalytic system in computational chemistry, it is of utmost importance to select a suitable basis to represent the number, position and nature of the particles. To achieve this, all these chemical parameters are integrated into *models* with the ultimate objective of predicting the chemical reality while the computational cost is minimised.

In the case of zeolites, cluster and periodic models are commonly used. Concerning cluster models, they are fragments cut out from the solid, and the boundary atoms of the model are saturated with hydrogen atoms or hydroxyl groups. In this way, cluster models are lighter in terms of computational cost, but it is not the only way to reduce it. A good alternative is partitioning the model into layers, which will be treated with different levels of theory depending on the proximity to the active site, the inner layers will be treated with higher levels of theory whereas the external layers will use fewer demanding methods.

Unfortunately, this approach to the system entails drawbacks like the limitation of the long-range interactions or the confinement effects and the topologic effect of porous crystalline solids.

In this thesis, periodic models have been employed. By the same token, the complete list of models used in this dissertation will be detailed in the next subsection.

2.7.1 Periodic Models

When studying a crystalline solid (like zeolites), introducing the entire structure of the crystal would be quite inefficient in terms of computational cost. For this reason, periodic models are used, and the unit cell (§1.2.2.1) is accommodated so that the replication of the unit cell in the three translational vectors of space forms the entire structure. In this context, *primitive cell* is called to the minimum expression of the unit cell and is characterised by the primitive vectors (*a, b, c*).

In comparison with cluster models, periodic models picture a closer chemical reality at the expense of more time-consuming calculations. They are well suited to describe crystalline solids, but less efficient to describe molecules or discrete systems, like the isolated metal clusters considered in this study.

In this dissertation, four distinct microporous materials were thoroughly studied for the Methane-to-Methanol (MTM) reaction mechanism, all of them sharing a trigonal unit cell and a CHA framework (See figure 2.9): SSZ-13, SAPO-34, Me^{IV}APO-34 and Me^{II}APO-34, "Me" referred to the tetravalent and divalent metals substituting the P and Al atoms, respectively. The notation of these materials comes from the IZA database, and a CIF code is attributed to each of them.[71] Furthermore, the configuration of the substituted atoms was selected in terms of the intrinsic stability of the system.

Before commencing the study, to get a better understanding of the catalyst while avoiding spurious and unrealistic interactions between molecules of each cell, a cubic box model was used.

Next, a more comprehensive exposition of the periodic models is provided below:

- A cubic box of 20x20x20 Å to represent the active components in an isolated system to avoid artificial interactions between the molecules of each cell. It is employed in chapter 3.

- An SSZ-13 of composition $Si_{36-y}O_{72}Al_y$ (y = 0, 1, 2), with dimensions of 13.746, 11.904 and 15.013 Å, and angles 90, 90 and 120, respectively. It is employed in chapter 4.

- A SAPO-34 of composition $Si_2Al_{18}P_{16}O_{72}$ with dimensions of 13.849, 11.993 and 15.048 Å, and angles 90, 90 and 120, respectively. It is employed in chapter 5.

- A Me^{IV}APO-47 of composition $M^{IV}_2Al_{18}P_{16}O_{72}$ with dimensions of 13.849, 11.993 and 15.048 Å, and angles 90, 90 and 120, respectively for $M^{IV} = Ti^{4+}$, Zr^{4+}, Sn^{4+}. It is employed in chapter 5.

- A Me^{II}APO-47 of composition $M^{II}_2Al_{16}P_{18}O_{72}$ with dimensions of 13.849, 11.993 and 15.048 Å with angles 90, 90 and 120, respectively for $M^{II} = Zn^{2+}$, Fe^{2+} and Mg^{2+}. It is employed in chapter 5.

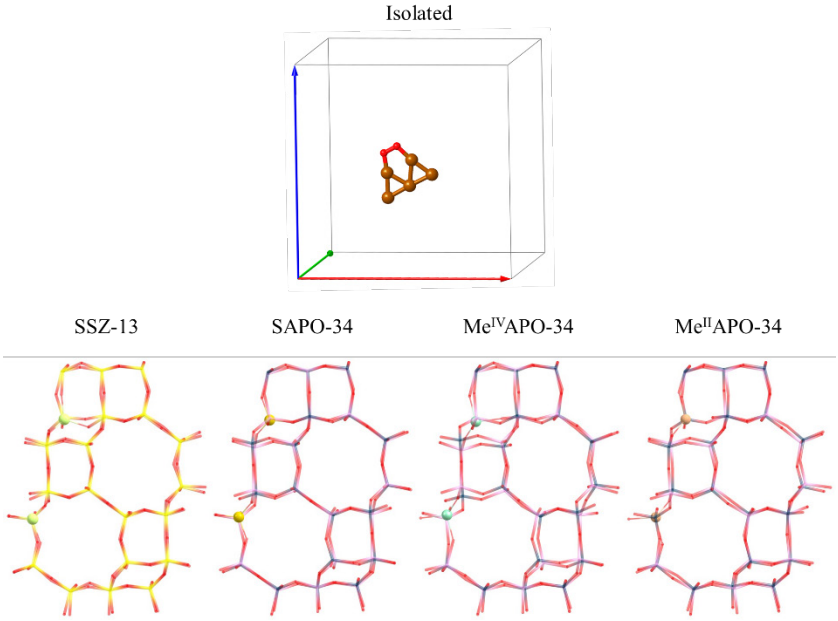

Figure 2.9 – Cubic (top) and trigonal (bottom) periodic models used in this work. For the isolated model, O and Cu atoms are depicted as red and copper-coloured. For microporous materials, thin sticks depict zeolite framework with Si, O, Al, and P atoms labelled as yellow, red, pink, and dark blue, respectively, whilst the substituted Al, Si, M^{IV} and M^{II} atoms in each material are depicted in light green, yellow, turquoise and flesh-coloured, respectively.

Once all of the employed theoretical fundamentals have been thoroughly explained, it is now time to present the hard work conducted over these years, contributing to the advancement of this field of science. Let us expound on the results of this dissertation.

Chapter 3 Selective Oxidation of Methane to Methanol with Molecular O_2 using Sub-nanometre Copper Clusters

Our studies with copper clusters began in gas phase, with the dissociation of a O_2 molecule, followed by the approach of a CH_4 molecule to start the reaction to turn methane into methanol. This study[502] has been used to settle the main pathways involved in this complex reaction and to get data about the different issues the reaction has to avoid in each step to selectively oxidise methane to methanol.

Furthermore, the chapter will delve into the requirements of atomicity and morphology that could result in an improved catalytic performance, thereby clarifying whether the reaction mechanisms on copper clusters are analogous to that proposed for Cu-exchanged zeolites.

3.1 Introduction

At the moment the corresponding paper to this chapter[502] was published, reports in the literature about methane activation in sub-nanometre clusters were widely found. As far as my literature search has reached, the great majority of them are theoretical studies that are focused on the partial oxidation of methane (POM) to achieve synthesis gas, like the studies conducted by Guo et al. in 2017 on anatase and rutile defective using a Rh_4 cluster[503] or by Tang et al. in 2021, achieving methane oxidation to synthesis gas on single-atom Rh_1O_5/TiO_2 clusters.[504]

Another part of the studies is focused only on H_2 release, but the remaining portion of the methane molecule cannot be utilised due to the formation of MCH_2 species. The first found dates back to 2007, where Xiao et al. studied methane activation on Pt and Pt_4 clusters, giving Pt_nCH_2 moieties as by-product.[505] There are also more recent works, like the ones carried out in 2019 by Hirabayashi et al, in which, methane activation is accomplished utilising W_n^+ and $W_nO_m^+$ clusters, generating W_nCH_2 and $W_nO_mCH_2$ species, respectively.[506]

In fact, only a few recent studies were found detailing catalytic systems for converting methane into methanol. The systems proposed were Au_4 clusters supported on defective graphene, conducted by J. Sirijaraensre and J. Limtrakul in 2015 employing N_2O as oxidant,[507] Au_{24} and Au_{25} complexes by Cai et al. in 2019 utilising H_2O_2 as oxidant,[508] a nickel-thiolate hexameric cluster that performed the photocatalytic oxidation of methane with O_2 under visible light by Hu et al. in 2021, which also produced formic acid,[509] and a $Ni_{4-x}Cu_x$ cluster supported on $CeO_2(111)$, studied by Lustemberg et al. in 2022, although this study preadsorb an O atom on the metal cluster to form the active centre and does not detail the previous steps to form the proposed catalyst.[510]

Considering all the data compiled, the transformation of methane into methanol on sub-nanometre clusters has not been exhaustively tackled at theoretical level, because only the most direct paths have been investigated, putting the study of the competitive reaction paths in the background. This dissertation will expand the current knowledge illustrating a complete image of the most relevant reaction mechanisms that are involved in the MTM process catalysed by sub-nanometre copper clusters using O_2 as oxidant.

If the attention is directed to a more familiar system that is well-known, Cu-exchanged zeolites, kinetic, spectroscopic, and computational studies[261,271,354,359,364,511] have indicated that methane C-H bond dissociation is homolytic and generates a hydroxyl group bound to Cu and a methyl intermediate that can either bind to Cu, form a framework-bound methoxy group, or yield methanol by recombination with the hydroxyl group following a radical rebound mechanism (Scheme 3.1). So, this chapter could verify whether the same pathways found in Cu-exchanged zeolites are also uncovered in Cu_n nanoclusters.

Scheme 3.1 - Radical and Non-radical Intermediates Proposed for methane Oxidation to Methanol on Cu-Exchanged Zeolites

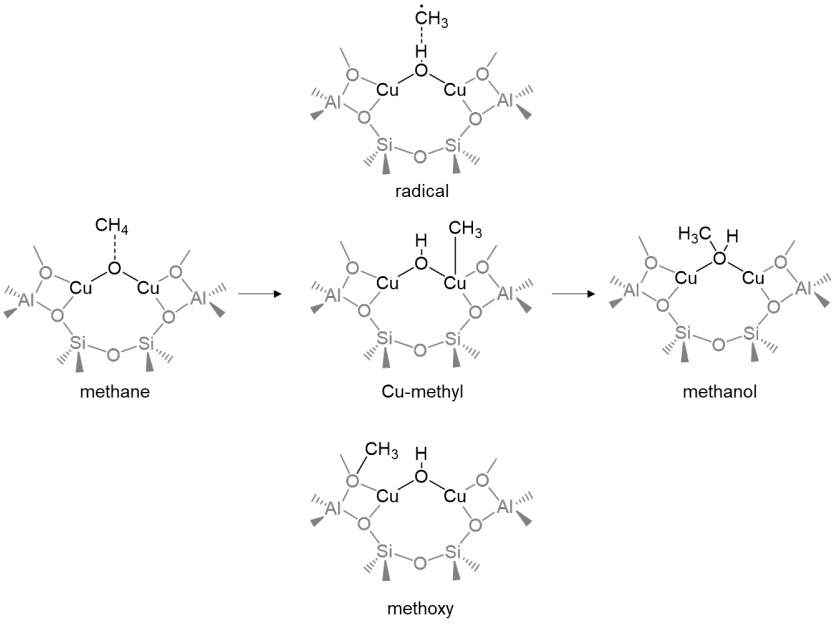

In a sustainability context, the methane-to-methanol reaction would imply the removal of a greenhouse gas from the atmosphere, with its corresponding impact in climate change,[512] and the revalorisation of a by-product in the oil industry, fostering circular economy model. In addition, new technologies are being developed to produce liquid fuels from methane to accelerate the transition to greener and sustainable energies.[513–515] Nonetheless, the most complex step, the overoxidation of the desired methanol, has not been resolved yet.[270,322,334,516–518] Therefore, to shed light to the reaction paths and the key aspects of the reaction in sub-nanometre metal clusters, a thorough computational study of the MTM process on Cu_n clusters with n = 5,7 was carried out.

3.2 O_2 dissociation over Cu_n clusters

To begin with, former theoretical and experimental studies have demonstrated that O_2 is able to adsorb on sub-nanometre Cu_n clusters, creating stable complexes in which the O-O bond is activated by charge transfer from the metal cluster to the π* orbital of O_2, facilitating its dissociation to produce adsorbed O atoms.[217,519,520] Interaction of O_2 with Cu_5-2D, Cu_5-3D and Cu_7 clusters is quite strong (calculated Gibbs free energies of adsorption are -171, -124 and -93 kJ/mol, respectively, see table 3.1). The structures obtained are labelled Cu_n-O_2 in figure 3.1.

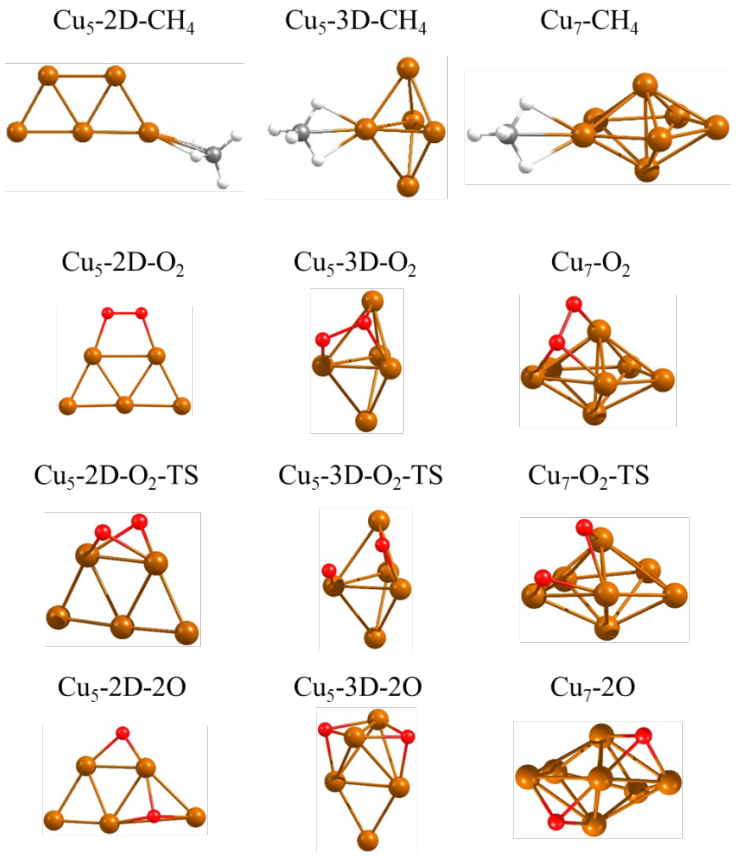

Figure 3.1 - Optimised structures of adsorbed CH_4, and O_2 dissociation mechanism on Cu_5-2D, Cu_5-3D and Cu_7 clusters.

Conversely, methane interaction with Cu_5-2D, Cu_5-3D and Cu_7 clusters was found to be negligible (calculated Gibbs free energies of adsorption are -9, -29 and -3 kJ/mol, respectively) so a merely presence of O_2 in the reaction flow will conduct to the oxygenated species.

With the aforementioned, partly oxidised Cu_5-2D, Cu_5-3D and Cu_7 clusters with two adsorbed O atoms are originated from O_2 dissociation. The process is considerably more difficult for Cu_5-2D than for Cu_5-3D and Cu_7 due in part to the high stability of Cu_5-2D-O_2, with O-O distances evolving from 1.389 in the minimum to 1.969 Å in the transition state. In addition, when this process was investigated using a much more computationally costly multi-reference approach,[521,522] a high barrier was also found for the transition from a physisorbed state with neutral O_2 and Cu_5-2D to a chemisorbed state with the associated charge transfer between the adsorbed molecule and the metal cluster. In the case of Cu_5-3D and Cu_7, O_2 dissociation is more favourable, as a result of longer O-O distances in the minima (1.498 Å for Cu_5-3D and 1.480 Å for Cu_7) indicative of a weaker O-O bond. These O-O distances give us an idea of the activation of the O-O bond, reflected in the Gibbs activation barriers (G_{act}) gathered in table 3.1. In addition, Gibbs reaction energies (ΔG) and Gibbs activation free energies (G_{act}) are in tune with the stability trend marked by the adsorption energies, requiring a considerable amount of energy in Cu_5-2D, yielding a product ~72 kJ/mol less stable than its counterparts.

Table 3.1 – Gibbs free energies and spin states for the activation of O_2 in Cu_n clusters. Methane adsorption energies are added for comparison.

Cluster	***G_{ads} CH_4 (kJ/mol)***	***G_{ads} O_2 (kJ/mol)***	***G_{act} (O-O) (kJ/mol)***	***ΔG (kJ/mol)***	***Spin***
Cu_5-2D	-9	-171	121	-160	D
Cu_5-3D	-29	-124	35	-243	D
Cu_7	-3	-93	38	-232	D

In terms of atomic charges (see table 3.2), it is noticeable that Cu_5-3D-O_2 and Cu_7-O_2 possess a higher amount of charge concentrated in the oxygen atoms in comparison with Cu_5-2D-O_2, which is related to the

difficulty to activate O_2 in this system. For the rest of data, all the systems share almost the same values of oxygen charge.

Table 3.2 – Bader atomic charges and O-O distances in the O_2 dissociation step.

Cluster	qO	rO-O
Cu_5-2D-O_2	-0.744	1.389
Cu_5-O_2-TS	-1.273	1.969
Cu_5-2O	-1.893	3.562
Cu_5-3D-O_2	-1.037	1.498
Cu_5-3D-O_2-TS	-1.278	1.997
Cu_5-3D-2O	-1.976	3.059
Cu_7-O_2	-1.012	1.480
Cu_7-O_2-TS	-1.303	1.908
Cu_7-2O	-1.981	3.603

On balance, all the parameters are in accordance with the oxidation resistance nature of Cu_5-2D, as revealed by Fernández et al.[217]

Respect to the different O_2 dissociations that can lead to bicoordinated or three-coordinated O atoms with potentially different reactivities, the O_2-dissociated species illustrated above were chosen as the initial systems to search for potential mechanisms in the selective methane oxidation to methanol catalysed by copper clusters. However, considering the strong O_2 affinity for Cu, the overoxidation of these species was also investigated.

When a new O_2 molecule approaches a Cu_n-2O system containing two adsorbed O atoms, new interactions within the quadruplet potential energy surface flourish, increasing the complexity of the process. To clarify whether multiple spin states can benefit lower activation barriers or entirely new reaction paths, these routes were studied.

Figure 3.2 depicts a new O_2 dissociation process over Cu_5 2D and 3D clusters.

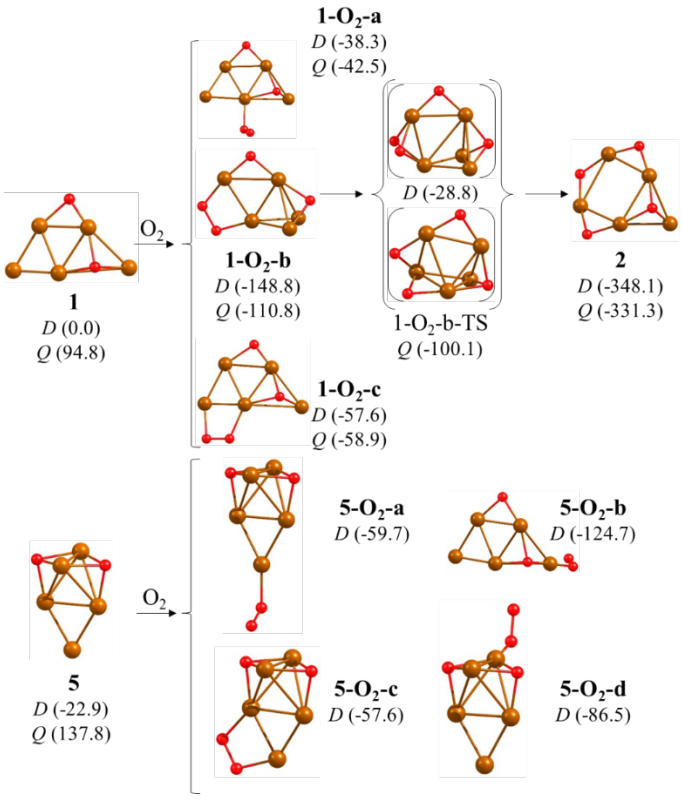

Figure 3.2 - Possible sites for O_2 adsorption on Cu_5-2O and Cu_5-3D-2O and optimised geometries of the most favourable pathway. Relative Gibbs energies are given in parenthesis for doublet (*D*) and quadruplet (*Q*) spin states in kJ/mol.

The Cu_5-2D-2O product, labelled from this point as structure **1**, originates structures 1-O_2-a (a), 1-O_2-b (b) and 1-O_2-c (c). As plotted, the possibility to obtain multiple spin surfaces cannot be ruled out. Nevertheless, structure 1-O_2-b (b) exhibits greater stability than the others, with the doublet state being 38 kJ/mol more stable than the quadruplet and with the new molecule of oxygen attached in bridge mode; thus, O_2 adsorption energies remain high for the most stable configuration. Interestingly, the process of O-O breakage employs almost the same energy as in the first O_2 dissociation step in the doublet state (*D*) (See table 3.1), 120 kJ/mol, with O-O distances that evolve from 1.395 to 1.898 for doublet, giving rise to an almost planar cluster with three bicoordinated oxygen atoms anchored on the catalyst, structure **2**. Although observing the relative Gibbs energies of the quadruplet state (*Q*), a more effective reaction pathway is visible. Consuming 38 kJ/mol to conduct structure (b) to the quadruplet state would involve a 10.7 kJ/mol barrier to get to structure **2**, with O-O distances elongating from 1.377 to 1.913 Å. Hence, if O_2 concentrations are high enough, Cu_5-2D clusters can overoxidise.

Just like Cu_5-2D, a new O_2 addition was also studied for the Cu_5-3D-2O product since it gives the most stable structure, 22.9 kJ/mol more stable than structure **1**. Labelled as structure **5**, it results in non-effective adsorption modes to dissociate the new O_2 molecule except for 5-O_2-c (c). However, its stability respect to 5-O_2-b (b) rules out any progression through Cu_5-3D. Interestingly, this latter configuration adopts the same geometric parameters as the Cu_5-2D configurations depicted in figure 3.2, indicating that Cu_5-3D and Cu_5-2D clusters can interconvert throughout the chemical process.

In reference to the atomic charges (see table 3.3), only a very subtle difference can be found in the clusters with four adsorbed O atoms, accommodating less charge in relation to the clusters with 2 O atoms anchored on their surface.

Table 3.3 - Bader atomic charges and O-O distances in the second consecutive O_2 dissociation step.

Cluster	qO	rO-O	Spin
1-O_2-b	-0.770	1.395	D
1-O_2-b-TS	-1.251	1.898	D
2	-1.764	3.491	D
1-O_2-b	-0.709	1.377	Q
1-O_2-b-TS	-1.277	1.913	Q
2	-1.786	3.458	Q
3-O_2-E	-1.038	1.505	D
3-E-TS	-1.310	1.959	D
4	-1.863	3.590	D
3-O_2-E	-0.955	1.459	Q
3-E-TS	-1.145	1.658	Q
4	-1.870	3.582	Q

In regard to Cu_7 nanoclusters, the competitive adsorption and dissociation of an additional O_2 molecule over the Cu_7-2O system (Structure **3**) follows the trend found in Cu_5, since the possibility to stabilise unpaired electrons increases as the difference in energy between the doublet (D) and quadruplet (Q) spin states decreases (figure 3.3):

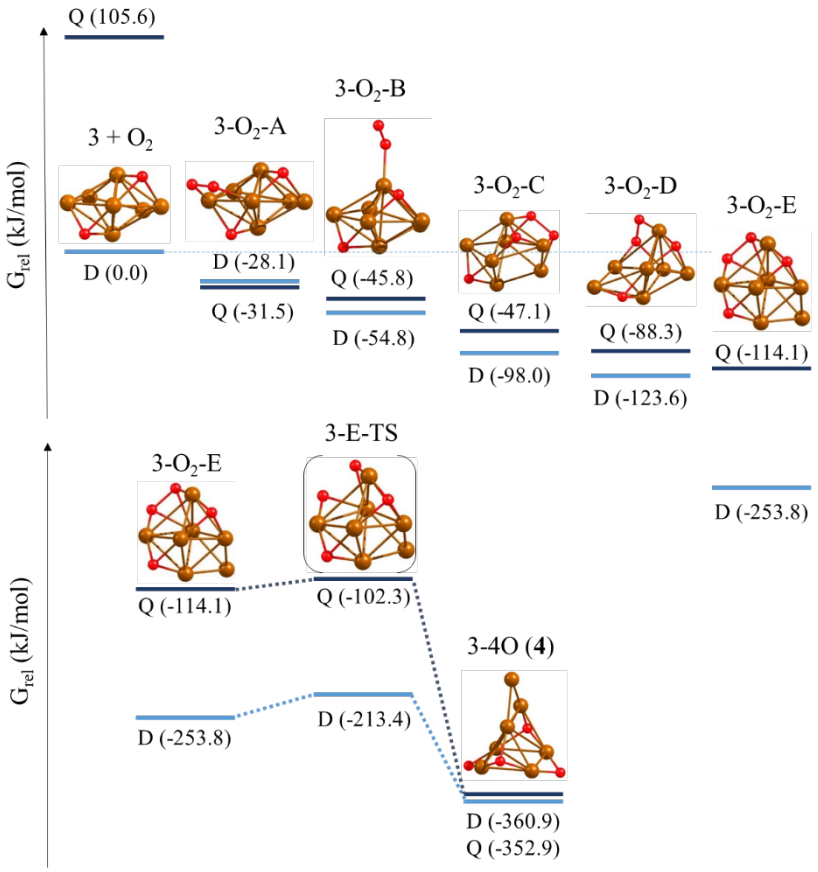

Figure 3.3 - Optimised geometries of the structures involved in O_2 adsorption and dissociation on a Cu_7-2O system and Gibbs relative energies of each structure in both doublet (D) and quadruplet (Q) states in relation to the initial reactant **3** + O_2 in its most stable D state. Cu, O, C and H atoms are depicted as orange, red, grey, and white balls, respectively.

The compiled data indicate that molecular O_2 interacts strongly with structure **3** and dissociates with an activation energy of only 40.4 kJ/mol, generating a symmetric Cu_7-4O system that contains two three-coordinated O atoms on the facets of the cluster and two bicoordinated O atoms placed at opposite edges, following the doublet state path (structure **4**).

Further oxidations were also explored at this point to know the behaviour of the catalyst at high concentrations of molecular oxygen (figure 3.4).

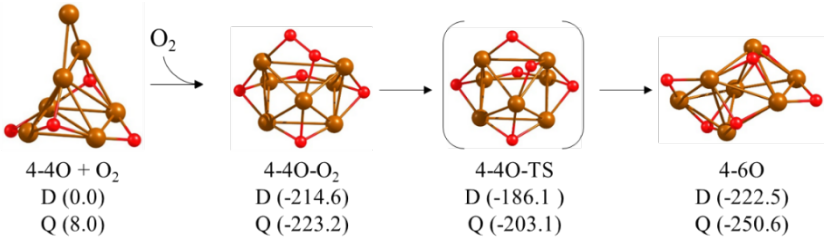

Figure 3.4 – Optimised geometries of the structures involved in O_2 adsorption and dissociation on a Cu_7-4O system and Gibbs relative energies of each structure in both doublet (D) and quadruplet (Q) states in relation to the initial reactant **4** + O_2 in its most stable D state. Cu, O, C and H atoms are depicted as orange, red, grey, and white balls respectively.

In this scenario, oxygen adsorption energies are still extremely high, being -215 and -223 kJ/mol, with activation energies of 28.6 and 20.1 kJ/mol, respectively for doublet (D) and quadruplet (Q) surfaces, and optimised O-O distances from 1.481 to 2.074 for doublet and 1.472 to 1.936 for quadruplet in the transition state. In addition to the predominant role of the quadruplet state in this pathway, this proves that Cu_7 clusters can easily suffer from overoxidation, supporting up to 6 O atoms on its surface.

In light of the results, Cu_5-4O (Structure **2**) and Cu_7-4O (structure **4**) would be the most plausible candidates for the methane conversion to methanol on account of the O_2 affinity of the clusters and the low activation barriers observed through the Q potential energy surfaces despite the easy formation of Cu_7-6O, but in this case, the excess of O atoms would not permit an optimal concentration of charge density over the O atoms to efficiently activate methane, since charge density would be widely distributed. In order to envision a complete image of the process, Cu_5 and Cu_7 with 2 adsorbed O atoms dissociated (structures **1**

and **3**) will be firstly investigated, and then, the study will proceed to the overoxidised species.

Reckoning with the possibility of weak binding of methane to the catalyst (See table 3.1), two types of reaction pathways were investigated for all systems: Langmuir-Hinshelwood (LH) pathways and Eley-Rideal (ER) pathways, which were explained in (§1.2.1.1) (Figures 1.6 & 1.7).

3.3 Methane Oxidation on 2D and 3D Cu_5 Clusters

First and foremost, the different possible methane adsorptions in structures **1** and **2** are depicted in figure 3.5. Methane is adsorbed on a low-coordinated Cu atom in direct contact with one of the O atoms present on the cluster, generating structure **1-a**. Compared to other adsorption sites with Cu only linked to two other Cu atoms (Sites **1-b** and **2-b**) or with a higher degree of coordination (Sites **c-e** of structure **1**), the calculations lead to less stable structures or to non-bonded systems.

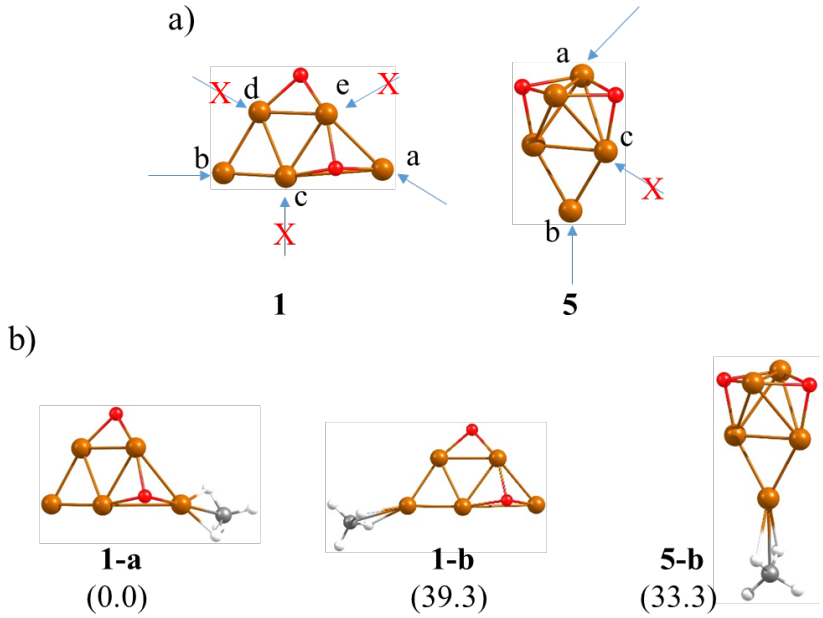

Figure 3.5 - Possible sites for CH_4 adsorption on Cu_5-2O (a), and optimised geometries of the most stable structures obtained (doublet state), with the relative stability given in parenthesis in kJ/mol (b).

Prominently, the interaction of methane with site **a** in the O containing 3D Cu_5 cluster (Structure **5**) produces its deformation into the same planar species (Structure **6** in figure 3.6), driving to the same reaction pathway on both Cu_5-2D and Cu_5-3D.

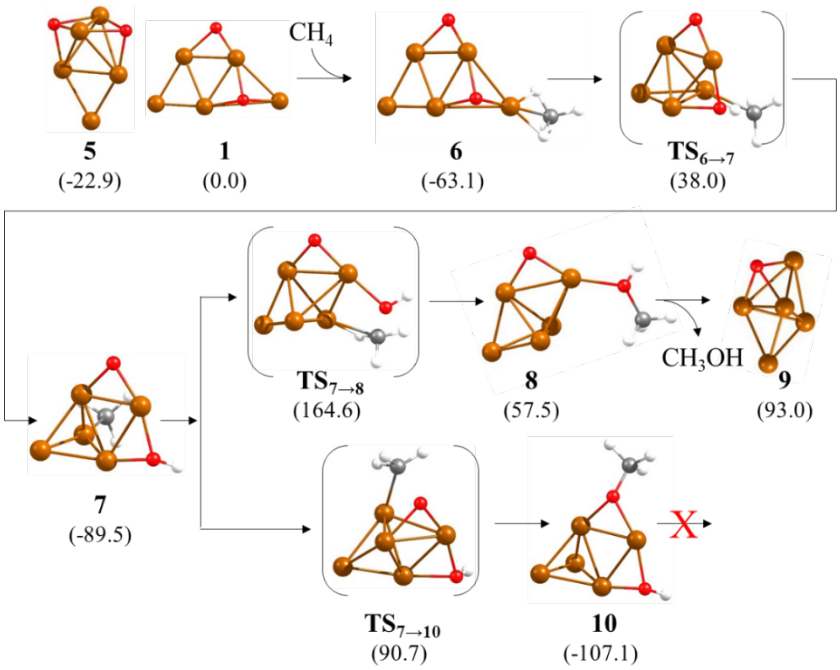

Figure 3.6 - Optimised geometries of the structures involved in the first part of the mechanism of methane oxidation on Cu_5 clusters following a Langmuir-Hinshelwood pathway. Relative Gibbs free energies of each structure in the doublet state respect to the initial reactant **1** are given in kJ/mol in parenthesis below the structure label. Cu, C and O atoms are depicted as orange, red, grey, and white balls respectively.

This process is energetically favourable, and two C-H bonds of methane become slightly activated by interaction with Cu, with optimised Cu-H and C-H distances of 1.831, 1.805, 1.125, and 1.129 Å respectively. Moving to C-H dissociation, it is facilitated by interaction of the H atom with the nearby O atom (**$TS_{6\rightarrow7}$**) with C-H and O-H distances of 1.397 and 1.336 Å respectively and an activation energy of 101.1 kJ/mol,

ensuing in structure **7**. In this intermediate, the hydroxyl group is coupled to two atoms at Cu-O distances of 1.887 and 1.951 Å, whereas the methyl group is monocoordinated on top of one Cu atom at a Cu-C distance of 1.916 Å. In order to form methanol by recombination of these two groups, the hydroxyl must break one of the Cu-O bonds while forming a new O-C bond with the surface methyl (**$TS_{7\rightarrow8}$**). The Cu-C, C-O and O-Cu optimised distances in this new transition state are 2.057, 1.837 and 1.923 Å respectively, indicating that the C atom is still bonded to Cu while the C-O bond is being formed.

Thermodynamically, this step is unfavourable and requires overcoming a prohibitive energy barrier of 254.1 kJ/mol. To surpass this drawback, alternative competing processes were investigated like the migration of the methyl group in intermediate **7.** Through transition state **$TS_{7\rightarrow10}$**, the methyl group is approached towards the adsorbed O atom resulting in Cu-C and C-O distances of 2.138 and 1.917 Å respectively, with a measured activation barrier of 180.2 kJ/mol and eventually forming an exceptionally stable methoxy group (Structure **10** in figure 3.6).

If the methoxy species **10** and the methyl intermediate **7** are compared, the methoxy product turn out to be 17.6 kJ/mol more stable, and several calculations were carried out to find a transition state after structure **10** with the purpose of producing methanol by reaction between the methoxy and hydroxyl groups but were unsuccessful. This situation is analogous to that described for Cu-exchanged zeolites, where the high stability of the methoxy species makes necessary an additional extraction step with water.[271,343,359]

Additional competitive processes starting for the strongly bound intermediate **7**, such as secondary C-H bond dissociation to form a CH_2 intermediate, also involve lower activation barriers than methanol production (figure 3.7), which suppose another hindrance for the process to become viable. To resume, all these different reaction paths altogether render the LH pathway kinetically non-accessible.

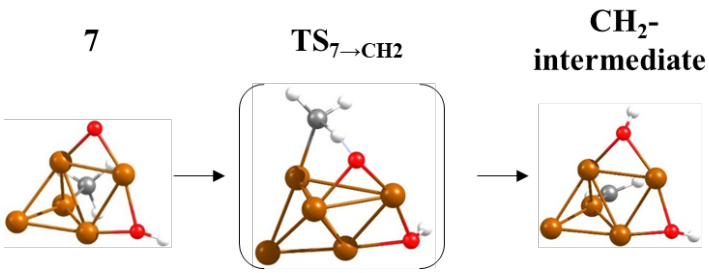

Figure 3.7 - Optimised geometries of the structures involved in the secondary C-H bond dissociation in intermediate **7**. The calculated activation and reaction free energies for this step are 96.7 and 11.0 kJ/mol in the doublet state, respectively. Cu, O, C and H atoms are depicted as orange, red, grey, and white balls, respectively.

In spite of the non-accessibility of this reaction path and in order to complete the study, the next reaction phase with only one O atom attached to the cluster was explored.

Starting from structure **9**, another methane molecule is approached, being preferentially adsorbed on an equatorial Cu atom of the 3D Cu_5 cluster, not in direct contact with O (Structure **11** in figure 3.8). For the purpose of activating the methane molecule, the H transfer from methane to O through transition state $\mathbf{TS_{11\rightarrow12}}$ entails the bending of both adsorbed groups but not the rupture of any Cu-O or Cu-C interaction. Consequently, the calculated activation energy is moderate (86.7 kJ/mol) and the optimised C-H and H-O distances are 1.379 and 1.420 Å respectively, similar to those obtained for $\mathbf{TS_{6\rightarrow7}}$. As a result, intermediate **12** is formed, with a monocoordinated methyl group anchored to a Cu atom and a bicoordinated hydroxyl group attached to a cluster edge. With a view to form methanol via a rebound mechanism, the compact geometry of the Cu_5 cluster forces the rupture of one Cu-O bond and the detachment of the methyl group to allow the formation of the desired product through transition state $\mathbf{TS_{12\rightarrow13}}$. This is the reason for the exceedingly activation barrier obtained for this step, 214.2 kJ/mol, which makes again the LH pathway kinetically difficult.

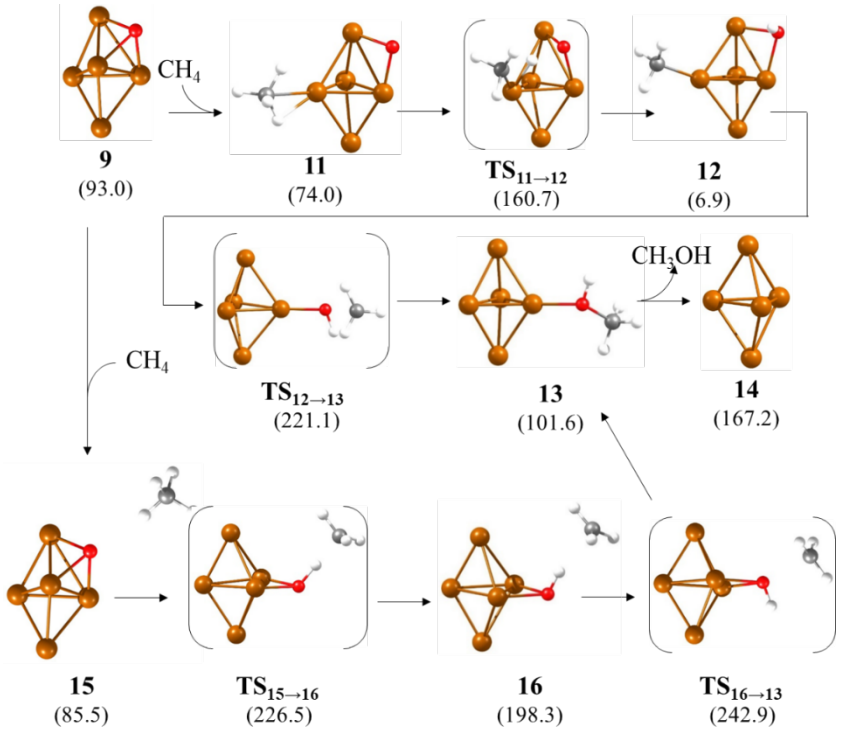

Figure 3.8 - Optimised geometries of the structures involved in the second part of the mechanism of methane oxidation on a 3D Cu_5 cluster. Relative Gibbs energies of each structure in the doublet state with respect to the initial reactant **1** are given in kJ/mol in parenthesis below the structure label. Cu, O, C and H atoms are depicted as orange, red, grey, and white balls, respectively.

Nevertheless, due to the demanding activation barrier required in **$TS_{12\rightarrow13}$**, alternative paths were investigated to find out new reaction paths to transform methane into methanol. This new pathway starts with a less stable reactant structure **15** in which methane does not interact with the 3D Cu_5 cluster. Next, the H transfer to the only O atom in the system is produced (**$TS_{15\rightarrow16}$**), requiring a large activation energy of 141.0 kJ/mol and yielding a metastable methyl radical intermediate **16** placed at a C-H distance of 2.152 Å. This methyl radical can directly react either with the bridged hydroxyl group through **$TS_{16\rightarrow13}$** to form adsorbed methanol **13** with a low activation barrier of 44.6 kJ/mol or

can be adsorbed on the cluster yielding the previously described stable structure **12**. In such case, the LH pathway would be followed with a high activation barrier for the methanol formation step of 214.2 kJ/mol. For this reason, the ER pathway through structure **15** would be the most accessible reaction path in this part of the process.

The other possible reaction path starts from methane physisorbed close to an O atom in structure **1**, and the interaction with the bicoordinated O atom is negligible, resulting in structure **17** (See figure 3.9), with the short O-H distance of 2.564 Å.

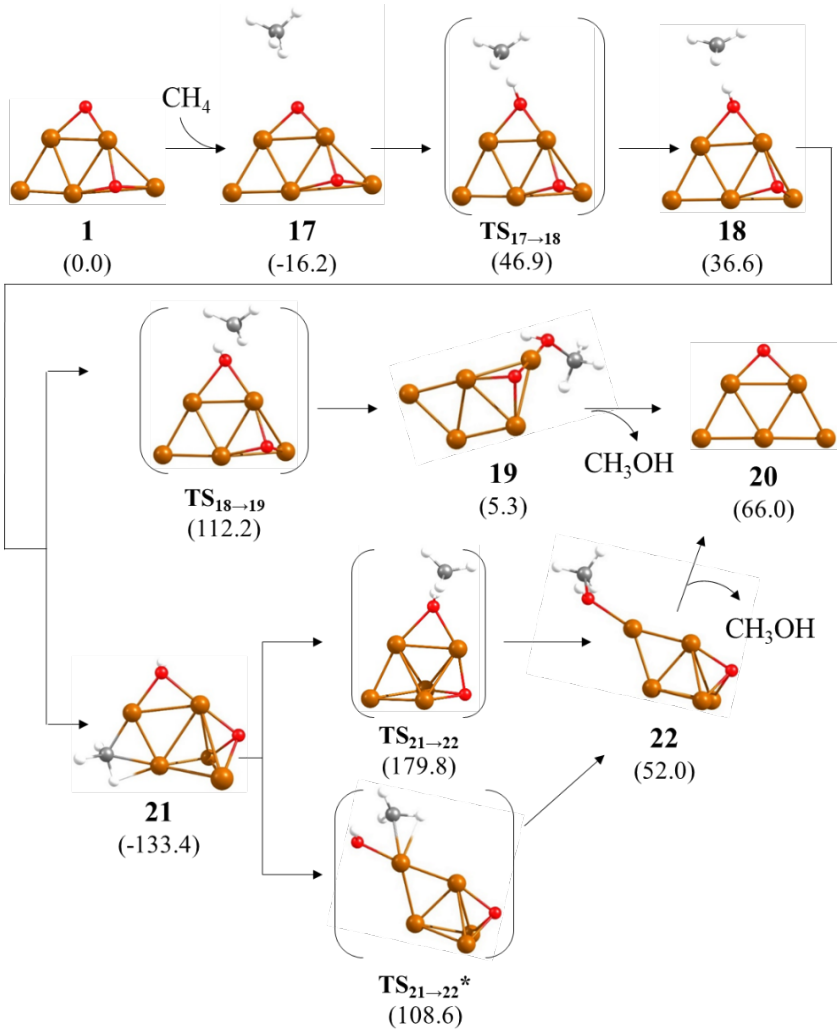

Figure 3.9 - Optimised geometries of the structures involved in the first part of the alternative mechanism of methane oxidation on Cu_5 clusters. Relative Gibbs energies of each structure in the doublet state respect to the initial reactant **1** are given in kJ/mol in parenthesis below the structure label. (Cu, O, C and H atoms are depicted as orange, red, grey, and white balls, respectively.

From this structure, it is significant that an H transfer from CH_4 to the O atom (**$TS_{17\rightarrow18}$**) is energetically accessible with a calculated activation

energy of 63.1 kJ/mol, yielding a metastable intermediate in which the ensuing methyl group is not interacting with the Cu cluster (Structure **18**). Focusing on the C-H and H-O distances, these evolve from 1.440 and 1.128 in $\mathbf{TS_{17\rightarrow 18}}$ to 2.104 and 0.986 in the intermediate **18**, evidencing the transfer of one of the H atoms to form a hydroxyl group. The nearly planar geometry of the non-interacting CH_3 fragment suggests a radical nature corroborated by a simple Bader analysis of the atomic charges (See table A3.1 in the appendix, §3.7).

From radical-like intermediate **18**, the reaction can evolve following three different routes. On one hand, attack of the methyl group to the bridged hydroxyl group in transition state $\mathbf{TS_{18\rightarrow 19}}$ results in formation of adsorbed methanol (Structure **19** in figure 3.9) with a calculated activation energy of only 75.6 kJ/mol. It is noticeable that methanol desorption from structure **19** does not require additional water, as the case with Cu-exchanged zeolites, leaving a highly stable planar Cu_5 cluster with an O atom adsorbed on its edge (Structure **20** in figure 3.9).

On the other hand, the unstable methyl group of structure **18** might directly adsorb on the Cu_5 cluster, forming either highly stable structures like **21**, with the C atom of the methyl group bridged between two Cu atoms, or a similarly stable methoxy intermediate as that in structure **10** (Figure 3.6). In order to produce methanol from intermediate **21**, two alternative routes were found. The pathway through $\mathbf{TS_{21\rightarrow 22}}$ involves a considerable activation barrier of 242.0 kJ/mol, but for $\mathbf{TS_{21\rightarrow 22}}$*****, it is mandatory to lose coordination of both methyl and hydroxyl groups, turning out to be an extremely demanding activation barrier of 313.2 kJ/mol. This is a proof that the bi-coordination of the methyl group signifies larger activation barriers, and therefore more difficult paths for the methane conversion to methanol.

Again, after the formation of the first methanol molecule, only one O atom remains adsorbed on the 2D Cu_5 cluster (Structure **20**), bridged on the short edge of the cluster (Figure 3.10).

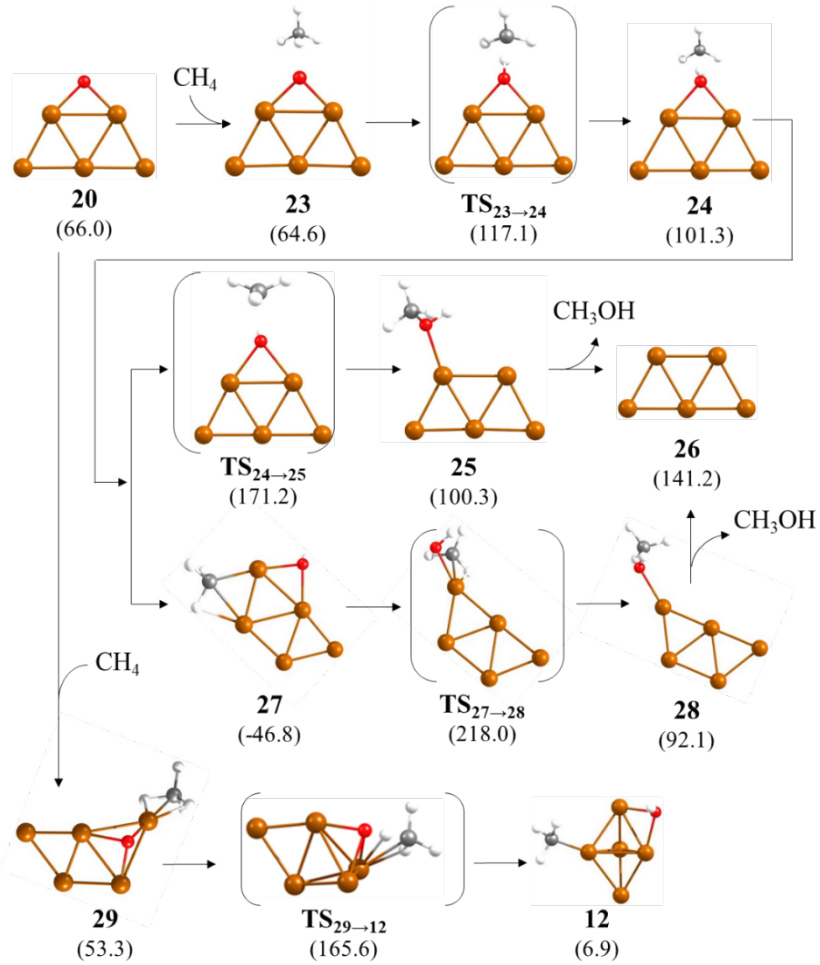

Figure 3.10 - Optimised geometries of the structures involved in the second part of the mechanism of methane oxidation on a planar Cu_5 cluster. Relative Gibbs energies of each structure in the doublet state with respect to the initial reactant **1** are given in kJ/mol in parenthesis below the structure label. Cu, O, C and H atoms are depicted as orange, red, grey, and white balls, respectively.

Considering that CH_4 does not adsorb on the Cu atoms in direct contact with a bridged O atom (See figure 3.5), besides the fact that CH_4 adsorbed on the bicoordinated Cu atoms on the long edge of Cu_5-2D is

too far from the O atom to react, in principle, only the ER pathway is geometrically accessible on this system.

Methane interaction with the O atom in structure **23** favours the H transfer step that initiates the ER mechanism, yielding intermediate **24** with a bicoordinated hydroxyl group and a methyl radical (See atomic charges in table A3.1). The corresponding activation energy for this H transfer is as low as 52.5 kJ/mol, being the process endothermic by 36.7 kJ/mol. The C-H optimised distances in $\mathbf{TS_{23\rightarrow24}}$ and intermediate **24** are 1.442 and 2.108 Å, respectively, similar to those found for the equivalent structures $\mathbf{TS_{17\rightarrow18}}$ (1.440 Å) and **18** (2.104 Å) in the first part of the cycle and shorter than in $\mathbf{TS_{15\rightarrow16}}$ (1.496 Å) and **16** (2.152 Å) on the Cu_5-3D cluster.

Again, direct methanol formation through transition state $\mathbf{TS_{24\rightarrow25}}$ requires a low activation energy of 69.9 kJ/mol but competes with the adsorption of the methyl group on a Cu atom conducting to structure **27**. The high stability of this intermediate containing both methyl and hydroxyl groups bicoordinated at the cluster edges implies an activation energy barrier of 264.8 kJ/mol to recombine the fragments and form adsorbed methanol (Structure **28** in figure 3.10), thus preventing the contribution of a LH pathway to methane conversion, just like in structure **21**.

Curiously, by forcing the adsorption of methane on a Cu atom of the Cu_5-2D-O system, structure **29** with the O atom three-coordinated on a facet of the cluster and close to adsorbed CH_4 is obtained. This structure is only 11.3 kJ/mol more stable than the feeble interacting intermediate **23** entailed in the ER pathway, and the activation energy required for C-H bond dissociation through $\mathbf{TS_{29\rightarrow12}}$ yielding adsorbed methyl and hydroxyl moieties (Structure **27** formerly described) is clearly higher (112.3 kJ/mol versus 52.5 kJ/mol for C-H bond rupture through $\mathbf{TS_{23\rightarrow24}}$). In light of the above, it can be concluded that 2D Cu_5 clusters and particularly the bicoordinated O atoms adsorbed at their edges, benefits the ER pathway via radical intermediates.

However, as explained in (§3.2), it is very likely that the catalyst reacts with additional O_2 molecules, giving rise to structure **2**. Thus, the reactivity of methane in Cu_5-4O cluster was also explored (Figure 3.11)

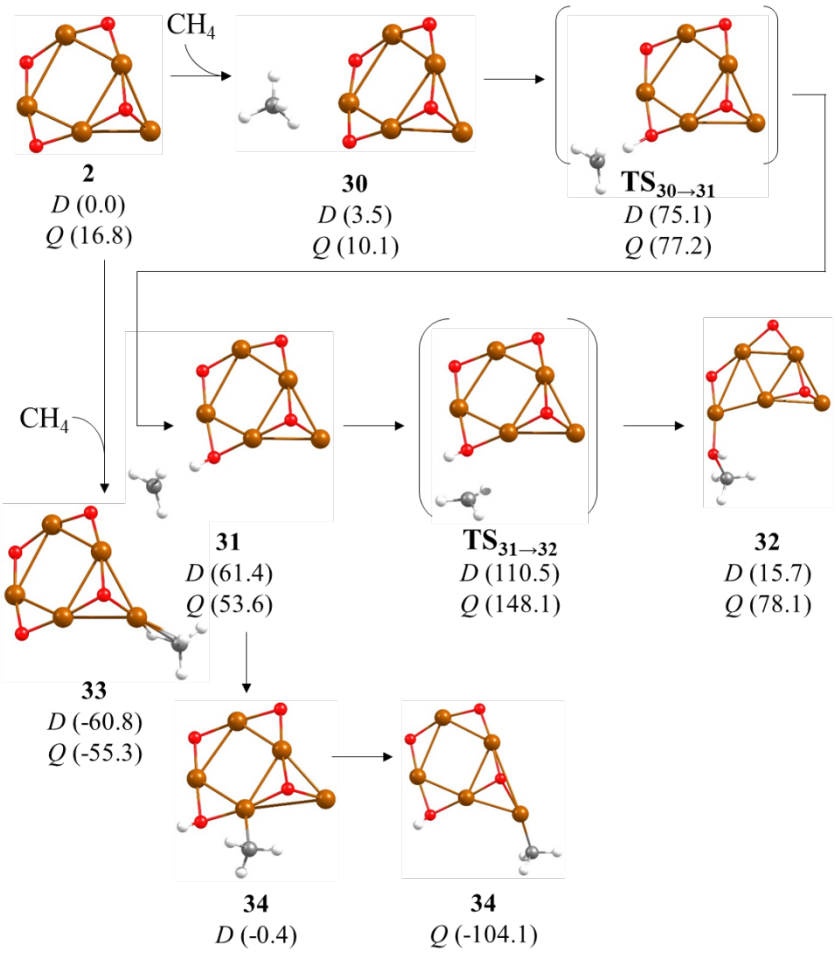

Figure 3.11 - Optimised geometries of the structures involved in the mechanism of methane oxidation on partly oxidised Cu_5-4O clusters. Relative Gibbs free energies of each structure in both doublet (D) and quadruplet (Q) states in relation to the initial reactant **2** in its most stable D state are given in kJ/mol in parenthesis below the structure label. Cu, O, C and H atoms are depicted as orange, red, grey, and white balls, respectively.

When the CH_4 molecule is approached, two affordable interactions are possible. First, structure **30** is obtained, resulting in C-H and O-H distances of 1.097 and 2.619 Å, respectively, corroborating the weak interactions with the cluster. Second, methane can be attached to the copper atom which possesses interactions with the three-coordinated O atom (structure **33**), with a Cu-C distance of 2.133 Å and a great stabilisation of at least 55 kJ/mol. The first route enables the C-H bond breakage through $\mathbf{TS_{30\rightarrow 31}}$, elongating C-H distance to 1.453 Å whilst O-H distance is shortened to 1.123 Å, requiring 71.6 and 67,1 kJ/mol for doublet (*D*) and quadruplet (*Q*) states, respectively. As a consequence, structure **31** is constructed, having a weak methyl radical interaction, located 2.068 Å away from the H atom bonded to the previously bicoordinated O atom. Interestingly, this structure gains more stability in the quadruplet state, being 7.8 kJ/mol more stable than its doublet counterpart.

From this intermediate, to conduct methanol formation (structure **32**), the radical group must be displaced to facilitate the interaction with the bicoordinated hydroxyl group in transition state $\mathbf{TS_{31\rightarrow 32}}$ with a calculated C-O distance of 2.181 Å, consuming 49.1 and 94.5 for *D* and *Q* potential surfaces, respectively. Focusing on structure **32**, the stability differences in the spin potential energy surfaces are noticeable, with the doublet state being the most stable. The same phenomenon occurs in the case the radical methyl group in structure **31** falls onto the cluster, forming structure **34**, in which the difference is even greater, this time in quadruplet's favour, being linked to a distinct attachment of the methyl group to the same copper atom as in structure **33**.

From this reaction path, it is important to observe that while all structures discussed up to the moment have only one unpaired electron and are therefore doublet (D), when a second O_2 molecule is added to the system, the probability of having D and Q potential energy surfaces is visible, confirming its importance in the course of the reaction.

At this point, and taking into consideration that O_2 dissociation on 2D Cu_5 clusters involves a higher activation energy than on 3D Cu_5 clusters (§3.2),[217,520] the possibility of CH_4 oxidation by adsorbed molecular O_2 was also investigated (Figure 3.12).

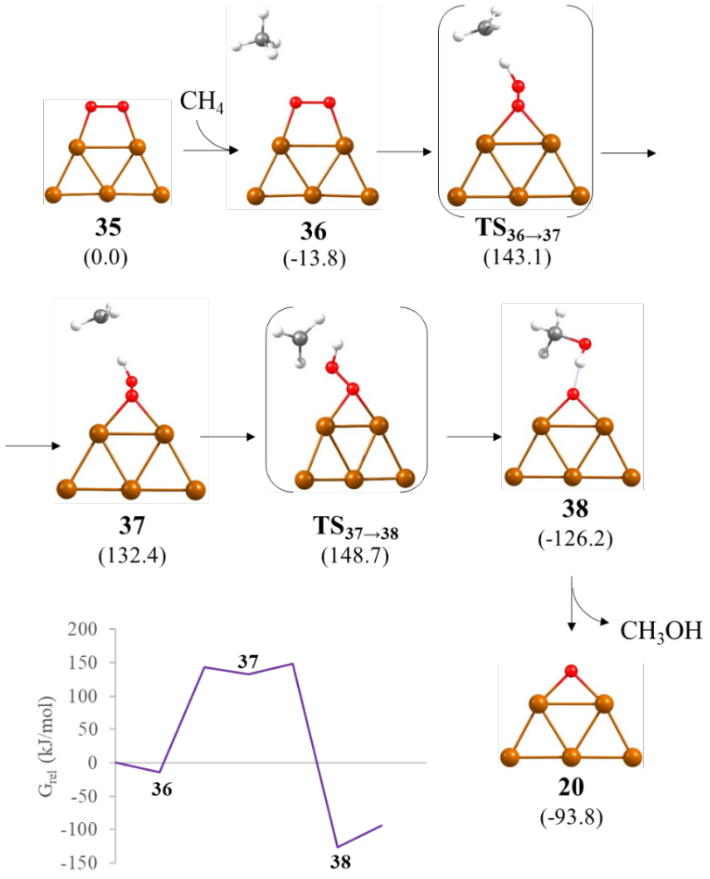

Figure 3.12 - Optimised geometries of the structures involved in the mechanism of methane oxidation with molecular O_2 on a planar Cu_5 cluster following an ER pathway and Gibbs free energy profile at 478 K. Relative Gibbs energies of each structure with respect to the initial reactant **35** in doublet state are given in kJ/mol in parenthesis below the structure label. Cu, O, C and H atoms are depicted as orange, red, grey, and white balls, respectively.

Commencing from O_2 adsorbed in a bridge mode on Cu_5-2D (Structure **35**), the dissociation of a C-H bond of weakly interacting methane (Structure **36**) through transition state $\mathbf{TS_{36\rightarrow37}}$ requires surpassing an

activation energy barrier of 157.0 kJ/mol and yields a radical methyl group (See charge distribution in table A3.1) and a hydroperoxide group bonded to Cu_5. From this metastable intermediate **37**, subsequent formation of methanol through transition state $\mathbf{TS_{37\rightarrow 38}}$ is kinetically easy and thermodynamically favoured, with the adsorbed methanol product **38** being 258.6 kJ/mol more stable than intermediate **37**. Nevertheless, the high activation energy required in the first step (See table 3.4 in discussion, §3.5) makes this route via molecular O_2 unlikely.

3.4 Methane Oxidation on Cu_7 clusters

Once the key aspects of the mechanism are established for 2D and 3D Cu_5 systems, the influence of cluster size was analysed by considering a Cu_7 cluster with 3D morphology and two O atoms adsorbed on opposite facets in a three-fold coordination.

First of all, methane is adsorbed on a low-coordinated Cu atom in direct contact with one of the O atoms present on the cluster (Site **3-a** in figure 3.13), forming structure **39** in figure 3.14, with optimised Cu-H and C-H distances of 1.979, 1.902, 1.113 and 1.120 Å respectively. Compared to other adsorption sites with Cu only linked to other Cu atoms (Site **3-b** in section **b**) and the Cu atoms located at the top or bottom and between both O atoms (Sites **c** and **d** in section **a** respectively), the calculations conduct to fewer stable structures, non-bonded systems or to systems that does not have any possibility to progress, like **3-b**.

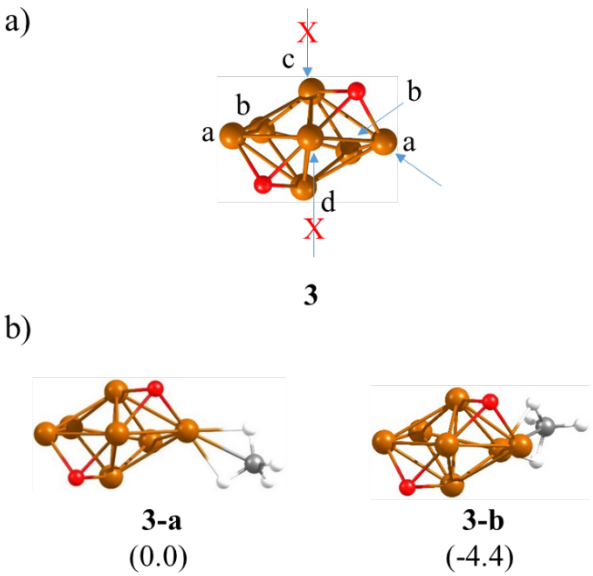

Figure 3.13 - Possible sites for CH_4 adsorption on Cu_7-2O (a), and optimised geometries of the most stable structures obtained, with the relative Gibbs stability given in parenthesis in kJ/mol (b).

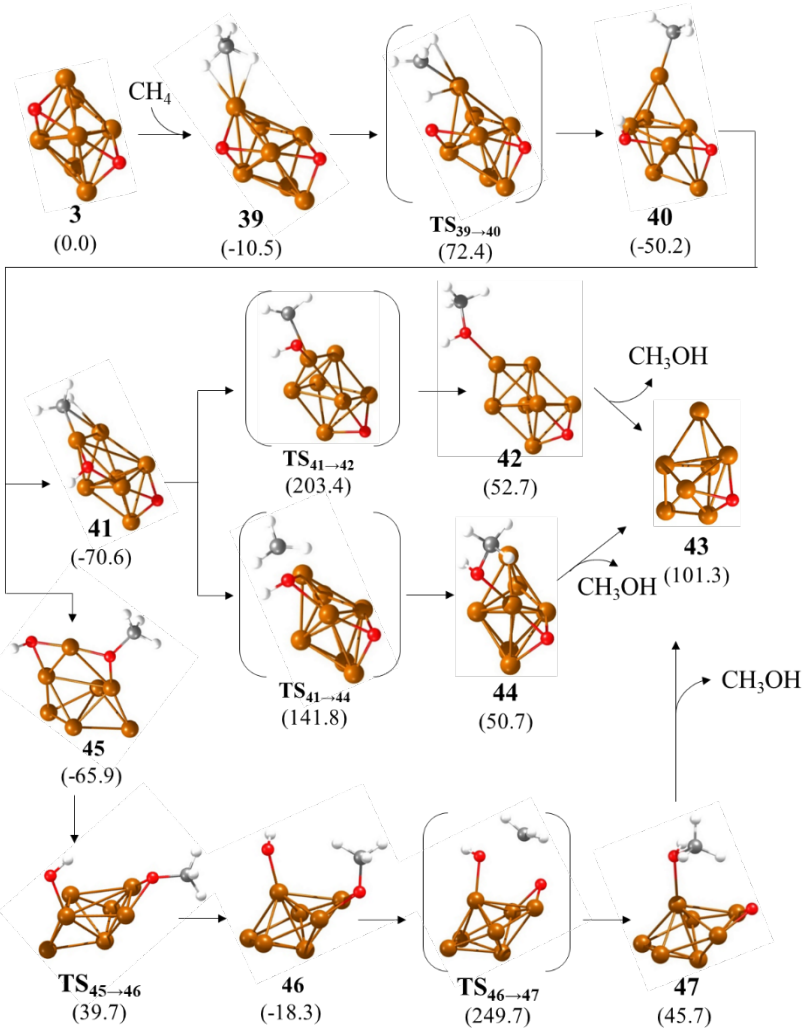

Figure 3.14 - Optimised geometries of the structures involved in the first part of the mechanism of methane oxidation on Cu_7 clusters. Relative Gibbs free energies of each structure with respect to the initial reactant **3** are given in kJ/mol in parenthesis below the structure label. Cu, O, C and H atoms are depicted as orange, red, grey, and white balls respectively.

Thanks to the presence of the nearby O atom, the dissociation of one of the C-H bonds via transition state (**$TS_{39\rightarrow40}$**) is facilitated with a

calculated activation energy of 82.8 kJ/mol, slightly lower than obtained for Cu_5-3D. The corresponding C-H and O-H distances in the transition state are 1.395 and 1.322 Å respectively, and the resulting intermediate **40** contains a methyl group monocoordinated on top of a Cu atom with a Cu-C distance of 1.917 Å and a hydroxyl group bonded to two Cu atoms. This intermediate rearranges quickly either to a 20.4 kJ/mol more stable intermediate **41** in which the methyl group is bicoordinated to two Cu atoms, or to a 15.7 kJ/mol more stable intermediate **45** with the formation of a methoxy group. Via the recombination of methyl and hydroxyl functional groups on account of the scission of one Cu-O bond and one Cu-C in **$TS_{41\rightarrow42}$**, a new methanol molecule is generated in structure **42** with a huge barrier of 273.9 kJ/mol, which makes this route impossible for the production of the desired product.

Another alternative way to produce methanol from structure **41** is via the displacement of the methyl group toward the adsorbed hydroxyl in **$TS_{41\rightarrow44}$**, producing an adsorbed methanol molecule in structure **44**, but the calculated activation barrier is extraordinarily high (212.3 kJ/mol), suggesting a bad performance of Cu_7 in the oxidation of methane. A closer inspection to the geometry and charge distribution of **$TS_{41\rightarrow44}$** indicates that it might be involved in an ER pathway, but it was no possible to stabilise a methyl radical intermediate connected to this transition state.

Otherwise, in case of following structure **45** pathway, the rupture of one of the two Cu-O bonds stabilizing the hydroxyl group involves an activation barrier of 105.5 kJ/mol, and the ensuing monocoordinated hydroxyl group in intermediate **46** enables the migration of the methyl fragment to yield methanol (Structure **47** in figure 3.14) through a distinct transition state corroborated by its geometric and electronic parameters (**$TS_{46\rightarrow47}$**), being **$TS_{18\rightarrow19}$** the most similar in terms of charge. Nevertheless, the calculated activation energy for this methyl shift in which the methyl group is at 2.180 and 2.235 Å from the two O atoms, is extremely demanding (268 kJ/mol), ruling out this path for the formation of methanol.

To sum up, through the LH pathway commencing from a reactant with two three-coordinated O atoms (Structure **39**), there is not an efficient path to transform methane into methanol without the involvement of

several secondary paths that awfully disturb the progress of the catalytic reaction.

Notwithstanding the clear evidence, to complete the computational study and encompass all the different perspectives, the study of the second catalytic cycle from structure **43** was explored (Figure 3.15):

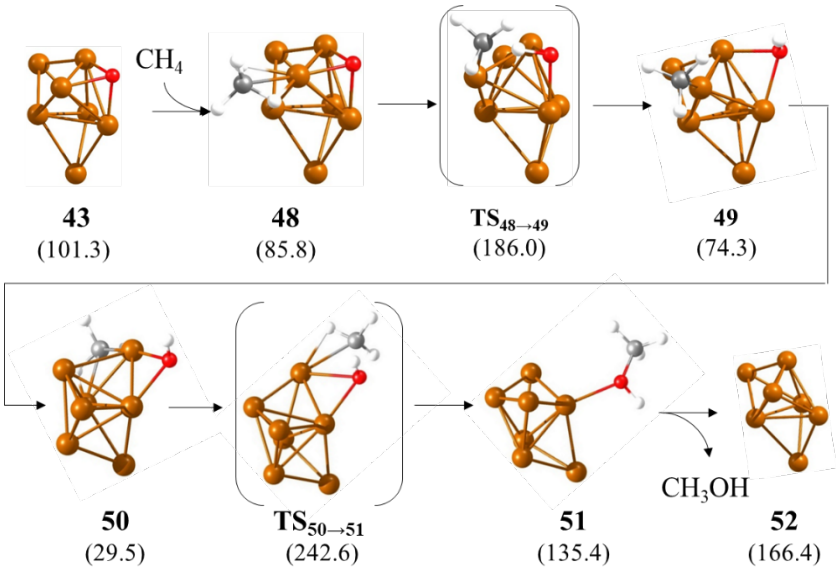

Figure 3.15 - Optimised geometries of the structures involved in the second part of the mechanism of methane oxidation on Cu_7 clusters. Relative energies of each structure with respect to the initial reactant **3** are given in kJ/mol in parenthesis below the structure label. Cu, O, C and H atoms are depicted as orange, red, grey, and white balls, respectively.

Observing the course of the reaction, it is clear that is similar to that formerly described for Cu_7 with two adsorbed O atoms. CH_4 is adsorbed on a Cu atom in direct contact with the adsorbed O (Structure **48**), which facilitates the C-H bond dissociation through **$TS_{48\rightarrow49}$**. Then a system with a monocoordinated methyl and a bicoordinated hydroxyl group (Structure **49**) is initially formed, which evolves to a more stable complex **50** in which the two reactant groups occupy bridge positions between two Cu atoms. The corresponding activation energy for the C-

H bond breaking step is relatively high (100.1 kJ/mol), but the subsequent recombination of fragments to produce methanol via $\mathbf{TS_{50\rightarrow 51}}$ is energetically forbidden, with a calculated barrier of 213.1 kJ/mol, demonstrating once again that a LH mechanism is inefficient to turn methane into methanol.

Nonetheless, there is an alternative pathway involving an ER mechanism if one of the Cu-O bonds of the three-coordinated O atoms in structure **3** is split, consuming 16.7 kJ/mol in the process and turning into a bi-coordinated O atom (Structure **53** in figure 3.16).

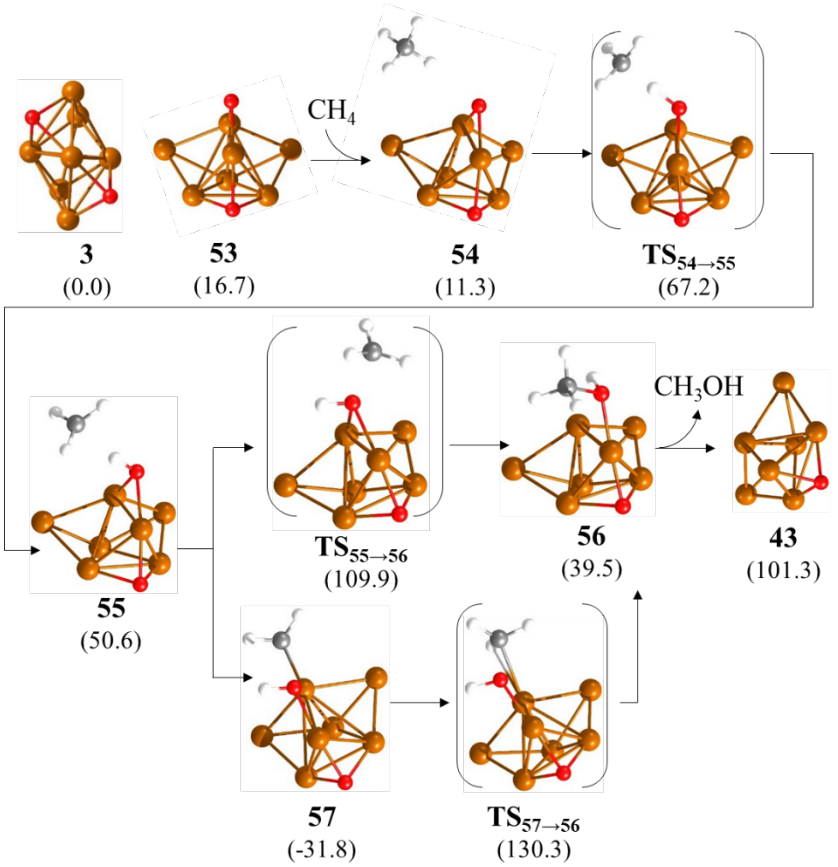

Figure 3.16 - Optimised geometries of the structures involved in the first part of the mechanism of methane oxidation on Cu_7 clusters following an Eley-Rideal pathway. Relative Gibbs free energies of each structure with respect to the initial reactant **3** are given in kJ/mol in parenthesis below the structure label. Cu, O, C and H atoms are depicted as orange, red, grey, and white balls, respectively.

As described above for Cu_5 (§3.3), starting from methane close to the bi-coordinated O atom (structure **54**), the product undergoes an H transfer from CH_4 to the O atom through $\mathbf{TS_{54\rightarrow55}}$ with C-H and H-O distances of 1.436 and 1.128 Å respectively, yielding a metastable methyl radical not in direct contact with any Cu atom, structure **55**. Interestingly, this transition state is similar to the one found in Cu_5

clusters in the ER pathway, **$TS_{17\rightarrow18}$**, with practically identical net atomic charges but differences in the activation and reaction energies, being 63.2 and 52.8 kJ/mol, respectively for Cu_5 and 55.9 and 39.3 kJ/mol, respectively for Cu_7 (For further information, consult §3.7).

Next, the direct reaction of the methyl radical with the adsorbed hydroxyl is produced, resulting in adsorbed methanol (Structure **56**) through a transition state **$TS_{55\rightarrow56}$** with a low activation energy of only 59.3 kJ/mol. However, the methyl radical moiety in intermediate **55** possess a more accessible route through structure **57**, anchoring the methyl radical to one Cu atom of the cluster, forming an 82.4 kJ/mol more stable intermediate. However, as in previous instances, the recombination of one methyl and one hydroxyl group, both anchored to Cu, involves necessarily the scission of Cu-O or Cu-C bonds with its associated energy cost. Therefore, and once again, it is necessary to avoid the adsorption of the methyl group into the cluster (Structure **57**) in order to evade the route with the high activation barrier of 162.1 kJ/mol (**$TS_{57\rightarrow56}$**). Observing the different parameters gathered in the appendix (§3.7), it is possible to confirm that the radical pathway possesses lower activation barriers than the one that goes through the LH mechanism, showing that the catalyst able to stabilise these radical moieties would be the best candidate for this reaction.

After the first catalytic cycle, structure **43** with one O atom adsorbed on a facet is obtained irrespective of the pathway followed. To complete the computational study and encompass all the different standpoints, the ER mechanism was examined (Figure 3.17):

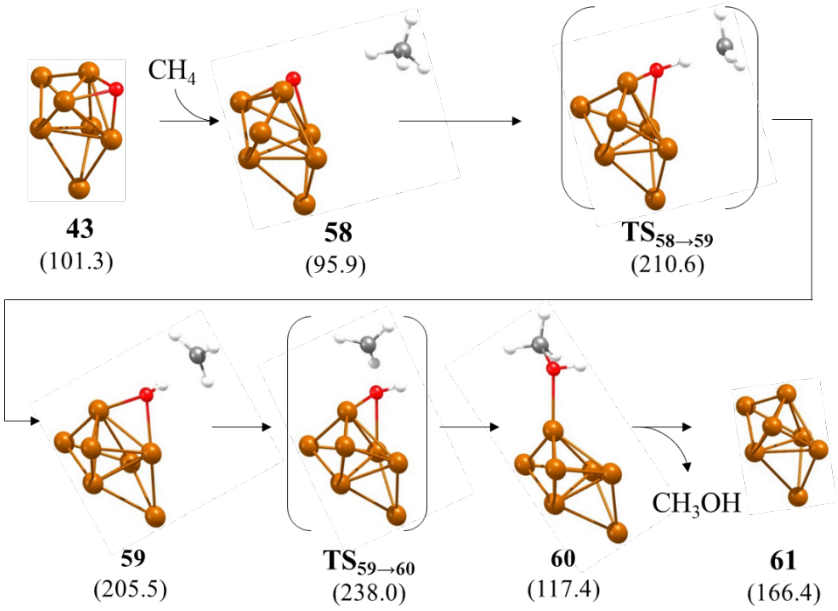

Figure 3.17 - Optimised geometries of the structures involved in the second part of the alternative mechanism of methane oxidation on Cu_7 clusters. Relative Gibbs free energies of each structure with respect to the initial reactant **3** are given in kJ/mol in parenthesis below the structure label. Cu, O, C and H atoms are depicted as orange, red, grey, and white balls, respectively.

Like in the previous phase, a new CH_4 molecule reacts from the gas phase (Structure **58**) transferring an H to adsorbed O (Structure $\mathbf{TS_{58\rightarrow 59}}$), thereby producing a non-adsorbed methyl radical (Structure **59**) with a moderate activation energy of 114.7 kJ/mol. The main reason for this augmented barrier is owing to the adsorbed three-coordinated O atom, because one of the Cu-O bonds must be broken to accept the H atom and form the adsorbed hydroxyl. The ensuing reaction of the methyl radical with the bridged hydroxyl is easier and only 32.5 kJ/mol is required to form adsorbed methanol through transition state $\mathbf{TS_{59\rightarrow 60}}$. Once structure **60** is constructed, the intermediate necessitates 49 kJ/mol to release the methanol molecule.

Lastly, taking into account that Cu_7 clusters are also very sensitive to O_2 concentration (§3.2), the reactivity of structure **4** with methane was studied (Figure 3.18).

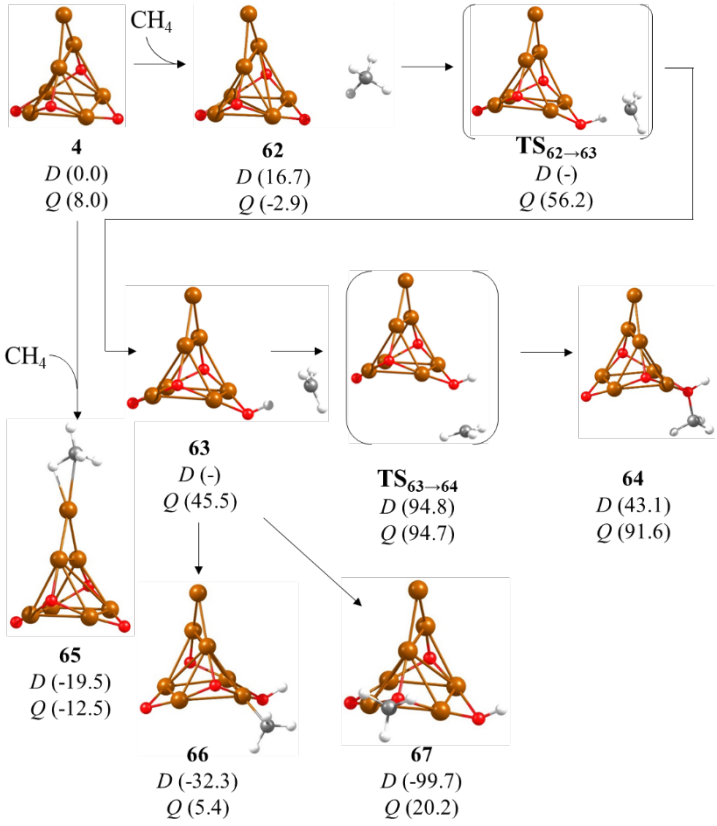

Figure 3.18 - Optimised geometries of the structures involved in the mechanism of methane oxidation on partly oxidised Cu_7-4O clusters. Relative Gibbs free energies of each structure in both doublet (*D*) and quadruplet (*Q*) states in relation to the initial reactant **4** in its most stable D state are given in kJ/mol in parenthesis below the structure label. Cu, O, C and H atoms are depicted as orange, red, grey, and white balls, respectively.

For both bicoordinated O atoms, methane has two possible affordable interactions. First, methane can weakly interact with the top Cu atom, not being in direct contact with O (Structure **65**) and second, it can also form a slightly less stable structure **62** via physisorption close to one of the bicoordinated O atoms at the edge of the cluster, which enables the

hydrogen transfer from physisorbed CH_4 to the bicoordinated O atom through transition state $\mathbf{TS_{62\rightarrow63}}$.

Surprisingly, the C-H dissociation transition state was not found in the doublet state and all the attempts resulted in the regeneration of the CH_4 molecule. In contrast, the H transfer reaction on the *Q* potential energy surface leads to an activation energy of 39.4 kJ/mol, generating a *Q* methyl radical intermediate **63** that can easily react with the just-formed hydroxyl group through transition state $\mathbf{TS_{63\rightarrow64}}$, yielding methanol (Structure **64**) with an activation energy of 49.3 kJ/mol. The same behaviour observed in $\mathbf{TS_{62\rightarrow63}}$. can also be applied to the doublet intermediate with the methyl radical moiety (Structure **63**), which also led to the reversal reaction yielding methane.

Therefore, keeping the aforementioned mechanism in mind, this ER pathway becomes competitive in Cu_7 clusters thanks to the additional bicoordinated O atoms that occupy bridge positions at the cluster edges. Unfortunately, the possibility to form more stable Cu-methyl (Structure **66**) or Cu-methoxy (Structure **67**) intermediates is real, from which formation of methanol is difficult despite the lower stability of these quadruplet intermediates in comparison with its doublet counterparts.

3.5 Discussion for both Langmuir-Hinshelwood and Eley-Rideal pathways in Cu_n clusters

To facilitate comparison of all the pathways described so far, table 3.4 compiles the activation energies and Gibbs energies for the key steps in all the reaction paths detailed in previous sections.

Table 3.4 – Comparison of Langmuir-Hinshelwood (LH) and Eley-Rideal (ER) pathways on different Cu_5 and Cu_7 clusters. Activation energies (E_{act}) and activation Gibbs free energies (G_{act}) at 478 K for the C-H dissociation in CH_4 (CH) and for CH_3OH formation (CO) steps are given in kJ/mol.

Cluster	**Pathway**	E_{act} **(CH) (kJ/mol)**	E_{act} **(CO) (kJ/mol)**	G_{act} **(CH) (kJ/mol)**	G_{act} **(CO) (kJ/mol)**
Cu_5-2O	LH	107.6	245.1	101.12	254.1
Cu_5-3D-O	LH	75.6	213.7	86.7	214.2
Cu_5-2D-O	LH	120.4	266.1	112.3	264.8
Cu_5-2D-O_2	LH	-	-	-	-
Cu_7-2O	LH	86.1	233.6	82.8	212.3
Cu_7-O	LH	107.7	220.3	100.1	213.1
Cu_5-2O	ER	57.2	61.3	63.2	75.6
Cu_5-3D-O	ER	132.1	25.7	140.9	44.5
Cu_5-2D-O	ER	57.3	50.4	52.5	69.9
Cu_5-2D-O_2	ER	154.5	12.4	157.0	16.2
Cu_5-4O	ER	77.1	35.5	71.6	49.1
Cu_7-2O	ER	60.0	41.6	56.0	59.3
Cu_7-O	ER	126.1	23.3	114.7	32.5
Cu_7-4O	ER	56.6	31.5	59.0	49.2

3.5.1 Cu_5 clusters

Next, the Gibbs free energy profiles at 478 K for all the processes involving atomic O in Cu_5 clusters are plotted together in figures 3.19 & 3.20:

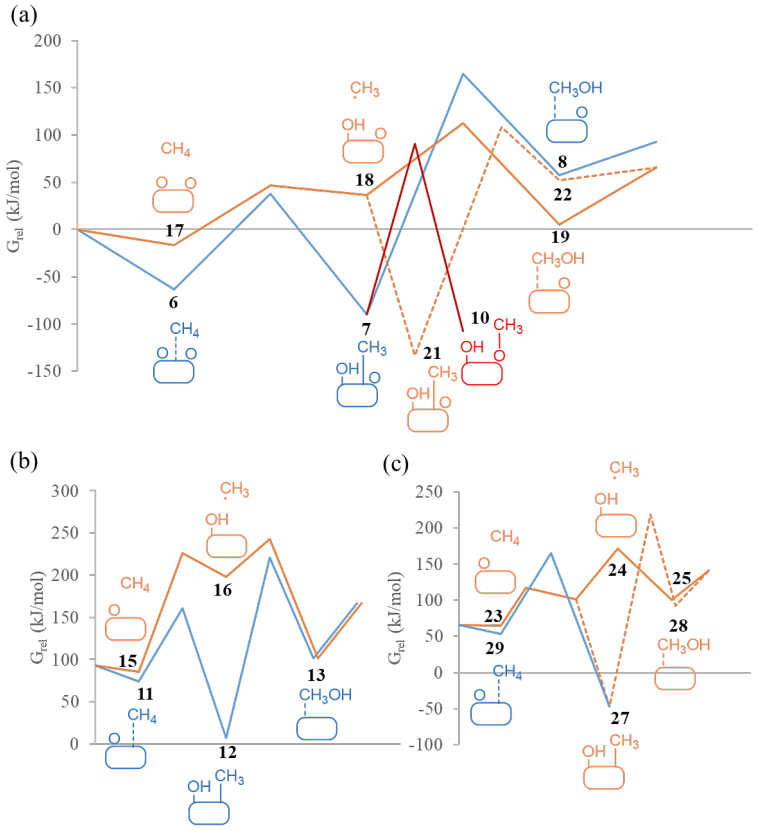

Figure 3.19 - Gibbs energy profiles for CH_4 oxidation to CH_3OH on (a) Cu_5-2O, (b) Cu_5-3D-O and (c) Cu_5-2D-O clusters at 478 K. Langmuir-Hinshelwood and Eley-Rideal pathways are plotted as blue and orange lines, respectively. Formation of methoxy intermediates is depicted in red. The labels correspond to the optimised structures shown in figures 3.6, 3.8, 3.9 and 3.10. The origin of Gibbs energies is in every case the

initial reactant structure **1**, and the relative electronic and relative Gibbs energy values are summarised in table A3.2, §3.7.

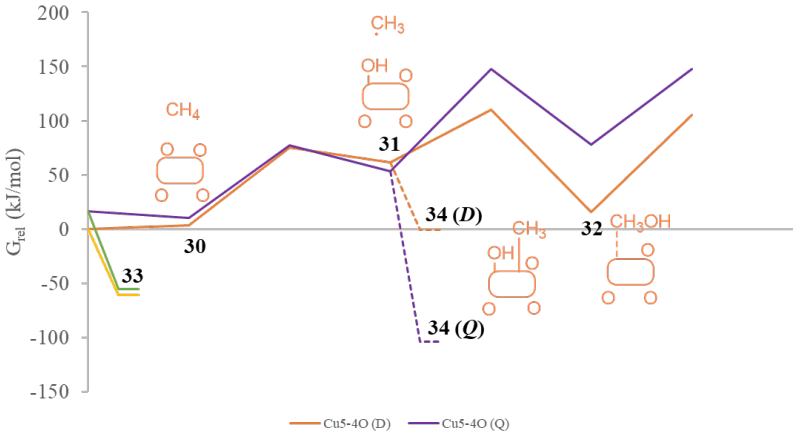

Figure 3.20 - Energy profiles for CH_4 oxidation to CH_3OH on Cu_5-4O calculated at 478 K. Eley-Rideal pathways in the doublet (*D*) and quadruplet (*Q*) potential energy surface are plotted as orange and purple lines, respectively. Formation of adsorbed methyl intermediate in the first step is depicted in yellow and light green lines for the *D* and *Q* surfaces, respectively, and subsequently, the formation of adsorbed methyl intermediates in the second step is depicted as orange and purple dash lines for the *D* and *Q* spin surfaces, respectively. The labels correspond to the optimised structures shown in figure 3.11. The origin of energies is the initial reactant structure **2**. Relative Gibbs energy values are summarised in table A3.2, §3.7.

For Cu_5 clusters with two adsorbed O atoms (Figure 3.19a) and for Cu_5-3D with one adsorbed O atom (Figure 3.19b), LH pathways in which methane interacts with Cu before reacting (Blue lines in figure 3.19b) involve high Gibbs activation energies for the dissociation of the first C-H bond (~87 kJ/mol) and unaffordable Gibbs activation energies (>210 kJ/mol) for the formation of methanol. The large stability of the methyl and hydroxyl fragments generated in the first step of the mechanism, which are in many cases bicoordinated to two Cu atoms of the cluster, explains the high energies necessary to detach these two

CH_3 and OH functional groups from Cu and combine them to form methanol as well as the difficult formation of methoxy groups by reaction of methyl with adsorbed O. In contrast, the alternative ER pathway according to which methane reacts from the gas phase, forming a hydroxyl group attached to Cu and a radical-like methyl intermediate (Orange lines in figure 3.19), requires lower Gibbs activation energies both for C-H bond dissociation (~63 kJ/mol) and C-O bond formation (~76 kJ/mol).

Nonetheless, this is only valid when the O atom participating in the reaction is bicoordinated to the Cu_5 cluster. For the Cu_5-3D-O system, with the O atom initially three-coordinated on a face of the cluster, the calculated activation energy for C-H bond scission is high (141 kJ/mol). The reason is the adsorbed O atom, which must migrate from the face to the edge of the cluster, thus decreasing its coordination to Cu atoms from 3 to 2 in order to react with CH_4.

Respect to the Gibbs energy profiles described for Cu_5-4O clusters in figure 3.20 (§3.5.1), the uncovered Eley-Rideal pathway demonstrates that if the system suffers from further oxidation, not only requires less energy to surpass the activation barriers to yield methanol, but also possesses multiple accessible active centres to perform the methane-to-methanol reaction, which might suppose an increase of the kinetics of the reaction. Nevertheless, the adsorption of the methyl group in the *Q* energy surface in structure **34** imposes a much higher activation energy that could severely hinder the methanol formation step, needing to overcome a 252.2 kJ/mol barrier in that case. This fact also proves the importance of having two feasible potential energy surfaces involved in the chemical reaction, since the doublet state would need at least 110.9 kJ/mol in the case of forming structure **34 (*D*)**, in comparison with the numbers achieved in the quadruplet state. Hence, the doublet spin surface is the most optimised reaction path for the conversion of methane into methanol.

Concerning the net atomic charges on the O and H atoms of the hydroxyl groups formed in the first step, both the LH and the ER pathways are similar, around -1*e* for O and 0.4*e* for H (table A3.1 in the

appendix, §3.7). Conversely, the net atomic charge on the C atom and the total charge on the methyl group are clearly negative in structures **$TS_{6\rightarrow7}$** and **7**, in which the methyl group is attached to Cu, and close to neutral in structures **$TS_{17\rightarrow18}$** and **18** with a non-interacting methyl group. There were several attempts to obtain a similar pathway involving the three-coordinated O atom of structure **1,** but all of them failed, and H transfer always resulted in the reverse formation of a methane molecule, evincing the importance of the coordination of O atoms on their reactivity

For the second step, both LH and ER pathways possess similar net atomic charge values than in the previous step, swinging from ∼-1.5*e* in the transition states to ∼-1e in the intermediates for O atoms and from ∼0.4*e* in transition states to 1e in the rest of structures for H atoms (table A3.1, §3.7). Likewise, the same behaviour is found for **$TS_{11\rightarrow12}$** and **12**, with negative net atomic charges on the C and methyl group, as well as for structures **$TS_{23\rightarrow24}$** and **24** in relation to structures **$TS_{17\rightarrow18}$** and **18**, presenting almost neutral charge, evidencing the same kind of mechanism for both reaction paths respectively.

On balance, the results presented up to now indicate that methane activation on O containing Cu_5 clusters via a LH mechanism is energetically accessible, but recombination of the resulting adsorbed methyl or methoxy groups with hydroxyl groups to form methanol is kinetically forbidden. Alternatively, an ER pathway in which methane reacts from gas phase through a radical-like methyl intermediate is energetically affordable, but the attachment of the methyl radical to the cluster surface and the subsequent formation of secondary products including methoxy groups must be avoided. This is clearly observed in the Gibbs free energy profiles at 478 K plotted in figure 3.19, with the smoothest profile (Full orange line) corresponding to the ER pathway through a radical intermediate. Additionally, the influence of O_2 coverage is quite important in the development of the reaction, implying a mix of doublet and quadruplet potential energy surfaces that can favour the process if the system is stabilised in the doublet state. Finally, it is noteworthy that there is a mix of Langmuir-Hinshelwood and Eley-

Rideal pathways in each step of the process, and always the ER pathway is the most kinetically accessible path to turn methane into methanol.

3.5.2 Cu_7 clusters

The general reactivity trends obtained for Cu_7 are summarised in figures 3.21 and 3.22 and the Gibbs free energies obtained for the dissociation of the C-H bond in the CH_4 molecule to produce CH_3OH by C-O bond formation are recapitulated in table 3.4 (See §3.5):

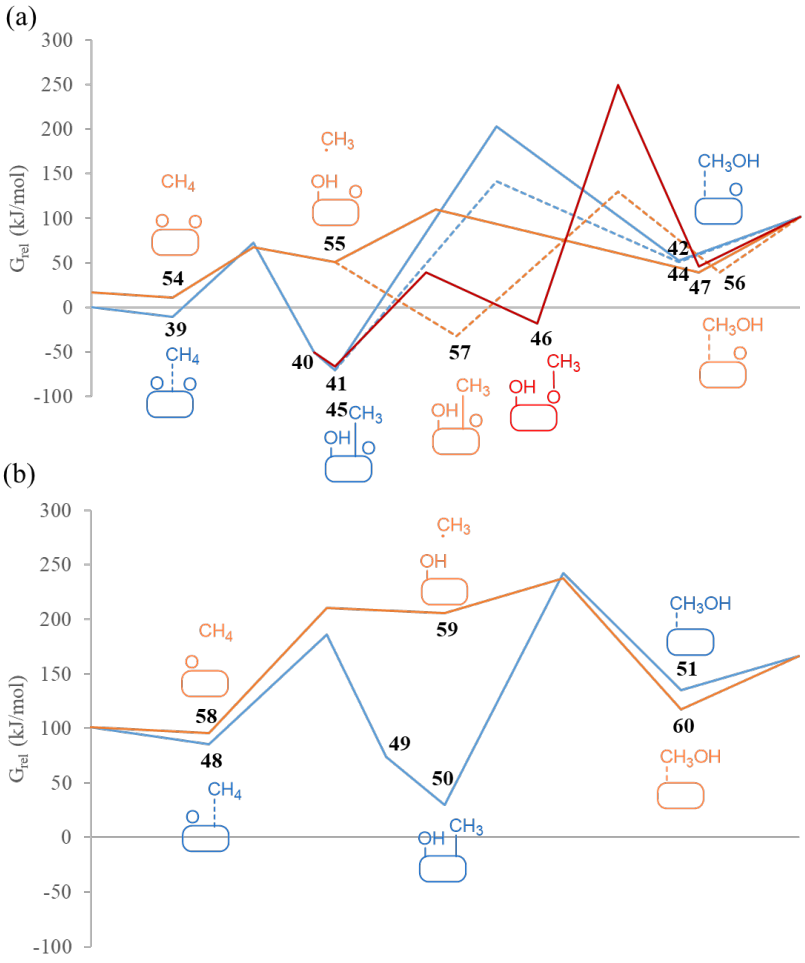

Figure 3.21 - Energy profiles for CH_4 oxidation to CH_3OH on (a) Cu_7-2O and (b) Cu_7-O calculated at 478 K. Langmuir-Hinshelwood and Eley-Rideal pathways are plotted as blue and orange lines respectively. Formation of methoxy intermediates is depicted in red. The labels

correspond to the optimised structures shown in figure 3.18. The origin of energies is the initial reactant structure **3**. Relative Gibbs energy values are summarised in table A3.2 (See appendix, §3.7)

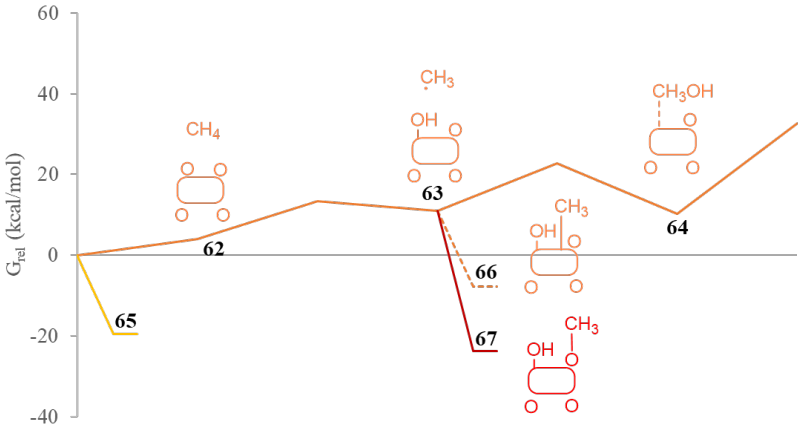

Figure 3.22 - Energy profiles for CH_4 oxidation to CH_3OH on Cu_7-4O calculated at 478 K. Eley-Rideal pathway is plotted as orange lines and formation of methoxy intermediates is depicted in red. The labels correspond to the optimised structures shown in figure 3.18. The origin of energies is the initial reactant structure **4**. Relative Gibbs energy values are summarised in table A3.2 (See appendix, §3.7)

As occurred in Cu_5, the LH pathways involving methyl adsorption on the metal cluster (blue lines in figure 3.21a) lead to high Gibbs activation energies of ~220 kJ/mol, for the methanol formation step. Even though methoxy intermediates are energetically accessible, their posterior transformation into methanol is kinetically forbidden (red line in figure 3.21b). In contrast, direct reaction of methane from the gas phase following an ER pathway is less energetically demanding, and the calculated Gibbs activation energies are lower than 60 kJ/mol if the adsorbed O atom is bicoordinated (Figure 3.21a). However, if the adsorbed O is three-coordinated to the Cu cluster, an additional energy is required to break one Cu-O bond to lower its atom coordination, thereby increasing the barriers to ~115 kJ/mol (Figure 3.21b) and making the process less viable. But still, the ER mechanism has

demonstrated once more that it is the only affordable pathway to turn methane into methanol if we are able to avoid the different secondary paths that can be involved in the process.

Concerning the Bader charge analysis, there are no significant divergences compared to Cu_5 clusters. The net atomic charges on the O and H atoms of the hydroxyl groups in the first step for both LH and ER pathways are around -1*e* and 0.4*e* respectively (Consult §3.7), and the net atomic charge on the C atom and CH_3 group are undoubtedly negative in structures $\mathbf{TS_{39\rightarrow40}}$ and **40**, with charges around -0.4*e* and -0.3*e* respectively, like their equivalents in the Cu_5 system in structures $\mathbf{TS_{6\rightarrow7}}$ and **7**. The same behaviour found in Cu_5 clusters for the non-interacting methyl group is also uncovered in this system, with structures $\mathbf{TS_{48\rightarrow49}}$ and **49** with close-to-neutral net atomic charges of -0.15*e* and -0.07*e* for the C atom and CH_3 group respectively, like their equivalents in the Cu_5 system in structures $\mathbf{TS_{17\rightarrow18}}$ and **18**. For the second step, both LH and ER pathways possess similar net atomic charge values than in the previous step, reflecting the same kind of behaviour previously described in Cu_5 clusters for Cu_7 clusters.

Regarding the Cu_7-4O system reactivity trends displayed in figure 3.22, (§3.7), the Eley-Rideal pathway shows evidence that a system with additional O_2 dissociated molecules on the cluster can outperform the Cu_7-2O system in terms of reactivity. Furthermore, since it is mandatory to perform the reaction in the Q potential energy surface, it can be beneficial for the desired process thanks to the following points: The decreased barrier for C-H activation thanks to a more activated product, the decreased barrier for the C-O bond formation and the decreased gap between the possible undesired products in comparison with the stability of doublet methoxy (Structure **67**) and doublet monocoordinated methyl product (Structure **66**) in the doublet alternative, so it is easier to reverse the reaction in the case a secondary product is formed. In fact, the activation barriers gathered in table 3.4 shows that Cu_7-4O is the less energy demanding system to pull off the activation of the C-H and the formation of the C-O bond in contrast with Cu_5-2O and Cu_7-2O systems. Moreover, it is noticeable the difference between the generated methanol in the quadruplet spin state

and doublet state is substantial in structure **64**, which assists an easier methanol desorption in the *Q* potential energy surface pathway. Likewise, there are different works in the literature supporting this high spin phenomenon.[327,364,523,524] Nevertheless, it is also mentioned that this high spin state not only lowers the C-H bond activation barrier but can enhance the overoxidation of methanol by reinforcing methanol adsorption, and needs to be properly modulated throughout the process.[518] Therefore, the spin state topic ought to be further studied to figure out its influence in the process.

Respect to the Bader net atomic charges in the transition states and intermediates, they agree with the values obtained in Cu_5 and Cu_7-2O systems for an Eley-Rideal mechanism despite the change in the spin state, with similar values in the transition states and intermediates for the selected atoms and groups compiled in table A3.1 (See §3.7).

On account of the recent study by Mahyuddin et al. that relates Cu-O-Cu angle with the activation energy for the C-H cleavage of methane,[524] this possibility was also contemplated in this dissertation. Starting with Cu_7, the ER reaction path in the first phase presents higher Cu-O-Cu angles compared to those in the LH pathway, combined with lower activation energies to turn methane into methanol, which might suggest an effect of the Cu-O-Cu angle over the C-H activation step of the process (consult table A3.2, §3.7). In the second phase of the LH pathway, the same indirect tendency upon this descriptor could be applied, with angle values remaining higher than those registered in the ER pathway until the formation of structure **50**, since the methanol formation step suffers from a great decrease in its angle value, with that reflected in lower activation energies. However, this can also be better explained on account of the coordination loss in the anchored O atom, since more energy will be required to transform the three-coordinated atom into a bi-coordinated atom and then, permitting the activation of methane. Respect to the Cu_7-4O system, it is very clear the influence of spin state in this descriptor. As showed in table A3.2 (§3.7), wider angles are acquired in the *Q* potential energy surface in the H abstraction through $\mathbf{TS_{62\rightarrow 63}}$, with its consequence in the relative energy

barriers, with an 84-degree angle for this system corresponding to the lowest activation barrier.

Regarding Cu_5 clusters, the same observed trend found in Cu_7 clusters is also present here. The data compiled in table A3.2, (§3.7) shows that the angle is around 80 degrees in almost every case except for $\mathbf{TS_{7\rightarrow 8}}$ and $\mathbf{TS_{21\rightarrow 22}}$ in the LH pathway, with notable decreases since one of the Cu-O bonds must be broken to generate methanol. In the case of $\mathbf{TS_{7\rightarrow 8}}$, it needs to start with a lower angle compared to $\mathbf{TS_{21\rightarrow 22}}$ because of the CH_4 adsorption nearby the three-coordinated atom. For the methanol formation step, an opposite behaviour is reflected compared to the first phase of the reaction. This time, the angle values are closer to 85 degrees with slight decreases in the transition states and the ER pathway, as in Cu_7 clusters, presents smaller angle values than the LH pathway, with minor differences between the transition state and the previous intermediate for the heterolytic reaction path. Respect to Cu_5-4O clusters, ∠Cu-O-Cu is enlarged to values ~94 degrees for both *D* and *Q* spin surfaces, with decreases once completed the methane activation step. Interestingly, despite the narrower angle in the *Q* surface in $\mathbf{TS_{30\rightarrow 31}}$, the activation barriers look almost identical. In the methanol formation step, the values are around 92 degrees in the doublet state and 81 in the quadruplet state, making the difference clear between both reaction surfaces.

Collecting all the data from Cu_5 and Cu_7 respect to the Cu-O-Cu angle values sheds light to the possible trends in this descriptor. A bad correlation with Gibbs free activation energies is found, depicted in figure 3.23, which concludes that this descriptor does not play a role in the methane activation in these systems, even if only the Eley-Rideal transition states are considered.

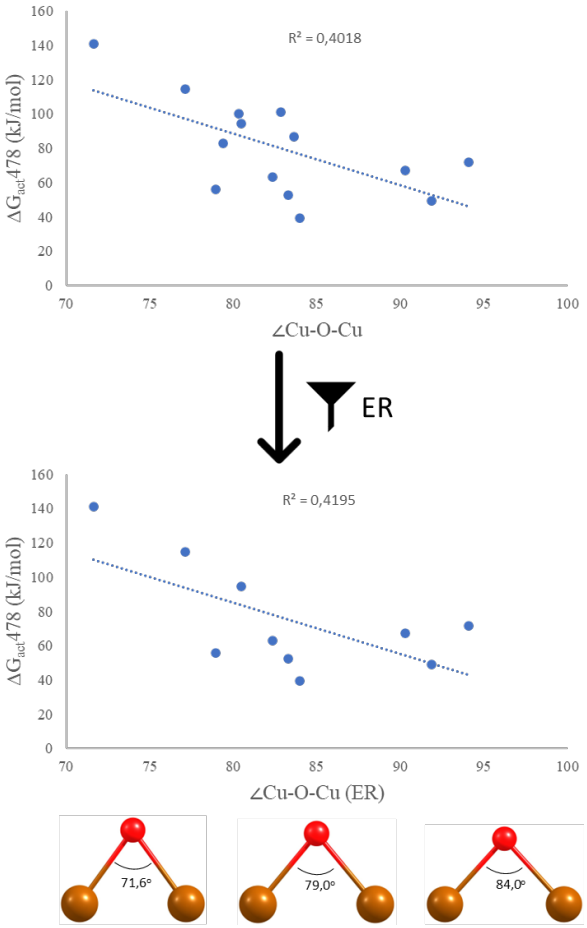

Figure 3.23 - Correlation between activation Gibbs free energies and Cu-O-Cu angles in the transition states in the Langmuir-Hinshelwood & Eley-Rideal mechanism (top) and only for Eley-Rideal after filtration (bottom) for Cu_5 and Cu_7 clusters. Activation Gibbs free energies (G_{act}) at 478 K for the C-H dissociation steps are given in kJ/mol.

In conclusion, as for Cu_5 clusters, the attachment of the methyl radical to the cluster surface and the subsequent formation of secondary products including methoxy groups must be avoided to transform methane into methanol efficiently. Moreover, further investigations must be performed to clarify the role of the spin state for avoiding the formation of by-products and the facilitation of the H transfer from the

CH_4 molecule to the active O atom, and the beneficial effect of higher O_2 coverage in the process with its consequent augmentation in the number of active sites on the catalyst. Finally, in order to optimise the MTM process, the active site must be protected by other functional groups or be restricted to a more constrained system like zeolites in order to avoid undesired reaction paths.

3.6 Conclusions

The mechanism of selective methane oxidation to methanol catalysed by sub-nanometre copper clusters has been thoroughly investigated by means of DFT calculations. In addition, the influence of cluster size and shape has been analysed by comparing the results obtained using Cu_5 clusters with different morphologies (2D and 3D) with those provided by 3D Cu_7. In the case of O_2 dissociation step, the adsorption, activation, and reaction energies indicate an enhanced oxidation resistance for Cu_5-2D clusters and similarities between Cu_5-3D and Cu_7, although this does not rule out the overoxidation of the clusters due to the sensitiveness of Cu_n catalyst to O_2 concentrations. In fact, Cu_5-2D may lose its inherent oxidation resistance in this scenario through the *Q* spin surface, remarking the O_2 affinity for these catalytic systems.

Different Langmuir-Hinshelwood and Eley-Rideal pathways have been explored, and the results confirm in all cases that homolytic dissociation of a C-H bond of methane is assisted by adsorbed O atoms and results in the formation of a hydroxyl group and a methyl species that must recombine in a second step to produce methanol. When the reaction follows a LH pathway, with all reactants and intermediates adsorbed on the copper cluster, the high stability of the hydroxyl and methyl intermediates makes their recombination energetically inaccessible. Formation of a methoxy intermediate by reaction of adsorbed O with methyl is energetically affordable, but its subsequent recombination to produce methanol is again kinetically forbidden, therefore adsorption of the reactant must be avoided at all costs.

In contrast, an alternative ER pathway according to a methane reaction from gas phase, producing a non-adsorbed radical-like methyl intermediate, is energetically favoured if bicoordinated O atoms are available. Such bicoordinated O atoms are stabilised at the edges of 2D clusters as opposite to 3D clusters that preferentially stabilise three-coordinated O atoms at their facets. Thus, cluster morphology indirectly determines the feasibility of the methane oxidation reaction through the stabilisation of distinct types of adsorbed O atoms.

Moreover, it is mandatory to avoid the adsorption of the methyl group on the copper clusters at any stage of the reaction. This could be achieved by selecting a proper support for the copper clusters, able to stabilise the desired morphology without altering their electronic and catalytic properties, while blocking the non-desired interaction of methyl species with undercoordinated Cu atoms or by means of bimetallic copper containing clusters that preferentially stabilise bicoordinated O atoms while weakening the interaction with methyl species.

Lastly, the experiments with an additional O_2 molecule in Cu_5 and Cu_7 clusters proved a higher O_2 coverage is not detrimental for the process, especially in the latter. The augment of functional active sites, the combination of multiple spin states and the possibility of yielding methanol more efficiently in specific spin surfaces, like the quadruplet state for Cu_7, catch a glimpse of the potential of these systems to avoid the formation of undesired products and intermediates, like bicoordinated methyl groups. However, formation of monocoordinated and methoxy groups on the catalyst surface cannot be discarded. Hence, these kinds of systems must be further investigated in proper supports in order to demonstrate their applicability.

3.7 Appendix

Table A3.1 - Net atomic charges on selected atoms and spin state of key intermediates and transition states involved in the mechanism of methane oxidation to methanol.

Structure	qO	qH	qC	qCH_3	qH (CH_3)	Spin
6	-1.06		-0.18			D
$TS_{6\rightarrow7}$	-1.00	0.39	-0.46	-0.33	0.04	D
7	-1.59	1.00	-0.33	-0.28	0.01	D
$TS_{7\rightarrow8}$	-1.40	1.00	-0.03	-0.09	0.04	D
8	-1.66	1.00	0.49	0.69	0.07	D
$TS_{7\rightarrow10}$	-0.84	1.00	-0.01	0.09	0.03	D
10	-1.31	1.00	0.75	0.73	-0.01	D
11	-1.95		-0.14			D
$TS_{11\rightarrow12}$	-1.01	0.36	-0.44	-0.33	0.04	D
12	-1.57	1.00	-0.25	-0.31	-0.02	D
$TS_{12\rightarrow13}$	-1.48	1.00	-0.15	-0.02	0.05	D
13	-1.64	1.00	0.58	0.70	0.04	D
15	-0.98		-0.04			D
$TS_{15\rightarrow16}$	-1.05	0.47	-0.15	-0.07	0.03	D
16	-1.58	1.00	-0.15	0.02	0.06	D
$TS_{16\rightarrow13}$	-1.51	1.00	0.02	0.10	0.03	D
17	-0.88		-0.10			D
$TS_{17\rightarrow18}$	-1.04	0.44	-0.14	-0.07	0.02	D
18	-1.60	1.00	-0.12	0.02	0.05	D
$TS_{18\rightarrow19}$	-1.49	1.00	0.12	0.20	0.03	D
19	-1.64	1.00	0.53	0.72	0.06	D
21	-1.60	1.00	-0.44	-0.39	0.02	D
$TS_{21\rightarrow22}$	-1.41	1.00	-0.05	0.15	0.07	D
$TS_{21\rightarrow22}$*	1.24	1.00	0.03	0.17	0.05	D
22	-1.68	1.00	0.60	0.71	0.04	D
23	-0.87					D
$TS_{23\rightarrow24}$	-1.04	0.43	-0.13	-0.05	0.03	D
24	-1.61	1.00	-0.14	0.02	0.05	D

$TS_{24\rightarrow25}$	-1.50	1.00	0.03	0.17	0.05	D
25	-0.69	1.00	0.60	0.72	0.04	D
27	-1.59	1.00	-0.41	-0.38	0.01	D
$TS_{27\rightarrow28}$	-1.39	1.00	-0.10	0.17	0.09	D
28	-1.67	1.00	0.54	0.71	0.06	D
30	-0.88		-0.02			D
$TS_{30\rightarrow31}$	-1.07	0.47	-0.21	-0.03	0.06	D
31	-1.60	1.00	-0.20	0.03	0.08	Q
$TS_{31\rightarrow32}$	-1.52	1.00	-0.01	0.18	0.06	D
32	-1.64	1.00	0.54	0.71	0.06	D
33	-0.88		-0.17			D
34	-1.57	1.00	-0.28	-0.29	0.00	Q
36	-0.38		-0.05			D
$TS_{36\rightarrow37}$	-1.06	1.00	-0.14	-0.03	0.04	D
37	-1.06	1.00	-0.16	0.03	0.06	D
$TS_{37\rightarrow38}$	-1.10	1.00	-0.08	0.09	0.05	D
38	-1.77	1.00	0.84	0.79	-0.01	D
39	-1.02		-0.11			D
$TS_{39\rightarrow40}$	-1.02	0.37	-0.41	-0.35	0.02	D
40	-1.57	1.00	-0.32	-0.29	0.01	D
41	-1.58	1.00	-0.40	-0.36	0.01	D
$TS_{41\rightarrow42}$	-1.39	1.00	-0.03	0.16	0.06	D
42	-1.68	1.00	0.63	0.72	0.03	D
$TS_{41\rightarrow44}$	-1.50	1.00	-0.01	0.14	0.05	D
44	-1.67	1.00	0.52	0.70	0.06	D
45	-1.30	1.00	0.73	0.73	0.00	D
$TS_{45\rightarrow46}$	-1.32	1.00	0.69	0.74	0.02	D
46	-1.30	1.00	0.66	0.74	0.03	D
$TS_{46\rightarrow47}$	-1.48	1.00	0.13	0.35	0.07	D
47	-1.63	1.00	0.57	0.69	0.04	D
48	-1.01		-0.16			D
$TS_{48\rightarrow49}$	-1.01	0.38	-0.36	-0.35	0.00	D
49	-1.57	1.00	-0.29	-0.30	0.00	D
50	-1.58	1.00	-0.37	-0.36	0.00	D

$TS_{50\rightarrow51}$	-1.43	1.00	0.04	0.12	0.03	D
51	-1.70	1.00	0.64	0.71	0.02	D
54	-0.84		-0.05			D
$TS_{54\rightarrow55}$	-1.03	0.45	-0.17	-0.07	0.03	D
55	-1.59	1.00	-0.16	0.02	0.06	D
$TS_{55\rightarrow56}$	-1.48	1.00	0.03	0.15	0.04	D
56	-1.67	1.00	0.55	0.69	0.05	D
57	-1.57	1.00	-0.28	-0.24	0.01	D
$TS_{57\rightarrow56}$	-1.43	1.00	0.01	0.15	0.05	D
58	-0.99		-0.02			D
$TS_{58\rightarrow59}$	-1.59	1.00	-0.12	-0.07	0.02	D
59	-1.59	1.00	-0.12	0.02	0.05	D
$TS_{59\rightarrow60}$	-1.52	1.00	-0.06	0.11	0.06	D
60	-1.68	1.00	0.59	0.71	0.04	D
62	-0.87		0.02			D
$TS_{62\rightarrow63}$	-1.06	0.41	-0.13	-0.03	0.03	Q
63	-1.59	1.00	-0.20	0.04	0.08	Q
$TS_{63\rightarrow64}$	-1.52	1.00	-0.07	0.18	0.08	D
64	-1.61	1.00	0.46	0.69	0.08	D
66	-1.54	1.00	-0.18	-0.03	0.05	D
67	-1.31	1.00	0.62	0.72	0.03	D

Table A3.2 - Relative energies (E_{rel}), Gibbs free energies (G_{rel}) and Cu-O-Cu angles for both doublet (D) and quadruplet (Q) spin states for all structures involved in the pathways depicted in figures 9, 14 , 15, 17 & 21.

Structure + Molecule	E_{rel} (kJ/mol)	G_{rel} (kJ/mol)	∠Cu-O-Cu Spin D (º)	∠Cu-O-Cu Spin Q (º)
1 + 2CH_4 (*D*)	0.0	0.0	87.3	
1 + 2CH_4 (*Q*)	90.4	94.8		
5 + 2CH_4 (*D*)	-7.7	-22.9		
5 + 2CH_4 (*Q*)	142.4	137.8		
6 + CH_4	-75.4	-63.1	81.4	
$TS_{6\rightarrow7}$ + CH_4	32.2	38.0	82.9	
7 + CH_4	-110.0	-89.5	79.2	
$TS_{7\rightarrow8}$ + CH_4	135.0	164.6	61.5	
8 + CH_4	33.0	57.5		
9 + CH_4 + CH_3OH	88.8	93.0	84.0	
$TS_{7\rightarrow10}$ + CH_4	64.4	90.7	82.6	
10 + CH_4	-137.2	-107.1	80.5	
11 + CH_3OH	60.7	74.0	86.0	
$TS_{11\rightarrow12}$ + CH_3OH	136.4	160.7	83.6	
12 + CH_3OH	-12.0	6.9	76.2	
$TS_{12\rightarrow13}$ + CH_3OH	201.7	221.1	16.0	
13 + CH_3OH	58.5	101.6		
14 + 2CH_3OH	143.6	167.2		
15 + CH_3OH	85.3	85.5	73.6	
$TS_{15\rightarrow16}$ + CH_3OH	217.4	226.5	71.6	
16 + CH_3OH	209.4	198.3	69.7	
$TS_{16\rightarrow13}$ + CH_3OH	235.2	242.9	66.5	
17 + CH_4	-3.0	-16.2	87.1	
$TS_{17\rightarrow18}$ + CH_4	54.2	46.9	82.4	
18 + CH_4	45.9	36.6	80.0	
$TS_{18\rightarrow19}$ + CH_4	107.2	112.2	75.3	
19 + CH_4	-22.6	5.3		

20 + CH_4 + CH_3OH	58.2	66.0	89.1	
21 + CH_4	-144.1	-133.4	87.9	
$TS_{21\rightarrow22}$ + CH_4	174.4	179.8	29.2	
$TS_{21\rightarrow22}$* + CH_4	102.2	108.4.	73.0	
22 + CH_4	41.8	52.0		
23 + CH_3OH	55.4	64.6	88.9	
$TS_{23\rightarrow24}$ + CH_3OH	112.7	117.1	83.3	
24 + CH_3OH	102.9	101.3	81.1	
$TS_{24\rightarrow25}$ + CH_3OH	153.3	171.2	75.0	
25 + CH_3OH	69.1	100.3		
26 + 2CH_3OH	118.5	141.2		
27 + CH_3OH	-68.5	-46.8	83.0	
$TS_{27\rightarrow28}$ + CH_3OH	197.5	218.0	12.9	
28 + CH_3OH	65.9	92.1		
29 + CH_3OH	30.4	53.3		
$TS_{29\rightarrow12}$ + CH_3OH	150.8	165.6		
30 + O_2 + CH_4	0.0	0.0	98.0	109.3
$TS_{30\rightarrow31}$ + O_2 + CH_4	-2.3	3.5	94.1	90.3
31 + O_2 + CH_4	0.0	75.1	88.7	88.8
$TS_{31\rightarrow32}$ + O_2 + CH_4	-2.3	61.4		
32 + O_2 + CH_4	74.8	110.5		
33 + O_2 + CH_4	57.5	15.7		
34+ O_2 + CH_4 (*D*)	-30.4	-0.4		
34+ O_2 + CH_4 (*Q*)	-129.9	-104.1		
35 + CH_4	0.0	0.0		
36 + CH_4	-2.2	-13.8		
$TS_{36\rightarrow37}$ + CH_4	152.2	143.1		
37 + CH_4	149.0	132.4		
$TS_{37\rightarrow38}$ + CH_4	161.4	148.7		
38 + CH_4	-138.5	-126.2		
3 + 2CH_4	0.0	0.0		
39 + CH_4	-21.4	-10.5	78.6	

$TS_{39\rightarrow40} + CH_4$	64.7	72.4	79.4	
$40 + CH_4$	-52.6	-50.2	79.4	
$41 + CH_4$	-97.4	-70.6	91.5	
$TS_{41\rightarrow42} + CH_4$	195.5	203.4	25.4	
$42 + CH_4$	40.2	52.7		
$43 + CH_4 + CH_3OH$	89.8	101.3	83.8	
$TS_{41\rightarrow44} + CH_4$	136.2	141.8	76.8	
$44 + CH_4$	30.6	50.7		
$45 + CH_4$	-79.9	-65.9	42.5	
$TS_{45\rightarrow46} + CH_4$	28.5	39.7	79.4	
$46 + CH_4$	-24.2	-18.3	86.6	
$TS_{46\rightarrow47} + CH_4$	239.3	249.7	88.3	
$47 + CH_4$	32.9	45.7	82.0	
$48 + CH_3OH$	63.0	85.8	80.2	
$TS_{48\rightarrow49} + CH_3OH$	170.7	186.0	80.3	
$49 + CH_3OH$	61.5	74.3	75.3	
$50 + CH_3OH$	7.9	29.5	82.4	
$TS_{50\rightarrow51} + CH_3OH$	228.2	242.6	67.4	
$51 + CH_3OH$	106.1	135.4		
$52 + 2CH_3OH$	136.5	166.4		
$53 + 2CH_4$	19.3	16.7	81.9	
$54 + CH_4$	15.7	11.3	79.0	
$TS_{54\rightarrow55} + CH_4$	75.7	67.2	77.0	
$55 + CH_4$	64.7	50.6	72.2	
$TS_{55\rightarrow56}$	106.3	109.9		
$56 + CH_4$	2.1	39.5	78.6	
$57 + CH_4$	-41.9	-31.8	60.7	
$TS_{57\rightarrow56} + CH_4$	127.2	130.3	82.0	
$58 + CH_3OH$	87.2	95.9	82.2	
$TS_{58\rightarrow59} + CH_3OH$	213.2	210.6	77.1	
$59 + CH_3OH$	208.1	205.5	75.1	
$TS_{59\rightarrow60} + CH_3OH$	231.3	238.0	72.0	
$60 + CH_3OH$	92.2	117.4		
$4 + CH_4$	0.0	0.0	96.8	99.5
$62 + CH_4$	-2.4	16.7	96.7	99.4
$TS_{62\rightarrow63} + CH_4$	56.4	56.2		84.0

63 + CH_4	44.8	45.5		82.6
$TS_{63\rightarrow64}$ + CH_4	72.4	94.8	89.2	74.0
64 + CH_3OH	-9.2	43.1	79.2	40.9
65 + CH_4	-21.1	-19.5	88.0	93.4
66 + CH_4	-61.7	-32.3	91.8	89.0
67 + CH_4	-142.5	-99.7	96.8	99.5

Chapter 4 Selective Oxidation of Methane into Methanol over Cu_n Clusters supported within CHA

Once the main pathways for the MTM process catalysed by Cu_5 and Cu_7 clusters have been settled in gas phase, new perspectives near chemical industry are explored more profoundly in this chapter.

This time, a proper support has been selected: Chabazite, a natural well-known zeolite for its structural simplicity with 8- and 6-member rings and for its catalytic applications in NO_x SCR with NH_3[525–528] and in the MTO process.[529–532]

In the present chapter,[533,534] we explore whether the trends formerly reported in chapter 3 are significantly distinct when the clusters are confined within the cavities of a zeolite with the chabazite (CHA) structure by using density functional (DFT) calculations, and whether the outcome results in a feasible catalyst to use for industrial applications.

4.1 Introduction

As introduced in (§1.3.1), zeolites are a high-efficient solid catalyst class with a huge versatility. Since the early 1960s, these crystalline inorganic frameworks have been used in the heterogeneous catalysis field[535,536] and from then on, a great abundance of several new applications have been discovered: Industrial processes[73,84,537–539], anticorrosion coatings[540], biotechnology and medicine[541], water purification[542], solar energy thermal storage[543], C1 and C2 molecule transformations[336,544–548], NO_x removal or reduction[549,550] and agricultural applications for soil neutrality[551] or agrochemicals[552]. Even machine learning studies[553–556] have been carried out to get to the bottom of the possibilities of these catalytic systems.

In relation to the MTM process, Cu-exchanged zeolites were introduced because of its capacity to perform mild oxidations (§1.5). Nevertheless, these systems have three primarily reasons that do not permit an optimal conversion: the utilisation of medium-high concentrations of molecular oxygen causes the displacement of the chemical reaction to overoxidised C1 products like CO_2,[265–269] the re-oxidation of the remaining Cu (I) species to close the catalytic cycle and regenerate the active sites is difficult,[369] and the use of water is necessary to aid methanol desorption,[264,332,378] complicating the technology transfer to a large-scale industry plant.

Undoubtedly, the evolution of the methyl intermediate and the global reactivity of the system relies on a combination of diverse factors such as Cu speciation, Al content, zeolite topology or reaction conditions and intense efforts are currently devoted to understand and control the influence of these parameters on the activity and selectivity of these systems.[277,314,339,358,367,371,557,558] The use of sub-nanometric copper clusters for this kind of reaction offers new perspectives, especially in the methanol desorption stage and in the activation of the reactants. In fact, the morphology of the cluster has an important influence on its intrinsic features. As examples, the activation energy for O_2 dissociation is much higher in planar 2D Cu_5 clusters than on 3D Cu_5 or Cu_7 clusters, making them more resistant against oxidation,[217,520] and

the coordination of the adsorbed O atoms implies significant changes in the reaction mechanism and so, in the activation barriers (§3.2).[502,559,560]

In the last chapter, it was concluded that the Eley-Rideal pathway is the most favourable for the selective oxidation of methane into methanol, and even low concentrations of O_2 can affect isolated Cu_n clusters conducting to Cu_n-4O systems. Thus, to avoid the overoxidation of methane to undesirable secondary products, adsorption of the reactant and methyl intermediates at any stage of the reaction must be avoided to the extent possible in order to eliminate the contribution of the Langmuir-Hinshelwood reaction paths (§3.6). Selecting a proper solid support can help to resolve these issues.

Scheme 4.1 – Graphical abstract of the MTM reaction over Cu_n-Al_y-CHA system (y = 0, 1, 2)

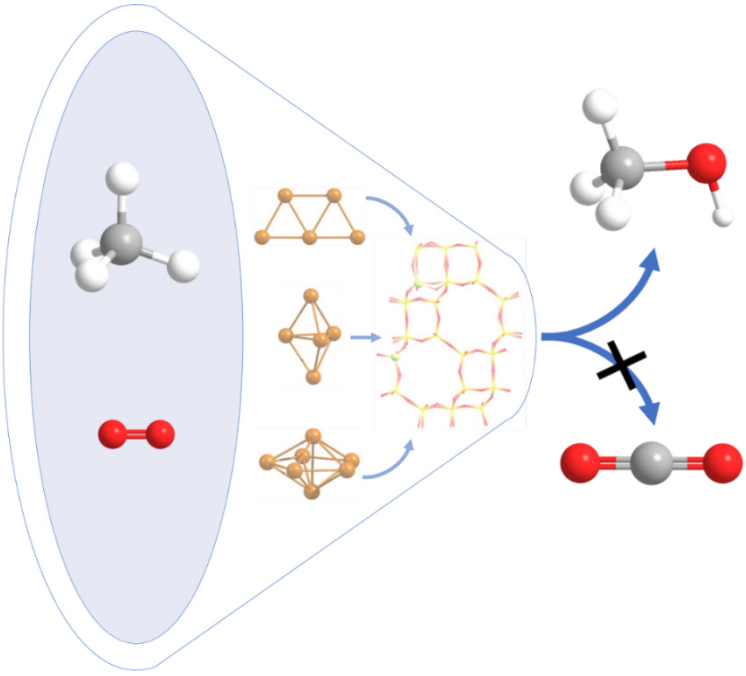

In this context, the CHA framework[561] has been chosen owing to its small unit cell, with its consequent computational cost reduction, and well-defined small pores able to lend confinement effects, which can alter the activation energies of the methane-to-methanol (MTM) process.[136,261,263,318,373,562–564] Using this structure will permit the comprehension of the O_2 dissociation reaction nature and the subsequent CH_4 activation. This approach will not use water molecules to release the product from the catalyst surface, bringing savings in energy use. The CHA model used in this research is described in detail in (§2.7.1).

From a sustainable point of view, the utilisation of O_2 as the primary green oxidant agent[316,565–569] would imply a great improvement with an abundant, cheap and harmless oxidant to the environment, but also in terms of high atom economy, atom efficiency and E-factor, giving water as by-product in the majority of cases. However, the implementation of O_2 at industrial level requires investment in high-pressure equipment, which signifies a budget increase, and solving the inherent problems of this molecule, like its solubility in water, the potential explosion risk in organic solvents[570] or the necessity to use a stoichiometry co-reductant in certain reactions.

4.2 O_2 dissociation over Cu_n-CHA clusters

To commence with, Cu_n clusters stabilised within the CHA structure will be studied to get a fundamental understanding of the catalyst. Then, adsorption and dissociation of O_2 on supported Cu_n clusters will be addressed and compared with Cu_n clusters in gas phase. Finally, an important realistic case will be discussed, the incorporation of multiple O_2 molecules and how these molecules affect the energy barriers and the stability of the system. Since the interaction of the reactant methane is weak compared to O_2, this phenomenon might interfere in the production of methanol at greater scales.

4.2.1 Confined Cu_n Clusters

Cu_5 and Cu_7 clusters were introduced within the cavities of CHA models containing 0, 1 and 2 framework Al atoms, obtaining the most stable structures through geometry optimisations (Figure 4.1):

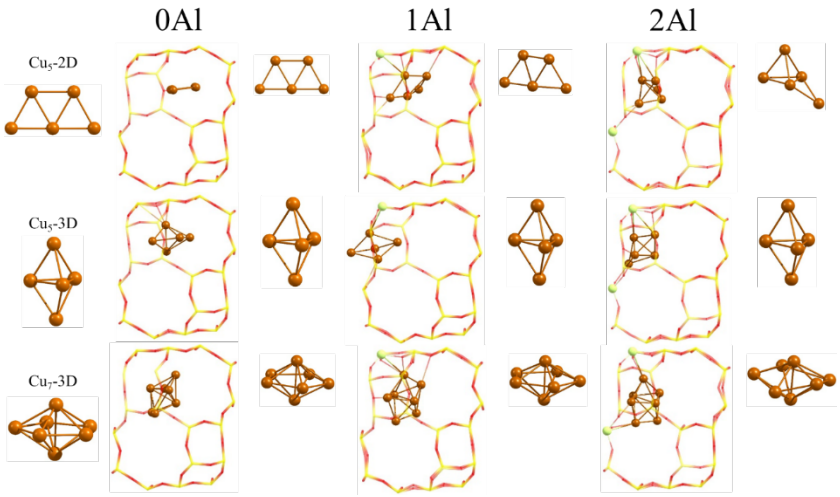

Figure 4.1 - Optimised structures of Cu_5-2D, Cu_5-3D and Cu_7-3D clusters, confined and isolated within CHA models containing 0, 1 and 2 framework Al atoms. Optimised structures in gas phase are located at the left. Si and O atoms are depicted as yellow and red wires and Cu

and Al are depicted as dark copper-coloured and light green balls, respectively.

Starting with the 0Al model, the interaction of Cu_n clusters with the pure silica CHA framework is weak and does not conduct to any relevant geometry deformation of the confined clusters. The shortest Cu–$O_{framework}$ distances are 2.387, 2.097 and 2.281 Å in Cu_5-2D, Cu_5-3D and Cu_7-3D, respectively, and all clusters become positively charged by less than 0.2 *e*, as showed in table 4.1.

Table 4.1 - Total atomic charges and spin values on Cu_n clusters calculated for the Cu_n clusters stabilised within the CHA zeolite for structures R, TS and P involved in O_2 dissociation. Gas values are added for comparison reasons.

	nAl	qCu_n (Catalyst)	qCu_n (R)	qCu_n (TS)	qCu_n (P)	Spin
Cu_5-2D (Gas)	-	0	0.744	1.273	1.893	D
Cu_5-3D (Gas)	-	0	1.037	1.278	1.976	D
Cu_7-3D (Gas)	-	0	1.012	1.303	1.981	D
Cu_5-2D (CHA)	0	0.167	0.918	1.442	2.169	D
	1	0.826	1.724	1.723	2.788	D
	2	1.510	2.158	2.655	3.354	D
Cu_5-3D (CHA)	0	0.143	0.991	1.454	1.983	D
	1	0.785	1.966	2.139	2.507	D
	2	1.453	2.166	2.656	3.389	D
Cu_7-3D (CHA)	0	0.205	1.217	1.414	2.181	D
	1	0.879	1.935	2.150	2.854	D
	2	1.549	2.496	2.768	3.327	D

However, the substitution of one Si atom by Al (1Al model) generates a net negative charge in the zeolite framework that is compensated by the appearance of a positive charge of ~0.8 *e* on the confined clusters. The shortest Cu–O_f distances in the 1Al model decrease to 1.974, 2.067 and 2.125 Å in Cu_5-2D, Cu_5-3D and Cu_7-3D, respectively, and the planar geometry of the Cu_5-2D cluster is slightly distorted.

When two Si atoms in the framework are replaced by Al (2Al model), all copper clusters interact strongly with the framework, illustrated by the deformation of copper clusters compared to its gaseous counterpart, forming at least 6 bonds with the shortest optimised Cu–O_f distances being 1.984, 1.982 and 2.022 in Cu_5-2D, Cu_5-3D and Cu_7-3D, respectively. The positive charge in the clusters increases to ~1.5 *e* and, as in the case of 0Al and 1Al models, this positive charge is always largest on Cu_7-3D because of its larger number of electrons available to be transferred

As shown above, the inclusion of Al atoms in the framework modifies slightly the geometry of the 3D Cu_5 and Cu_7 clusters but has a more pronounced effect on the shape of the planar Cu_5-2D clusters.

4.2.2 O_2 adsorption on supported Cu_n Clusters

When an O_2 molecule is added to the system, the differences between gas phase and confined systems are pristine clear, especially as the quantity of framework Al atoms increases. The entire step is resumed in figure 4.2. Since these structures are the reactant species in the O_2 dissociation process, they are labelled as "R" in table 4.2 and table 4.3, summarising calculated charges and optimised O-O bond lengths, respectively. Transition states and product species are labelled "TS" and "P", respectively.

In isolated clusters where all the electrons are available to be transferred (§3.2), the activation of molecular O_2 depends on the cluster size and on the geometry of adsorption on the cluster: the larger the number of Cu–O contacts, the larger the charge transferred to O_2[200,571]. However, when clusters are supported within a zeolite, the availability of electrons to be transferred decreases by increasing the Al content in the framework, adding a new variable to this process.

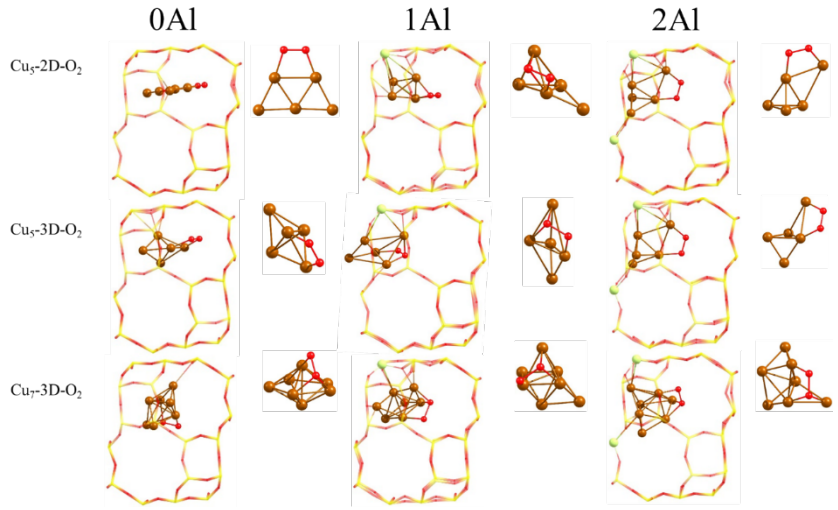

Figure 4.2 - Optimised reactant structures of O_2 adsorbed on Cu_5-2D, Cu_5-3D and Cu_7-3D clusters confined within CHA models containing 0, 1 and 2 framework Al atoms. Si and O are depicted as yellow and red wires and Cu and Al are depicted as dark copper-coloured and light green balls, respectively.

As depicted above, molecular O_2 is adsorbed on Cu_n clusters forming two or three Cu–O bonds, forming stable complexes in which the O–O bond is activated by charge transfer from the metal cluster to the π^* orbital of O, facilitating its dissociation to produce adsorbed O atoms. In the systems not containing Al, the geometry of the cluster is not drastically modified after O_2 adsorption, but for 1Al and 2Al models, the clusters undergo important restructuration upon interaction with O_2, leading to lower symmetry structures, deviating from what we observed in gas phase. For Cu_5-2D cluster, its planarity is lost in the presence of one and two framework Al atoms, evolving into an analogous 3D structure product to that obtained for the Cu_5-3D cluster. For Cu_5-3D, a weak bending is found for the central copper atoms in the 1Al model, and a very similar structure to Cu_5-2D-O_2 as said above for the 2Al model. In the Cu_7-3D case, the geometry deformation is clear, adopting a configuration with 3 Cu-O bonds for both 1 and 2Al models.

Table 4.2 - Total atomic charges on adsorbed O_2 (qO_2, in e) calculated for structures R, TS and P involved in O_2 dissociation. Gas values are added for comparison reasons

	nAl	qO_2 (R)	qO_2 (TS)	qO_2 (P)
Cu_5-2D (Gas)	-	-0.744	-1.273	-1.893
Cu_5-3D (Gas)	-	-1.037	-1.278	-1.976
Cu_7-3D (Gas)	-	-1.012	-1.303	-1.981
Cu_5-2D (CHA)	0	-0.858	-1.370	-2.101
	1	-1.000	-1.011	-2.070
	2	-0.741	-1.242	-1.986
Cu_5-3D (CHA)	0	-0.913	-1.368	-1.983
	1	-1.208	-1.377	-1.773
	2	-0.732	-1.249	-2.016
Cu_7-3D (CHA)	0	-1.065	-1.324	-2.075
	1	-1.171	-1.387	-2.087
	2	-1.036	-1.296	-1.894

In all cases, a net transfer of electron density from the catalyst to O_2 took place, conducting to a net negative charge on adsorbed O_2 and a net positive charge on the Cu_n clusters that follows the trend with the Al content reported for the confined clusters without adsorbates, which is also reflected in O-O distances. The parameters are compiled in tables 4.1, 4.2 and 4.3.

Table 4.3 - Optimised values of the O-O distance (rO-O, in Å) in structures R, TS and P involved in O_2 dissociation. Gas values are included for comparison reasons.

	nAl	rO-O (R)	rO-O (TS)	rO-O (P)
Cu_5-2D (Gas)	-	1.389	1.969	3.562
Cu_5-3D (Gas)		1.498	1.997	3.059
Cu_7-3D (Gas)	-	1.480	1.908	3.603
Cu_5-2D (CHA)	0	1.404	1.935	3.359
	1	1.468	1.883	3.616
	2	1.386	1.860	3.505
Cu_5-3D (CHA)	0	1.422	1.852	3.551
	1	1.580	1.874	3.394
	2	1.383	1.872	3.421
Cu_7-3D (CHA)	0	1.492	1.820	3.681
	1	1.565	1.932	3.650
	2	1.493	1.841	3.520

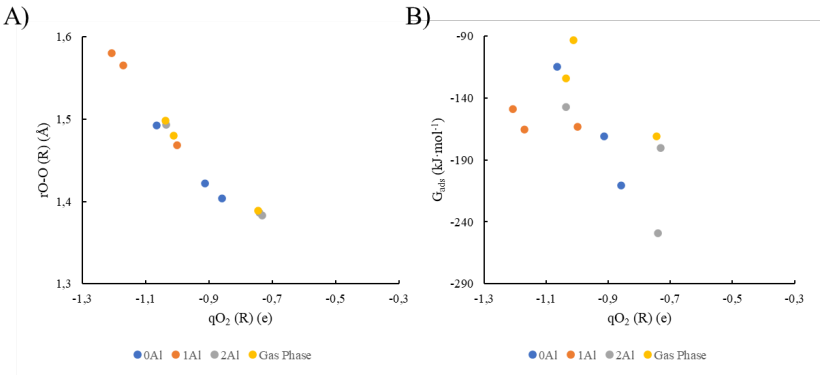

Figure 4.3 - Correlation between the optimised O-O bond length and the total charge of O_2 in R structures (A) and calculated Gibbs adsorption energy G_{ads} versus total charge of O_2 in R structures (B). Yellow dots corresponding to gas phase results and are included for comparison reasons.

However, not all the electron density lost by the metal clusters culminates in O_2. According to the results compiled in table 4.2, the largest capture of electron density by O_2 occurs in the systems with only one framework Al. Consequently, the increase in the optimised O-O bond length is also the largest in the 1Al models, and the correlation between rO-O and the net charge on O_2 previously reported on isolated clusters is maintained here (see figure 4.3A), whereas this effect is the lowest in the 2Al models, even less than in isolated clusters for Cu_5 clusters. This phenomenon can be explained understanding the important role that the zeolite framework plays in charge distribution. The pure silica framework is neutral and doesn't tend to extract electron density from the copper atoms, thus obtaining similar values to isolated clusters. This equilibrium is disrupted by the presence of Al atoms in the framework. To compensate the negative charge generated by the presence of Al, the copper clusters become positively charged, leading to the situation described above for 1Al. In the case of the 2Al model, the copper atoms have transferred so much electron density to the framework that they cannot donate much electron density to the adsorbed O_2, resulting in a poorer activation of the molecule reflected in their calculated rO-O and qO_2 values.

By and large, the calculated adsorption energies (G_{ads}) summarised in table 4.4, are greater in the planar cluster Cu_5-2D than in Cu_5-3D and less favourable in Cu_7-3D. From these results, a general trend in the system could be inferred: They are less negative as the charge transferred to O_2 increases (see figure 4.3).

Table 4.4 – Calculated Gibbs adsorption (G_{ads}), activation (G_{act}) and reaction (ΔG) energies (in $kJ \cdot mol^{-1}$) for O_2 dissociation on Cu_n clusters stabilised in CHA.

	nAl	G_{ads}	G_{act}	ΔG
Cu_5-2D (Gas)	-	-171	121	-176
Cu_5-3D (Gas)	-	-124	35	-242
Cu_7-3D (Gas)	-	-93	38	-232
Cu_5-2D (CHA)	0	-210	145	-217
	1	-163	47	-275
	2	-249	103	-218
Cu_5-3D (CHA)	0	-171	62	-255
	1	-149	31	-172
	2	-180	114	-256
Cu_7-3D (CHA)	0	-115	32	-285
	1	-165	28	-281
	2	-147	55	-242

4.2.3 O_2 dissociation on supported Cu_n Clusters

Figure 4.4 presents the optimised structures of the transition states for the O_2 dissociation step:

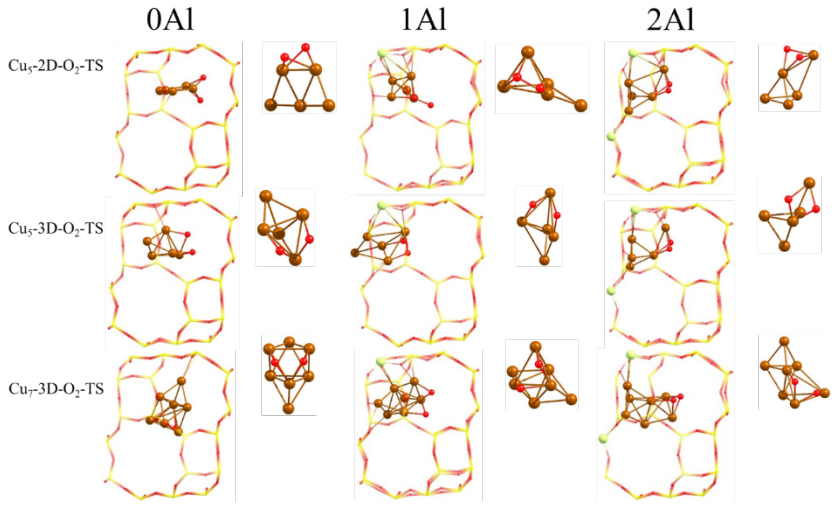

Figure 4.4 - Optimised structures of the transition states for O_2 dissociation on Cu_5-2D, Cu_5-3D and Cu_7-3D clusters confined within CHA models containing 0, 1 and 2 framework Al atoms. Si and O are depicted as yellow and red wires and Cu and Al are depicted as dark copper-coloured and light green balls, respectively.

As depicted in figure 4.3, the electron density transferred to adsorbed O_2 weakens the O-O bond, promoting its dissociation. In the transition states, the two O atoms are always interacting with at least two Cu atoms of the cluster with the exception of Cu_5-2D within the 1Al model, with one of these O atoms monocoordinated forming a more unfavourable transition state. The optimised O-O distances in the TS structures range from 1.82 to 1.94 Å (see table 4.3) and respect to the transferred electron density from Cu_n clusters to O_2 (See table 4.1) it has increased, following the trend with the Al content described in (§4.2.2).

The activation energies for the dissociation of O_2 on the supported Cu_n clusters are plotted in figure 4.5 to facilitate its analysis (For more details, visit table 4.4):

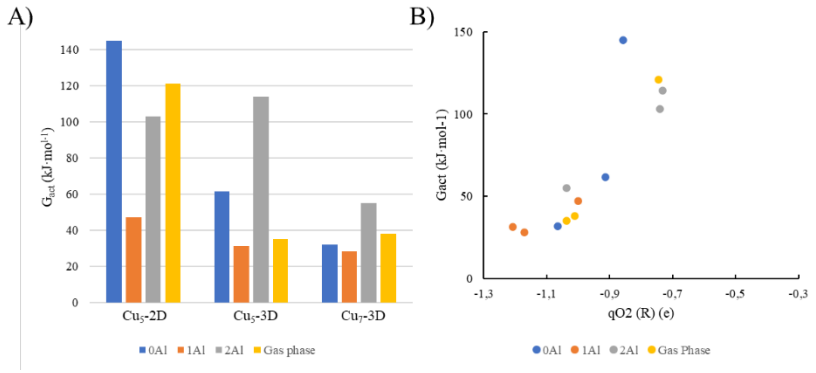

Figure 4.5 – Gibbs activation energy for O_2 dissociation on Cu_n clusters (A) and correlation between the Gibbs activation energy G_{act} and total charge of O_2 in (R) structures (B). Yellow dots are referred to gas phase for comparison reasons.

In the systems without framework Al, the trend in activation energies is quite similar to that previously reported for isolated clusters: high activation barriers for planar Cu_5-2D, which decrease when changing to the 3D morphology (Cu_5-3D) and with the increasing cluster size (Cu_7-3D), in which the energy required is the lowest. In the presence of framework Al atoms, the planar Cu_5-2D cluster rearranges upon interaction with O_2 adopting a 3D structure that, in turn, leads to a lower activation energy for O_2 dissociation. The three G_{act} values in the 1Al models are similar and low, 47 and 31 $kJ \cdot mol^{-1}$ for Cu_5 and 28 $kJ \cdot mol^{-1}$ for Cu_7. Moving to the 2Al model with more positively charged Cu_n clusters, it results in an increase of all the calculated activation energies except for Cu_5-2D, being more noticeable according to the less availability of electron density to activate O_2.

As previously reported for isolated clusters[217], there is a correlation between the calculated activation energies E_{act} and the total charge of O_2 in the reactant species R (see figure 4.5B), suggesting that the degree

of activation of the O-O bond in adsorbed O_2 through electron density transfer to the π* anti-bonding orbital is what determines the energy that will be necessary to break this bond and dissociate molecular O_2. As illustrated above, the zeolite framework provides lower activation barriers, especially for the 1Al model, linked to a stronger electron density concentrated over the oxygen atoms.

After dissociation, the two O atoms tend to occupy positions on the surface of the Cu_n clusters, either three-coordinated on the facets or bi-coordinated at the cluster edges (See figure 4.6).

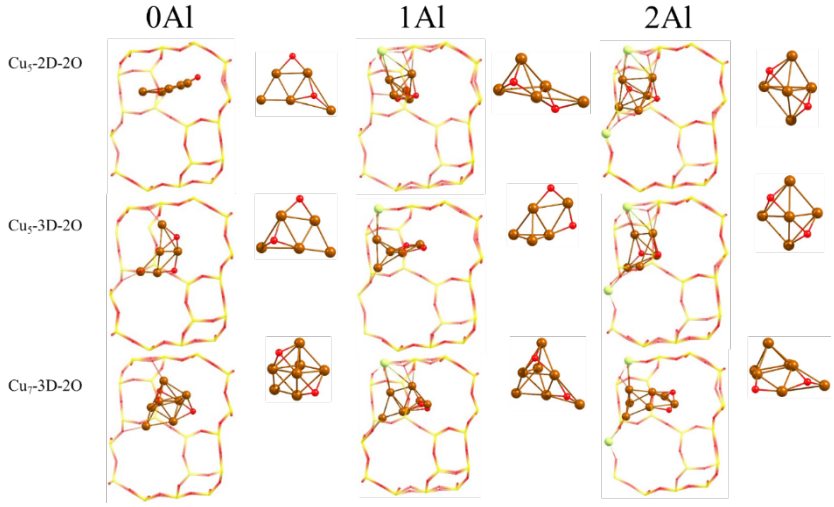

Figure 4.6 - Optimised structures of two O atoms adsorbed on Cu_5-2D, Cu_5-3D and Cu_7-3D clusters confined within CHA models containing 0, 1 and 2 framework Al atoms. Si and O are depicted as yellow and red wires and Cu and Al atoms are depicted as dark copper-coloured and light green balls, respectively.

The total positive charge on the Cu_n clusters increases to values between ~2.0 and ~3.4 *e* (see table 4.1) and the adsorbed O atoms become negatively charged by ~-1.0 *e* (see table 4.2). The process is always clearly exothermic, with calculated Gibbs reaction energies (ΔG) between -217 and -285 $kJ \cdot mol^{-1}$ (consult table 4.4). The only exception

is the product of O_2 dissociation on the Cu_5-3D cluster supported on the 1Al zeolite model (Centre image in figure 4.6), in which the reaction energy is less favourable, -172 $kJ \cdot mol^{-1}$, and the net negative charge on the O atoms is also the lowest, -0.88 *e* on average on each atom. It could be related to the fact that after O_2 dissociation, the two O atoms are bi-coordinated at the neighbouring edges of the cluster sharing one Cu atom, which is a less stable situation than having at least one three-coordinated O atom as in all other cases. For the rest of systems, a predominance of the three-coordinated O atoms is clear, which is reflected in the stability of the products marked by the reaction energies.

In the previous chapter, it was elucidated that bicoordinated oxygen atoms are the active species participating in the ER pathway to optimally turn methane into methanol. To discern which catalysts will be most appropriate ones to perform the MTM reaction, an analysis of the possibilities of each group is detailed below.

In the case of 0Al, as the clusters are not strongly attached to the zeolite framework, the odds to suffer from leaching are considerable, as well as the risks of overoxidation in Cu_7.

For the 1Al scenario, in principle, they would be the best candidates for the MTM process, specially the Cu_5-3D, since it possesses two bicoordinated O atoms, as well as low activation barriers that will bestow an easier activation of O_2 at lower temperatures. Nevertheless, this incredible feature can act as a double-edge sword for Cu_n-1Al systems since excessive low activation barriers for the O_2 dissociation step would make these systems more prone to overoxidation.

Lastly, 2Al products offer the best equilibrium between activation barriers and stability. The Al pairs contribute to a strong binding of the cluster into the 8MR channel with its consequent more predictable behaviour, less probability of leaching and in Cu_5 2D and 3D clusters case, enhanced charge density over the oxygen atoms in comparison with Cu_5 clusters in gas phase. Furthermore, these systems represent the most common scenario for Al-enriched zeolites.

Regarding Cu_5 clusters, they are quite similar in terms of geometry but there is a subtle difference in the slightly displaced O atoms to the edges of the catalyst for those that come from the 3D structure, therefore both structures will be mixed in the reaction path. Unfortunately, none of them possess bicoordinated O atoms, which will rise the activation barriers for the methane activation step. In the context of Cu_7 clusters, a relatively low barrier of 55 $kJ \cdot mol^{-1}$ could pose challenges under high enough partial pressures of O_2 in the flow. Nonetheless, a bicoordinated oxygen atom is observed, aligning with the desired characteristics that are sought in these catalytic systems for CH_4 conversion.

For all these reasons, it was decided that the study will only proceed in the 2Al models. But prior to expound on the CH_4 activation and all the possible secondary paths involved, we explored the possibility of overoxidation of the Cu_n clusters as in gas phase (§3.2) to prove whether the zeolite framework can hamper the process.

4.2.4 Successive dissociation of multiple O_2 molecules on supported Cu_n clusters

Before starting, it is imperative to note that some structures in this section will be further explained in this chapter, since they result from predominant pathways in the MTM reaction using Cu_n clusters within a CHA-2Al framework. So, to envision a complete perspective of multiple oxygen atoms adsorbed on the system and how these atoms alter unalike characteristics, these structures will be presented in advance.

4.2.4.1 Cu_5 clusters

In light of the possibility of undesired overoxidation of Cu_n clusters, additional O_2 molecules were added to the systems obtained after the first O_2 dissociation on Cu_n clusters stabilised within the CHA-2Al model, in order to understand their influence on the stability and reactivity of the catalyst.

The adsorption of a second O_2 molecule on the product labelled as Cu_5-2D-2O with two framework Al atoms in figure 4.6 interestingly results in an inefficient mono adsorption mode, which implies that the catalyst does not possess enough electron density to dissociate new O_2 molecules. This makes a significant difference between the isolated Cu_5 cluster shown in the former chapter (§3.2) and the zeolite supported cluster and demonstrates the possibility to control the overoxidation of the catalyst by using a zeolite as a support. Figure 4.7 shows the different possibilities of O_2 adsorption over Cu_5-2O clusters:

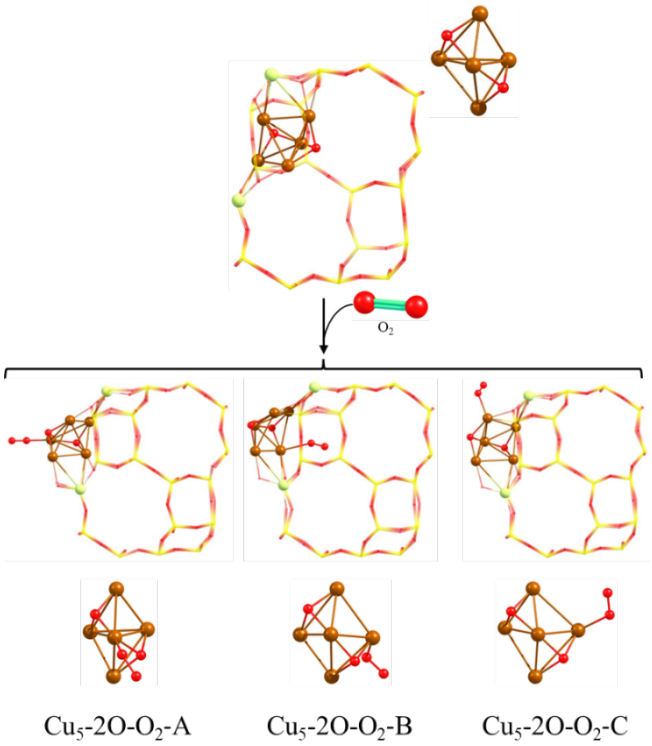

Figure 4.7 - Possible O_2 adsorptions on Cu_5-2O cluster confined within a CHA model containing 2 framework Al atoms. Si and O are depicted as red and yellow wires and Cu and Al atoms are depicted as dark copper-coloured and light green balls, respectively.

As a consequence of this result, the only way to progress through this perspective is to incorporate new O_2 molecules after the first methanol desorption over Cu_5 clusters in the MTM process, in simpler terms, when only one O atom is adsorbed at the facet of the cluster. Figure 4.8 represents the possible adsorptions on Cu_5-2D-O_x clusters:

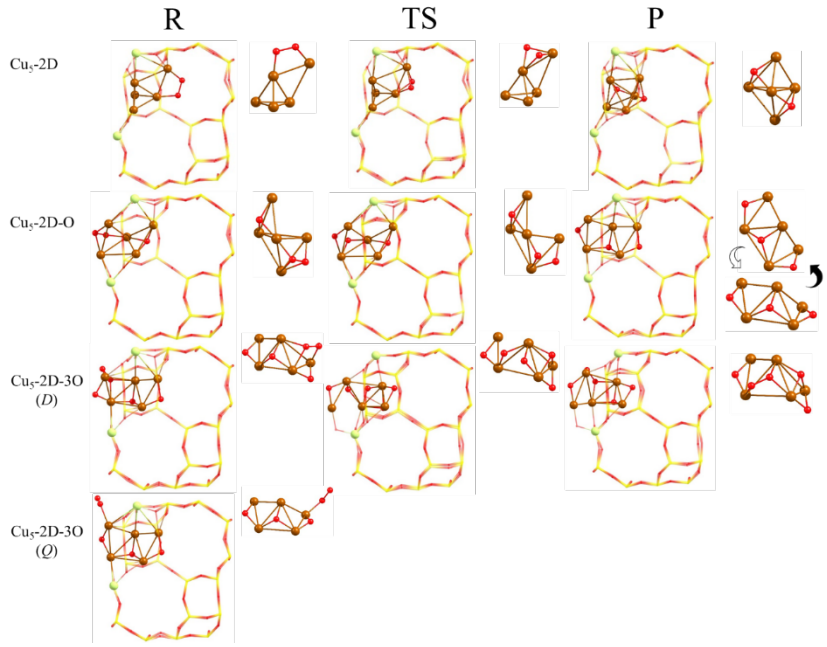

Figure 4.8 - Optimised structures for two, three and five O atoms adsorbed on Cu_5-2D clusters confined within a CHA model containing 2 framework Al atoms. Si and O are depicted as red and yellow wires and Cu and Al atoms are depicted as dark copper-coloured and light green balls, respectively.

When only one O atom is adsorbed on the cluster confined in CHA with 2 framework Al atoms, labelled as Cu_5-3D-O in figure 4.8, the electron density transferred to O_2 is increased to -1.087 *e* with its role in a larger O-O bond length of 1.538 Å (See table 4.5). This result suggests an already activated O-O bond, which is reflected in the activation energy required to perform the dissociation of only 13 $kJ \cdot mol^{-1}$. So, in the moment that one O_2 molecule is approached to the Cu_5-3D-O system, it is very likely to get a cluster with 3 adsorbed O atoms on it and most importantly, a structure with 2 bi-coordinated O atoms located at the edges of the cluster, becoming a very appropriate system to carry out the MTM reaction. Furthermore, the reaction is exothermic by 70 $kJ \cdot mol^{-1}$, with negative charges on the resulting adsorbed O atoms of ~-0.9 *e*.

Table 4.5 - Total atomic charges on adsorbed O_2 (qO_2, in e), optimised values of the O-O distance (r_{O-O}, in Å) in structures R, TS and P involved in O_2 dissociation, and calculated Gibbs adsorption (G_{ads}), activation (G_{act}) and reaction (ΔG) energies (in $kJ \cdot mol^{-1}$) for O_2 dissociation on Cu_5-3D clusters with the increasing amount of adsorbed O stabilised in a CHA zeolite model with 2 framework Al atoms.

	Cu_5-2D	Cu_5-2D-O	Cu_5-2D-3O	Cu_5-OH-OCH_3
qCu_n (R)	2.158	3.532	4.490	3.481
qCu_n (TS)	2.655	3.740	4.842	3.752
qCu_n (P)	3.354	4.072	4.610	4.127
qO_2 (R)	-0.741	-1.087	-0.555	-1.074
qO_2 (TS)	-1.242	-1.284	-1.268	-1.321
qO_2 (P)	-1.986	-1.854	-0.780	-1.787
r_{O-O} (R)	1.386	1.538	1.318	1.513
r_{O-O} (TS)	1.860	1.873	1.894	1.871
r_{O-O} (P)	3.505	3.017	1.370	2.484
G_{ads}	-249	-111	43/-55[a]	-101
G_{act}	103	13	172	3
ΔG	-218	-74 / -64[a]	58	-62
Spin (R)	D	D	D	D
Spin (TS)	D	D	D	D
Spin (P)	D	D	Q	Q

[a]Quadruplet state.

Adding another O_2 molecule to this product, the structure labelled as Cu_5-3D-3O (R) is created. This time, two possibilities were explored concerning the spin state. For the doublet (*D*) state only -0.555 *e* are transferred to O_2, being the lowest value found for Cu_5 clusters due to oxygen saturation, since copper atoms do not have enough electron density to donate for the new added molecule. The same occurs with the O-O bond length, 1.318 Å, being the shortest for Cu_5 clusters. Another remarkable fact comes with the O_2 adsorption energy, that is endothermic by 43 $kJ \cdot mol^{-1}$, and it is the first time this behaviour is encountered. In addition to this improbable scenario, new O_2 molecules cannot be dissociated and only transition states in which new O_2 molecules are formed have been found. For the quadruplet state, an exothermic adsorption of 55 $kJ \cdot mol^{-1}$ was identified, but no effective adsorption of the new O_2 molecule was observed, anchoring in mono

mode, another proof that consolidates this step as very unlikely, and the most possible scenario as three O atoms adsorbed on Cu_5 clusters as the process continues.

The last scenario contemplated in this section is the O_2 dissociation over Cu_5-OH-OCH_3 species that appear as a consequence of the competitive reaction paths involving methoxy species in the transformation of methane into methanol (§4.4). This course of the reaction is not unexpected, since as explained in the previous chapter, the possibility to form methoxy groups on the catalyst is very likely. Hence, in order to verify if the process can continue despite the formation of methoxy groups, the O_2 dissociation step was investigated, giving rise to the structures depicted in figure 4.9.

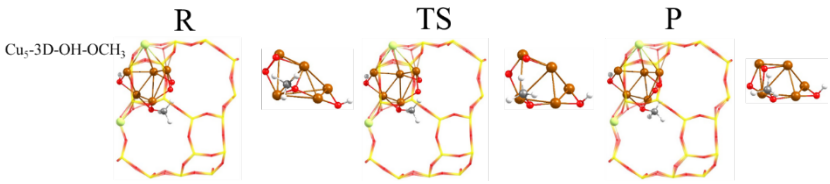

Figure 4.9 - Optimised structures for the successive O_2 dissociation over Cu_5-OH-OCH_3 clusters confined within a CHA model containing 2 framework Al atoms. Si and O are depicted as red and yellow wires and Cu and Al atoms are depicted as dark copper-coloured and light green balls, respectively.

The structure labelled as Cu_5-OH-OCH_3 (R) in figure 4.9 is originated from the adsorption of O_2 in structure **44** displayed in figure 4.19, bringing about very exothermic adsorption energies of 101 kJ/mol Attending to the resulting O-O bond length and O_2 charge, 1.513 Å and -1.074 *e*, respectively (see table 4.5), this implies an activated O-O bond similar to the one reported for the Cu_5-3D-O system in order to obtain the Cu_5-3O system. This is in agreement with the very small activation barrier found of only 3 $kJ \cdot mol^{-1}$, indicating that the system can be easily functionalised creating a product that possesses an O atom bridged to two copper atoms, in other words, the active centre of the reaction, granting stability to the process. The reaction is exothermic by 62 $kJ \cdot mol^{-1}$ and the negative charges of the anchored O atoms are around -1.8 *e*.

4.2.4.2 Cu_7 clusters

As occurred in the previous part, after the first O_2 molecule dissociation all clusters have significantly increased their positive charge, reaching values larger than 3.3 *e* in the systems with two framework Al atoms (see qCu_n (P) values in table 4.1), and considering that the electron density transfer to adsorbed O_2 is the key to promote its dissociation, the possibility to avoid the undesired overoxidation of Cu_n clusters by supporting them on zeolites with the appropriate amount of Al was investigated. Figure 4.10 depicts all plausible Cu_7-3D-O_x structures made of multiple O_2 dissociations:

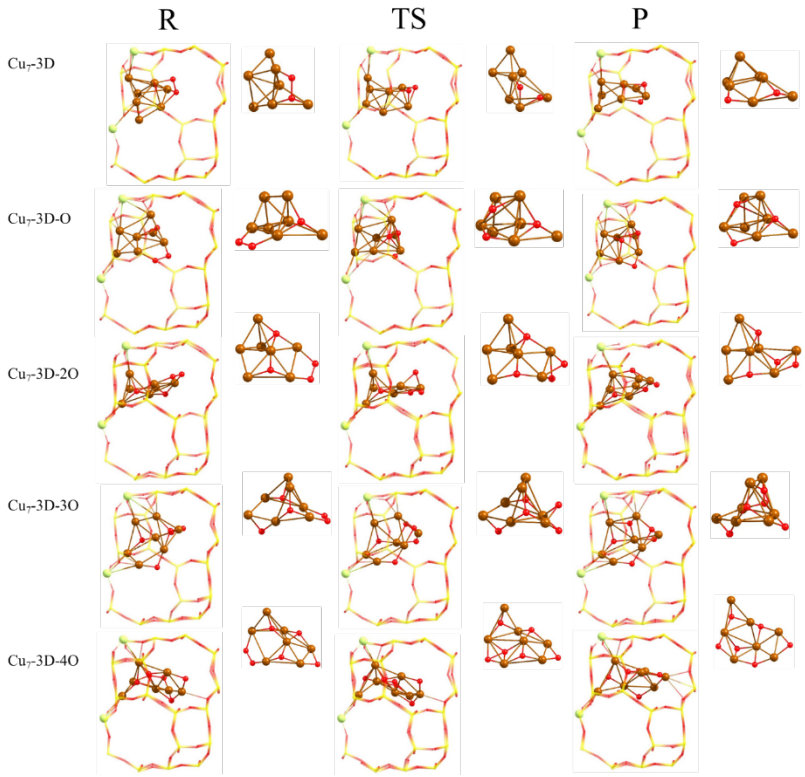

Figure 4.10 - Optimised structures from two to six O atoms adsorbed on Cu_7-3D clusters confined within CHA models containing 2 framework Al atoms. Si and O are depicted as red and yellow wires and Cu and Al atoms are depicted as dark copper-coloured and light green balls, respectively.

For this purpose, a second O_2 molecule was adsorbed on the product P structure obtained for Cu_7-3D, labelled as Cu_7-3D-2O in figure 4.6 and 4.10.

As expected, less electron density is transferred to O_2 in this system, only -0.384 *e* (see table 4.6), leading to a shorter optimised O-O bond length, 1.388 Å, and to a higher activation energy for O_2 dissociation, 143 kJ·mol^{-1}. Curiously, this value is similar to that obtained for the planar Cu_5-2D cluster in the 0Al model, 145 kJ·mol^{-1}, probably because of the similar geometry obtained for the adsorbed O_2 molecule at the edge of the cluster and for the transition state with the two O atoms sharing the same two Cu atoms forming the cluster edge (see figure 4.6). In addition, as opposed to all the other systems studied in this work, the dissociation of O_2 on the Cu_7-3D-2O cluster is endothermic by 55 kJ mol^{-1}, and the negative charge on the resulting adsorbed O atoms is small, ~-0.4 *e*.

Table 4.6 - Total atomic charges on Cu_n (qCu_n in *e*) adsorbed O_2 (qO_2 in *e*), optimised values of the O-O distance (r_{O-O}, in Å) in structures R, TS and P involved in O_2 dissociation, and calculated Gibbs adsorption (G_{ads}), activation (G_{act}) and reaction (ΔG) energies (in $kJ \cdot mol^{-1}$) for O_2 dissociation on Cu_7-3D clusters with increasing amount of adsorbed O stabilised within a CHA zeolite model with 2 framework Al atoms.

	Cu_7-3D	Cu_7-3D-O	Cu_7-3D-2O	Cu_7-3D-3O	Cu_7-3D-4O	Cu_7-OH-OCH_3
qCu_n (R)	2.496	3.328	4.315	5.087	6.035	3.577
qCu_n (TS)	2.768	3.857	4.830	5.547	6.511	3.903
qCu_n (P)	3.327	4.377	5.201	6.078	6.870	4.738
qO_2 (R)	-1.036	-0.735	-0.768	-0.678	-0.710	-1.016
qO_2 (TS)	-1.296	-1.309	-1.282	-1.169	-1.207	-1.339
qO_2 (P)	-1.894	-1.848	-1.768	-1.779	-1.641	-1.895
r_{O-O} (R)	1.493	1.383	1.388	1.368	1.359	1.458
r_{O-O} (TS)	1.841	1.830	1.916	1.893	1.649	1.902
r_{O-O} (P)	3.520	2.939	2.705	2.952	2.550	3.578
G_{ads}	-147	-249	-192	-260	-103	-243
G_{act}	55	109	143	125	34	75
ΔG	-242	-16 / -25[a]	55	-12	-67[a]	-180
Spin (R)	D	D	D	D	D	D
Spin (TS)	D	D	D	D	D	D
Spin (P)	D	D	D	D	Q	D

[a]Quadruplet state.

Adding another O_2 molecule to this system generates Cu_7-3D-4O, depicted in figure 4.10. As expected, the electron density is lower than in Cu_7-3D-2O, becoming -0.355 *e*, and thus conducting to a briefer optimised O-O bond length of 1.359 Å. Notwithstanding, a smaller activation energy of 34 kJ·mol^{-1} is found compared to the catalyst with 4 adsorbed O atoms but bigger than Cu_7-3D with 2 anchored O atoms. This is possibly owing to a low stability of the reactant structure for the contiguous coppers involved in the reaction, as these metallic atoms can possess more charge since they only have one near O atom each, supporting the process (See figure 4.10). With all of this, the O_2 dissociation is exothermic by 67 kJ·mol^{-1} forming a quadruplet product in the progress, confirming the potential presence of multiple spin states at the same time as new O_2 molecules are added to the system, following the trend reported in gas phase (§3.3 & 3.4). Furthermore, the adsorption and dissociation of an O_2 molecule on Cu_7 clusters containing one and three O adsorbed atoms labelled as Cu_7-3D-O and Cu_7-3D-3O in figure 4.10, were also investigated. For more details, see table 4.6.

In the case of Cu_7-3D-O, the charge transferred to O_2 is surprisingly low, -0.368 *e*, even less than in Cu_7-3D-2O, which entails a greater resistance against oxidation after the first methanol desorption, with an O-O bond length of 1.383 Å. Despite the smaller charge transferred and the shorter bond length, the catalyst is able to activate the adsorbed O_2 more than in Cu_7-3D-2O, which is in accord with the activation barrier value of 109 kJ·mol^{-1}. This is mostly on account of the configuration of the cluster since more copper atoms can be involved in the process of O_2 dissociation. Lastly, the process is slightly exothermic by 16 kJ·mol^{-1}, and the negative charge on the resulting adsorbed O atoms is small, ~-0.4 *e*.

For Cu_7-3D-3O, the charge transferred to O_2 is decreased to -0.339 *e*, being the lowest of the compiled data in table 4.6. The reason behind this fact is related to the geometry of the cluster. The O atoms located at the facet of the cluster are extracting too much charge from the same Cu atoms which already had charge deficiency due to the other O atoms previously adsorbed, not permitting the charge transfer to other Cu

atoms in an easy way. The same grounds can also be applied to the gathered activation barrier for this structure of 125 kJ·mol^{-1}, since the actual conformation does not facilitate the activation of the O-O bond as figured in table 4.6, with a value of 1.893 Å. Despite all inconveniences, the process is slightly exothermic by 12 kJ·mol^{-1} and the negative charge on the resulting adsorbed O atoms is also small, ~-0.4 *e*, smaller than Cu_7-3D-O product, agreeing with the compiled values.

The last case examined was the O_2 dissociation over Cu_7-OH-OCH_3 clusters. As in Cu_5, the O_2 affinity is very strong, causing the adsorption of another O_2 molecule. With that said, the step is pictured in figure 4.11:

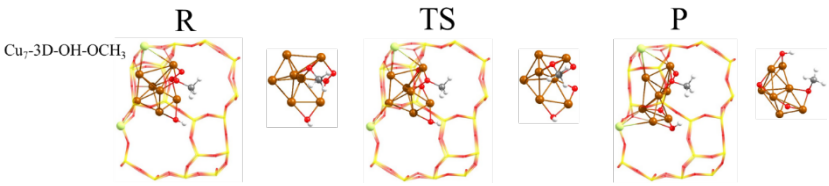

Figure 4.11 - Optimised structures for the successive O_2 dissociation over Cu_7-OH-OCH_3 clusters confined within a CHA model containing 2 framework Al atoms. Si and O are depicted as red and yellow wires and Cu and Al atoms are depicted as dark copper-coloured and light green balls, respectively.

Providing an advanced explanation for the generation of these structures, the structure labelled as Cu_7-OH-OCH_3 (R) is created from structure **79** as a result of the competitive paths involving methoxy species in Cu_7 clusters (figure 4.29, §4.6). When a O_2 molecule is introduced, the interaction with the cluster marks a very strong adsorption of 243 kJ·mol^{-1}, which is also reflected in the charge transferred to O_2, becoming -1.016 *e*, and in an elongated O-O bond of 1.458 Å, showing more similar values to the ones found for the Cu_7-1Al system. From this intermediate, the system requires 75 kJ·mol^{-1} to

overcome the transition state, evidencing more problems than Cu_5 clusters in order to continue the process through the competitive reaction pathways. Finally, a product with one bicoordinated O atom is generated, making the reaction very exothermic by 180 $kJ \cdot mol^{-1}$, with negative charges ~1.9 e^-.

To summarise, table 4.7 compiles the energetic parameters to envision a complete image of the O_2 dissociation step over Cu_n nanoclusters.

Table 4.7 - Calculated Gibbs adsorption, activation, and reaction energies in kJ/mol for the dissociation of molecular O_2 on different catalyst models. The optimised structures are depicted in figures 4.4, 4.6, 4.8, 4.9, 4.10 and 4.11.

	Structure	G_{ads} (kJ/mol)	G_{act} (kJ/mol)	G_{reac} (kJ/mol)
Cu_5		-249	103	-218
Cu_5-2O	1	-57	-	-
Cu_5-O	5	-111	13	-74
Cu_5-3O	20	43 / -55[a]	172	58
Cu_5-OH-OCH_3	44	-101	3	-62
Cu_7		-147	55	-242
Cu_7-2O	48	-192	143	55
Cu_7-4O		-103	34	-67
Cu_7-O	52	-249	109	-16 / -25[a]
Cu_7-3O	61	-260	125	-12
Cu_7-OH-OCH_3		-243	75	-180

[a]Quadruplet spin state.

These findings indicate that deep oxidation of zeolite supported Cu_n clusters by successive dissociation of O_2 molecules is disfavoured both kinetically and thermodynamically, making zeolites promising supports to stabilise metallic Cu. Cu_5 clusters present a clear direction to the Cu_5-

3O system thanks to the action of the support that prevents further oxidations in contrast to the Cu_5-4O system found in isolated clusters in the former chapter (§3.2). In Cu_7 case, the overoxidation resistance is enhanced, as reflected in the activation barrier for the formation of Cu_7-2O and Cu_7-3O systems, eventually conducting to the latter system, just as Cu_5, avoiding the formation of Cu_7-4O regarding the isolated cluster. However, Cu_7 possesses a lower activation energy for the formation of Cu_7-5O respect to the 172 $kJ \cdot mol^{-1}$ required for Cu_5, which might create issues in the long run.

That said, let us move to the most profound part of this dissertation, the transformation of methane into methanol using Cu_n nanoclusters supported within a CHA with 2 framework Al atoms.

4.3 CH_4 activation over Cu_5-CHA-2Al clusters

Following the partly oxidised Cu_5-2O cluster stabilised within a CHA cage containing two Al atoms in the framework (structure **1** in figure 4.12 and table A4.1), on account of its location close to the 8-ring window connecting two CHA cages, CH_4 only interacts favourably with one of the Cu atoms, forming structure **2** with an optimised Cu-C distance of 2.264 Å and a calculated Gibbs free interaction energy of -33 kJ/mol. Since the two O atoms are not equivalent, four possible pathways labelled *A* to *D* have been explored to convert methane into methanol on Cu_5-2O (figure 4.12).

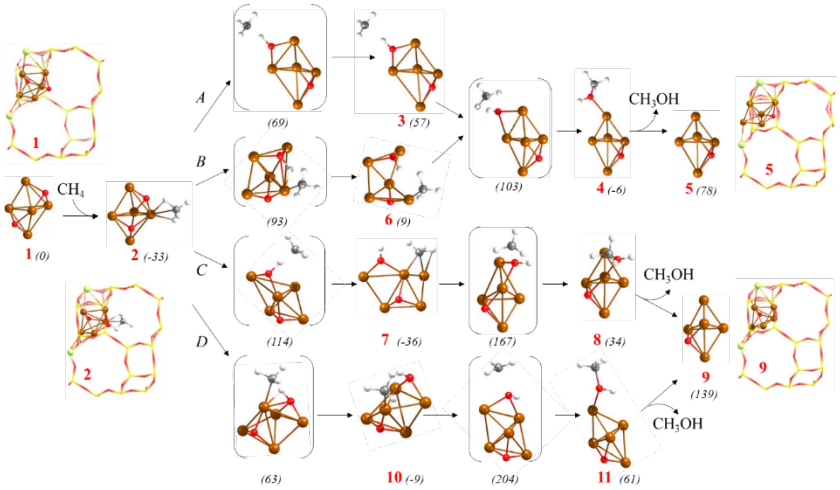

Figure 4.12 - Optimised geometries of minima and transition state structures involved in the oxidation of methane to methanol on a Cu_5-2O cluster supported on CHA zeolite following different pathways *A* to *D*. Si and O atoms in the framework depicted as yellow and red wires, Al, Cu and reactant O depicted as light green, brown and red balls, respectively. Relative Gibbs energies at 478.15 K given in brackets in $kJ \cdot mol^{-1}$.

The first route considered (*A*) proceeds through formation of a radical-like intermediate (structure **3**, in figure 4.12 and table A4.1) in which the methyl group formed after the C-H bond dissociation is not interacting with the Cu cluster. The C-H bond length increases from 1.096 Å in reactant **2** to 1.461 Å in $\mathbf{TS_{2\rightarrow3}}$ and 1.906 Å in intermediate **3**, while the O-H distance follows the opposite trend and decreases from 3.039 Å in **2** to 1.120 Å in $\mathbf{TS_{2\rightarrow3}}$ and finally 1.000 Å in **3**. The calculated activation Gibbs energy is 102 kJ/mol (see table 4.8) and intermediate **3** is 90 kJ/mol less stable than **2**.

Table 4.8 - Calculated Gibbs activation energies (G_{act}) in kJ/mol for the C-H bond dissociation in CH_4 (CH) and the CH_3OH formation (CO) steps and for the competing formation of methoxy groups (OCH_3) and dissociation of a second CH bond (CH_2).

Model	Pathway	G_{act} (CH) (kJ/mol)	G_{act} (CO) (kJ/mol)	G_{act} (OCH_3) (kJ/mol)	G_{act} (CH_2) (kJ/mol)
Cu_5-2O	*A*	102	46		
	B	126	94	199	104
	C	146	203	134	176
	D	96	213	109	148
	H	64	129		
Cu_5O	*E*	113	75		
	F	124	188		
Cu_5-3O	*G (Q)*	90	94	50	159
	I	25[a]			96[b]
	J	85	67/148	103[c]	
Cu_7-2O	*K*	65	140	74	
	L	85	114		
	O	139	118		
Cu_7O	*M*	197	277		
Cu_7-3O	*N (Q)*	91	83	124	99
	P	129	72/113		

[a]to formaldehyde
[b]to water
[c]to dimethyl ether (DME)

In a second step, the non-adsorbed methyl fragment reacts with the adsorbed hydroxyl group forming a methanol molecule mono-coordinated to the Cu_5 cluster at a Cu-O distance of 2.065 Å (structure **4**, table A4.1). The optimised C-O distance in $\mathbf{TS_{3\rightarrow4}}$ is 2.077 Å, and because of the low stability of intermediate **3**, the calculated activation Gibbs energy for the CO bond formation step is only 46 kJ/mol (see table A4.5, §4.9).

An alternative pathway *B* involving the same O atom occurs via a LH mechanism. In the transition state connecting structures **2** and **6** for C-H dissociation, $\mathbf{TS_{2\rightarrow6}}$, the optimised Cu-C, C-H and O-H distances are 1.981, 1.443 and 1.290 Å, respectively, and the methyl group is attached to Cu with a Cu-C bond length of 1.904 Å in intermediate **6**. This additional interaction forces the geometry of the O atom involved in the H transfer, leading to a greater stabilisation with its impact in the Gibbs barrier for C-H dissociation (126 kJ/mol), and C-O bond formation (94 kJ/mol) through the same transition state structure involved in pathway *A,* yielding adsorbed methanol **4**. Comparison of the Gibbs energy profiles for routes *A* and *B* at 478.15 K shows that the main difference between them is the stability of the methyl intermediate, hence the highest barrier for the overall process is in both cases below 130 kJ/mol.

The two routes remaining involves the other O atom of the Cu_5-2O cluster and also differ in the nature of the transition state for the C-H bond dissociation, with an ER pathway in $\mathbf{TS_{2\rightarrow7}}$ following pathway *C,* and with a monocoordinated methyl in $\mathbf{TS_{2\rightarrow10}}$ following pathway *D*, which is reflected in the calculated activation Gibbs energies, 146 and 96 kJ/mol, respectively (see table A4.5).

However, none of the two intermediates formed is a radical-like species, and the methyl group is in both cases attached to the Cu_5-2O cluster, bicoordinated in **7** with Cu-C distances of 1.991 and 2.076 Å, and monocoordinated in **10** with a Cu-C distance of 1.911 Å. As a result of these interactions, intermediate **7** is 27 kJ/mol more stable than **10**, and the activation Gibbs energies for the subsequent C-O bond formation step are considerably high in both cases, 203 and 213 kJ/mol,

following pathways *C* and *D*, respectively. The optimised C-O distances in $\mathbf{TS_{7\rightarrow 8}}$ and $\mathbf{TS_{10\rightarrow 11}}$ are similar, 2.143 and 2.130 Å, and the reaction product is methanol adsorbed either on an axial (structure **8**) or an apical (structure **11**) Cu atom, the former system being 27 kJ/mol more stable than the latter. Regarding Gibbs energy profiles, routes *C* and *D* are less favourable than those described for pathways *A* and *B*, mostly due to the high barriers found for the reaction of adsorbed methyl and hydroxyl groups.

After the first CH_4 oxidation and CH_3OH desorption, two non-equivalent Cu_5-O structures, **5** and **9**, appear as the initial species that further react with a second CH_4 molecule following pathways *E* and *F* (see figure 4.13 and table A4.2, §4.9).

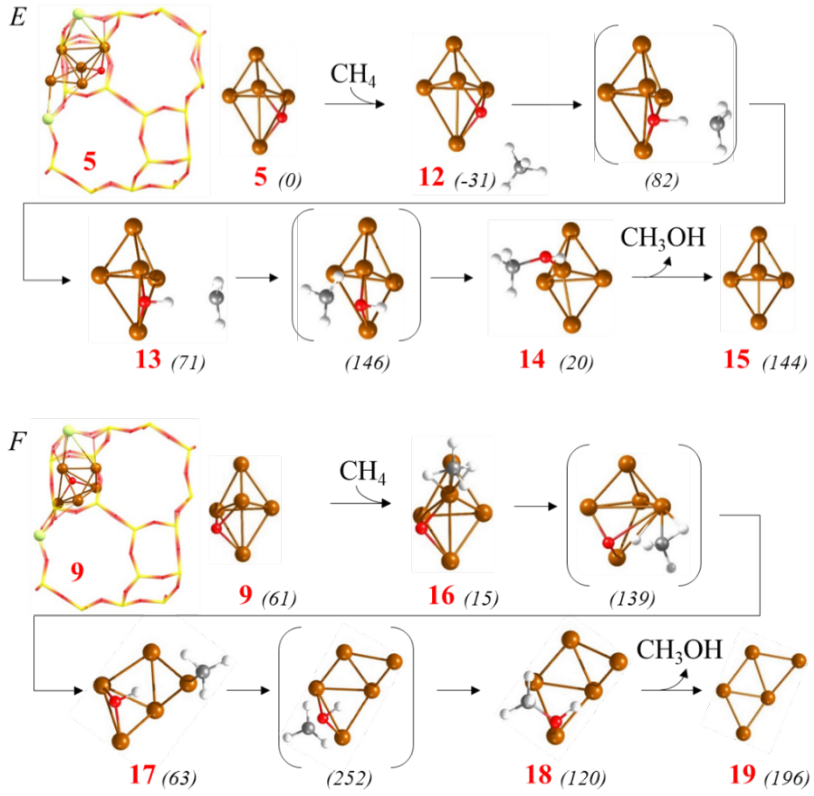

Figure 4.13 - Optimised geometries of minima and transition state structures involved in methane oxidation following pathways E and F on Cu_5-O clusters supported on CHA zeolite. Si and O atoms in the framework depicted as yellow and red wires, Al, Cu, reactant O, C and H atoms depicted as light green, brown, red, grey, and white balls, respectively. Relative Gibbs energies at 478.15 K given in brackets in kJ/mol.

In the Eley-Rideal pathway labelled *E*, CH_4 does not interact with the Cu_5-O cluster, as indicated by the optimised value of 3.739 Å for the Cu-C distance in structure **12**. The C-H bond dissociation produces a metastable radical-like intermediate **13** with the C-H and O-H distances evolving from 1.376 and 1.170 Å in $\mathbf{TS_{12\rightarrow13}}$ to 1.974 and 0.994 Å in intermediate **13**, and with moderate activation Gibbs energies for C-H bond breaking and C-O bond formation, 113 and 75 kJ/mol,

respectively. In contrast, when following pathway *F*, CH_4 adsorbs directly on the Cu_5-O cluster with an optimised Cu-C distance of 2.291 Å in structure **16**, which decreases to 2.027 Å in $\mathbf{TS_{16\rightarrow17}}$ and to only 1.932 Å in the mono-coordinated methyl intermediate **17**. During the C-H bond dissociation step, the cluster rearranges and becomes planar, a geometry that remains during the formation of the new C-O bond making this step energetically demanding, with a Gibbs energy of activation of 189 kJ/mol (see table 4.8).

Whilst the results presented up to now indicate that CH_4 could be oxidised to CH_3OH through pathways *A* or *B* followed by *E* with activation Gibbs energies below 130 kJ/mol, the highly exothermic adsorption of O_2 on the Cu_5-O structure **5** obtained at the end of the first cycle, and its subsequent dissociation with an activation energy of only 13 kJ/mol (table 4.7) produces a stable Cu_5-3O system (structure **20** in figure 4.14 and table A4.3 in the appendix) whose reactivity should be explored (pathway *G*).

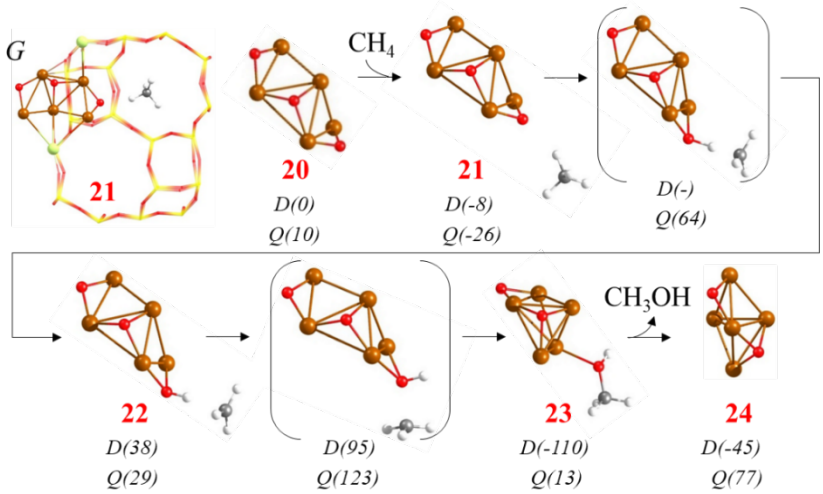

Figure 4.14 - Optimised geometries of minima and transition state structures involved in methane oxidation following pathway *G* on Cu_5-3O clusters supported on CHA zeolite. Si and O atoms in the framework depicted as yellow and red wires, Al, Cu, reactant O, C and H atoms depicted as light green, brown, red, grey, and white balls, respectively.

Relative Gibbs energies at 478.15 K for doublet (*D*) and quadruplet (*Q*) spin states are given in brackets in kJ/mol.

As explained in (§4.2.4.1), further oxidation of Cu_5-3O to Cu_5-5O is not energetically favoured (figure 4.8), as the unique possibility for this system is located in the quadruplet state and does not conduct to an effective O_2 dissociation. Returning to the cluster with 3 adsorbed oxygen atoms, owing to the high O coverage in structure **20** CH_4 does not adsorb on any Cu atom, but interacts with a bicoordinated O atom with an optimised O-H distance of 2.470 Å (structure **21** in figure 4.14), allowing only an Eley-Rideal mechanism.

The high O coverage leads to a greater stabilization of the quadruplet state for the system in comparison with its most stable counterpart in gas phase (§3.3.2), shorten the difference of spin states from 38 kJ/mol in gas phase to merely 10 kJ/mol when supported in the zeolite, thereby attaining the coexistence of both spin surfaces. This is crucial for the reaction. For structure **21**, the doublet (*D*) state is 18 kJ/mol less stable than the quadruplet (*Q*), and the transition state for C-H bond dissociation $\mathbf{TS_{21\rightarrow 22}}$ yielding a non-adsorbed methyl radical (structure **22**) could only be localised on the *Q* potential energy surface with an activation Gibbs energy of 90 kJ/mol. Attempts to find the transition state on the *D* spin state were unsuccessful. As a result, intermediate **22** is 55 kJ/mol less stable than reactant **21** on the *Q* surface whereas the difference between **22** and **21** on the *D* energy surface is quite similar, 46 kJ/mol. The similarities can also be applied to all the optimised geometries, suggesting an easy crossing between both surfaces.

From that point, the transition state for C-O bond formation $\mathbf{TS_{22\rightarrow 23}}$ and the product CH_3OH are clearly more stable on the *D* potential energy and the calculated activation barrier for the second step of the process is only 57 kJ/mol. Desorption of the methanol product from structure **23** leaves a Cu_5-2O cluster, labelled **24** in figure 4.15, that is 37 kJ/mol less stable than the catalyst model **1** considered initially.

To check whether the different conformation of the Cu atoms in **1** and **24** might lead to relevant reactivity differences an additional pathway *H* was explored on this system.

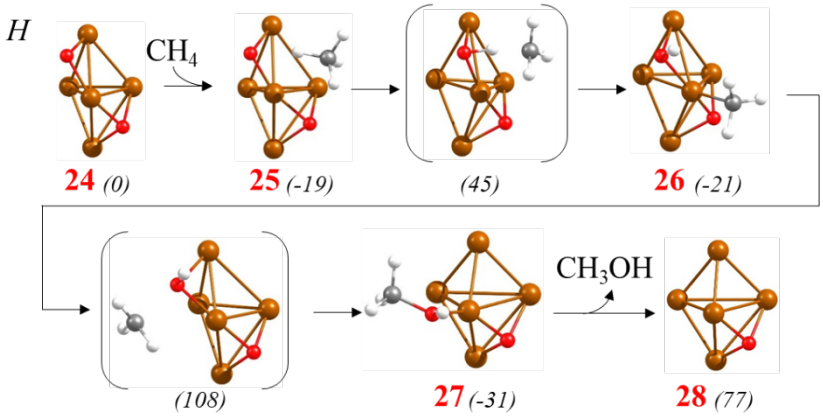

Figure 4.15 - Optimised geometries of minima and transition state structures involved in methane oxidation following pathway *H* on Cu_5-2O clusters supported on CHA zeolite. Si and O atoms in the framework depicted as yellow and red wires, Al, Cu, reactant O, C and H atoms depicted as light green, brown, red, grey, and white balls, respectively. Relative Gibbs energies at 478.15 K are given in brackets in kJ/mol.

In reactant **25**, CH_4 does not adsorb on the cluster but after the dissociation of the C-H bond through $\mathbf{TS_{25\rightarrow26}}$ with a calculated activation Gibbs energy of 64 kJ/mol, the resulting methyl group remains monocoordinated to a Cu atom with an optimised Cu-C bond length of 2.049 Å. The relatively high stability of intermediate **26** results in an activation Gibbs energy of 129 kJ/mol for the C-O bond formation step producing methanol, which after desorbing leaves a Cu_5-O system (structure **28**) 36 kJ/mol less stable than **5** and 24 kJ/mol more stable than **9**. In relation to the Gibbs energy profile for pathway *H*, it is similar to that obtained for pathway *B* (see table 4.8 for more detail), confirming that CH_4 oxidation to CH_3OH can proceed on Cu_5 clusters supported on CHA zeolite with activation energies below 130 kJ/mol. Interestingly, the smoothest energy profile with the lowest activation barriers is located on the Cu_5-3O cluster with the highest O coverage, with activation barriers not surpassing 100 kJ/mol.

In summary, all of the Gibbs energy profiles described so far except for Cu_5-3O clusters are depicted in figure 4.16:

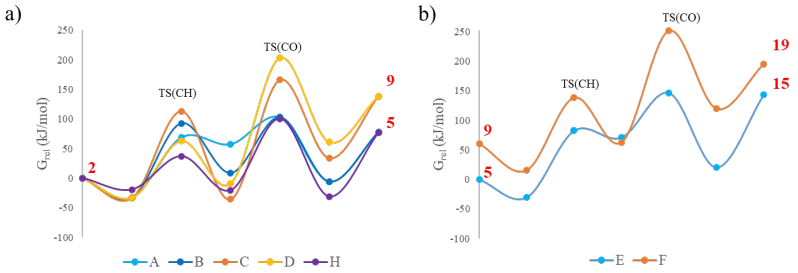

Figure 4.16 - Calculated Gibbs energy profiles at 478.15 K for methane oxidation and some competitive processes on (a) Cu_5-2O and (b) Cu_5-O clusters supported on CHA zeolite. The transition states for methane C-H bond dissociation (TS(CH)) and C-O bond formation (TS(CO)) are indicated on the plots. The red numbers correspond to some relevant structures involved in the mechanisms.

4.4 Competing Processes in Cu_5 clusters

Since the main drawback of the methane to methanol reaction is the easy over-oxidation of the product to CO_2, the feasibility of this and other undesired processes was investigated. Two main competing reactions were explored, the dissociation of a second C-H bond in adsorbed CH_3OH or CH_3 starting the unselective oxidation to CO_2, and the formation of surface methoxy (CH_3O) groups leading to catalyst blocking because they are not able to abstract a H from co-adsorbed OH to form CH_3OH, as explained in the last chapter. Both of them are illustrated in figure 4.17 and the relative energies are summarized in table A4.4 in the appendix (§4.9).

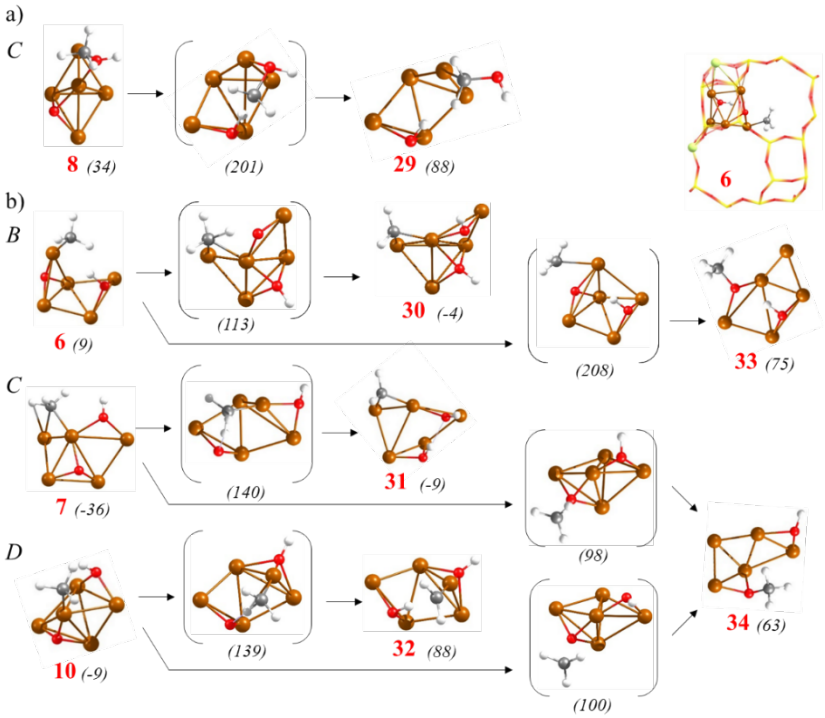

Figure 4.17 - Optimised geometries of minima and transition state structures involved in competitive processes on Cu_5-2O clusters supported on CHA zeolite. a) CH bond dissociation in adsorbed methanol in pathway *C*. b) CH bond dissociation and methoxy formation from adsorbed methyl intermediates in pathways *B*, *C* and *D*,

respectively. Si and O atoms in the framework depicted as yellow and red wires, Al, Cu, and reactant O depicted as light green, brown and red balls, respectively. Relative Gibbs energies at 478.15 K given in brackets in kJ/mol.

As a consequence of the small size of the Cu_5 cluster and its structural deformation due to interactions with the zeolite framework or with adsorbed species, CH_3OH is usually obtained monocoordinated to one Cu atom and far from any additional O atom able to abstract H, with the only exception of structure **8** involved in pathway *C* (figure 4.12 and 4.17a) in which the shortest O-H distance is 4.196 Å. Dissociation of the C-H bond is possible but endothermic by 54 kJ/mol and requires surpassing an activation barrier of 167 kJ/mol, which is also hindered by the high activation barriers required in both *C* and *D* pathways.

Alternatively, the adsorbed methyl groups formed as intermediates in pathways *B*, *C* and *D* (structures **6**, **7** and **10**, in figure 4.12 and 4.17b) are always closer to the co-adsorbed O atom, with O-H distances of 4.101, 4.063 and 4.131 Å, respectively. The reaction is endothermic starting from structures **7** or **10**, with the CH_2 species being 27 and 97 kJ/mol less stable than the initial CH_3 groups, with calculated activation Gibbs energies of 176 and 149 kJ/mol, respectively. However, the reaction mechanism depicted above for structure **6** shows a slightly exothermic process that involves an activation Gibbs energy of 105 kJ/mol, indicating that formation of structure **30** with one CH_2 and two OH groups could compete with methanol production (see energy profiles in figure 4.18a and table 4.8).

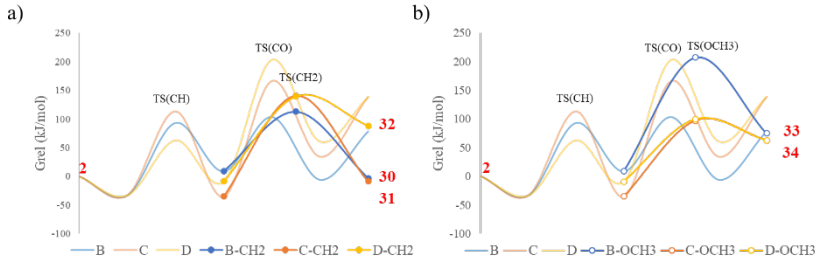

Figure 4.18 - Calculated Gibbs energy profiles at 478.15 K for competing (a) C-H bond breaking in adsorbed methyl and (b) formation of methoxy on Cu_5-2O clusters supported on CHA zeolite. The transition states for methane C-H bond dissociation [TS(CH)], C-O bond formation [TS(CO)], C-H bond breaking in methyl [TS(CH2)] and formation of methoxy [TS(OCH3)] are indicated on the plots. The red numbers correspond to some relevant structures involved in the mechanisms.

On the other hand, migration of a methyl group from a Cu atom in **6**, **7** and **10** to a proximal O atom yielding methoxy intermediate structures **33** or **34** in figure 4.17 is endothermic by 66, 99 and 72 kJ/mol, respectively, and requires surpassing high activation barriers of 199, 134 and 109 kJ/mol, respectively (see table 4.8). Therefore, the probability to form undesired methoxy species on Cu_5-2O clusters supported on CHA zeolite seems to be low except for structure **10** in the *D* pathway, which reflects a barrier that could compete with the C-O bond formation step, hampering the transformation to methanol.

The situation is different on Cu_5-3O. The non-adsorbed methyl radical present in structure **22** might adsorb on the Cu_5-3O cluster forming a new Cu-C bond and generating a system 71 kJ/mol more stable (structure **35** in figure 4.19 and table A4.5 in the appendix, §4.9). Dissociation of one C-H bond in this system to produce structure **36** is endothermic and involves a high activation Gibbs energy of 141 kJ/mol, but migration of the methyl group to one of the three surface O atoms requires a much lower barrier of 50 kJ/mol and produces a very stable methoxy intermediate, structure **37**.

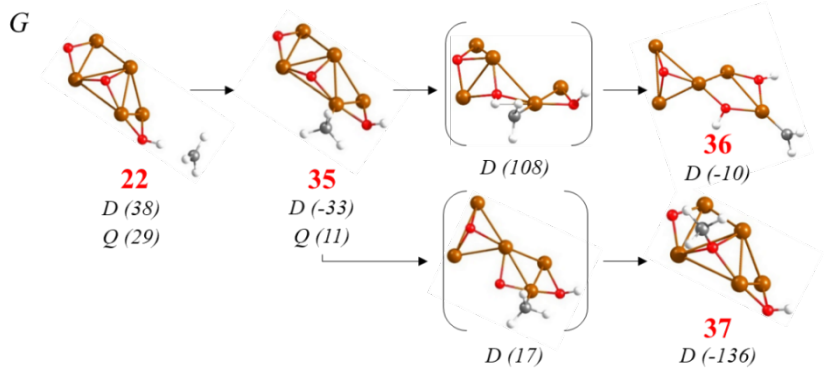

Figure 4.19 - Optimised geometries of minima and transition state structures involved in (a) competing processes on a Cu_5-3O cluster supported on CHA zeolite. Cu, C, H, and reactant O atoms are depicted as brown, grey, white, and red balls, respectively. Relative Gibbs energies for methane oxidation on Cu_5-OH-OCH_3 and Cu_5-OH-OH-CH_2 catalytic systems for doublet (*D*) and quadruplet (*Q*) spin surfaces at 478.15 K are given in brackets in kJ/mol.

Taking into consideration the stability differences between the doublet and the quadruplet state in structure **35**, only the doublet potential surface was investigated. Henceforth, two new reaction paths are upon us (See figure 4.20).

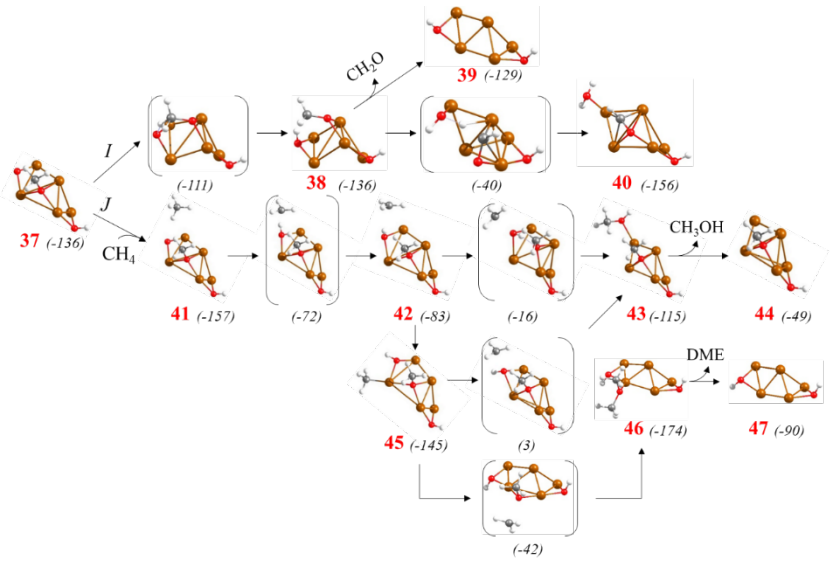

Figure 4.20 - Optimised geometries of minima and transition state structures involved in competing processes on a Cu_5-O-OH-OCH_3 cluster supported on CHA zeolite. Pathway *I* describes methoxy overoxidation and pathway *J* details methane oxidation. Cu, C, H, and reactant O depicted as brown, grey, white, and red balls, respectively. Relative Gibbs energies at 478.15 K given in brackets in kJ/mol.

Pathway *I* leads to the dissociation of a C-H bond in the methoxy group, requiring only 25 kJ/mol and yielding formaldehyde (structure **38**), which may either desorb from the cluster or transfer a H atom to a neighbouring OH group to form H_2O and an adsorbed OCH group (structure **40**). Considering Gibbs energy profiles (see figure 4.21b), desorption of formaldehyde is the more likely event, as only 34 kJ/mol are needed in comparison to the 96 kJ/mol for the water formation, which opens the possibility of considering this catalytic system for formaldehyde production, avoiding the ultimate oxidation to CO_2.

Pathway *J* describes methane oxidation over the remaining bicoordinated O atom. The new molecule approaches reaching an optimised O-H distance of 2.386 Å in structure **41**, followed by a reduction in the transition state to 1.129 Å, a C-H distance of 1.461 Å and an activation energy of 85 kJ/mol. Shortly after, structure **42** can evolve from two different paths, one of them through the radical

intermediate with activation barriers of 67 kJ/mol and an optimised C-O distance of 2.259 Å, while the other ensues through the monocoordinated methyl in structure **45**, featuring Cu-C distances of 1.958 Å and unluckily, a great stabilisation of 62 $kJ \cdot mol^{-1}$. Curiously, the uncovered transition state in this route shares a great resemblance with the previously mentioned, leading to a C-O distance of 1.995 Å, but to produce methanol, it is necessary to overcome a higher activation barrier, 148 kJ/mol. Eventually, both paths generate structure **43** and structure **44** consequently.

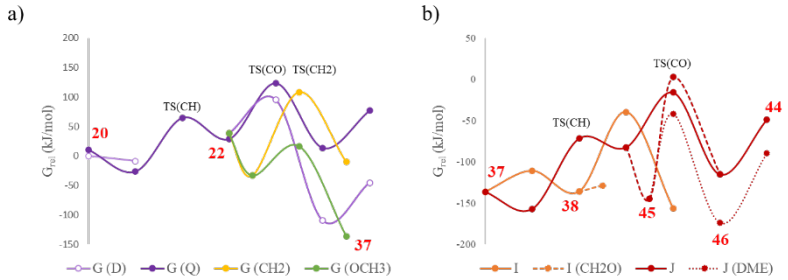

Figure 4.21 - Calculated Gibbs energy profiles at 478.15 K for methane oxidation and some competitive processes on (a) Cu_5-3O and (b) Cu_5-OH-OCH_3 clusters supported on CHA zeolite. The transition states for methane C-H bond dissociation [TS(CH)], C-O bond formation [TS(CO)] and C-H bond breaking in methyl [TS(CH2)] are indicated on the plots. The red numbers correspond to some relevant structures involved in the mechanisms.

Lastly, taking into consideration the proximity of the monocoordinated methyl to the methoxy group (3.834 Å) in structure **45**, formation of dimethyl ether (DME) was explored. Interestingly, the resulting transition state with a C-O distance of 2.205 Å has an activation energy of 103 kJ/mol, yielding structure **46**, with a desorption energy of 84 kJ/mol. This implies that the production of the intermediate **45** provokes the generation of DME as a secondary product, just like formaldehyde produced in pathway *I*.

These findings suggest that, once formed, methanol is stable against further oxidation, but some methoxy intermediates possibly appearing on Cu_5 clusters with three adsorbed O atoms are prone to break their

C-H bonds to generate either formaldehyde or DME, but never CO_2. Despite that, the catalytic system is able to turn methane into methanol with activation barriers lower than 90 kJ/mol if attachment of the methyl group is avoided.

4.5 CH_4 activation over Cu_7-CHA-2Al clusters

Continuing with the results for the partly oxidised Cu_7-2O cluster formulated in (§4.2.3) (structure **48** in figure 4.22 and table A4.6 in the appendix, §4.9), owing to its stabilisation within the CHA cage in a similar position to the one found for Cu_5-2O depicted in structure **1**, the interaction with CH_4 is limited to the point that it is not able to adsorb on the cluster surface. However, the bicoordinated O atom is more accessible, permitting two distinct reaction paths based on an Eley-Rideal mechanism labelled as *K* and *L*.

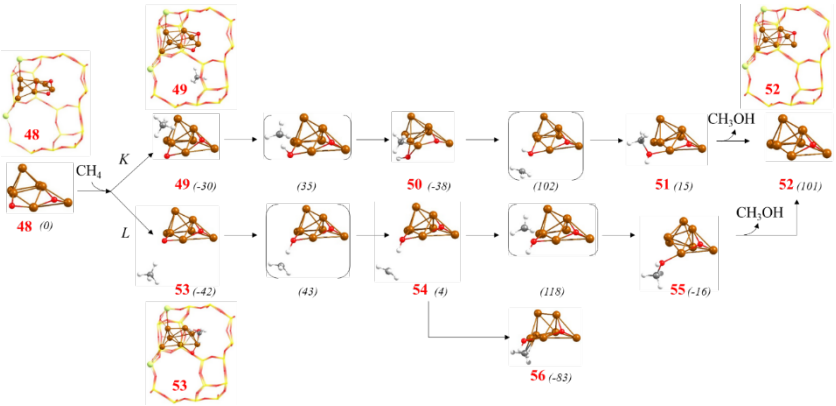

Figure 4.22 - Optimised geometries of minima and transition state structures involved in the oxidation of methane to methanol on a Cu_7-2O cluster supported on CHA zeolite following pathways *K* and *L*. Si and O atoms in the framework depicted as yellow and red wires, Al, Cu and reactant O depicted as light green, brown and red balls, respectively. Relative Gibbs energies at 478.15 K given in brackets in kJ/mol. All of the structures are located in the doublet spin surface.

Pathway *K* proceeds through structure **49** with a calculated Gibbs free interaction energy of -30 kJ/mol, where the C-H and O_{bi}-H distances measure 1.097 and 2.465 Å, respectively. After C-H bond dissociation, C-H distances increase to 1.374 Å in the transition state and to 1.947 Å in intermediate **50** while O_{bi}-H distances show the opposite trend, decreasing to 1.185 and 0.976 Å, respectively. Overcoming the activation barrier consumes 65 $kJ \cdot mol^{-1}$, forming a

monocoordinated methyl group attached to one of the bridged copper atoms with a Cu-C distance of 1.947 Å in the process.

In the next step, structure **50** requires 140 kJ·mol^{-1} to surpass the next transition state due to the stability provided by the monocoordinated methyl group, with an optimised C-O distance of 1.945 Å. After that, structure **51** is produced, reflecting the adsorbed methanol molecule in a Cu-O distance of 1.911 Å. To desorb methanol and therefore finish pathway *K*, 86 kJ/mol are needed to generate structure **52**, leaving the Cu_7 cluster with the remaining three-coordinated O atom.

On the other hand, pathway *L* starts with structure **53**, with a Gibbs interaction energy 12 kJ·mol^{-1} greater than structure **49** and optimised C-H and O_{bi}-H distances measuring 1.099 Å and 2.307 Å, respectively. From this minimum, a very similar transition state is found, requiring more efforts than the other path, 85 kJ/mol, probably on account of the stability of the previous structure, increasing C-H distance to 1.417 Å and shortening O_{bi}-H to 1.145 Å, giving rise to structure **54**.

Here, the first problem for the reaction is found in this system, since it is likely to form a bicoordinated methyl group 87 kJ/mol more stable than the former intermediate, structure **56**, making very difficult to progress through this path. In the case of avoiding this potential well, the reaction would proceed through another radical transition state with an activation barrier of 114 kJ/mol and calculated C-O distance of 1.958 Å. Next, structure **55** is generated. Curiously, this minimum conducts to the same structure after methanol desorption in pathway *K*, structure **52**, unifying both pathways for the next step of the MTM chemical reaction (See figure 4.23). Liken the Gibbs energy profiles for both routes, they are quite similar. Both routes present comparable geometric parameters and activation barriers subjected to the stability of the intermediate between C-H breakage and methanol formation (Structures **50** and **54**), but in all cases it results in less favourable routes in relation to the results of Cu_5 clusters (§4.3).

Moving to the Cu_7-O system (pathway *M*), introducing a new CH_4 molecule generates structure **57** with a Gibbs free interaction energy of -46 kJ/mol, not directly interacting with the cluster (see energies in table A4.7 in the appendix, §4.9). Due to the three-coordinated O

atom, the cluster is forced to change its geometry to provoke C-H scission, paying a great price for it, 197 kJ/mol in the activation barrier. In exchange, the methyl group is attached to one of the bridged copper atoms with a Cu-C value of 2.165 Å and with calculated C-H and O_{bi}-H values of 1.406 and 1.262 Å, respectively.

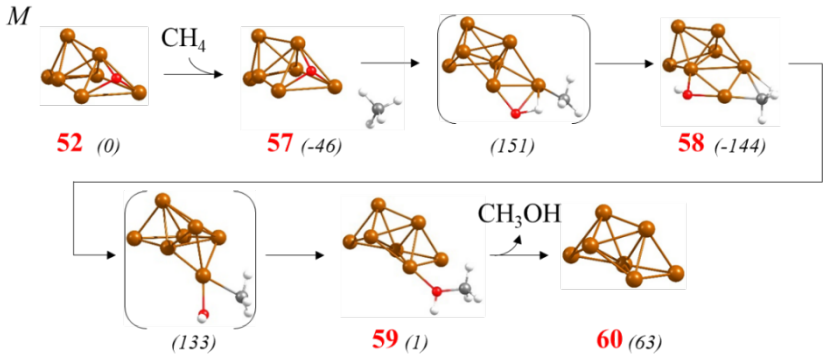

Figure 4.23 - Optimised geometries of minima and transition state structures involved in methane oxidation following pathway *M* on Cu_7-O clusters supported on CHA zeolite. Cu, O, C and H atoms are depicted as copper-coloured, red, grey, and white balls, respectively. Relative Gibbs energies in the spin doublet state at 478.15 K are given in brackets in kJ/mol.

As a result, structure **58** is created with a huge stability increase thanks to the bicoordinated methyl group generated in the process. Naturally, a very stable intermediate has consequences in the course of the reaction, because to overcome the next transition state, the system is obliged to change its conformation and break one of the Cu-O and Cu-C bonds, respectively for each functional group involved in the reaction coordinate. The calculated activation energy reaches an astonishing peak of 277 kJ/mol, and the optimised values for the Cu-O and Cu-C distances are 2.080 and 1.972 Å, respectively. Surpassing this barrier yields structure **59**, with an adsorbed monocoordinated methanol group with a Cu-O distance of 2.007 Å and takes 62 kJ/mol to desorb the desired product, resulting in structure **60**. With regards to the Gibbs energy profile, this route is very unlikely to occur, the huge energy barriers make it rather inefficient, much worse than the ones detailed in (§4.3, figure 4.13) for Cu_5 clusters. It is clear when

table 4.8 is consulted to compare the different pathways entailed in the MTM reaction.

Considering the fantastic O_2 affinity that these nanoclusters possess (See table 4.6, §4.2.4.2) and the two possible potential energy surfaces found in the Cu_5-3O system, the MTM reaction over the Cu_7-3O system was also studied in two distinct spin surfaces, doublet (*D*) and quadruplet (*Q*) (Figure 4.24, pathway *N*). Starting with structure **61** extracted from figure 4.10 (§4.2.4.2), it holds the singularity that this time, the quadruplet state is 9 kJ/mol more stable than the doublet spin surface in regard to the Cu_5-3O route illustrated in figure 4.14 (§4.3). When a CH_4 molecule is added, it has a weaker interaction in comparison with Cu_7-2O and Cu_7-O systems, only 22 and 19 kJ/mol for doublet and quadruplet spin state, respectively (see all energies in table A4.8 in the appendix). Nevertheless, just like in path *G*, only the quadruplet spin surface is able to break the C-H bond, with C-H and O_{bi}-H distances evolving from 1.097 and 1.425 Å in structure **62** to 2.314 and 1.139 Å in the transition state, respectively, giving an activation barrier of 91 kJ/mol. Attempts to find the doublet transition state turn out in the regeneration of the CH_4 molecule.

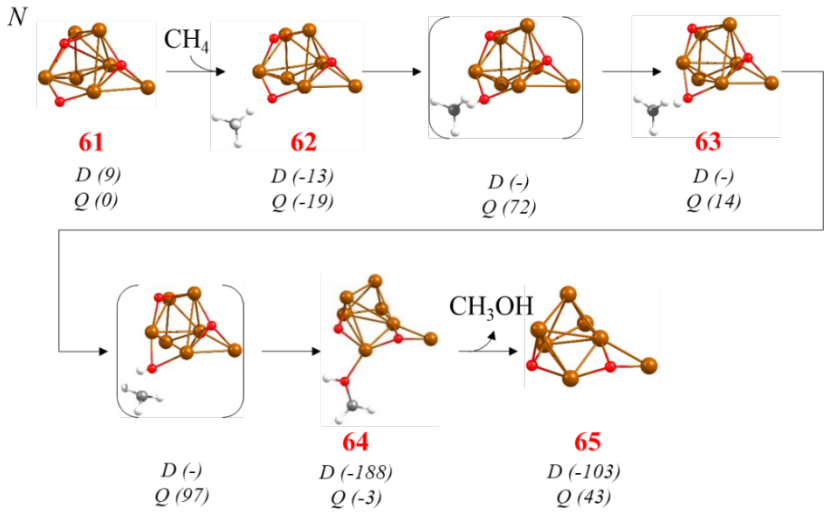

Figure 4.24 - Optimised geometries of minima and transition state structures involved in methane oxidation following pathway *N* on Cu_7-3O clusters supported on CHA zeolite. Cu, O, C and H atoms are depicted as copper-coloured, red, grey, and white balls, respectively. Relative Gibbs energies at 478.15 K for doublet (*D*) and quadruplet (*Q*) spin states are given in brackets in kJ/mol.

After this, structure **63** is born. As in the previous transition state, it fulfils the same behaviour as in the Cu_5-3O cluster, since this intermediate is solely found in the quadruplet state, obtaining the regeneration of the methane molecule in the doublet state. The calculated C-H and O_{bi}-H distances are 1.951 and 0.996 Å, respectively. In contrast, the transition state for the methanol formation only occurred in the quadruplet state compared to Cu_5, due to the fact that the transition state found for the doublet state has an imaginary frequency that corresponds to the regeneration of the methane once again. The measured C-O distance is 1.904 and to produce structure **64**, 100 kJ/mol are necessary. The new structure with the adsorbed methanol at a distance of 1.997 Å is overwhelmingly more stable in the doublet state than in the quadruplet one, so once the methanol formation is finished, all the population of the quadruplet state will go to the doublet spin surface. By desorbing the methanol molecule with an energy of 85 kJ/mol, an analogue configuration to the structure **48** is obtained, structure **65**, being 87

kJ/mol more stable than our initial structure in the MTM reaction over Cu_7-2O clusters.–In general, Cu_5 and Cu_7 clusters possess a very similar energy profile, reflected in almost the same activation energies in the C-H dissociation step (90 vs 91 kJ/mol, see figures 4.14 and 4.24) except for a different activation barrier for the methanol formation step in favour of Cu_5 considering the most optimal route (57 vs 83 kJ/mol). In this scenario, Cu_5 would be the preferable choice on account of the availability of a second bicoordinated O atom in structure **20** compared to the only bicoordinated O atom in Cu_7-3O (structure **61**), which would accelerate the reaction process.

Still, to present a thorough study of the Cu_7 systems, the subsequent step of the reaction after the desorption of the CH_3OH molecule in the Cu_7-3O system was studied (figure 4.25 and table A4.6 in the Appendix, §4.9). On the basis of structure **65**, a Gibbs free interaction energy of -21 kJ/mol is encountered, originating structure **66**. Due to the fact that this structure does not have bicoordinated O atoms, more energy is needed to surpass the transition state, 139 kJ/mol, in comparison with the 65 and 85 kJ/mol required in pathways *K* and *L*, respectively (See figure 4.26a). In addition to this, the C-H distances are elongated from 1.099 to 1.400 Å whilst the O_{bi}-H distances are shortened from 2.640 to 1.152 Å.

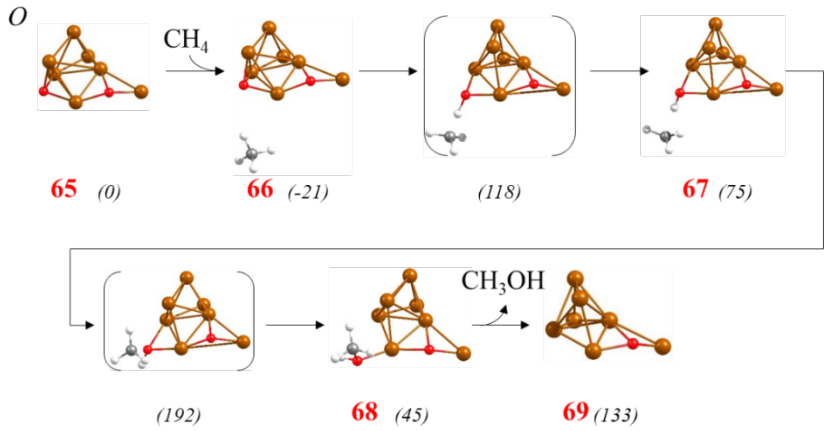

Figure 4.25 - Optimised geometries of minima and transition state structures involved in methane oxidation following pathway *O* on Cu_7-2O clusters supported on CHA zeolite. Cu, O, C and H atoms are depicted as copper-coloured, red, grey, and white balls, respectively. Relative Gibbs energies at 478.15 K in the doublet spin state are given in brackets in kJ/mol.

After this, structure **67** is constructed, with a C-H distance of 1.942 Å. To form methanol in the next step, a 117 kJ/mol barrier must be overcome, giving an optimised C-O distance of 2.012 Å and being 22 kJ/mol lower than its analogous transition state represented in pathway *K* but 3 kJ/mol higher than its corresponding TS in pathway *L*. (See figure 4.26). Then, structure **68** come to existence, with an adsorbed methanol molecule that necessitates 88 kJ/mol for its desorption, creating structure **69**, a Cu_7-O system that is 54 kJ/mol more stable than structure **52** pictured in pathway *M*, figure 4.23.

Therefore, as illustrated in figure 4.26a, pathway *O* is demanding for activating new methane molecules, demonstrating that the progression of the reaction on Cu_7 clusters is not favourable. Cu_5 systems are superior in this scenario since pathway *H* gives lower activation barriers in relation to pathways A and B. Moreover, figure 4.26b illustrates the stability of structures with monocoordinated methyl groups (structures **71** and **73**) which are key for the competitive processes explained in the next section. They are depicted in figure 4.27.

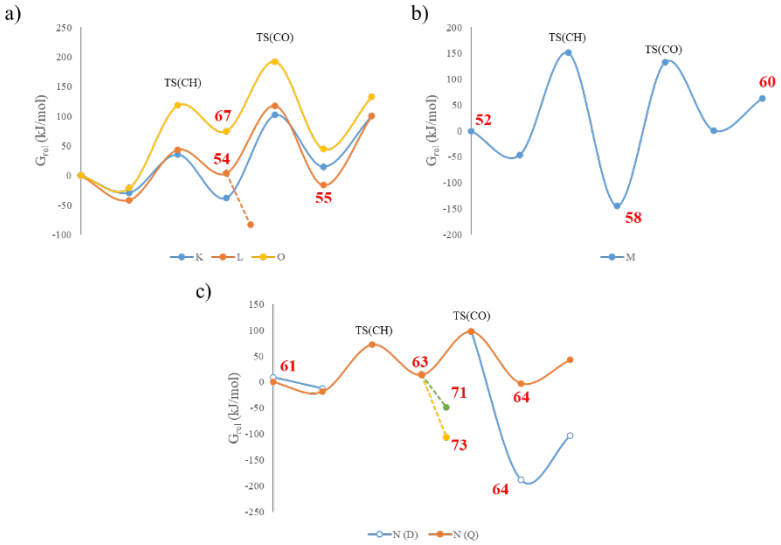

Figure 4.26 - Calculated Gibbs energy profiles at 478.15 K for methane oxidation and some competitive processes on (a) Cu_7-2O, (b) Cu_7-O and (c) Cu_7-3O clusters supported on CHA zeolite. The transition states for methane C-H bond dissociation (TS(CH)) and C-O bond formation (TS(CO)) are indicated on the plots. The red numbers correspond to some relevant structures involved in the mechanisms.

4.6 Competing processes in Cu_7 clusters

As explained at the beginning of (§4.4), the principal problem of the MTM reaction is the unselective overoxidation to CO_2. Considering that, the formation of the surface methoxy (CH_3O) group and the C-H scission on the methyl group throughout the reaction were explored (see figure 4.27 and table A4.9 in the appendix, §4.9).

Just like in Cu_5, the monocoordinated methyl groups are close to at least one of the co-adsorbed O atoms on the cluster in pathways *K* and *N*, with O-H distances from the closest H atom of the methyl group to the O of the OH group of 3.711, 2.867 and 3.097 Å in structures **50**, **71** and **73**, respectively. Interestingly, it is worth mentioning that these distances are shorter when compared to the results reported in Cu_5 for structures **6**, **7** and **10** (§4.4), which could be attributed to the atomicity of the cluster, as with an increasing number of atoms, less adjustments to the geometry parameters are needed to accommodate all the electric charge, which is translated to smaller O-H distances. This possibility permits a transition state that connects structures **50** and **70** with an optimised C-O distance of 1.940 Å and an activation energy of 74 kJ/mol, which directly competes with the methanol formation step (140 kJ/mol), hampering the reaction on Cu_7 clusters. Moreover, the relative Gibbs energy gathered in brackets (Plot in figure 4.28) show that the formation of the anchored methyl group in pathway *N* is very likely, achieving a great stabilisation of 121 $kJ \cdot mol^{-1}$ respect to structure **73**, which is almost two times larger than the one reported in Cu_5 for the monocoordinated methyl group (121 vs 62 $kJ \cdot mol^{-1}$).

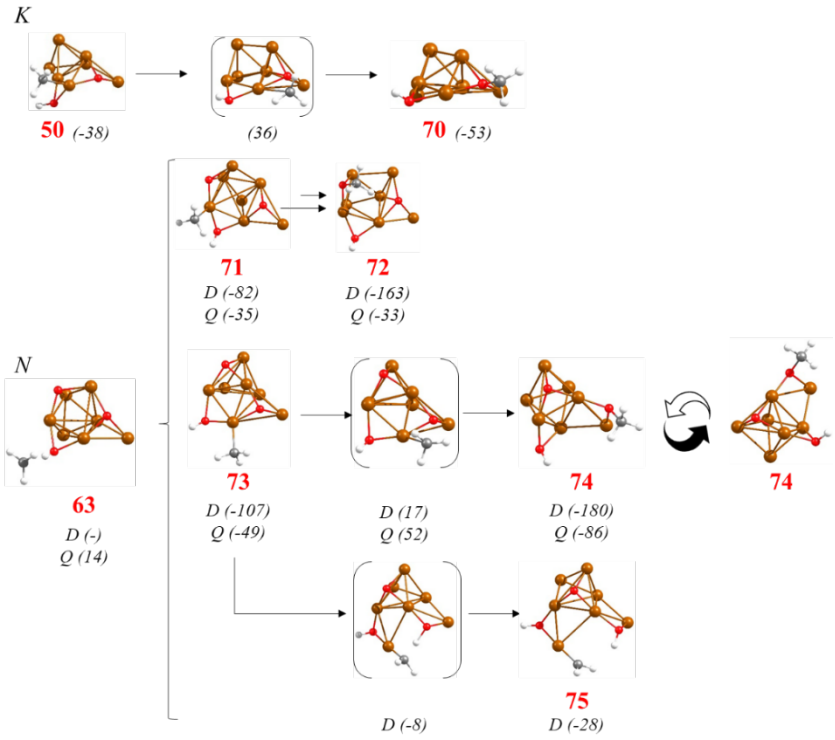

Figure 4.27 - Optimised geometries of minima and transition state structures involved in competitive processes on Cu_7-2O and Cu_7-3O clusters supported on CHA zeolite. All processes illustrate methoxy formation through an anchored monocoordinated methyl group intermediate in pathways *K* and *N*, respectively. Cu, O, C and H atoms are depicted as copper-coloured, red, grey, and white balls, respectively. Relative Gibbs energies at 478.15 K given in brackets for the doublet (*D*) and quadruplet (*Q*) potential energy surfaces in kJ/mol.

Equally, two different methoxy groups can be generated in pathway *N*, structures **72** and **74**, but according to the stabilities of the monocoordinated methyl groups, only the transition state that goes through structure **73** was studied. The resultant transition state brought an optimised C-O distance of 1.937 Å and an activation energy of 124 kJ·mol^{-1}, requiring 41 kJ·mol^{-1} more energy than the one associated with the methanol formation, $\mathbf{TS_{63\rightarrow 64}}$, but still, the formation of the methoxy group is more favourable than methanol production due to the likely production of structure **73** and its intrinsic stability in the doublet state.

Unfortunately, another issue comes to light when a second C-H breakage, this time in the methyl group, is considered in structure **73** since this dissociation competes with the methoxy formation with an activation barrier of 99 $kJ \cdot mol^{-1}$, being 25 $kJ \cdot mol^{-1}$ more favourable than the methoxy formation (See figure 4.28b), which brings about an additional problem that is completely avoided in the Cu_5-3O system (See figure 4.21a).

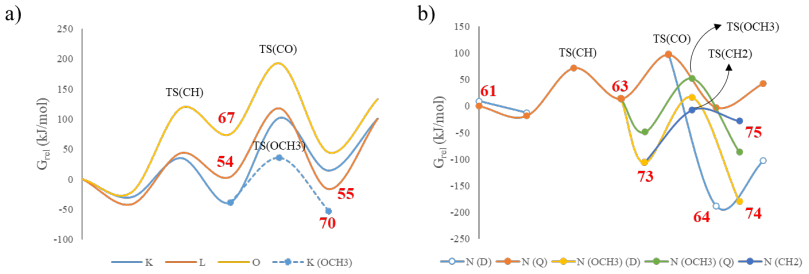

Figure 4.28 - Calculated Gibbs energy profiles at 478.15 K for competing formation of methoxy on (a) Cu_7-2O and (b) Cu_7-3O clusters supported on CHA zeolite. The transition states for methane C-H bond dissociation [TS(CH)], C-O bond formation [TS(CO)], formation of methoxy [TS(OCH3)] and C-H bond breaking in methyl [TS(CH2)] are indicated on the plots. The red numbers correspond to some relevant structures involved in the mechanisms.

Furthermore, these experiments confirm that after formation of structure **63**, doublet PES becomes predominant when the CH_2 or the methoxy species are formed, as displayed in figures 4.19 and 4.27, reinforcing the results reported in Cu_5 clusters. Hence, only the doublet state was studied in the next steps of the reaction.

In order to complete the study, the reaction with the remaining three-coordinated O atom in pathway *P* was investigated. The entire pathway is plotted in figures 4.29 and 4.30:

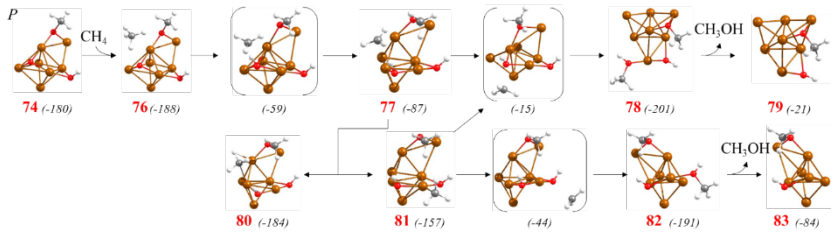

Figure 4.29 - Optimised geometries of minima and transition state structures involved in competing processes on a Cu_7-O-OH-OCH_3 cluster supported on CHA zeolite. Cu, C, H, and O atoms are depicted as brown, grey, white, and red balls, respectively. Relative Gibbs energies in the doublet potential energy surface at 478.15 K are given in brackets in kJ/mol.

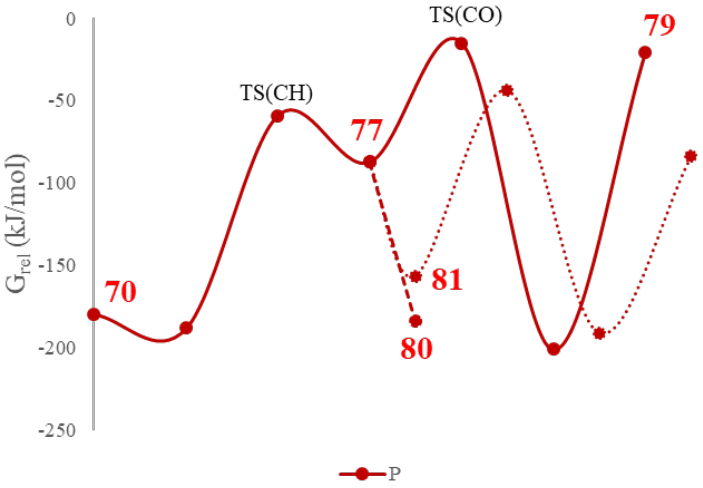

Figure 4.30 - Calculated Gibbs energy profiles at 478.15 K for methane oxidation and some competitive processes on Cu_7-O-OH-OCH_3 clusters supported on CHA zeolite. The transition states for methane C-H bond dissociation (TS(CH)) and C-O bond formation (TS(CO)) are indicated on the plots. The red numbers correspond to some relevant structures involved in the mechanisms.

Approaching a new methane molecule give rise to structure **76**, with a very weak exothermic interaction of 8 kJ/mol. Then, to perform the C-H dissociation, C-H and O-H distances must evolve from 1.092 to 1.581 Å and from 2.538 to 1.061 Å, respectively to surpass a demanding 129 kJ/mol barrier. After this, structure **77** is created, which may progress through a transition state in which the calculated C-O distance is 2.097 Å and the activation energy is 72 kJ/mol to yield structure **78** with a huge stabilisation of 186 kJ/mol. Nevertheless, this fact provokes a very demanding step for the desorption of methanol, 180 kJ/mol, which is very unfeasible in relation to the Cu_5 route depicted in figure 4.20 that requires 66 kJ/mol, becoming the highest value to perform methanol desorption step.

The alternatives for this route are discouraging. Structure **80** has a bicoordinated methyl group that sinks the reaction in a potential well very difficult to escape, stabilising 97 kJ/mol respect to structure **77**. The remaining path take place through structure **81**, with a monocoordinated methyl group attached to the copper atom between the two hydroxyl groups, measuring 2.002 Å. Despite this structure is not as stable as the bicoordinated species (70 kJ/mol of stabilisation), its configuration could facilitate methanol formation through two transition states, one of them being identical to the one that connects structures **77** and **78** except for the 142 kJ/mol barrier to surpass this occasion, and the other one reacting with the vicinal hydroxyl group already formed in structure **74**, with an optimised C-O distance of 2.099 Å and an activation barrier of 113 kJ/mol, generating a methanol molecule in structure **82**. Finally, 107 kJ/mol are needed to desorb methanol, obtaining structure **83**.

4.7 Discussion of the selective oxidation of methane into methanol over Cu_n-2Al-CHA

These series of computational calculations demonstrate that Cu_5 clusters are better than Cu_7 clusters for the conversion of methane into methanol. To discuss each point of the reaction, the normal course of the reaction will be followed.

Firstly, in systems with two adsorbed oxygen atoms, both of them exhibit very similar activation energies (See figure 4.31), except for the step following methanol formation from the Cu_n-3O system (Pathways *H* & *O*), in which Cu_5 offers a milder energy profile compared to Cu_7. Furthermore, if the adsorption of the methyl group is taken into account, it would tip the scales much more in Cu_5's favour because of the formation of structure **56**, featuring a bicoordinated methyl group that grants a lot of stability to the intermediate, and therefore, signifying a hindrance to the process.

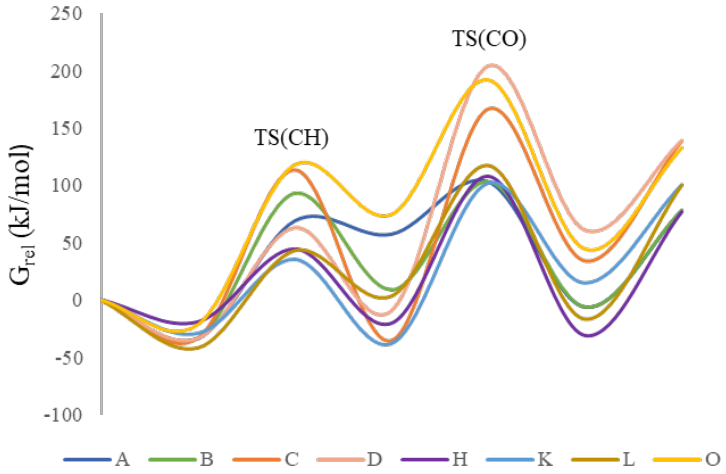

Figure 4.31 - Calculated Gibbs energy profiles at 478.15 K for methane oxidation into methanol for Cu_5-2O and Cu_7-2O clusters supported on CHA zeolite. The transition states for methane C-H bond dissociation [TS(CH)] and C-O bond formation [TS(CO)] are indicated on the plots.

Only the most optimal paths for the methane conversion to methanol have been considered.

Secondly, concerning systems with only one attached O atom, Cu_5 is considerably the best option (See figure 4.32). The energy profiles to obtain methanol are smoother considering that the initial structures here (Structures **5**, **9** and **52**) have three-coordinated oxygen atoms, and again, the intervention of bicoordinated methyl groups in pathway *M* (structure **58**) makes the conversion to methanol rather difficult. In addition to Cu_5 systems, bi-coordination of the methyl group is avoided, although the monocoordination remains inevitable (pathway *F*).

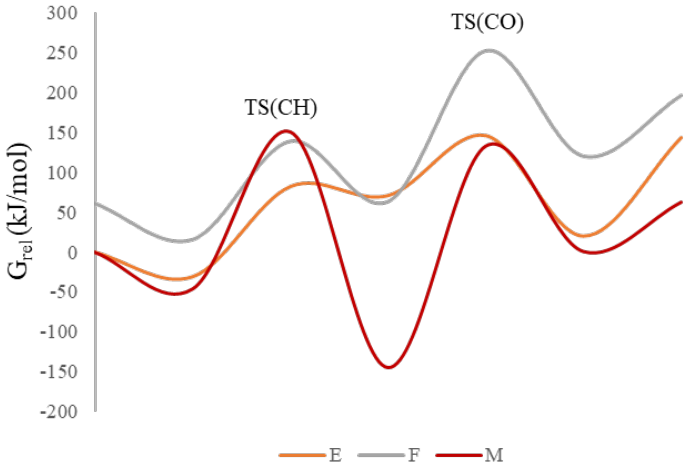

Figure 4.32 - Calculated Gibbs energy profiles at 478.15 K for methane oxidation into methanol for Cu_5-O and Cu_7-O clusters supported on CHA zeolite. The transition states for methane C-H bond dissociation [TS(CH)] and C-O bond formation [TS(CO)] are indicated on the plots. Only the most optimal paths for the methane conversion to methanol have been considered.

Thirdly, Cu_n-3O systems possess a particular characteristic, the possibility to react on *D* and *Q* potential energy surfaces which in Cu_5 and Cu_7, makes the quadruplet spin surface the only one effective for

the conversion of methane into methanol. Looking at the energy profiles collected in figure 4.33, both catalysts present similar activation barriers, but the heart of the matter is located in the secondary routes. This time, the bi-coordination of the methyl group is eluded thanks to the O coverage, but again, as in Cu_n-O systems, it is impossible to escape from the monocoordination of the methyl group. In this case, Cu_5 clusters have a very important advantage respect to Cu_7, and the thing is the generation of CH_2 species is utterly evaded, being the formation of the methoxy group the only side effect. This fact might finally tip the scale in Cu_5's favour, since this is the most probable path to Cu_7, and has not any possibility of progress to yield methanol.

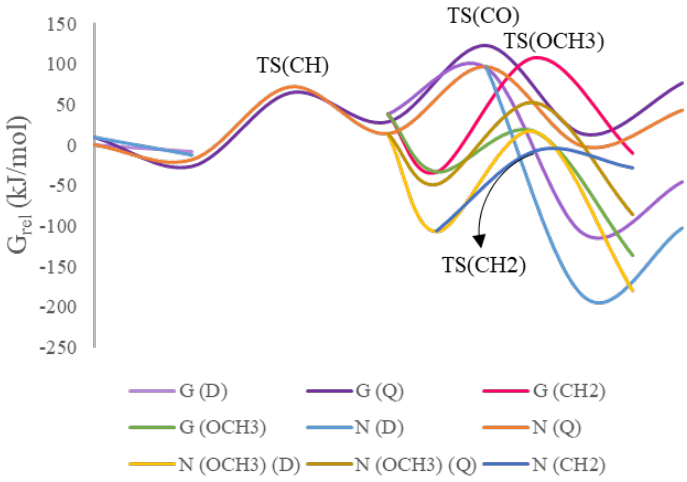

Figure 4.33 - Calculated Gibbs energy profiles at 478.15 K for methane oxidation into methanol for Cu_5-3O and Cu_7-3O clusters supported on CHA zeolite. The transition states for methane C-H bond dissociation [TS(CH)], C-O bond formation [TS(CO)], formation of methoxy [TS(OCH3)] and C-H bond breaking in methyl [TS(CH2)] are indicated on the plots. Only the most optimal paths for the methane conversion to methanol have been considered.

To conclude, Cu_n-O-OH-CH_3 system energy profiles demonstrate that sub-nanometre clusters can also function as a catalyst to produce a more variety of C1 products different from methanol (See figure 4.34). Once again, Cu_5 proves to be the superior catalyst because of

the desorption barrier in pathway *P* to release methanol, which hinders even more the consideration of Cu_7 as the chosen catalyst for the MTM reaction, but not only that, the last straw comes in the form of a bicoordinated methyl group in structure **80** that makes the conversion very unlikely to happen. However, Cu_5 not only maintains reasonable activation barriers, but also opens the possibility to produce unique value-added products to the chemical industry and still avoiding CO_2 formation.

As in the former systems described, monocoordination of the methyl group is unavoidable, creating a scenario where the stabilisation of the monocoordinated group is moderate and the activation energies are significantly high for methanol conversion, even for Cu_5 (structure **45**). Nevertheless, under this situation, the Cu_5 system is prone to yield dimethyl ether (DME) with milder activation barriers, a colourless gas easy to transport used for different purposes such as aerosol environmentally friendly alternative to chlorofluorocarbons (CFCs), a promising fuel alternative for diesel, gasoline or liquified petroleum gas (LPG) or as a chemical H_2 carrier among other applications.[572–574] In fact, following the thermodynamic trends give as a result the formation of DME as secondary product, which entails a mix of methanol and DME might be found in the long run, adding added value to the process carried out by sub-nanometre copper clusters for the chemical industry.

On the other hand, pathway *I* conducts to the formation of formaldehyde, a colourless, volatile and toxic gas capable of produce resins, disinfectants, cosmetics, etc., being one of the most produced chemicals worldwide owing to its versatility, reactivity and low cost.[575,576] Thus, the production of methoxy groups on Cu_5 clusters supported within CHA leads to useful more oxygenated chemicals in exchange of selectivity.

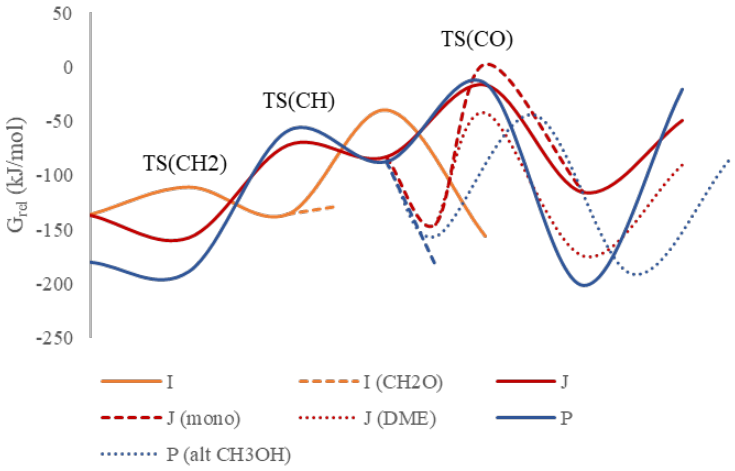

Figure 4.34 - Calculated Gibbs energy profiles at 478.15 K for methane oxidation into methanol for Cu_5-O-OH-OCH_3 and Cu_7-O-OH-OCH_3 clusters supported on CHA zeolite. The transition states for methane C-H bond dissociation [TS(CH)] and C-O bond formation [TS(CO)] and C-H bond breaking in methyl [TS(CH2)] are indicated on the plots. Only the most optimal paths for the methane conversion to methanol have been considered.

On balance, all the hints conduct to Cu_5 as the best candidate for the conversion of methane into methanol.

To facilitate the comparative discussion of all the processes investigated, kinetic constants *k* calculated at 478.15 K for all elementary steps are summarised in table 4.9 for Cu_5 and Cu_7 clusters. For the chosen candidate, methanol can be produced efficiently via pathway *A* through a radical-like intermediate, with the kinetic constant *k* for the second-best pathway *B* being two orders of magnitude lower. Only a bifurcation in path *B* leading to an adsorbed CH_2 group might compete when starting from Cu_5-2O system (See figures 4.17 & 4.18). After the first methanol desorption leaving Cu_5-O, a second catalytic cycle producing methanol and regenerating the Cu_5 cluster (path *E*) is also favourable. Alternatively, the fast adsorption and dissociation of O_2 leading to Cu_5-3O also produces methanol efficiently (path *G*). Even the competing formation of a

methoxy group (Cu_5-O-OH-OCH_3 system) might produce methanol, as well as by-products like DME (path *J*), and formaldehyde (Path *I*).

As for Cu_7 clusters, methanol is primarily yielded via pathway *L* through an Eley-Rideal mechanism despite pathway *K* being two orders of magnitude faster in the C-H activation step. The decisive step is located in the methanol formation step, in which pathway *L* is three orders of magnitude faster than pathway *L* (See figure 4.22). In addition, pathway *K* is prone to produce methoxy species in contrast to the alternative route, which would be detrimental for the course of the reaction. After the first methanol desorption, Cu_7-O cluster is formed and the reaction finds great obstacles through pathway *M*, with the smallest kinetic constants of the methane-to-methanol process (see table 4.9). On the other hand, a very favourable adsorption and dissociation of O_2 provokes the generation of Cu_7-3O clusters, although the formation of CH_2 species can compete with the production of methanol, being only one order of magnitude higher for the methanol formation step, which presents a catalytic system with remarkable difficulties to selectively transform methane into methanol. Furthermore, the possibility of generating methoxy species cannot be ruled out through pathway *P* considering the kinetic constant is only three orders of magnitude lower than the generation of CH_2 species, but even in this competitive reaction path a great hindrance is found for the formation of methanol due to the generation of a bi-coordinated methyl group in structure **80** (See figure 4.29).

Table 4.9 - Kinetic constants for the C-H bond dissociation in CH_4 (CH) and the CH_3OH formation (CO) steps and for the competing formation of methoxy groups (OCH_3) and dissociation of a second CH bond (CH_2), calculated at T = 478.15 K.

Model	Pathway	k (CH) (s^{-1})	k (CO) (s^{-1})	k (OCH_3) (s^{-1})	k (CH_2) (s^{-1})
Cu_5-2O	*A*	7.17E+01	9.40E+07		
	B	1.71E-01	5.37E+02	1.82E-09	4.34E+01
	C	1.12E-03	6.64E-10	2.29E-02	5.92E-07
	D	3.25E+02	5.37E-11	1.23E+01	6.77E-04
	H	1.02E+06	8.06E-02		
Cu_5-O	*E*	4.51E+00	6.39E+04		
	F	2.83E-01	2.89E-08		
Cu_5-3O	*G (Q)*	1.47E+03	5.37E+02	3.44E+07	4.26E-05
	I	1.85E+10[a]	9.96E+12		3.25E+02[b]
	J	5.16E+03	4.78E+05/ 6.77E-04	5.58E+01[c]	
Cu_7-2O	*K*	7.90E+05	5.07E-03	8.21E+04	
	L	5.16E+03	3.51E+00		
	O	6.51E-03	1.28E+00		
Cu_7O	*M*	3.01E-09	5.48E-18		
Cu_7-3O	*N (Q)*	1.14E+03	8.54E+03	2.83E-01	1.53E+02
	P	8.06E-02	1.36E+05/ 4.51E+00		

[a]to formaldehyde
[b]to water
[c]to dimethyl ether (DME)

4.8 Conclusions

The present computational study shows that the stabilization of Cu_n clusters within Al-containing zeolites modifies their charge and morphology, and consequently, their reactivity towards O_2. The total positive charge on the Cu_n clusters increases with the number of Al atoms in the zeolite framework. O_2 adsorption and its subsequent dissociation into two O atoms requires an additional transfer of electron density from the catalyst to the O_2 and O species, leaving the Cu_n clusters highly charged after the reaction takes place. As a consequence, deep oxidation of zeolite supported Cu_n clusters by successive adsorption and dissociation of additional O_2 molecules is unlikely, which can be exploited to stabilise the metallic oxidation state under oxidising conditions, necessary for some challenging reactions.

The mechanism of the selective oxidation of methane to methanol and of the most relevant competing reactions that decrease the selectivity of this challenging reaction has been theoretically investigated using periodic DFT calculations. The proposed catalyst consists of small Cu_5 clusters stabilised within a CHA zeolite with a high Si/Al ratio of 17. The high stability against deep oxidation of such clusters facilitates the dissociation of the methane C-H bond and desorption of the methanol formed, making difficult its over-oxidation to CO_2. Among the different pathways explored, the one proceeding through a radical-like non-adsorbed methyl intermediate is the most efficient, allowing to close the catalytic cycle with Gibbs activation energies lower than 115 kJ/mol, of the same order as those reported experimentally for Cu-exchanged zeolites, presenting a lot of its similarities.[371,524] Furthermore, higher spin states proved to be essential for the chemical reaction, as they enable methane activation in high O coverage systems reducing the H transfer transition state and therefore, improving the process overall by enhancing methanol formation.

The mechanism and the competing reactions have been also studied for Cu_7 clusters stabilised in the same support. In spite of similar activation barriers as reported in Cu_5 clusters, the formation of bicoordinated

methyl groups with its associated high stability and Cu_7-3O system tendency to dissociate C-H bonds of the methyl group rule out its consideration to optimally perform the MTM chemical reaction.

The present findings open an avenue to design catalytic materials based on their ability to stabilise radical species.

4.9 Appendix

Table A4.1 - Relative energies (E_{rel}) and Gibbs energies (G_{rel}) in kJ/mol for all the structures involved in methane oxidation on Cu_5-2O clusters. Optimised structures depicted in figures 4.12 & 4.15.

Structure	E_{rel} (kJ/mol)	G_{rel} (kJ/mol)
1 + CH_4	0	0
2	-43	-33
TS(2→3)	74	69
3	67	57
TS(3→4)	106	103
4	-15	-6
5 + CH_3OH	74	78
TS(2→6)	59	93
6	-6	9
TS(2→7)	107	114
7	-47	-36
TS(7→8)	136	167
8	14	34
9 + CH_3OH	132	139
TS(2→10)	32	63
10	-24	-9
TS(10→11)	195	204
11	45	61
24 + CH_4	0	0
25	-23	-19
TS(25→26)	49	45
26	-26	-21
TS(26→27)	95	108
27	-41	-31
28 + CH_3OH	72	77

Table A4.2 - Relative energies (E_{rel}) and Gibbs energies (G_{rel}) in kJ/mol for all the structures involved in methane oxidation on Cu_5-O clusters. Optimised structures depicted in figure 4.13.

Structure	E_{rel} (kJ/mol)	G_{rel} (kJ/mol)
5 + CH_4	0	0
12	-28	-31
TS(12→13)	79	82
13	67	71
TS(13→14)	121	146
14	-5	20
15 + CH_3OH	132	144
9 + CH_4	58	61
16	7	15
TS(16→17)	128	139
17	50	63
TS(17→18)	227	252
18	91	120
19 + CH_3OH	169	196

Table A4.3 - Relative energies (E_{rel}) and Gibbs energies (G_{rel}) in kJ/mol for all the structures involved in methane oxidation on Cu_5-3O clusters, both in doublet (D) and quadruplet (Q) spin states. Optimised structures depicted in figure 4.14.

Structure	E_{rel} (kJ/mol)		G_{rel} (kJ/mol)	
	D	Q	D	Q
20 + CH_4	0	4	0	10
21	-23	-24	-8	-26
TS(21→22)	-	48	-	64
22	37	35	38	29
TS(22→23)	85	96	95	123
23	-163	-7	-110	13
24 + CH_3OH	-69	78	-45	77

Table A4.4 - Relative energies (E_{rel}) and Gibbs energies (G_{rel}) in kJ/mol for all the structures involved in competitive processes on Cu_5-2O clusters. Optimised structures depicted in figure 4.17.

Structure	E_{rel} (kJ/mol)	G_{rel} (kJ/mol)
8	14	34
TS(8→29)	183	201
29	77	88
6	-6	9
TS(6→30)	101	113
30	-16	-4
TS(6→33)	192	208
33	57	75
7	-47	-36
TS(7→31)	129	140
31	-20	-9
TS(7→34)	83	98
34	27	63
10	-24	-9
TS(10→32)	120	139
32	87	88
TS(10→34)	94	100
34	27	63

Table A4.5 - Relative energies (E_{rel}) and Gibbs energies (G_{rel}) in kJ/mol for all the structures involved in competitive processes on Cu_5-3O and Cu_5-OH-OCH_3 clusters. Optimised structures depicted in figures 4.19 & 4.20.

Structure	E_{rel} (kJ/mol)	G_{rel} (kJ/mol)
35	-50	-33
TS(35→36)	109	126
36	-30	-10
TS(35→37)	-4	17
37	-160	-136
TS(37→38)	-133	-111
38	-154	-136
39 + CH_2=O	-120	-129
TS(38→40)	-43	-40
40	-177	-156
37 + CH_4	-160	-136
41	-192	-157
TS(41→42)	-104	-72
42	-116	-83
TS(42→43)	-56	-16
43	-155	-115
44 + CH_3OH	-78	-49
45	-202	-145
TS(45→43)	-57	3
TS(45→46)	-99	-42
46	-218	-174
47	-136	-90

Table A4.6 - Relative energies (E_{rel}) and Gibbs energies (G_{rel}) in kJ/mol for all the structures involved in methane oxidation on Cu_7-2O clusters. Optimised structures depicted in figures 4.22 & 4.25.

Structure	E_{rel} (kJ/mol)	G_{rel} (kJ/mol)
48 + CH_4	0	0
49	-30	-30
TS(49→50)	36	35
50	-41	-38
TS(50→51)	61	102
51	-6	15
52 + CH_3OH	99	101
53	-31	-42
TS(53→54)	20	43
54	9	4
TS(54→55)	82	118
55	-21	-16
56	-89	-83
65 + CH_4	-139	-103
66	-167	-124
TS(66→67)	-37	15
67	-48	-28
TS(67→68)	21	90
68	-124	-58
69	-12	30

Table A4.7 - Relative energies (E_{rel}) and Gibbs energies (G_{rel}) in kJ/mol for all the structures involved in methane oxidation on Cu_7-O clusters. Optimised structures depicted in figure 4.23

Structure	E_{rel} (kJ/mol)	G_{rel} (kJ/mol)
52 + CH_4	0	0
57	-31	-46
TS(57→58)	137	151
58	-159	-144
TS(58→59)	86	133
59	-30	1
60 + CH_3OH	56	63

Table A4.8 - Relative energies (E_{rel}) and Gibbs energies (G_{rel}) in kJ/mol for all the structures involved in methane oxidation on Cu_7-3O clusters. Optimised structures depicted in figure 4.24.

Structure	E_{rel} (kJ/mol)		G_{rel} (kJ/mol)	
	D	Q	D	Q
61 + CH_4	5	0	9	0
62	-21	-26	-13	-19
TS(62→63)	-	38	-	72
63	-	11	-	14
TS(63→64)	-	75	-	97
64	-226	-38	-188	-3
65 + CH_3OH	-139	14	-103	43

Table A4.9 - Relative energies (E_{rel}) and Gibbs energies (G_{rel}) in kJ/mol for all the structures involved in competitive processes on Cu_7-2O and Cu_7-3O clusters. Optimised structures depicted in figure 4.27.

Structure	E_{rel} (kJ/mol)		G_{rel} (kJ/mol)	
	D	Q	D	Q
50	-41	-	-38	-
TS(50→70)	26	-	36	-
70	-69	-	-53	-
71	-124	-77	-82	-35
72	-210	-65	-163	-33
73	-138	-73	-107	-49
TS(73→74)	-28	31	17	52
74	-223	-114	-180	-86
TS(73→75)	-47		-8	
75	-68		-28	

Table A4.10 - - Relative energies (E_{rel}) and Gibbs energies (G_{rel}) in kJ/mol for all the structures involved in competitive processes on Cu_7-OH-OCH_3 clusters. Optimised structures depicted in figure 4.29.

Structure	E_{rel} (kJ/mol)	G_{rel} (kJ/mol)
74 + CH_4	-223	-180
76	-244	-188
TS(76→77)	-115	-59
77	-138	-87
TS(77→78)	-69	-15
78	-260	-201
79 + CH_3OH	-77	-21
80	-251	-184
81	-214	-157
TS(81→82)	-106	-44
82	-270	-191
83 + CH_3OH	-132	-84

Chapter 5 Alternative Zeotype Systems for the selective partial oxidation of methane into methanol

Cu_5 clusters demonstrated their ability to carry out the selective oxidation of methane into methanol while avoiding overoxidation to CO_2. However, the former chapters only focused on zeolite systems as supports for the copper clusters, and new perspectives of the MTM reaction on analogous systems would envision a more complete image of the chemical fundamentals involved.

This chapter marks the full stop of this dissertation, delving into zeotype systems that might modulate the catalytic properties of the supported clusters and foster enhancements to the uncovered mechanistic insights.

5.1 Introduction

Zeotypes are crystalline microporous materials structurally analogous to zeolites but with different chemical composition, as described in chapter 1 (§1.5). The use of zeotypes such as aluminophosphates (AlPOs), silicoaluminophosphates (SAPOs) or metal-containing aluminophosphates (MeAPOs) for the methane-to-methanol reaction has been scarcely investigated.[136,385] By and large, the use of SAPOs is dedicated to the MTO process and for gases purification.[109,133] However, owing to their acidic properties, these zeotypes can also be applied to other catalytic routes.[577] Conversely, MeAPOs (metal-containing aluminophosphates) have a pronounced redox character[386] that could be applied specifically for this reaction, this being the objective of this chapter.

Six metallic elements have been selected to be introduced in a MeAPO-34 framework: Zn^{2+}, Fe^{2+}, Mg^{2+}, Ti^{4+}, Zr^{4+} and Sn^{4+}. The reasons behind this decision are localised in the periodic table, in which each one pertains to a different periodic group, encompassing both divalent and tetravalent metals. Indeed, a set of these materials were successfully synthesised in the past.[110,386,578,579] The only exceptions here are Ti and Zr cases, which can be explained because of the results obtained in the fourth group (§5.3.5 and 5.3.6). Their unique features will be tested to see their implications in the stabilisation of the Cu_5 cluster, its reactivity towards O_2 and CH_4 later on in the MTM process.

All of the embedded metals occupy an equivalent spot in the zeotype cage, just like the zeolite chabazite system in previous chapters. Two divalent metals substituted two framework Al^{3+} atoms whilst the same is applied to tetra-valent metals with framework P^{5+} atoms. The same cage as in previous chapters is used to preserve the consistency of this dissertation.

From a sustainable perspective, MeAPOs offer a lot of versatility since they can function as bifunctional catalysts and as a CO_2 scavenger in petrochemical industry among other applications.[138,580] In turn, MeAPOs provide the prospect of extending a niche subject area that has previously achieved green goals like the use of hydrogen peroxide in the conversion of cyclohexene,[581] entailing our bet to expand the current knowledge barrier.

5.2 O_2 dissociation over Cu_5-zeotype clusters

The same procedure followed in the previous chapters will be applied to the zeotype systems. First, Cu_5 clusters will be stabilised within the zeotype cage to get a fundamental understanding of the catalyst. Then, the O_2 adsorption on supported Cu_5 clusters and its subsequent dissociation will be addressed and compared with the same process catalysed by Cu_5 clusters within the CHA-2Al model.

5.2.1 AlPO & SAPO systems

In a first step, the geometry of the bi-dimensional Cu_5-2D cluster embedded within the cavity of AlPO-34 (0Si) and SAPO-34 (2Si) zeotypes was fully optimised without restrictions. In AlPO-34 its geometry barely changed with respect to that of the isolated Cu_5-2D cluster, but in SAPO-34 it evolved to a three-dimensional Cu_5-3D cluster, as represented in figure 5.1. Hence, Cu_5-3D clusters were not further optimised in SAPO-34, and the structure resulting from the initial optimization of the Cu_5-2D cluster was employed along the mechanistic study.

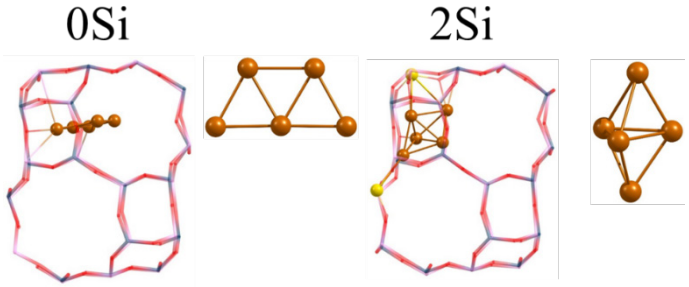

Figure 5.1 - Optimised structures of Cu_5-2D confined within AlPO-34 and SAPO-34 models containing 0 and 2 framework Si atoms, respectively. Al, P and O atoms are depicted as dark blue, pink, and red wires, respectively. Cu and Si atoms are depicted as dark copper-coloured and yellow balls, respectively.

The weak interaction between the Cu_5 cluster and the 0Si model is manifested in the large value of the shortest Cu-$O_{framework}$ distance, 2.262 Å. In contrast, the copper cluster interacts stronger with the framework of the 2Si model, forming five Cu-$O_{framework}$ bonds with distances 2.078, 2.118, 1.977, 1.996 and 2.008 Å, and adopting the 3D configuration.

To quantify the transfer of electron density between the zeotype framework, the embedded clusters and the adsorbed species, we use in this chapter the DDEC6 method explained in chapter 2 (§2.6.5), since the Bader method was found to be limited at calculating charge distribution in these zeotype systems. The total atomic charges on the Cu_5 clusters, on the framework M atom and on the adsorbed oxygen species are summarized in table 5.1.

Table 5.1 - Total atomic charges on Cu_5 clusters (qCu_5, in e), on adsorbed O_2 (qO_2, in e), and on the included framework atom (q_M) calculated with the DDEC6 method for the structures involved in O_2 dissociation on Cu_5 clusters stabilised within SSZ-13 zeolite and SAPO-34 zeotype.

	SSZ-13		SAPO-34	
Atom (M)	0Al	2Al	0Si	2Si
qCu_5	-0.055	0.895	-0.103	0.732
$qCu_{5\,(R)}$	0.270	1.082	0.518	1.088
$qCu_{5\,(TS)}$	0.685	1.462	0.926	1.488
$qCu_{5\,(P)}$	1.237	2.050	1.426	2.131
q_M	-	3.574	-	3.595
$q_{M\,(R)}$	-	3.531	-	3.595
$q_{M\,(TS)}$	-	3.532	-	3.598
$q_{M\,(P)}$	-	3.553	-	3.601
$qO_{2(R)}$	-0.441	-0.370	-0.653	-0.363
$qO_{2(TS)}$	-0.811	-0.726	-1.059	-0.739
$qO_{2(P)}$	-1.413	-1.229	-1.559	-1.264

Using this method to calculate the charge distribution, the copper clusters become negatively charged when they are stabilized within the neutral frameworks of SSZ-13 zeolite (-0.055 *e*) and especially of

AlPO-34 (-0.103 *e*). In contrast, the negative values turn into positive ones in SAPO-34 with 2Si atoms in the framework (0.732 *e*), slightly less charged than in the SSZ-13 zeolite with 2 framework Al atoms (0.895 *e*).

Then, the reaction mechanism for O_2 dissociation was investigated on the two systems, AlPO-34, and SAPO-34 with 2Si. The optimised structures are illustrated in figure 5.2 and all the relevant parameters of this step are summarised in table 5.2.

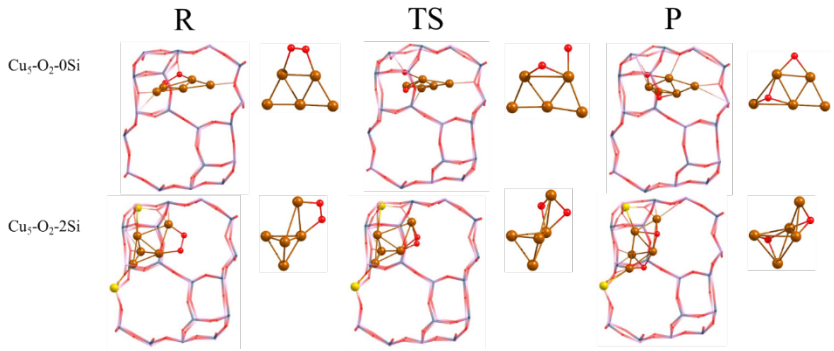

Figure 5.2 - Optimised structures of reactant (R) transition state (TS) and product (P) of the O_2 dissociation step on Cu_5-2D clusters confined within SAPO-34 models containing 0 and 2 framework Si atoms. Al, P and O atoms are depicted as dark blue, pink, and red wires, respectively. Cu, Si and O atoms are depicted as dark copper-coloured, yellow and red balls, respectively.

Table 5.2 - Optimised values of the OO distance (rOO, in Å), and calculated Gibbs adsorption (G_{ads}), activation (G_{act}) and reaction (ΔG) energies (in kJ/mol) for O_2 dissociation on Cu_5 clusters stabilised within SSZ-13 zeolite and SAPO-34 zeotype.

	SSZ-13		SAPO-34	
Atom (M)	0Al	2Al	0Si	2Si
$\mathbf{rOO_{(R)}}$	1.404	1.386	1.451	1.384
$\mathbf{rOO_{(TS)}}$	1.935	1.860	2.096	1.867
$\mathbf{rOO_{(P)}}$	3.359	3.505	3.597	3.593
$\mathbf{G_{ads}O_2}$	-210	-249	-236	-195
$\mathbf{G_{act}}$	145	103	90	111
$\mathbf{\Delta G}$	-217	-218	-266	-153

Starting with the AlPO-0Si model, the O_2 molecule is adsorbed at the short edge of the cluster forming 2 Cu-O bonds with a slightly bent O-O bond. As explained in (§4.2.2), the zeolite framework plays a role in the charge transfer from the catalyst to the π^* orbital of O_2. In the case of AlPOs, this effect is lightly reinforced, in the form of more positive copper atoms (0.5 vs 0.3 *e* in CHA-0Al) and more donation of electron density to the O-O bond (-0.6 vs -0.4 e in CHA-0Al). Notwithstanding, the calculated O-O distance is 1.451 Å, which is a more elongated bond than the 1.404 Å obtained for CHA-0Al.

In the transition state, a singular phenomenon occurs since a similar transition state structure has not been found so far. The O-O distance elongates to 2.096 Å in AlPO-0Si (vs 1.935 in CHA-0Al) and the transferred electron density reaches -1.1 *e*, again being more polarised than the ones for the CHA-0Al system (-0.8 *e*). Consequently, the activation barrier for the zeotype system is 95 $kJ \cdot mol^{-1}$, 39 $kJ \cdot mol^{-1}$ lower than the energy required for the analogous step in zeolite SSZ-13. However, this could be explained considering the hints that the SAPO-34 cage provides us. The O atom that only has one Cu-O bond is also linked to a framework Al atom at a distance of 1.901 Å, thereby transferring charge to the catalytic system and so, facilitating the O_2 dissociation step.

The resultant structure is similar to the one in the CHA-0Al system but with a different orientation within the cage, with an optimised O-O distance of 3.597 Å and an O_2 net charge value of -1.6 *e*. The O_2 dissociation step is marked with exothermic reaction energies of -266 $kJ \cdot mol^{-1}$ and equally strong adsorption energies of -236 $kJ \cdot mol^{-1}$.

Moving to the SAPO-2Si system, the differences in regard to the CHA-2Al system are not disproportionated. A strong O_2 adsorption energy of -195 $kJ \cdot mol^{-1}$ conducts to a distinct Cu_5-3D configuration in which the O_2 molecule is attached to two copper atoms in bridge mode, with an optimised O-O distance of 1.384 Å vs 1.386 Å in CHA-2Al and bearing a net atomic charge of -0.363 *e* (vs -0.370 *e* value in CHA-2Al).

To dissociate the adsorbed O_2 molecule, the system requires to overcome a barrier of 104 $kJ \cdot mol^{-1}$ (vs 93 $kJ \cdot mol^{-1}$ in CHA-2Al). The transition state is almost identical to the one found in its analogous SSZ-13 system but located in a different orientation, possessing a very similar O_2 net atomic charge (-0.739 *e* in SAPO-2Si vs -0.726 *e* in CHA-2Al)

Progressing through the reaction, the product consists of two three-coordinated O atoms at a distance of 3.597 Å bearing a net negative charge of -1.3 *e*, which implies that O atoms on Cu_5 clusters stabilised in SAPO-2Si are less charged than those in CHA-2Al.

5.2.2 MeAPO systems

In a similar way as in SAPO-34 with 2 Si atoms, when Cu_5-2D clusters are stabilised within the MeAPO-34 zeotypes considered in this work, their geometry evolves to a three-dimensional structure, forming different configurations of Cu_5-3D as depicted in figure 5.3. Hence, to save time and computational power, the stabilisation of Cu_5-3D clusters in MeAPO-systems was not carried out, and only the three-dimensional structure obtained for Cu_5-2D, labelled Cu_5 from now on, was further considered.

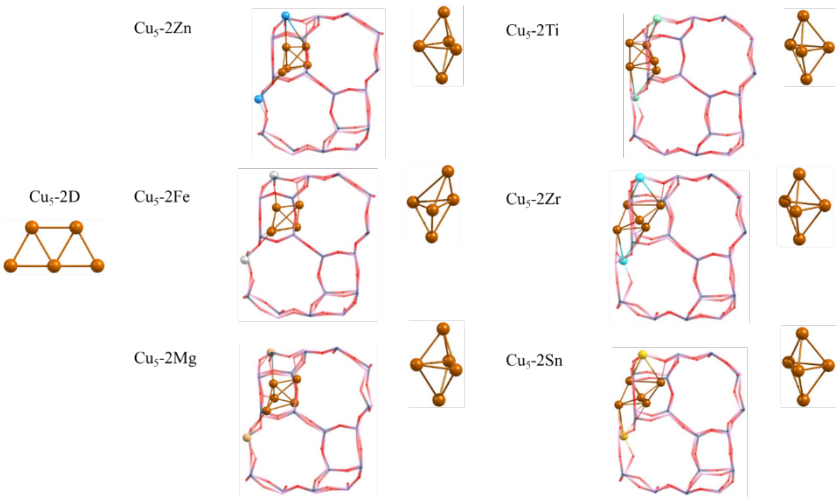

Figure 5.3 - Optimised structures of Cu_5-2D clusters, confined and isolated within MeAPO-34 models containing 2 framework M atoms (M = Zn, Fe, Mg, Ti, Zr, Sn). Optimised structure in gas phase is located at the left. Al, P and O atoms are depicted as dark blue, pink, and red wires, respectively. Cu, and O atoms are depicted as dark copper-coloured, yellow and red balls, respectively. Zn, Fe, Mg, Ti, Zr and Sn atoms are depicted as dark blue, light grey, carnation, turquoise, light blue and golden, respectively.

Regarding the total charge on the copper clusters, the values of qCu_5 gathered in table 5.3 reveal the following trend: Zn > Mg > Fe > Ti > Sn > Zr, manifesting a stronger electron density transfer in the tetravalent metal systems and a weaker charge exchange in divalent metal systems. These values also demonstrate that Fe atoms work with the oxidation state (II) in this case.

Table 5.3 - Total atomic charges on Cu_5 clusters (qCu_5, in e), on adsorbed O_2 (qO_2, in e), and on the included framework atom (q_M) calculated with the DDEC6 method for the structures involved in O_2 dissociation on Cu_5 clusters stabilised within different MeAPO frameworks.

	MeAPO					
Atom (M)	2Zn	2Fe	2Mg	2Ti	2Zr	2Sn
qCu_5	0.791	0.682	0.730	0.614	0.549	0.612
qCu_5 (R)	1.293	1.051	1.078	1.297	1.265	1.424
qCu_5 (TS)	1.561	1.355	1.480	1.469	1.538	1.663
qCu_5 (P)	2.145	2.043	1.956	2.106	2.022	2.056
q_M	2.222	1.953	2.990	4.056	4.433	3.659
q_M (R)	2.200	1.977	2.994	4.047	4.419	3.600
q_M (TS)	2.199	2.032	2.990	4.035	4.419	3.571
q_M (P)	2.213	2.050	2.998	4.091	4.457	3.678
qO_2(R)	-0.462	-0.439	-0.353	-0.590	-0.602	-0.612
qO_2(TS)	-0.745	-0.771	-0.730	-0.744	-0.878	-0.832
qO_2(P)	-1.275	-1.397	-1.179	-1.243	-1.213	-1.224

The species involved in the adsorption and dissociation of an O_2 molecule on Cu_5 clusters stabilized within the six different MeAPOs investigated in this section are depicted in figure 5.4, and the most relevant geometric parameters and calculated adsorption, activation and reactions Gibbs energies are summarized in table 5.4. It should be noted that of all the structures obtained are found in the doublet state expect those localised in the Fe-zeotype that are obtained with a spin value of 9.

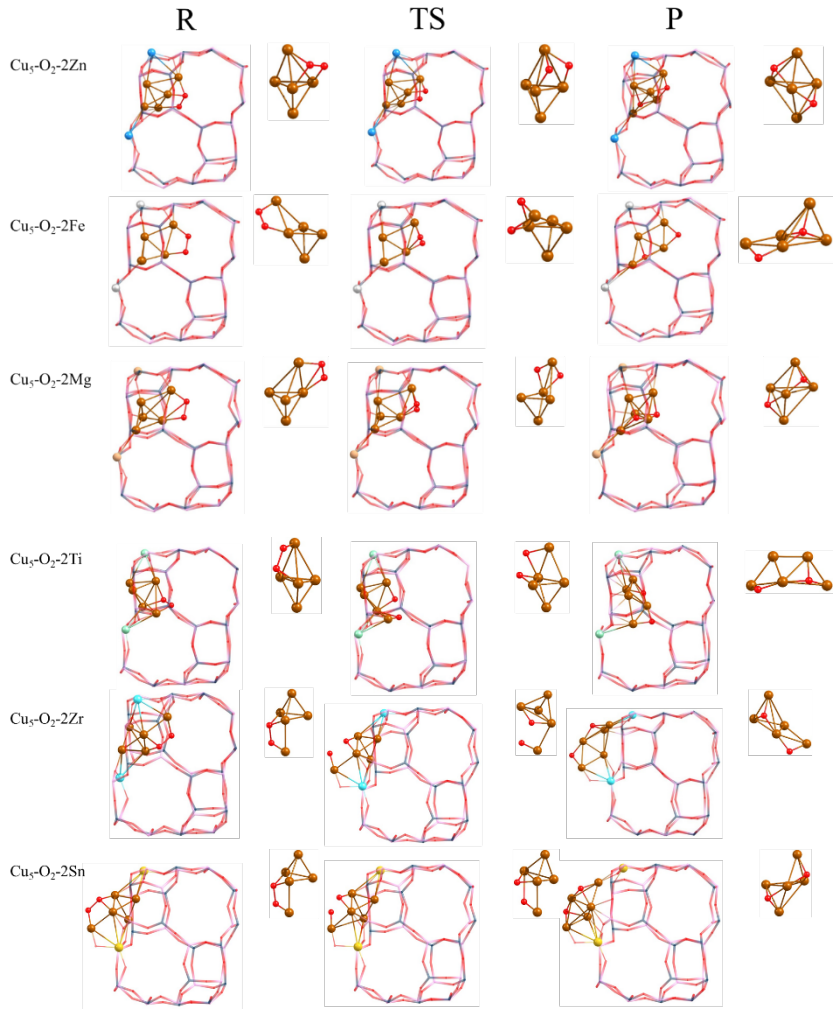

Figure 5.4 – Optimised structures for the O_2 dissociation step on Cu_5 clusters confined within MeAPO-34 models containing 2 framework M atoms (M: Zn, Fe, Mg, Ti, Zr, Sn). Al, P and O atoms are depicted as dark blue, pink, and red wires, respectively. Cu, and O atoms are depicted as dark copper-coloured and red balls, respectively. Zn, Fe, Mg, Ti, Zr and Sn atoms are depicted as dark blue, light grey, carnation, turquoise, light blue and golden, respectively.

Table 5.4 - Optimised values of the OO distance (rOO, in Å), and calculated Gibbs adsorption (G_{ads}), activation (G_{act}) and reaction (ΔG) energies (in kJ/mol) for O_2 dissociation on Cu_5 clusters stabilised within different MeAPO zeotypes.

Atom (M)	2Zn	2Fe	2Mg	2Ti	2Zr	2Sn
$\mathbf{rOO_{(R)}}$	1.448	1.406	1.382	1.498	1.499	1.500
$\mathbf{rOO_{(TS)}}$	1.927	1.891	1.871	1.852	1.980	1.905
$\mathbf{rOO_{(P)}}$	3.597	3.599	3.589	3.528	3.531	3.609
$\mathbf{G_{ads}\,O_2}$	-166	-190	-190	-166	-170	-163
$\mathbf{G_{act}}$	34	85	103	62	44	66
$\mathbf{\Delta G}$	-237	-230	-211	-133	-226	-247

When an O_2 molecule is introduced in the MeAPO zeotypes, it adsorbs strongly on the Cu_5 clusters with adsorption Gibbs energies greater than 160 $kJ \cdot mol^{-1}$, giving rise to the structures labelled as "R" in figure 5.4. For the reactant "R" there are two structures similar to the one obtained in the CHA-2Al model, which correspond to the Fe and Mg containing materials. In these two systems the O_2 molecule is adsorbed in a bridge mode at the edge of the cluster, while in all other cases O_2 adsorbs in a h-111 mode with one of the O atoms directly bonded to two Cu atoms.

In terms of electron density captured by O_2, in Zn and Fe-MeAPOs the qO_2 values are around -0.45 *e*, they decrease to -0.35 *e* in MgAPO, and Ti, Zr and Sn-containing materials show higher values about -0.6 *e*. This is translated into larger O-O bond lengths for tetravalent metals and shorter O-O distances for the divalent metals, with an excellent correlation between optimised O-O distances and net charge on O_2 (see figure 5.5A). Furthermore, the trend that could be inferred in CHA-2Al in which relates O_2 net atomic charges with Gibbs adsorption energies (§4.2.2) is also present in MeAPOs (figure 5.5B).

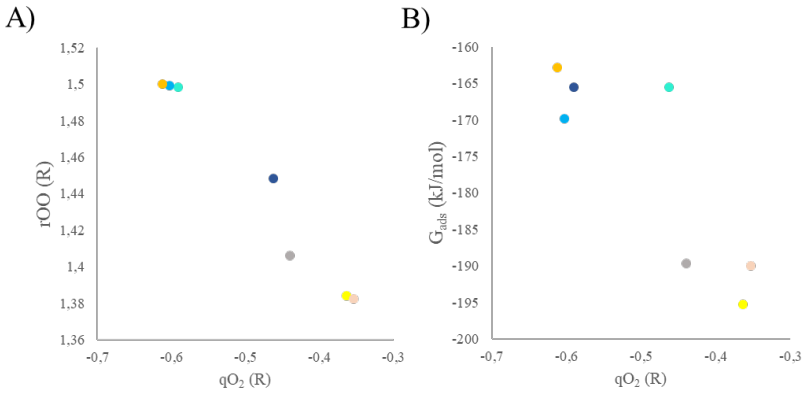

Figure 5.5 - Correlation between the optimised O-O bond length and the total charge of O_2 in R structures (A) and calculated adsorption Gibbs energy G_{ads} versus total charge of O_2 in R structures (B). The yellow, dark blue, grey, carnation, turquoise, blue, and golden points are referred to Si, Zn, Fe, Mg, Ti, Zr, and Sn systems, respectively.

Interestingly, there is a direct correlation between the electron density on O_2 in reactant species qO_2 (R) and the activation energies for O_2 dissociation (see figure 5.6), with the only exception of the ZnAPO system that exhibits the lowest activation energy, 34 $kJ \cdot mol^{-1}$. in comparison with the 93 $kJ \cdot mol^{-1}$ calculated for Cu_5 clusters within an SSZ-13 zeolite with two framework Al atoms (See figure 5.6A). Nevertheless, as expound on (§4.2.3), having a very low activation barrier for the O_2 dissociation step does not mean that a catalytic system is the best candidate for the MTM reaction, so these results must be prudently taken. For the remaining systems, the increased net charge on O_2 permits lower activation barriers with the exception of the Mg system, whose result aligns with the activation energy obtained in the SAPO.

In relation to the transition states, the O-O bond lengths range from 1.852 to 1.980 Å (see table 5.4. Excluding the Zr system, all of them exhibit two copper atoms sharing the same oxygen atom. Moreover, the obtained TS for the Mg system bears resemblance to that uncovered in the CHA-2Al system, and the transition states pertaining to the Zr and Sn systems share a very similar configuration. (See figure 5.4)

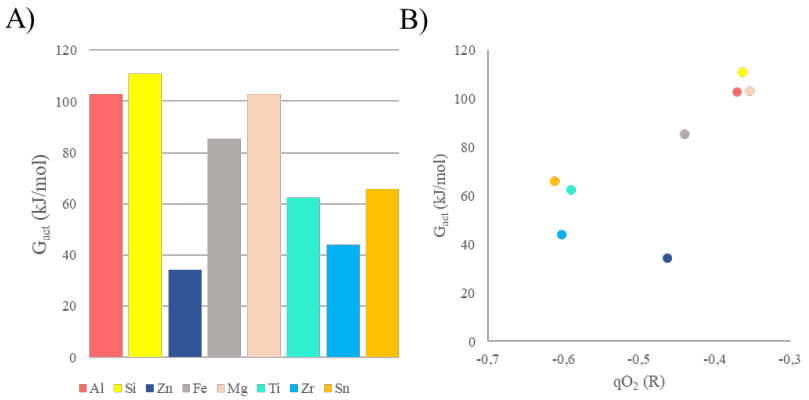

Figure 5.6 - Activation energy for O_2 dissociation on Cu_n clusters supported on different zeotypes (A) and correlation between the Gibbs activation energy G_{act} and total charge of O_2 in (R) structures (B). The yellow, dark blue, grey, carnation, turquoise, blue, and golden points in (B) are referred to Si, Zn, Fe, Mg, Ti, Zr, and Sn MeAPOs, respectively. The red bar and the red point for the CHA-2Al model are included for comparison.

The resultant products, labelled P, are prone to stabilise the O atoms either bicoordinated in Fe, Ti and Zr-zeotypes, three-coordinated as displayed in Zn, Mg, Ti, and Sn-containing systems, and four-coordinated, a new type of coordination not manifested before which is found in FeAPO and ZrAPO. Concerning the structure of the Cu_5 clusters, those in Zn, Mg and Sn-MeAPOs are quite similar to the Cu_5 structures uncovered in CHA-2Al, in FeAPO and ZrAPO they share a very similar structure except for the orientation in the CHA cage, and when stabilised in TiAPO, the clusters present the most unique configuration, preserving part of the planarity of the original Cu_5-2D cluster.

In relation to the total positive charge on Cu_5 clusters in the structures labelled P, it increases to values of ~2.1 *e*, slightly higher than those obtained in the CHA-2Al models, ~2.0 *e*. This is in line with the

calculated negative charges on the two O atoms, ranging from -1.1 to -1.4 *e* (see table 5.3), which in the case of CHA-2Al system is ~1.2 *e* (refer to table 5.2). Accordingly, MeAPOs offer a similar charge distribution between the metal cluster and the O atoms, but with lower activation barriers for the O_2 dissociation step and enhanced reaction energies (ΔG) ranging from -133 $kJ \cdot mol^{-1}$ for the TiAPO, to -247 $kJ \cdot mol^{-1}$ for the SnAPO. The Cu_5 positive charge order is Mg < Zr < Fe < Sn < Ti < Zn, whereas the negative charge on O_2 follows the order: Mg > Zr > Sn > Ti > Zn > Fe. The exact values are compiled in tables 5.1 and 5.3.

5.3 CH_4 activation over Cu_5-2O zeotype systems

In principle, based on the results obtained with Cu_5 clusters isolated and stabilized within CHA-2Al model, the most prominent candidates for the MTM reaction would be the ones with stabilised bicoordinated O atoms in its structure, in other words, Si, Fe, Ti and Zr-zeotypes. To confirm or refuse this hypothesis, the results obtained for the SAPO and the six MeAPOs investigated are described next.

5.3.1 SAPO system

The zeotype system with 2 framework Si atoms presents a promising pathway in which the presence of a methane molecule provokes the migration of one of the three-coordinated O atoms to one of the edges of the cluster (structure **2** in figure 5.7), resulting in a calculated O-H distance of 2.475 Å and a weaker interaction of 25 $kJ \cdot mol^{-1}$ in comparison with the 33 $kJ \cdot mol^{-1}$ achieved in the CHA-2Al model. Several attempts to obtain an adsorbed methane were carried out, all of them leading to the desorption of the molecule.

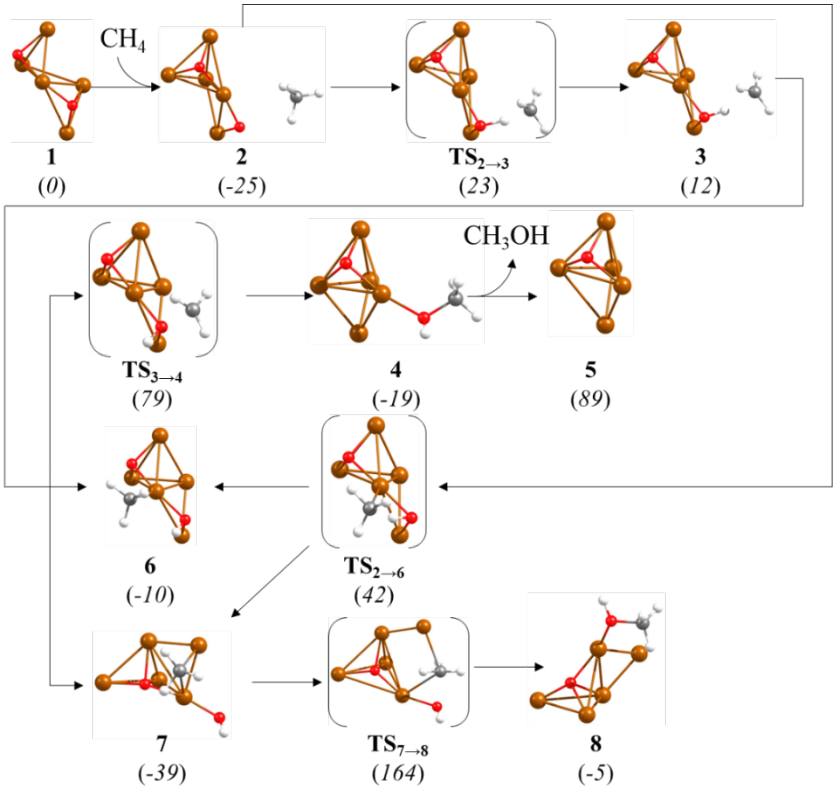

Figure 5.7 - Optimised geometries of minima and transition state structures involved in the oxidation of methane to methanol on a Cu_5-2O cluster supported on SAPO zeotype. Cu, O, C and H atoms are depicted as copper-coloured, red, grey, and white balls, respectively. Relative Gibbs energies at 478.15 K are given in brackets in $kJ \cdot mol^{-1}$. All the depicted structures are located in the doublet state.

Despite this, an extremely low activation barrier is found for the C-H dissociation step, requiring only 48 $kJ \cdot mol^{-1}$ to surpass the transition state. In this step, the configuration of **$TS_{2\rightarrow3}$** is practically the same except for the changes in C-H and O-H distances, being 1.407 and 1.158 Å, respectively. After this, structure **3** is generated with a methyl radical at a distance of 1.958 Å of the H atom bonded to the bicoordinated O atom. In order to achieve methanol, the O-H bond must rotate to maximise the interaction between the methyl fragment and the O atom,

bringing about a transition state with an optimised C-O distance of 1.973 Å and an activation barrier of 67 kJ·mol^{-1}, yielding structure **4** in the process. The desorption step to form structure **5** takes 108 kJ·mol^{-1}, which is the highest energy in this MTM pathway.

Nevertheless, from intermediate **3** there are multiple reaction paths that conduct to the mono-coordination and bi-coordination of the methyl radical (structures **6** and **7**, respectively). An alternative transition state was found that connects structures **2** and **6** through a monocoordinated methyl group with calculated C-H and Cu-C distances of 1.388 and 2.402 Å, respectively, and a Gibbs activation energy of 67 kJ·mol^{-1}, greater than the one through the radical TS. To form the most stable structure **7** from intermediate **3** a great deformation of the metal cluster is necessary to accommodate the bicoordinated methyl group with Cu-C distances of 2.222 and 1.964 Å. In addition, the transition state that connects minimum **7** with structure **8** is tremendously unstable, leading to an activation energy of 203 kJ·mol^{-1} that makes impossible the transformation of methane to methanol through this pathway. Therefore, the adsorption of the methyl moiety only entails greater activation barriers for the formation of methanol via reverse methyl desorption yielding **3** and subsequent reaction through $\mathbf{TS_{3\rightarrow4}}$, becoming 89 and 118 kJ·mol^{-1} from structures **6** and **7**, respectively.

5.3.2 ZnAPO System

The MTM process on the Zn system is displayed in figure 5.8, starting with the approach of the methane molecule creating structure **10** with an exothermic interaction energy of -31 kJ·mol^{-1}.

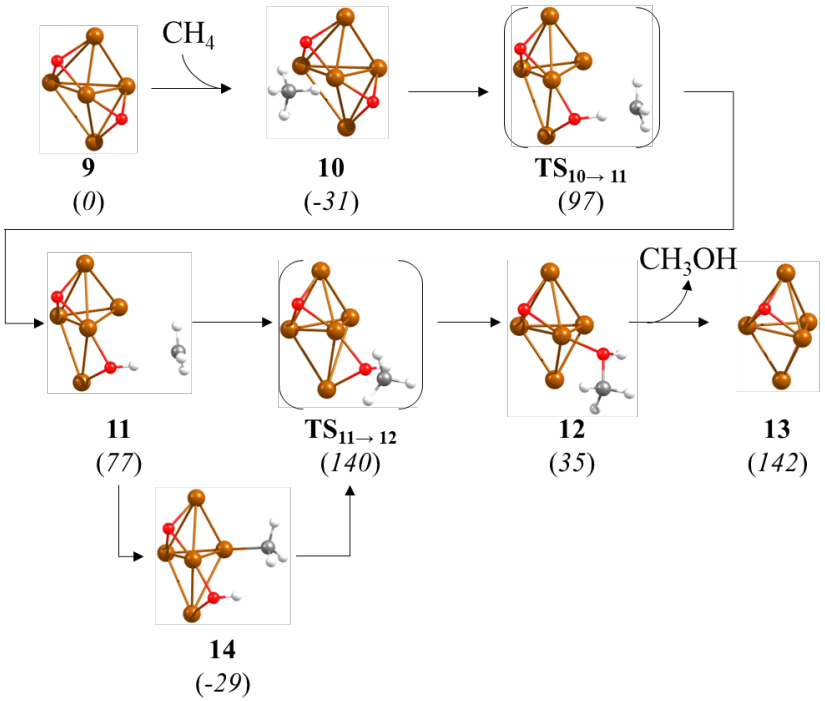

Figure 5.8 - Optimised geometries of minima and transition state structures involved in the oxidation of methane to methanol on a Cu_5-2O cluster supported on ZnAPO zeotype. Cu, O, C and H atoms are depicted as copper-coloured, red, grey, and white balls, respectively. Relative Gibbs energies at 478.15 K are given in brackets in kJ·mol^{-1}. All the structures are optimised in the doublet spin state.

To activate methane, the cluster acquires a more stretched shape in which one of the three-coordinated O atoms goes to one of the edges to reach the transition state **$TS_{10\rightarrow11}$** with an activation barrier of 128

kJ·mol^{-1}. As a result, the optimised C-H and O-H distances are 1.451 and 1.130 Å, respectively. The C-H bond dissociation produces a metastable radical-like intermediate **11** in which the C-H distance elongates to 1.951 Å whereas the O-H distance is stabilised in 0.997 Å. From this structure, the migration of the methyl group creates $\mathbf{TS_{11\rightarrow12}}$ with a calculated C-O distance of 2.066 Å, requiring 63 kJ·mol^{-1} to produce the anchored methanol in structure **12.** However, this activation barrier can increase if the methyl fragment in structure **11** is adhered to one of the copper atoms of the metal cluster, being structure **14** the most stable intermediate with a Cu-C bond length of 1.924 Å. From this point, the reaction might have issues since 169 kJ·mol^{-1} are necessary to overcome the transition state, which generates doubts about the viability of the process using this system. To desorb methanol, and therefore progress to structure **13**, the system needs 107 kJ·mol^{-1} to form a geometrically similar configuration to structure **5**, with one three-coordinated O atom remaining.

5.3.3 FeAPO System

The Fe system is characterised by a mix of spin states, in which spin values 9 and 7 are predominant over the rest. But only the spin value 9 will be treated with Gibbs energy values in this chapter since it is the most stable. For further details, check the Gibbs energies gathered in table A5.3 , §5.8. Returning to the FeAPO system, figure 5.9 illustrates the complete pathway for the MTM reaction.

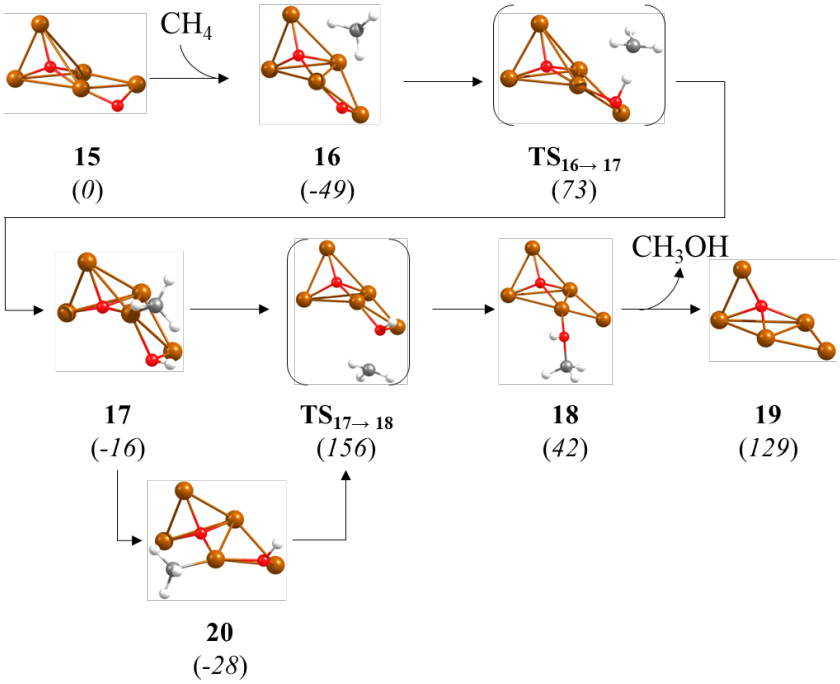

Figure 5.9 - Optimised geometries of minima and transition state structures involved in the oxidation of methane to methanol on a Cu_5-2O cluster supported on FeAPO zeotype. Cu, O, C and H atoms are depicted as copper-coloured, red, grey, and white balls, respectively. Relative Gibbs energies at 478.15 K are given in brackets in $kJ \cdot mol^{-1}$. All the structures are optimised in the spin value 9.

The introduction of a methane molecule in the catalytic system leads to structure **16** with a calculated adsorption energy of -49 kJ·mol^{-1} and with the shortest O-H distance being 2.536 Å. Despite possessing a bicoordinated O atom, the transition state to convert structure **16** into intermediate **17** (**$TS_{16\rightarrow17}$**) is less stable than the equivalent **$TS_{2\rightarrow3}$** obtained in the SAPO system. The activation energy to provoke the C-H bond breakage is 122 kJ·mol^{-1}, very close to the value obtained in the Zn zeotype, and the optimised C-H distance is 1.468 Å.

The intermediate formed after the C-H dissociation step, structure **17**, presents the migration of the methyl fragment to the copper atom bonded to the two O atoms of the metal cluster with a Cu-C bond length of 1.923 Å. If this radical is detached, it can interact with the OH group through transition state **$TS_{17\rightarrow18}$** to yield methanol, although the energy required to surpass it is unbelievably high, 172 kJ·mol^{-1}, which rules out the consideration of this system as a candidate for the MTM process. This step can even be worse if structure **17** is transformed into a slightly more stable structure **20**, which would mark an activation energy of 184 kJ·mol^{-1}. Finally, the methanol desorption step yielding structure **19** is endothermic by 87 kJ·mol^{-1}.

5.3.4 MgAPO System

Because of the earth alkaline nature of the framework Mg atom in MgAPO, the O atoms in the Cu_5-2O cluster in structure **21** (figure 12) are less negatively charged than in any other system (see table 5.3). When a CH_4 molecule was approached to one of the three-coordinated O atoms in the metal cluster forming structure **22** (see figure 5.10), the interaction was found to be weak despite having a Cu-C distance of 2.240 Å, which is shorter in comparison with Zn (3.158 Å) and Fe zeotypes (3.200 Å), giving a calculated adsorption energy of only -19 $kJ \cdot mol^{-1}$.

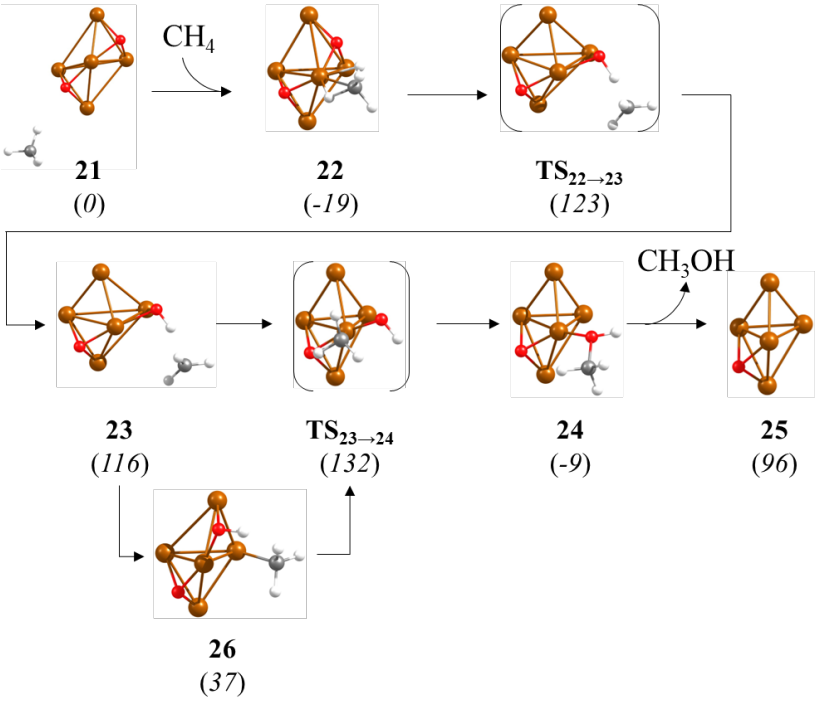

Figure 5.10 - Optimised geometries of minima and transition state structures involved in the oxidation of methane to methanol on a Cu_5-2O cluster supported on MgAPO zeotype. Cu, O, C and H atoms are depicted as copper-coloured, red, grey, and white balls, respectively. Relative Gibbs energies at 478.15 K are given in brackets in $kJ \cdot mol^{-1}$. All the structures are optimised in the doublet spin state.

Nevertheless, to reach the C-H bond dissociation transition state $\mathbf{TS_{22\rightarrow 23}}$, 142 kJ·mol^{-1} must be consumed, forming a structure with an equatorial OH group and a methyl radical. After this, the methyl radical is stabilised in a metastable structure **23** that can evolve through transition state $\mathbf{TS_{23\rightarrow 24}}$ to the methanol formation, needing only 16 kJ·mol^{-1}. This reaction path is not truthful, since the methyl radical in structure **23** can be adsorbed in the vicinal equatorial copper atom that does not have any bond with the O atoms anchored on the cluster, generating a much more stable structure **26**. From this structure, 95 kJ·mol^{-1} are required for the methanol formation. Lastly, desorption of methanol from structure **24** is endothermic by 105 kJ·mol^{-1}.

Therefore, the Mg system can be discarded from the list of potential systems to perform the MTM process due to its considerably high activation barriers.

5.3.5 TiAPO System

The planarity of the metal cluster in the TiAPO system presents a unique opportunity to uncover new chemistry in the MTM process. Furthermore, these materials have been synthesised in the past and used for different applications like photocatalysis, liquid-phase oxidation catalysis, solvent-free reactions and so on and so forth.[581–584] The elementary steps of MTM reaction catalysed by Cu_5 clusters in TiAPO zeotype are depicted in figure 5.11.

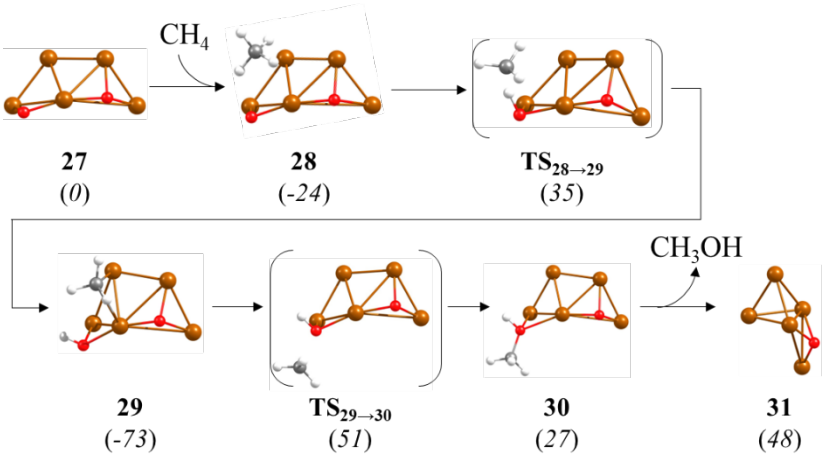

Figure 5.11 - Optimised geometries of minima and transition state structures involved in the oxidation of methane to methanol on a Cu_5-2O cluster supported on TiAPO zeotype. Cu, O, C and H atoms are depicted as copper-coloured, red, grey, and white balls, respectively. Relative Gibbs energies at 478.15 K are given in brackets in $kJ \cdot mol^{-1}$. All the structures are optimised in the doublet spin state.

As in all previous cases, by approaching a methane molecule to the metal cluster, the reactant does not interact with the active centre, generating structure **28** with the shortest O-H distance to the bicoordinated O atom being 2.608 Å. In order to activate methane, this system only requires 59 $kJ \cdot mol^{-1}$ to provoke C-H scission, which is a low value in comparison with the results achieved in the previous

chapter. In this transition state, the calculated C-H and O-H distances are 1.397 and 1.184 Å, respectively.

In the next intermediate the methyl fragment is stabilised with two Cu-C bonds of 2.309 and 1.989 Å, forming structure **29**, but despite that the activation energy to form adsorbed methanol is 124 $kJ \cdot mol^{-1}$, which is a very promising value for the worst scenario. Lastly, methanol is found bicoordinated to two copper atoms through the hydroxyl group (structure **30**), and the desorption energy is found in an extremely low value of 21 $kJ \cdot mol^{-1}$, generating structure **31**.

5.3.6 ZrAPO System

As the Fe system, ZrAPO possesses both four-coordinated and bicoordinated O atoms that could facilitate CH_4 activation. Given the chemical similarity between Ti and Zr, this system might achieve similar activation barriers to those observed in the TiAPO. The CH_4 activation step is pictured in figure 5.12.

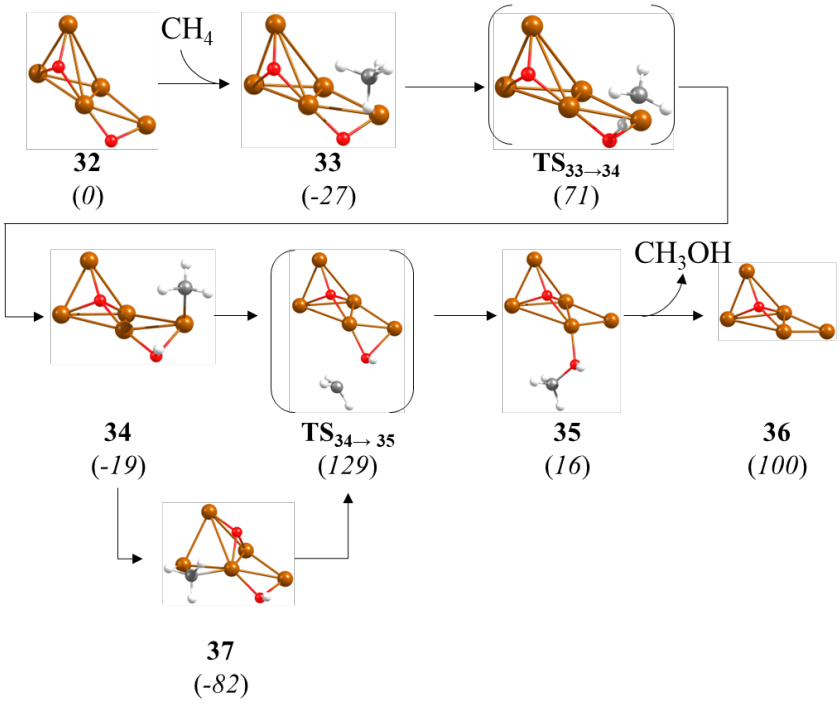

Figure 5.12 - Optimised geometries of minima and transition state structures involved in the oxidation of methane to methanol on a Cu_5-2O cluster supported on ZrAPO zeotype. Cu, O, C and H atoms are depicted as copper-coloured, red, grey, and white balls, respectively. Relative Gibbs energies at 478.15 K are given in brackets in $kJ \cdot mol^{-1}$. All the structures are optimised in the doublet spin state.

When the reactant is introduced in the ZrAPO catalyst model, structure **33** is created consisting of a weakly interacting methane molecule at a C-H distance of 2.537 Å from the bicoordinated O atom with a consequent stability of -27 $kJ \cdot mol^{-1}$. Advancing to the transition state here lies the first difference with respect to the Ti system, with an activation barrier of 98 $kJ \cdot mol^{-1}$ making it more similar to the energies uncovered for the CHA-2Al system (98 vs 102 $kJ \cdot mol^{-1}$). The resultant C-H and O-H distances are 1.423 and 1.165 Å, respectively.

The first intermediate after the C-H bond dissociation is structure **34**, with a methyl group monocoordinated to Cu at a Cu-C distance of 2.020 Å. To achieve methanol formation, 148 $kJ \cdot mol^{-1}$ are necessary, which marks another difference with the Ti system. Considering that structure **34** can be relaxed to structure **37** with a methyl bicoordinated species, the most realistic scenario reach activation barriers of 211 $kJ \cdot mol^{-1}$, discarding this system from the candidates for a feasible MTM reaction. Finally, structure **35** is generated after the transition state with a monocoordinated methanol that needs 84 $kJ \cdot mol^{-1}$ to be desorbed from the catalyst.

5.3.7 SnAPO System

Taking into account the Lewis activity of tin and the results obtained for the tetravalent metals in the MTM process, the CH_4 activation was also investigated in this system (figure 5.13)

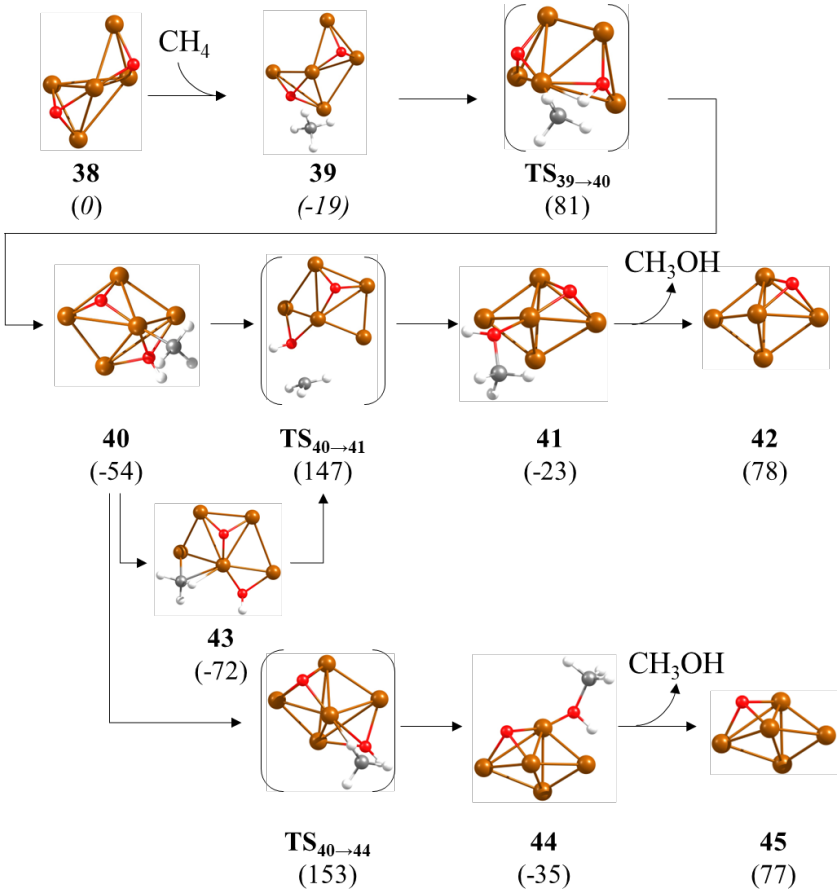

Figure 5.13 - Optimised geometries of minima and transition state structures involved in the oxidation of methane to methanol on a Cu_5-2O cluster supported on SnAPO zeotype. Cu, O, C and H atoms are depicted as copper-coloured, red, grey, and white balls, respectively. Relative Gibbs energies at 478.15 K are given in brackets in $kJ \cdot mol^{-1}$. All the structures are optimised in the doublet spin state.

As in the Zn system, which has similar geometric parameters, methane does not interact strongly with the metal cluster (structure **39**) approaching to one of the three-coordinated O atoms at a H-O distance of 2.319 Å. Nevertheless, the cluster acquires a more planar configuration in $\mathbf{TS_{39\rightarrow 40}}$ in which the active three-coordinated O atom is more displaced to the edges of its facet, resulting in C-H and O-H distances of 1.421 and 1.265 Å, respectively, and an activation energy of 100 $kJ \cdot mol^{-1}$. Once the hydroxyl group is formed, the methyl moiety is adsorbed in the central copper atom of the metal cluster, generating structure **40** with a Cu-C distance of 1.920 Å. From this point, three reaction pathways are possible: the first one is the direct formation of methanol through $\mathbf{TS_{40\rightarrow 41}}$, with a planar structure very similar to the one found in TiAPO, but with an extremely high barrier of 201 $kJ \cdot mol^{-1}$ and a C-O distance of 1.987 Å. The second pathway involves the bi-coordination of the methyl group creating structure **43**, which further increases the activation energy to a total of 219 $kJ \cdot mol^{-1}$. The alternative reaction path remaining entails a LH transition state ($\mathbf{TS_{40\rightarrow 44}}$) with an activation energy of 207 $kJ \cdot mol^{-1}$, which is not a great improvement in comparison with the other reaction paths. Thus, the SnAPO system is not relevant for the optimisation of the MTM process. At the end, structures **41** and **44** are formed with their respective adsorbed methanol, giving desorption energies of 101 and 112 $kJ \cdot mol^{-1}$, respectively.

5.3.8 Brief discussion of the CH_4 activation on Cu_5-2O-zeotype systems

Compiling all the energy profiles into one single plot (see figure 5.14), it is demonstrated that the CH_4 activation step on TiAPO and SAPO systems is more efficient than the CHA-2Al treated in the former chapter, achieving lower Gibbs energies to transform methane into methanol. For the rest of the systems, similar activation barriers are found for the C-H dissociation step for Zr and Sn systems, but regarding the methanol formation step, none of them achieve lower activation energies than the Al-containing zeolite.

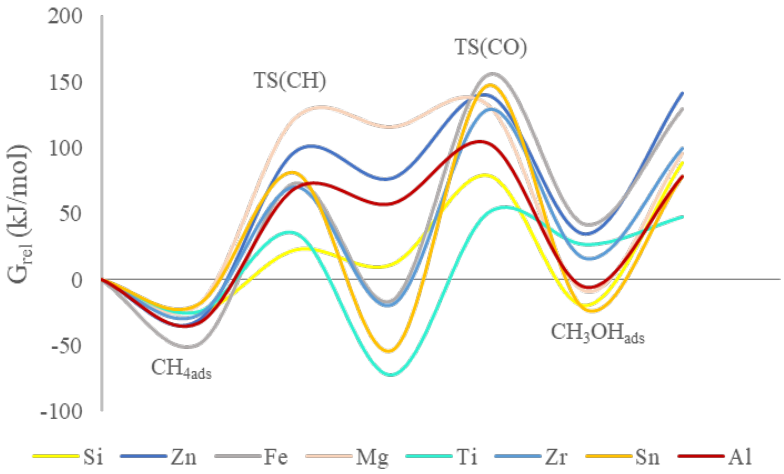

Figure 5.14 – Global scheme of the Gibbs energy profiles for the investigated zeotype systems. The transition states for methane C-H bond dissociation (TS(CH)) and C-O bond formation (TS(CO)) are indicated on the plots. Energy profile of the most favourable reaction path of the CHA-2Al system (reaction path A in §4.3) was plotted in red for comparison reasons.

In favour of the Ti zeotype system, the transition states to activate methane and to form methanol are at relative Gibbs energies of 35 and 51 $kJ \cdot mol^{-1}$, respectively, which correspond to activation Gibbs energy

barriers of 59 and 124 kJ·mol^{-1}, obtaining a very competitive path despite the formation of a bicoordinated methyl species as reaction intermediate. This must be primarily attributed to the planar cluster obtained in this system, which is also resistant to further oxidations as described in (§5.4), although in this subject CHA-2Al does not suffer the deformation of the metal cluster, which represents a more robust catalyst in the presence of O_2. Additionally, the Ti system possesses the lowest methanol desorption energy, 21 kJ·mol^{-1}, which limits the influence of the remaining O atom on the cluster to perform the methanol overoxidation, minimising the residence time of the product.

In relation to the SAPO system, it presents the smoothest Gibbs energy profile with relative Gibbs energies reaching 23 and 79 kJ·mol^{-1} for the C-H dissociation and methanol formation step, respectively. Furthermore, the hindrance due to the formation of the bicoordinated methyl species only entails an activation barrier of 118 kJ·mol^{-1}, which is still competitive for the MTM process, although the desorption energies are closer to the ones obtained for Zr and Mg systems, being the zeolite system superior in this case. In spite of the absence of O_2 saturation and competing processes simulations, these results position the SAPO system as a promising candidate to effectively transform methane into methanol, and future works must address the theoretical and experimental aspects that this dissertation could not contemplate.

5.4 Successive dissociation of O_2 molecules over Cu_5-TiAPO systems

The scope of this dissertation reached the O_2 saturation simulations with only the most promising zeotype system, as shown in figure 5.14. With that said, the further oxidations undergone in TiAPO system are illustrated in figure 5.15. To see full details of the relevant parameters in this step, consult table 5.5.

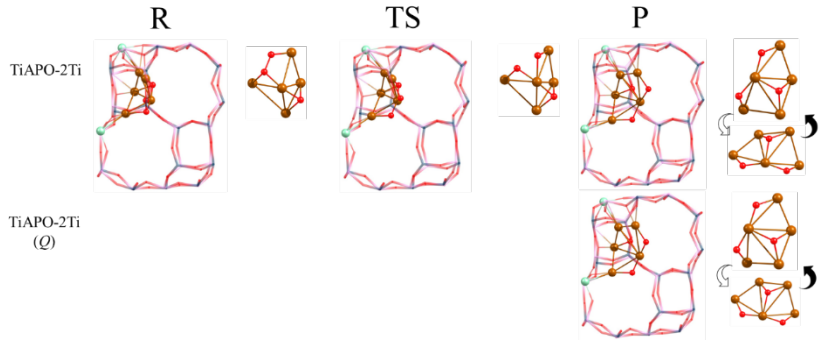

Figure 5.15 - Optimised structures for three O atoms adsorbed on Cu_5 clusters confined within TiAPO models containing 2 framework Ti. Framework Al, P and O atoms are depicted as dark blue, pink, and red wires, respectively, whilst Cu, Ti, and reactant O atoms are depicted as dark copper-coloured, turquoise, and red balls, respectively.

When a new O_2 molecule is introduced to the Cu_5-O structure resulting from the MTM reaction over TiAPO system illustrated in figure 5.11 (structure **31**), a very similar reaction path as the one in CHA-2Al is found (§4.2.4.1). The added O_2 molecule is adsorbed very exothermically in the opposed facet with an adsorption energy of 121 $kJ \cdot mol^{-1}$, giving rise to a more planar structure with an optimised O-O bond length of 1.448 Å and a total positive charge on the copper cluster of 1.8 *e* (see table 5.5), being a less polarised system than the CHA-2Al model atoms.

In this configuration, the transition state adopts a slightly different shape in which the recently introduced O atoms form two Cu-O bonds at the edges of the cluster, resulting in a O-O distance of 1.815 Å with is subsequent change in the O_2 charge density, evolving from -0.5 *e* in the labelled "R" product to -0.7 *e* in the transition state, needing less charge to dissociate O_2, which is surprising considering that only 45 $kJ \cdot mol^{-1}$ are required to overcome this transition state. This is probably owing to the lower stability of the R structure, which permits a better O_2 dissociation.

After the transition state, the generated Cu_5-3O is simultaneously encountered in two distinct spin states, doublet (*D*) and quadruplet (*Q*) which is in accordance with the results uncovered in the CHA-2Al system. Once again, the quadruplet state manifests a larger charge density over the O atoms and longer O-O distances. This time, the exothermic reaction energies are practically equal for the *D* and *Q* state, being 80 and 84 $kJ \cdot mol^{-1}$, respectively.

Table 5.5 - Total atomic charges on adsorbed O_2 (qO_2, in e), optimised values of the O-O distance (r_{O-O}, in Å) in structures R, TS and P involved in O_2 dissociation, and calculated Gibbs adsorption (G_{ads}), activation (G_{act}) and reaction (ΔG) energies (in $kJ \cdot mol^{-1}$) for O_2 dissociation on Cu_5-clusters over the TiAPO system.

Framework	TiAPO
System	Cu_5-O
qCu_n (R)	1.871
qCu_n (TS)	2.135
qCu_n (P)	2.891/ 2.951[a]
qO_2 (R)	-0.500
qO_2 (TS)	-0.714
qO_2 (P)	-1.355/ -1.384[a]
qM (R)	4.073
qM (TS)	4.086
qM (P)	4.109/ 4.110[a]
r_{O-O} (R)	1.448
r_{O-O} (TS)	1.815
r_{O-O} (P)	3.412/ 3.488[a]
G_{ads}	-121
G_{act}	45
ΔG	-80/ -84[a]

[a]Quadruplet spin state (Q).

Additionally, the overoxidation of Cu_5-2O clusters was investigated in order to confirm the catalytic system resistance. In this case, the Cu_5 oxidation resistance nature is manifested when it is exposed to new O_2 molecules, although on this occasion h-111 adsorptions appear, able to dissociate O_2 if the reaction conditions were suitable. Fortunately, the most stable adsorption mode corresponds to a mono adsorption, which is at least 54 $kJ \cdot mol^{-1}$ more stable than the other configurations, in contrast to the structures uncovered in CHA-2Al, demonstrating that TiAPO systems prevent the overoxidation to Cu_5-4O systems (see figure 5.16).

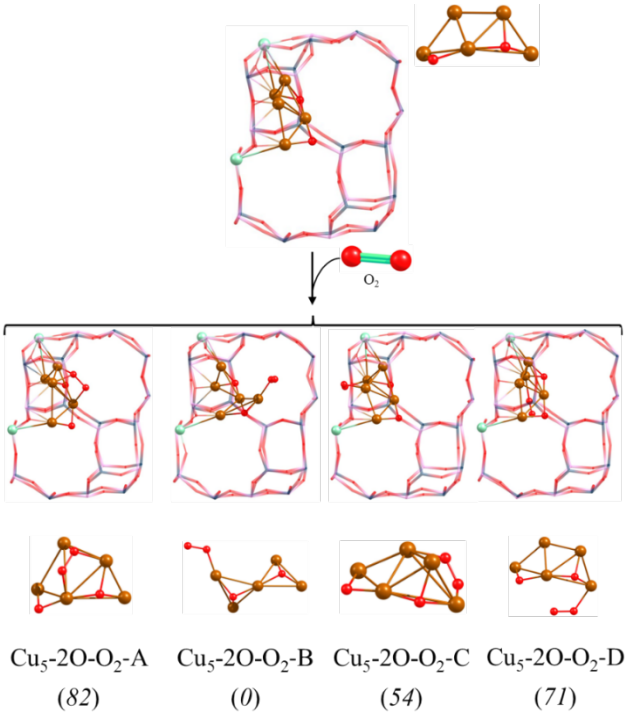

Figure 5.16 - Possible O_2 adsorptions on Cu_5-2O cluster confined within a TiAPO model containing 2 framework Ti atoms. Al, P and O atoms are depicted as dark blue, pink, and red wires, respectively, whilst Cu, Ti, and reactant O atoms are depicted as dark copper-coloured, turquoise, and red balls, respectively. Relative Gibbs energies at 478.15 K are given in brackets in $kJ \cdot mol^{-1}$.

5.5 CH_4 activation over Cu_5-3O TiAPO systems

The elementary steps of the MTM reaction catalysed by Cu_5-3O clusters in TiAPO systems are illustrated in figure 5.17.

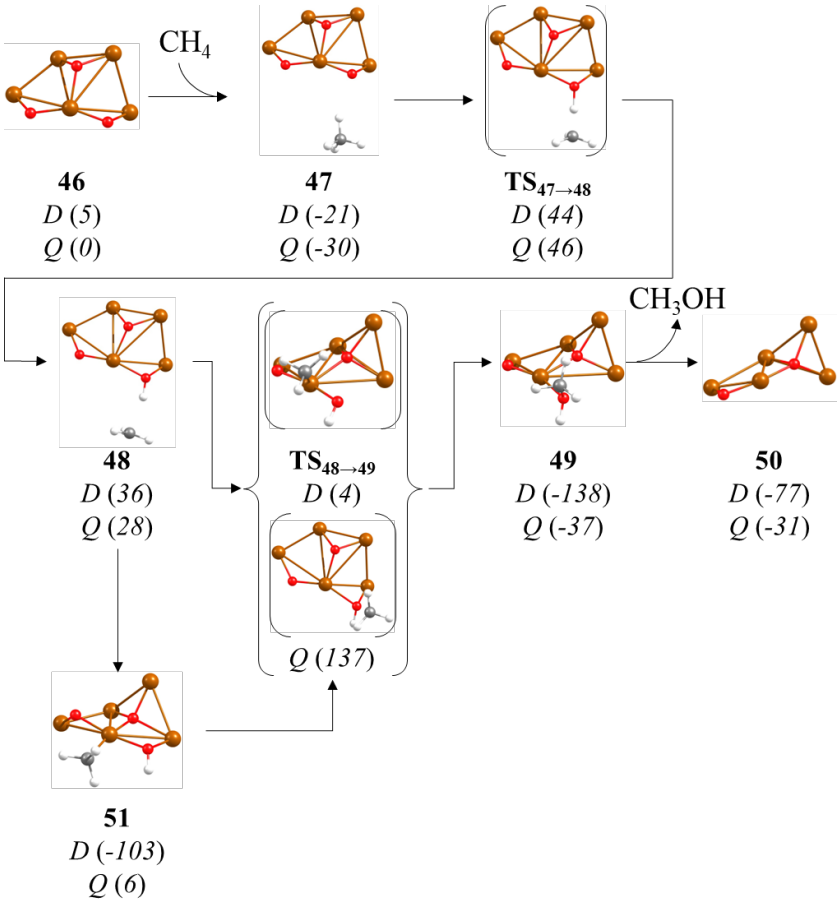

Figure 5.17 - Optimised geometries of minima and transition state structures involved in methane oxidation on Cu_5-3O clusters supported on TiAPO zeotype. Cu, reactant O, C and H atoms depicted as copper-coloured, red, grey, and white balls, respectively. Relative Gibbs energies at 478.15 K for doublet (*D*) and quadruplet (*Q*) spin states are given in brackets in kJ/mol.

Structure **46**, as the result of the consecutive O_2 dissociation described in figure 5.15 (§5.4) gets stabilised when a new methane molecule is introduced in the catalytic system, creating structure **47**. Notice that the *Q* surface is slightly more stable than the *D* surface, with exothermic adsorption energies of 30 and 21 kJ·mol^{-1}, respectively. The shortest O-H distance is 2.459 Å. In order to surpass the transition state and provoke C-H bond breakage, activation energies of 65 and 76 kJ·mol^{-1} are achieved for *D* and *Q* surfaces, respectively with very subtle geometric changes, requiring slightly higher energies than in the Cu_5-2O system due to the greater instability of $\mathbf{TS_{47\rightarrow48}}$. This time, the C-H and O-H distances measure 1.404 and 1.156 Å, respectively for the doublet state whilst the same distances are 1.406 and 1.160 Å, respectively for the quadruplet.

The immediate intermediate **48** is barely stabilised with the methyl radical at 2.004 Å respect to the hydroxyl group, and the next step to produce methanol needs a severe reconfiguration of the metal cluster in the doublet state, surprisingly giving a transition state $\mathbf{TS_{48\rightarrow49}}$ that acts as a barrierless step with Cu-C and C-O distances of 2.109 and 1.850 Å, respectively. The *Q* reaction path, however, has a considerable barrier of 109 kJ·mol^{-1} with Cu-C and C-O distances being 3.481 and 1.854 Å, respectively, acquiring a similar configuration to structure **48**. Notwithstanding, this reaction path is unrealistic considering that structure **48** can evolve to structure **51**, acquiring a more similar configuration to the methanol formation transition state with the Cu-C distance measuring 1.934 Å and a very strong stabilisation of the doublet intermediate respect to the quadruplet one. From this structure, 107 kJ·mol^{-1} are consumed to generate the adsorbed methanol in structure **49**, preserving the four-coordinated O atom formed in structure **51**, demonstrating that the TiAPO system is able to turn methane into methanol using the *D* spin surface as opposed to the uncovered reaction path in CHA-2Al, in which at least one of the crucial transition states must pass through the higher spin state. Lastly, 61 and 6 kJ·mol^{-1} are required for the desorption of the product in the *D* and *Q* surfaces, respectively, creating structure **50**.

Taking into consideration the entire Gibbs energy profile for both Cu_5-2O and Cu_5-3O systems, it entails a subtle improvement of 7 $kJ \cdot mol^{-1}$ in terms of relative Gibbs energy in comparison with the Cu_5-2O system through the *D* surface, but a promising performance when it is compared to the CHA-2Al zeolite, with the highest relative Gibbs energy being 44 $kJ \cdot mol^{-1}$, again in the doublet state (figure 5.18).

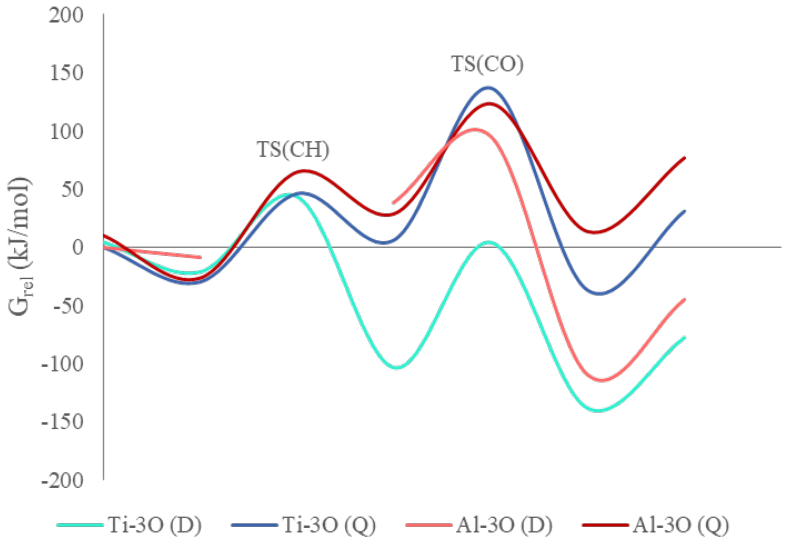

Figure 5.18 - Comparison scheme of the Gibbs energy profiles for the MTM process over Cu_5-3O systems within TiAPO zeotype and CHA-2Al zeolite. The transition states for methane C-H bond dissociation (TS(CH)) and C-O bond formation (TS(CO)) are indicated on the plots.

Although this fact does not necessarily mean that the reaction pathway through Cu_5-3O systems will be more beneficial respect to the zeolite system since it suggest a likely formation of methoxy species to a greater extent and CH_2 species to a lesser extent in structure **51**.

5.6 Competitive Processes on Cu_5-2O TiAPO system

As described in previous chapters, the main competing route in the oxidation of methane to methanol is the formation of methoxy species by reaction of methyl intermediates with adsorbed O atom. This possibility has been studied on Cu_5-2O clusters supported on TiAPO systems, yielding the results illustrated in figures 5.19 and 5.20.

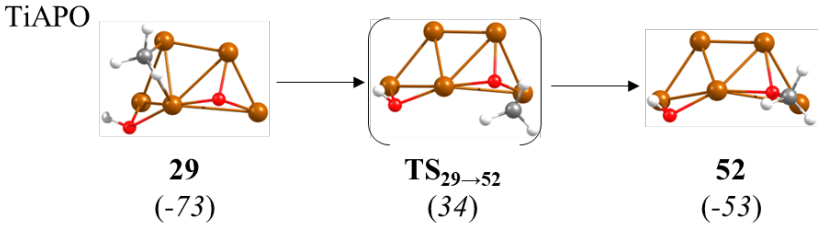

Figure 5.19 - Optimised geometries of minima and transition state structures involved in competitive processes on Cu_5-2O clusters supported on TiAPO zeotype, involving methoxy formation from adsorbed methyl intermediates. Cu, reactant O, C and H atoms are depicted as copper-coloured, red, grey, and white balls, respectively. Relative Gibbs energies at 478.15 K given in brackets in kJ/mol. All the structures are optimised in the doublet spin state.

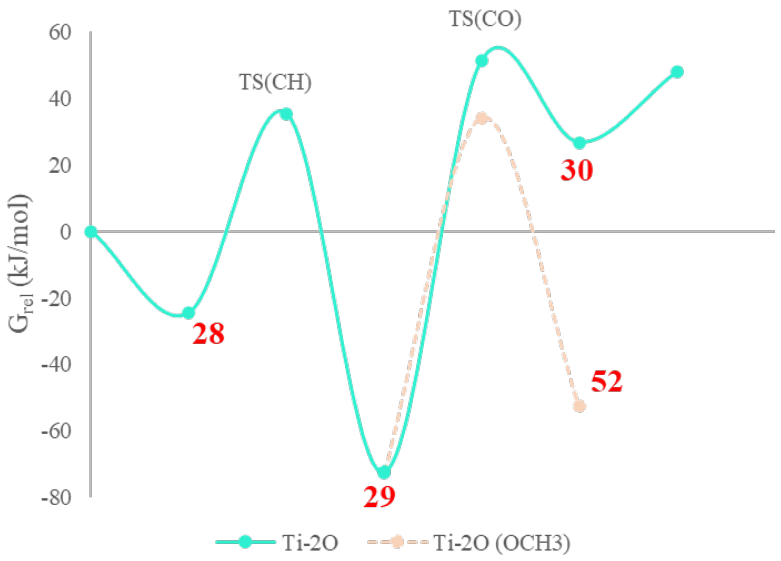

Figure 5.20 - Calculated Gibbs energy profiles at 478.15 K for methane oxidation and methoxy formation on Cu_5-2O clusters supported on TiAPO zeotype. The transition states for methane C-H bond dissociation [TS(CH)] and C-O bond formation [TS(CO)] are indicated on the plots. The red numbers correspond to some relevant structures involved in the mechanisms.

In the same manner as CHA-2Al, the small size of the Cu_5 cluster provokes that the adsorbed bicoordinated methyl group is close to the co-adsorbed O atom at a C-O distance of 3.183 Å, much closer than in the zeolite system (§4.4). The methoxy formation reaction is endothermic by 20 kJ·mol^{-1} and involves an activation energy of 107 kJ·mol^{-1}, slightly lower than the 124 kJ·mol^{-1} obtained for the desired formation of methanol through $TS_{29\rightarrow30}$. Therefore, TiAPO system also suffers from the direct competition of undesired processes, and more experiments must be carried out in future investigations to know the behaviour of this catalytic system in harsher reaction conditions.

5.7 Conclusions

The present computational study demonstrates that the stabilisation of Cu_5 clusters within metal-containing zeotypes SAPO and MeAPO (Me = Zn, Fe, Mg, Ti, Zr, Sn) modifies their charge and morphology, and therefore their reactivity towards O_2. The localised electron density on the Cu_5 clusters and O_2 in the O_2 dissociation step follows the same principles as in the SSZ-13 zeolite treated in the former chapter, incrementing the positive charge on copper atoms, and rising the negative charge on O atoms along the reaction coordinate. Nevertheless, the activation barriers obtained for O_2 dissociation reflect a general improvement except for Si and Mg systems, with values ranging from 34 to 111 $kJ \cdot mol^{-1}$. In addition, further oxidation simulations over TiAPO-2O proved that the successive adsorption and dissociation of additional O_2 molecules is unlikely but it entails a reconfiguration of the metal cluster, whilst TiAPO systems with one anchored O atom adopt similar configurations to the ones presented in CHA-2Al, promoting CH_4 activation, stabilising the metallic oxidation state, and revealing the robustness of these catalytic systems in contact with O_2.

The mechanism of the selective oxidation of methane to methanol has been theoretically investigated using periodic DFT calculations. The stabilised Cu_5-2O system optimally undergo the dissociation of methane C-H bond and the formation of adsorbed methanol through an Eley-Rideal mechanism, just as reported in the SSZ-13 zeolite model. Among the studied systems, the formation of mono and bicoordinated methyl groups is inevitable; still, two systems stand out because of their lower Gibbs activation energies compared to the zeolite system, SAPO and TiAPO zeotypes, being both of them below 80 $kJ \cdot mol^{-1}$, although slightly better desorption energies were found in chabazite respect to the SAPO system. In this respect, the TiAPO system exhibits the lowest methanol desorption energy found so far in this dissertation, 21 $kJ \cdot mol^{-1}$. The rest of zeotype systems reflected less efficiency to transform methane into methanol in the methanol formation step. Furthermore, higher O_2 coverage on the Ti system not only involves lower Gibbs relative energies, but also is able to proceed with the reaction in the

doublet state more efficiently than in quadruplet state, quite the contrary to the achieved results for the SSZ-13 zeolite.

To conclude, this chapter uncovered two promising candidates for the MTM chemical reaction on Cu_5 clusters that improves the results reported in CHA-2Al: SAPO and TiAPO zeotypes. If this investigation is expanded in the future, experimental works might confirm the promising features to perform this reaction in a more sustainable way.

5.8 Appendix

Table A5.1 - Relative energies (E_{rel}) and Gibbs energies (G_{rel}) in kJ/mol for all the structures involved in the selective methane oxidation on Cu_5-2O clusters on the SAPO system. Optimised structures depicted in figure 5.7.

Structure	E_{rel} (kJ/mol)	G_{rel} (kJ/mol)
1 + CH_4	0	0
2	-34	-25
TS(2→3)	22	23
3	11	12
TS(3→4)	72	79
4	-34	-19
5 + CH_3OH	84	89
6	44	42
TS(2→7)	-32	-10
7	-49	-39
TS(7→8)	144	164
8	-30	-5

Table A5.2 - Relative energies (Erel) and Gibbs energies (Grel) in kJ/mol for all the structures involved in the selective methane oxidation on Cu_5-2O clusters on the ZnAPO system. Optimised structures depicted in figure 5.8.

Structure	E_{rel} (kJ/mol)	G_{rel} (kJ/mol)
9 + CH_4	0	0
10	-27	-31
TS(10→11)	94	97
11	87	77
TS(11→12)	143	140
12	22	35
13 + CH_3OH	141	142
14	-34	-29

Table A5.3 - Relative energies (Erel) and Gibbs energies (Grel) in kJ/mol for all the structures involved in the selective methane oxidation on Cu_5-2O clusters on the FeAPO system with spin values 9 and 7. Optimised structures depicted in figure 5.9

	Spin 9		Spin 7	
Structure	E_{rel} (kJ/mol)	G_{rel} (kJ/mol)	E_{rel} (kJ/mol)	G_{rel} (kJ/mol)
15 + CH_4	0	0	22	26
16	-27	-49	-5	8
TS(16→17)	62	73	64	68
17	-35	-16	-29	3
TS(17→18)	121	156	121	139
18	7	42	9	38
19 + CH_3OH	112	129	119	133
20	-49	-28	-39	-18

Table A5.4 - Relative energies (Erel) and Gibbs energies (Grel) in kJ/mol for all the structures involved in the selective methane oxidation on Cu_5-2O clusters on the MgAPO system at the spin value 9. Optimised structures depicted in figure 5.10.

Structure	E_{rel} (kJ/mol)	G_{rel} (kJ/mol)
21 + CH_4	0	0
22	-31	-19
TS(22→23)	123	123
23	114	116
TS(23→24)	112	132
24	-38	-9
25 + CH_3OH	88	96
26	30	37

Table A5.5 - Relative energies (Erel) and Gibbs energies (Grel) in kJ/mol for all the structures involved in the selective methane oxidation on Cu5-2O clusters on the TiAPO system. Optimised structures depicted in figures 5.11 & 5.19.

Structure	E_{rel} (kJ/mol)	G_{rel} (kJ/mol)
27 + CH_4	0	0
28	-32	-24
TS(28→29)	36	35
29	-81	-73
TS(29→30)	48	51
30	-6	27
31 + CH_3OH	50	48
TS(29→52)	31	34
52	-65	-53

Table A5.6 - Relative energies (Erel) and Gibbs energies (Grel) in kJ/mol for all the structures involved in the selective methane oxidation on Cu_5-2O clusters on the ZrAPO system. Optimised structures depicted in figure 5.12.

Structure	E_{rel} (kJ/mol)	G_{rel} (kJ/mol)
32 + CH_4	0	0
33	-29	-27
TS(33→34)	56	71
34	-42	-19
TS(34→35)	98	129
35	-9	16
36 + CH_3OH	85	100
37	-103	-82

Table A5.7 - Relative energies (Erel) and Gibbs energies (Grel) in kJ/mol for all the structures involved in the selective methane oxidation on Cu_5-2O clusters on the SnAPO system. Optimised structures depicted in figure 5.13.

Structure	E_{rel} (kJ/mol)	G_{rel} (kJ/mol)
38 + CH_4	0	0
39	-38	-19
TS(39→40)	44	81
40	-68	-54
TS(40→41)	130	147
41	-61	-23
42 + CH_3OH	66	78
43	-89	-72
TS(40→44)	143	153
44	50	77
45 + CH_3OH	65	77

Table A5.8 - Relative energies (E_{rel}) and Gibbs energies (G_{rel}) in kJ/mol for all the structures involved in methane oxidation on Cu_5-3O clusters on TiAPO system. Optimised structures depicted in figure 5.17.

Structure	E_{rel} (kJ/mol)		G_{rel} (kJ/mol)	
	D	Q	D	Q
46 + CH_4	0	1	5	0
47	-30	-28	-21	-30
TS(47→48)	41	45	44	46
48	29	32	36	28
TS(48→49)	-7	124	4	137
49	-158	-53	-138	-37
50 + CH_3OH	-83	25	-77	31
51	-135	-11	-103	6

Chapter 6
Conclusions

In this chapter, the concluding remarks of this dissertation will be presented to provide an overview of the achievements resulting from the efforts invested in the direct MTM subject area.

This dissertation displays a complete and thorough study of the direct methane-to-methanol reaction catalysed by sub-nanometre copper clusters formed by 5 and 7 copper atoms with different morphologies (2D and 3D) employing computational chemistry methodologies.

Firstly, a preliminary study was conducted in gas phase to elucidate the main pathways implicated in this reaction and to identify the different issues the reaction must tackle in each step to convert methane into methanol. In O_2 dissociation, cluster morphology plays an important role when stabilising O atoms, since 2D clusters favour the stabilisation of bicoordinated O atoms in contrast to 3D clusters that preferentially stabilise three-coordinated O atoms at their facets.

Two reaction mechanisms were explored, Langmuir-Hinshelwood (LH) and Eley-Rideal (ER), in which the C-H bond scission is assisted by adsorbed O atoms resulting in the formation of a hydroxyl group and an adsorbed methyl or a methyl radical, respectively, that must recombine in a second step to produce methanol. The ER pathway fosters smoother Gibbs energy profiles when bicoordinated O atoms at the edges of the cluster are available, whereas LH pathway with the intrinsic high stability of the hydroxyl and methyl intermediates makes their recombination energetically inaccessible. Nevertheless, the formation of a methoxy intermediate by reaction of adsorbed O with methyl is energetically affordable in both paths, and its subsequent recombination to produce methanol is again kinetically forbidden, therefore adsorption of the reactant must be avoided to the extent possible.

Moreover, further oxidation simulations in Cu_5 and Cu_7 clusters demonstrated that a higher O_2 coverage is not detrimental for the process and involves an increase in functional active sites and the possibility of yielding methanol with a combination of multiple spin surfaces, but these metal clusters are very sensitive to O_2 concentration, and Cu_n-4O species are generated in more saturated O_2 flows. Additionally, these reaction paths avoid the formation of bicoordinated

methyl groups, but the generation of monocoordinated and methoxy groups on the catalyst surface is still present.

Secondly, the copper clusters were translated to an SSZ-13 framework with an increasing amount of framework Al atoms up to 2 to analyse the changes in charge, morphology, and reaction paths in comparison with the observed behaviour in gas phase.

It was found that the total positive charge on the Cu_n clusters increases with the number of Al atoms in the zeolite framework, and the O_2 dissociation step that result in two O atoms on the cluster surface requires an additional transfer of electron density from the catalyst to the O_2 and O species, leaving the Cu_n clusters highly positively charged after the reaction takes place. Consequently, deep oxidation of zeolite supported Cu_n clusters by successive adsorption and dissociation of additional O_2 molecules was proved to be unlikely, which can be exploited to stabilise catalytic systems with metallic oxidation state under oxidising conditions, which is necessary for some challenging reactions.

Thanks to the high stability against deep oxidation of these clusters, the dissociation of the methane C-H bond and desorption of the methanol formed is facilitated, making difficult its over-oxidation to CO_2. As in the isolated Cu_n clusters in gas phase, the reaction path proceeding through a radical-like non-adsorbed methyl intermediate is the most efficient, allowing to close the catalytic cycle with Gibbs activation energies lower than 115 kJ/mol, of the same order as those reported experimentally for Cu-exchanged zeolites.[371,524] Furthermore, higher spin states proved to be essential for the chemical reaction, as they enable methane activation in high O coverage systems reducing the H transfer transition state and therefore, improving the process overall by enhancing methanol formation. In addition, it was demonstrated that Cu_7 clusters are not suitable for the MTM chemical reaction since they suffer from the formation of bicoordinated methyl groups with its associated high stability and when the system possesses three O atoms anchored on its surface, it is prone to dissociate C-H bonds of the methyl

group, leading to CH_2 species which on the other hand, are completely evaded in Cu_5 clusters.

Finally, taking into account the results obtained in the SSZ-13 model, the study of Cu_5 clusters was expanded to metal-containing zeotypes SAPO-34 and MeAPO-34 (Me = Zn, Fe, Mg, Ti, Zr, Sn) to explore analogous systems that could potentially foster enhancements to the MTM process in terms of reaction mechanisms and Gibbs activation energies.

In the O_2 dissociation step, all the systems presented similar charge distributions as in the SSZ-13 model with small variations depending on the incorporated metal; Cu_5 clusters increased their total positive charge and O atoms accumulated increasing amounts of electron density along the reaction coordinate. Despite this fact, lower Gibbs activation barriers were found for every zeotype system in comparison with the zeolite framework except for SAPO-34 and MgAPO-47, with values ranging from 34 to 111 $kJ \cdot mol^{-1}$.

Additionally, the uncovered MTM reaction mechanisms followed the same trends as in the chabazite with 2 Al atoms; the reaction proceeds through an Eley-Rideal mechanism in which the adsorption of methyl group to the cluster is very likely. Nonetheless, two zeotypes were found to be more efficient in the first cycle of the reaction than the zeolite model: SAPO-34 and TiAPO-34, with Gibbs energy profiles below 80 $kJ \cdot mol^{-1}$. Among these two, TiAPO-34 was found to be the most promising candidate, as not only is able to effectively perform the MTM reaction despite the formation of a bicoordinated methyl group, but also exhibits the lowest methanol desorption energy with a value of only 21 $kJ \cdot mol^{-1}$.

In order to verify the oxidation resistance of the Cu_5 clusters supported on TiAPO-34, several further oxidation simulations were carried out, demonstrating that the catalytic system evades the formation of Cu_5-4O

species after the first O_2 dissociation step. In addition, when the Cu_5-O system is undergone to a second O_2 dissociation, it adopts a similar configuration to the one presented in the SSZ-13 model, with Gibbs relative energies in the CH_4 activation step below 44 $kJ \cdot mol^{-1}$, all of this in the doublet state in contrast to the SSZ-13, which requires higher spin states to carry on the reaction.

The findings collected in this dissertation demonstrate that sub-nanometre Cu_5 clusters have the potential to become a promising candidate for the MTM reaction at mild conditions while providing an excellent opportunity to design catalytic materials that fulfil the requirements needed in the current transition era, following the principles of green chemistry.

Summary

Sub-nanometre metal clusters composed by just a few atoms exhibit electronic, optical, and catalytic properties different from those of larger nanoparticles and bulk metals, which are associated to the accessibility of their low coordinated atoms and to a molecular-like electronic structure with discrete energy levels and localized orbitals. The catalytic properties of metal clusters depend strongly on their size and shape and can be altered by interactions with protecting ligands or when they are stabilised on inorganic supports. Understanding the nature and extent of these modifications is key to potentially achieve a fine tuning of their catalytic performance.

In this dissertation, the catalytic behaviour of sub-nanometre copper clusters was investigated in the methane to methanol (MTM) reaction supported in zeolites and zeotypes using O_2 as oxidant with no water molecules assisting the process.

In chapter 1, the fundamentals of heterogeneous catalysis, zeolites and metal clusters were described in order to set the reasons and motivations behind this work.

Next in chapter 2, the concepts of computational chemistry that were used throughout this dissertation were discussed. These included the development of the theoretical models like Hartree-Fock, the basics of Density Functional Theory (DFT), the exchange-correlation functionals, the concept of Potential Energy Surface (PES) and the use of the VASP program to predict the characteristics of a material in a specific chemical environment.

To begin with, the research was conducted on isolated Cu_5 and Cu_7 clusters in order to settle the main pathways involved in this complex reaction and to identify the main problems in each step of the reaction. It was found that the reaction can effectively proceed through an Eley-Rideal mechanism when bicoordinated oxygen atoms are stabilised at the edges of the clusters, involving relatively low activation energy

barriers. However, the adsorption of the methyl group and the formation of methoxy groups on the clusters are inevitable, which entails a significant obstacle to the process. Additional further oxidation simulations were carried out in Cu_5 and Cu_7 clusters demonstrating that higher O_2 coverages are not detrimental to the reaction, as they provide more available active sites and spin surfaces to efficiently yield methanol thanks to its natural oxidation resistance.

In a second step an SSZ-13 zeolite model was selected as support for the copper clusters to explore whether the trends formerly reported in gas phase are considerably distinct when the clusters are confined within the cavities of an Al-containing zeolite and whether this catalytic system can relieve the issues related to secondary routes and undesirable methyl adsorptions. The O_2 dissociation simulations reported an increase in the total positive charge on the Cun clusters with the number of Al atoms in the zeolite framework and a more concentrated electron density over the O atoms that facilitates the dissociation step. Additionally, it was proved that supported Cun clusters restrain deep oxidation in presence of new O_2 molecules evading the formation of Cu_n-4O species, which can be exploited to stabilise a catalytic system under oxidising conditions while preserving a metallic oxidation state.

To investigate the CH_4 activation, only the most common scenario was contemplated, which is the zeolite framework with 2 Al atoms. The uncovered reaction mechanism is analogous to the one found in gas phase with Gibbs activation barriers less than 115 $kJ \cdot mol^{-1}$ as those reported experimentally for Cu-exchanged zeolites along with a remarkable importance of higher spin states that enhance the H transfer step from the methane to the anchored O atom on the cluster, since only the quadruplet surface permits an effective H abstraction in more oxidising conditions in presence of Cu_n-3O species. Significant differences among Cu_5 and Cu_7 clusters were found. Cu_5 is able to transform methane into methanol while avoiding the generation of CH_2 species and the bi-coordination of methyl groups in contrast to Cu_7, which offers a worse alternative in almost every aspect. In addition, Cu_5 clusters open the possibility to generate new chemicals like

formaldehyde and DME when methoxy species are generated on the cluster, providing added value to the process.

Lastly, analogous systems to SSZ-13, SAPO-34, and MeAPO-34, were explored to uncover metal-containing zeotype systems with two metal atoms that foster better catalytic properties and more optimised mechanistic insights for the production of methanol. Taking into account the results obtained for the SSZ-13 model, in this occasion only Cu5 clusters were considered for this study. Six elements were selected attending to their position in the periodic table and unique characteristics and they were introduced in equivalent spots to the Al atoms embedded in the chabazite model: Zn^{2+}, Fe^{2+}, Mg^{2+}, Ti^{4+}, Zr^{4+} and Sn^{4+}. These zeotype systems follow the same principles as the SSZ-13 in reference to the total positive charge of copper atoms and more localised electron density on O atoms which vary depending on the selected metal. Nonetheless, improvements on the O_2 dissociation activation barriers were found except for the Si and Mg zeotypes, with values ranging from 34 to 111 $kJ \cdot mol^{-1}$.

The mechanism for the MTM reaction in these systems resulted as reported above, an Eley-Rideal reaction path that cannot evade the adsorption of the methyl groups; but in which two candidates were found to be more efficient than the SSZ-13 with two Al atoms in terms of a lower Gibbs energy profile for the first cycle: SAPO-34 and TiAPO-34 zeotypes, being both of them below 80 $kJ \cdot mol^{-1}$. In fact, the TiAPO-34 turned out to be the most promising system since it achieves these results despite the formation of a bicoordinated methyl group and possesses the lowest methanol desorption energy reported in this dissertation, 21 $kJ \cdot mol^{-1}$.

To further explore the TiAPO-34 system, additional oxidation simulations were carried out, confirming the catalytic system avoids the production of Cu_5-4O species just as reported in the zeolite model. The resultant Cu_5-3O is alike to the one reported in SSZ-13, improving the Gibbs relative energies but unlike the zeolite model, the TiAPO-34 performs the MTM reaction in the doublet state.

On balance, the present findings of this dissertation open an avenue to design catalytic materials based on their ability to stabilise radical species while fulfilling the main goals of green chemistry.

Resumen

Los clústeres metálicos subnanométricos están compuestos por unos pocos átomos que exhiben propiedades catalíticas, electrónicas, y ópticas diferentes de sus agregados y de las nanopartículas. Esto está asociado con la accesibilidad de los átomos con baja coordinación, con una estructura electrónica similar a las moléculas con niveles discretos de energía y orbitales localizados. Las propiedades catalíticas de los clústeres metálicos dependen fuertemente de su tamaño y forma, además se pueden alterar con interacciones con ligandos protectores o cuando se estabilizan en soportes inorgánicos. Entender la naturaleza y la importancia de estas modificaciones es vital para conseguir un ajuste preciso de su rendimiento catalítico.

En esta tesis se investigó el comportamiento catalítico de clústeres subnanométricos de cobre en la reacción de metano a metanol (MTM) soportados en zeolitas y zeotipos usando como oxidante O_2 y sin la intervención de moléculas de agua en todo momento.

En el capítulo 1, los fundamentos de la catálisis heterogénea, las zeolitas y los clústeres metálicos se desarrollaron para explicar las razones y las motivaciones detrás de este estudio.

A continuación, en el capítulo 2, se explicaron en detalle los conceptos de química computacional que se han usado a lo largo de esta tesis doctoral, desde el desarrollo de los modelos teóricos como Hartree-Fock pasando por las bases de la "teoría del funcional de densidad" (DFT), los funcionales de intercambio-correlación, el concepto de superficie de energía potencial (PES) y el uso del programa VASP para predecir las características de un material en un entorno químico concreto.

Para empezar, la investigación se llevó a cabo en clústeres aislados de Cu_5 y Cu_7 para descubrir los principales caminos de reacción y para identificar los principales problemas que pueden ocurrir en cada etapa de la reacción. Se encontró que la reacción transcurre eficientemente a

través de un mecanismo Eley-Rideal cuando existen átomos de O bicoordinados estabilizados en las aristas de los clústeres, conduciendo a menores barreras de activación. Sin embargo, la adsorción del grupo metilo y la formación de grupos metoxilo en los clústeres es inevitable, lo que supone un importante obstáculo para el proceso. Además, se realizaron experimentos de sobreoxidación en los clústeres de Cu_5 y Cu_7 demostrando que mayores cantidades de O_2 no son perjudiciales en el proceso, ya que permiten una mayor disponibilidad de centros activos y superficies de spin para producir de forma efectiva metanol gracias a su resistencia natural a la oxidación.

A continuación, se seleccionó el modelo de zeolita SSZ-13 para soportar los clústeres de cobre y explorar si las tendencias observadas en fase gas son significativamente distintas cuando los clústeres se encuentran confinados en las cavidades de una zeolita con cantidades variables de Al y si este sistema catalítico puede paliar los problemas relacionados con los caminos secundarios y la adsorción indeseada de los grupos metilo. Las simulaciones en la disociación de O_2 arrojaron un incremento en la carga total positiva de los clústeres Cu_n conforme al número de átomos de Al en la matriz zeolítica y que una mayor concentración de densidad de carga sobre los átomos de O facilita este paso. Asimismo, se probó que los clústeres Cu_n soportados son capaces de restringir la sobreoxidación en presencia de nuevas moléculas de O_2, evitando así la formación de especies Cu_n-4O, lo cual puede aprovecharse para estabilizar un sistema catalítico bajo condiciones oxidantes a la vez que se mantiene un estado de oxidación metálico.

Para estudiar la activación de CH_4, solo el escenario más común fue contemplado, cuando la zeolita tiene en su matriz 2 átomos de Al. El mecanismo de reacción descubierto es análogo al encontrado en fase gas, con energías de activación de Gibbs menores a 115 $kJ \cdot mol^{-1}$ siendo similares a las reportadas experimentalmente para las zeolitas de Cu intercambiado junto a una importancia considerable de los estados mayores de spin, que mejoran el paso de transferencia de H desde el metano al O bicoordinado estabilizado en el clúster, ya que solo el estado de spin cuadruplete permite una abstracción efectiva del H en condiciones más oxidantes con presencia de especies Cu_n-3O. Se encontraron diferencias significativas entre el Cu_5 y el Cu_7. El Cu_5 es

capaz de transformar metano en metanol a la vez que evita la generación de especies CH_2 y la bicoordinación de los grupos metilo en contraposición al Cu7, el cual ofrece una alternativa peor en casi todos los aspectos. Además, los clústeres de Cu5 abren la posibilidad de producir nuevos productos como el formaldehído o el DME cuando se generan especies metoxilo en el clúster, aportando valor añadido al proceso.

Por último, sistemas análogos a la SSZ-13 como SAPO-34 y MeAPO-34 se estudiaron para descubrir sistemas zeotipo con 2 átomos de un elemento metálico que promuevan mejores propiedades catalíticas y unos mecanismos de reacción óptimos y dirigidos a la producción de metanol. Teniendo en cuenta los resultados obtenidos en el modelo SSZ-13, en esta ocasión solo se exploró la reactividad del Cu_5. Seis elementos fueron seleccionados atendiendo a su posición en la tabla periódica y se introdujeron en huecos equivalentes a los átomos de Al en el modelo de chabazita: Zn^{2+}, Fe^{2+}, Mg^{2+}, Ti^{4+}, Zr^{4+} y Sn^{4+}. Estos sistemas zeotipo se rigen por los mismos principios que el modelo SSZ-13, obteniendo tendencias muy similares en la carga total positiva de los cobres y en la densidad electrónica localizada en los átomos de O, las cuales varían dependiendo del metal seleccionado. No obstante, se obtuvieron mejoras en las barreras energéticas de activación para la disociación de O_2 excepto para los casos del Si y el Mg, con valores oscilando entre los 34 y los 111 $kJ \cdot mol^{-1}$.

El mecanismo de reacción descubierto en estos sistemas es similar a los casos anteriores, un mecanismo Eley-Rideal que no puede evitar la adsorción de grupos metilo; pero lo más destacable de estos resultados fue encontrar dos candidatos capaces de realizar de forma más óptima la reacción MTM en comparación con el modelo SSZ-13 con dos átomos de Al en el primer ciclo de reacción: SAPO-34 y TiAPO-34, con perfiles energéticos de Gibbs por debajo de los 80 $kJ \cdot mol^{-1}$. De hecho, el TiAPO-34 resultó el sistema más prometedor, ya que consigue estos resultados a pesar de formar un grupo metilo bicoordinado al clúster y posee la particularidad de tener la menor energía de desorción de metanol encontrada en esta tesis doctoral, 21 $kJ \cdot mol^{-1}$.

Para explorar en mayor profundidad el sistema TiAPO-34, se realizaron simulaciones en las que se añadía nuevas moléculas de O_2 al sistema

catalítico, confirmando que el catalizador evita la producción de especies Cu_5-4O al igual que en el modelo de SSZ-13. La especie Cu_5-3O resultante de estas simulaciones es bastante parecida geométricamente a la encontrada en la SSZ-13, mejorando las energías relativas de Gibbs, pero en contraste con el modelo zeolítico, la reacción en el sistema TiAPO-34 transcurre a través del estado doblete.

En conclusión, los hallazgos recopilados en esta tesis doctoral permitirán abrir una nueva manera de diseñar materiales catalíticos basados en su habilidad para estabilizar especies radicalarias a la vez que se cumple con los objetivos establecidos por la química verde.

Resum

Els clústers metàl·lics subnanomètrics estan compostos per uns pocs àtoms que exhibeixen propietats catalítiques, electròniques i òptiques diferents dels seus agregats i de les nanopartícules. Açò està associat amb l'accessibilitat dels àtoms amb baixa coordinació i amb una estructura electrònica similar a les molècules amb nivells discrets d'energia i orbitals localitzats. Les propietats catalítiques dels clústers metàl·lics depenen estretament de la seua grandària i forma, a més es poden alterar amb interaccions amb lligands protectors o quan s'estabilitzen en suports inorgànics. Entendre la natura i la importància d'estes modificacions és vital per aconseguir un ajust precís del seu rendiment catalític.

En esta tesi s'investigà el comportament catalític de clústers subnanomètrics de coure en la reacció de metà a metanol (MTM) suportats en zeolites i zeotipus usant com oxidant O_2 i sense la intervenció de molècules d'aigua en tot moment.

En el capítol 1, els fonaments de la catàlisi heterogènia, les zeolites i els clústers metàl·lics es desenvolupen per explicar les raons i les motivacions darrere d'este estudi.

A continuació, en el capítol 2, es van explicar en detall els conceptes de química computacional que s'han usat al llarg d'esta tesi doctoral, des del desenvolupament dels models teòrics com Hartree-Fock passant per la base de la "teoria del funcional de densitat" (DFT), els funcionals d'intercanvi-correlació, el concepte de superfície d'energia potencial (PES) i el ús del programa VASP per predir les característiques d'un material en un entorn químic concret.

Per començar, la investigació es portà a terme en clústers aïllats de Cu_5 i Cu_7 per descobrir els principals camins de reacció i per identificar els principals problemes que poden ocórrer en cada etapa de la reacció. Es trobà que la reacció transcorre eficientment a través d'un mecanisme Eley-Rideal quan existixen àtoms de O bicoordinats estabilitzats en les

aristes dels clústers, conduint a menors barreres d'activació. No obstant, l'absorció del grup metil i formació de grups metoxils en els clústers és inevitable, cosa que suposa un important obstacle per el procés. Simulacions addicionals d'oxidació dels clústers de Cu_5 i Cu_7 van demostrar que els recobrimentes més alts de no són perjudicials per a la reacció, ja que permeten una major disponibilitat de centres actius i superfícies de spin per produir de forma efectiva metanol gràcies a la seua resistència natural a l'oxidació.

En una segona etapa es va seleccionar el model de zeolita SSZ-13 per suportar els clústers de cobre i explorar si les tendències observades en fase gas són significativament distintes quan els clústers es troben confinats en les cavitats d'una zeolita amb quantitats variables del Al i si este sistema catalític pot pal·liar els problemes relacionats amb els camins secundaris i l'absorció no desitjada dels grups metil. Les simulacions en la dissociació d'O_2 van llançar un increment en la càrrega total positiva dels clústers Cu_n conforme al nombre d'àtoms de Al en la matriu zeolitica i que una major concentració de densitat de càrrega sobre els àtoms d'O facilita este pas. Així mateix, es provà que els clústers Cu_n suportats poden restringir la sobreoxidació en presència de noves molècules d'O_2 evitant així la formació d'espècies Cu_n-4O, cosa que pot aprofitar-se per a estabilitzar un sistema catalític baix condicions oxidants a la volta que es manté un estat d'oxidació metàl·lic.

Per estudiar l'activació de CH_4, soles l'escenari més comú ha estat contemplat, quan la zeolita té en la seua matriu 2 àtoms de Al. El mecanisme de reacció descobert és anàleg al que s'ha trobat en fase gas, amb energies d'activació de Gibbs menors a 115 $KJ \cdot mol^{-1,}$ similars a les reportades experimentalment per les zeolites de Cu intercanviat. També s'ha descobert una importància considerable dels estats majors de spin, que milloren el pas de transferència de H des del metà al O bicoordinat estabilitzat en el clúster, ja que sols l'estat de spin quadruplet permet una abstracció efectiva del H en condicions més oxidants amb presència d'espécies Cu_n-3O. No obstant, es trobaren diferencies significatives per al Cu_5 i el Cu_7. El Cu_5 pot transformar el metà en metanol a la volta que evita la generació d'espècies CH_2 i la bicoordinació dels grups metilo.

A més, els clústers de Cu_5 obrin la possibilitat de produir nous productes com el formaldehid o el DME quan es generen especies metoxil en el clúster, aportant valor afegit al procés.

Per últim, sistemes anàlegs a la SSZ-13 com el SAPO-34 i el MeAPO-34 s'estudiaren per descobrir sistemes zeotipus amb 2 àtoms d'un element metàl·lic que promoguen millors propietats catalítiques i uns mecanismes de reacció òptims i dirigits a la producció de metanol. Tenint en compte els resultats obtinguts en el model SSZ-13, en esta ocasió només s'explorà la reactivitat del Cu_5. Sis elements van ser seleccionats atenent la seua posició en la taula periòdica i s'introduïren en llocs equivalents als àtoms de Al en el model de cabazita: Zn^{2+}, Fe^{2+}, Mg^{2+}, Ti^{4+}, Zr^{4+} y Sn^{4+}. Estos sistemes zeotipus es regeixen pels mateixos principis que el model SSZ-13, obtenint tendències molt similars en la càrrega total positiva dels coures i en la densitat electrònica localitzada en els àtoms de O, les quals varien depenent del metall seleccionat. No obstant, es van obtindre millores en les Si i el Mg, amb valors oscil·lant entre els 34 i els 111 $KJ \cdot mol^{-1}$.

El mecanisme de reacció descobert en estos sistemes és similar als casos anteriors, un mecanisme Eley-Rideal que no pot evitar l'absorció de grups metilo, però el més destacable d'estos resultats va ser trobar dos candidats capaços de realitzar de forma més òptima la reacció MTM en comparació amb el model SSZ-13 amb dos àtoms de Al en el primer cicle de reacció: SAPO-34 i TiAPO-34, amb perfils energètics de Gibbs per sota dels 80 $KJ \cdot mol^{-1}$. De fet, el TiAPO-34 va resultar el sistema més prometedor, ja que aconsegueix estos resultats a pesar de formar un grup metilo bicoordinat al clúster i posseeix la particularitat de tindre la menor energia de desorció de metanol trobada en esta tesi doctoral, 21 $KJ \cdot mol^{-1}$.

Per explorar en major profunditat el sistema TiAPO-34, es van realitzar simulacions en les quals s'agregaven noves molècules d'O_2 al sistema catalític, confirmant que el catalitzador evita la producció d'espècies Cu_5-4O com també en el model de SSZ-13. L'espècie Cu_5-3O resultant d'estes simulacions és prou pareguda geomètricament a la trobada en la

SSZ-13, millorant les energies relatives de Gibbs, però, en contrast, amb el model zeolític, la reacció en el sistema TiAPO-34 transcorre a través de l'estat doblet.

En conclusió, les troballes recopilades en esta tesi doctoral permetran obrir una nova manera de dissenyar materials catalítics basats en la seua habilitat per estabilitzar espècies radicalàries a la volta que es compleix amb els objectius establerts per la química verda.

List of Publications

- Gallego, M.; Corma, A.; Boronat, M. An Alternative Catalytic Cycle for Selective Methane Oxidation to Methanol with Cu Clusters in Zeolites. *Phys. Chem. Chem. Phys.* **2024**. https://doi.org/10.1039/D3CP05802F.

- Gallego, M.; Corma, A.; Boronat, M. Influence of the Zeolite Support on the Catalytic Properties of Confined Metal Clusters: A Periodic DFT Study of O2 Dissociation on Cun Clusters in CHA. *Phys. Chem. Chem. Phys.* **2022**, *24* (48), 30044–30050. https://doi.org/10.1039/D2CP04915E.

- Gallego, M.; Corma, A.; Boronat, M. Sub-Nanometer Copper Clusters as Alternative Catalysts for the Selective Oxidation of Methane to Methanol with Molecular O2. *J. Phys. Chem. A* **2022**. https://doi.org/10.1021/acs.jpca.2c02895.

References

(1) Berzelius, J. J. Sur Un Force Jusqu'ici Peu Remarquée Qui Est Probablement Active Dans La Formation Des Composes Organiques, Section on Vegetable Chemistry. *Jahres-Ber.* **1835**, *14*, 237.
(2) Roberts, M. W. Birth of the Catalytic Concept (1800-1900). *Catal. Lett.* **2000**, *67* (1), 1–4. https://doi.org/10.1023/A:1016622806065.
(3) Wisniak, J. The History of Catalysis. From the Beginning to Nobel Prizes. *Educ. Quím.* **2010**, *21* (1), 60–69. https://doi.org/10.1016/S0187-893X(18)30074-0.
(4) Cordus, V. *Le guidon des Apotiquaires. C'est à dire, la vraye forme et maniere de composer les medicamens. Premierement traittee par Valerius Cordus. Traduite de Latin en François, et repurgee d'une infinité de fautes. La page suivante enseigne ce qui est traité en ce livre,*. https://www.biusante.parisdescartes.fr/histoire/medica/resultats/index.php?do=chapitre&cote=30252 (accessed 2023-05-15).
(5) Sabatier, P.; Senderens, J. Action Du Nickel Sur l'éthylène. Synthèse de l'éthane. *CR Acad Sci Paris* **1897**, *124*, 1358–1360.
(6) Ostwald, W. *Lehrbuch Der Allgemeinen Chemie*; W. Engelmann, 1903; Vol. 1.
(7) Rideal, E. K.; Taylor, H. S. *Catalysis in Theory and Practice*; Macmillan and Company, limited, 1926.
(8) Gibbs, J. W. A Method of Geometrical Representation of the Thermodynamic Properties of Substances by Means of Surfaces. *Trans. Conn. Acad. Arts Sci.* **1873**, No. 2, 382–404.
(9) Rosenberg, R. M.; Klotz, I. M. *Chemical Thermodynamics: Basic Concepts and Methods*, 7th ed.; Wiley: Hoboken, N.J., 2008.
(10) Atkins, P.; Atkins, P. W.; de Paula, J. *Atkins' Physical Chemistry*; Oxford university press, 2014.
(11) Eyring, H. The Activated Complex in Chemical Reactions. *J. Chem. Phys.* **1935**, *3* (2), 107–115. https://doi.org/10.1063/1.1749604.
(12) Evans, M. G.; Polanyi, M. Some Applications of the Transition State Method to the Calculation of Reaction Velocities, Especially in Solution. *Trans. Faraday Soc.* **1935**, *31* (0), 875–894. https://doi.org/10.1039/TF9353100875.
(13) Laidler, K. J.; King, M. C. Development of Transition-State Theory. *J. Phys. Chem.* **1983**, *87* (15), 2657–2664. https://doi.org/10.1021/j100238a002.

(14) Taylor, H. S. A Theory of the Catalytic Surface. *Proc. R. Soc. Lond. Ser. Contain. Pap. Math. Phys. Character* **1925**, *108* (745), 105–111. https://doi.org/10.1098/rspa.1925.0061.
(15) Hu, K.-J.; Plant, S. R.; Ellis, P. R.; Brown, C. M.; Bishop, P. T.; Palmer, R. E. Atomic Resolution Observation of a Size-Dependent Change in the Ripening Modes of Mass-Selected Au Nanoclusters Involved in CO Oxidation. *J. Am. Chem. Soc.* **2015**, *137* (48), 15161–15168. https://doi.org/10.1021/jacs.5b08720.
(16) Fernández, E.; Liu, L.; Boronat, M.; Arenal, R.; Concepcion, P.; Corma, A. Low-Temperature Catalytic NO Reduction with CO by Subnanometric Pt Clusters. *ACS Catal.* **2019**, *9* (12), 11530–11541. https://doi.org/10.1021/acscatal.9b03207.
(17) Schmidt, F. The Importance of Catalysis in the Chemical and Non-Chemical Industries. In *Basic Principles in Applied Catalysis*; Baerns, M., Ed.; Springer Series in Chemical Physics; Springer: Berlin, Heidelberg, 2004; pp 3–16. https://doi.org/10.1007/978-3-662-05981-4_1.
(18) Armor, J. N. A History of Industrial Catalysis. *Catal. Today* **2011**, *163* (1), 3–9. https://doi.org/10.1016/j.cattod.2009.11.019.
(19) Arinaga, A. M.; Ziegelski, M. C.; Marks, T. J. Alternative Oxidants for the Catalytic Oxidative Coupling of Methane. *Angew. Chem. Int. Ed.* **2021**, *60* (19), 10502–10515. https://doi.org/10.1002/anie.202012862.
(20) Fan, Y.; Xia, W.; Ma, C.; Huang, Y.; Li, S.; Wang, X.; Qian, C.; Chen, K.; Liu, D. Recent Advances of Computational Studies on Bioethanol to Light Olefin Reactions Using Zeolite and Metal Oxide Catalysts. *Chem. Eng. Sci.* **2023**, *270*, 118532. https://doi.org/10.1016/j.ces.2023.118532.
(21) Hawkins, J. M.; Watson, T. J. N. Asymmetric Catalysis in the Pharmaceutical Industry. *Angew. Chem. Int. Ed.* **2004**, *43* (25), 3224–3228. https://doi.org/10.1002/anie.200330072.
(22) Roughley, S. D.; Jordan, A. M. The Medicinal Chemist's Toolbox: An Analysis of Reactions Used in the Pursuit of Drug Candidates. *J. Med. Chem.* **2011**, *54* (10), 3451–3479. https://doi.org/10.1021/jm200187y.
(23) Fryszkowska, A.; Devine, P. N. Biocatalysis in Drug Discovery and Development. *Curr. Opin. Chem. Biol.* **2020**, *55*, 151–160. https://doi.org/10.1016/j.cbpa.2020.01.012.
(24) Stadler, B. M.; Wulf, C.; Werner, T.; Tin, S.; de Vries, J. G. Catalytic Approaches to Monomers for Polymers Based on Renewables. *ACS Catal.* **2019**, *9* (9), 8012–8067. https://doi.org/10.1021/acscatal.9b01665.

(25) Ellis, L. D.; Rorrer, N. A.; Sullivan, K. P.; Otto, M.; McGeehan, J. E.; Román-Leshkov, Y.; Wierckx, N.; Beckham, G. T. Chemical and Biological Catalysis for Plastics Recycling and Upcycling. *Nat. Catal.* **2021**, *4* (7), 539–556. https://doi.org/10.1038/s41929-021-00648-4.

(26) Blaser, H.-U.; Malan, C.; Pugin, B.; Spindler, F.; Steiner, H.; Studer, M. Selective Hydrogenation for Fine Chemicals: Recent Trends and New Developments. *Adv. Synth. Catal.* **2003**, *345* (1–2), 103–151. https://doi.org/10.1002/adsc.200390000.

(27) Yu, T.; Ding, Z.; Nie, W.; Jiao, J.; Zhang, H.; Zhang, Q.; Xue, C.; Duan, X.; Yamada, Y. M. A.; Li, P. Recent Advances in Continuous-Flow Enantioselective Catalysis. *Chem. – Eur. J.* **2020**, *26* (26), 5729–5747. https://doi.org/10.1002/chem.201905151.

(28) Khalil, M.; Kadja, G. T. M.; Ilmi, Moh. M. Advanced Nanomaterials for Catalysis: Current Progress in Fine Chemical Synthesis, Hydrocarbon Processing, and Renewable Energy. *J. Ind. Eng. Chem.* **2021**, *93*, 78–100. https://doi.org/10.1016/j.jiec.2020.09.028.

(29) Shipman, M. A.; Symes, M. D. Recent Progress towards the Electrosynthesis of Ammonia from Sustainable Resources. *Catal. Today* **2017**, *286*, 57–68. https://doi.org/10.1016/j.cattod.2016.05.008.

(30) Chorkendorff, I.; Niemantsverdriet, J. W. *Concepts of Modern Catalysis and Kinetics*, Third, completely revised and enlarged edition.; WILEY-VCH Verlag GmbH & Co KG: Weinheim, 2017.

(31) Anastas, P. T.; Warner, J. C. *Green Chemistry: Theory and Practice*; Oxford University Press: Oxford [England] ; New York, 1998.

(32) Anastas, P. T.; Kirchhoff, M. M. Origins, Current Status, and Future Challenges of Green Chemistry. *Acc. Chem. Res.* **2002**, *35* (9), 686–694. https://doi.org/10.1021/ar010065m.

(33) Isac-García, J.; Dobado, J. A.; Calvo-Flores, F. G.; Martínez-García, H. Chapter 12 - Green Chemistry. In *Experimental Organic Chemistry*; Isac-García, J., Dobado, J. A., Calvo-Flores, F. G., Martínez-García, H., Eds.; Academic Press, 2016; pp 409–415. https://doi.org/10.1016/B978-0-12-803893-2.50012-7.

(34) Erythropel, H. C.; Zimmerman, J. B.; Winter, T. M. de; Petitjean, L.; Melnikov, F.; Lam, C. H.; Lounsbury, A. W.; Mellor, K. E.; Janković, N. Z.; Tu, Q.; Pincus, L. N.; Falinski, M. M.; Shi, W.; Coish, P.; Plata, D. L.; Anastas, P. T. The Green ChemisTREE:

20 Years after Taking Root with the 12 Principles. *Green Chem.* **2018**, *20* (9), 1929–1961. https://doi.org/10.1039/C8GC00482J.
(35) Kate, A.; Sahu, L. K.; Pandey, J.; Mishra, M.; Sharma, P. K. Green Catalysis for Chemical Transformation: The Need for the Sustainable Development. *Curr. Res. Green Sustain. Chem.* **2022**, *5*, 100248. https://doi.org/10.1016/j.crgsc.2021.100248.
(36) Stahl, S. S.; Labinger, J. A.; Bercaw, J. E. Homogeneous Oxidation of Alkanes by Electrophilic Late Transition Metals. *Angew. Chem. Int. Ed.* **1998**, *37* (16), 2180–2192. https://doi.org/10.1002/(SICI)1521-3773(19980904)37:16<2180::AID-ANIE2180>3.0.CO;2-A.
(37) Sperger, T.; Sanhueza, I. A.; Kalvet, I.; Schoenebeck, F. Computational Studies of Synthetically Relevant Homogeneous Organometallic Catalysis Involving Ni, Pd, Ir, and Rh: An Overview of Commonly Employed DFT Methods and Mechanistic Insights. *Chem. Rev.* **2015**, *115* (17), 9532–9586. https://doi.org/10.1021/acs.chemrev.5b00163.
(38) Védrine, J. C. Heterogeneous Catalysis on Metal Oxides. *Catalysts* **2017**, *7* (11), 341. https://doi.org/10.3390/catal7110341.
(39) Chadha, U.; Selvaraj, S. K.; Ashokan, H.; Hariharan, S. P.; Mathew Paul, V.; Venkatarangan, V.; Paramasivam, V. Complex Nanomaterials in Catalysis for Chemically Significant Applications: From Synthesis and Hydrocarbon Processing to Renewable Energy Applications. *Adv. Mater. Sci. Eng.* **2022**, *2022*, e1552334. https://doi.org/10.1155/2022/1552334.
(40) Samanta, D.; Sani, R. K. Methane Oxidation via Chemical and Biological Methods: Challenges and Solutions. *Methane* **2023**, *2* (3), 279–303. https://doi.org/10.3390/methane2030019.
(41) Bukhtiyarova, M. V.; Echevsky, G. V. Modern Research in the Field of Zeolites and Zeolite-Like Materials: A Review of the Works of the Boreskov Institute of Catalysis, Siberian Branch, Russian Academy of Sciences. *Pet. Chem.* **2019**, *59* (8), 802–821. https://doi.org/10.1134/S0965544119080048.
(42) Nørskov, J. K.; Abild-Pedersen, F.; Studt, F.; Bligaard, T. Density Functional Theory in Surface Chemistry and Catalysis. *Proc. Natl. Acad. Sci.* **2011**, *108* (3), 937–943. https://doi.org/10.1073/pnas.1006652108.
(43) Thomas, J. M.; Thomas, W. J. *Principles and Practice of Heterogeneous Catalysis*; John Wiley & Sons, 2014.
(44) Fogler, H. S. *Elements of Chemical Reaction Engineering*; Pearson Boston, 2020.

(45) Palmisano, G.; Jitan, S. A.; Garlisi, C. Chapter 2 - Fundamentals of the Adsorption Process. In *Heterogeneous Catalysis*; Palmisano, G., Jitan, S. A., Garlisi, C., Eds.; Elsevier, 2022; pp 27–62. https://doi.org/10.1016/B978-0-323-89845-4.00004-7.
(46) Cusinato, L.; Rosal, I. del; Poteau, R. Shape, Electronic Structure and Steric Effects of Organometallic Nanocatalysts: Relevant Tools to Improve the Synergy between Theory and Experiment. *Dalton Trans.* **2017**, *46* (2), 378–395. https://doi.org/10.1039/C6DT04207D.
(47) Langmuir, I. THE ADSORPTION OF GASES ON PLANE SURFACES OF GLASS, MICA AND PLATINUM. *J. Am. Chem. Soc.* **1918**, *40* (9), 1361–1403. https://doi.org/10.1021/ja02242a004.
(48) Langmuir, I. Part II.—"Heterogeneous Reactions". Chemical Reactions on Surfaces. *Trans. Faraday Soc.* **1922**, *17* (0), 607–620. https://doi.org/10.1039/TF9221700607.
(49) Hinshelwood, C. N.; Sidgwick, N. V. On the Theory of Unimolecular Reactions. *Proc. R. Soc. Lond. Ser. Contain. Pap. Math. Phys. Character* **1926**, *113* (763), 230–233. https://doi.org/10.1098/rspa.1926.0149.
(50) Rideal, E. K. A Note on a Simple Molecular Mechanism for Heterogeneous Catalytic Reactions. *Math. Proc. Camb. Philos. Soc.* **1939**, *35* (1), 130–132. https://doi.org/10.1017/S030500410002082X.
(51) Eley, D. D.; Rideal, E. K. Parahydrogen Conversion on Tungsten. *Nature* **1940**, *146* (3699), 401–402. https://doi.org/10.1038/146401d0.
(52) Eley, D. D. The Catalytic Activation of Hydrogen. In *Advances in Catalysis*; Frankenburg, W. G., Komarewsky, V. I., Rideal, E. K., Eds.; Academic Press, 1948; Vol. 1, pp 157–199. https://doi.org/10.1016/S0360-0564(08)60675-6.
(53) *International Tables for Crystallography: X-Ray Absorption Spectroscopy and Related Techniques*, 1st ed.; Chantler, C. T., Boscherini, F., Bunker, B., Eds.; International Union of Crystallography: Chester, England, 2020; Vol. I. https://doi.org/10.1107/97809553602060000116.
(54) Martínez-Ripoll, M. *Crystallography - Cristalografia*. https://www.xtal.iqfr.csic.es/Cristalografia/index-en.html (accessed 2023-06-26).
(55) Ashcroft, N. W.; Mermin, N. D. *Solid State Physics*; Holt, Rinehart and Winston: New York, 1976.

(56) Xie, C.; Yan, D.; Li, H.; Du, S.; Chen, W.; Wang, Y.; Zou, Y.; Chen, R.; Wang, S. Defect Chemistry in Heterogeneous Catalysis: Recognition, Understanding, and Utilization. *ACS Catal.* **2020**, *10* (19), 11082–11098. https://doi.org/10.1021/acscatal.0c03034.
(57) Khodayar, M.; Franzson, H. Fracture Pattern of Thjórsárdalur Central Volcano with Respect to Rift-Jump and a Migrating Transform Zone in South Iceland. *J. Struct. Geol.* **2007**, *29* (5), 898–912. https://doi.org/10.1016/j.jsg.2006.11.007.
(58) Barrer, R. M. 435. Syntheses and Reactions of Mordenite. *J. Chem. Soc. Resumed* **1948**, No. 0, 2158–2163. https://doi.org/10.1039/JR9480002158.
(59) Breck, D. W.; Eversole, W. G.; Milton, R. M. NEW SYNTHETIC CRYSTALLINE ZEOLITES. *J. Am. Chem. Soc.* **1956**, *78* (10), 2338–2339. https://doi.org/10.1021/ja01591a082.
(60) Corma, A. Inorganic Solid Acids and Their Use in Acid-Catalyzed Hydrocarbon Reactions. *Chem. Rev.* **1995**, *95* (3), 559–614. https://doi.org/10.1021/cr00035a006.
(61) Corma, A. From Microporous to Mesoporous Molecular Sieve Materials and Their Use in Catalysis. *Chem. Rev.* **1997**, *97* (6), 2373–2420. https://doi.org/10.1021/cr960406n.
(62) Wang, H.; Wang, Z.; Huang, L.; Mitra, A.; Holmberg, B.; Yan, Y. High-Surface-Area Zeolitic Silica with Mesoporosity. *J. Mater. Chem.* **2001**, *11* (9), 2307–2310. https://doi.org/10.1039/B102216O.
(63) Pérez-Ramírez, J.; Christensen, C. H.; Egeblad, K.; Christensen, C. H.; Groen, J. C. Hierarchical Zeolites: Enhanced Utilisation of Microporous Crystals in Catalysis by Advances in Materials Design. *Chem. Soc. Rev.* **2008**, *37* (11), 2530–2542. https://doi.org/10.1039/B809030K.
(64) Derouane, E. G. Shape Selectivity in Catalysis by Zeolites: The Nest Effect. *J. Catal.* **1986**, *100* (2), 541–544. https://doi.org/10.1016/0021-9517(86)90127-2.
(65) Jae, J.; Tompsett, G. A.; Foster, A. J.; Hammond, K. D.; Auerbach, S. M.; Lobo, R. F.; Huber, G. W. Investigation into the Shape Selectivity of Zeolite Catalysts for Biomass Conversion. *J. Catal.* **2011**, *279* (2), 257–268. https://doi.org/10.1016/j.jcat.2011.01.019.
(66) Chai, Y.; Dai, W.; Wu, G.; Guan, N.; Li, L. Confinement in a Zeolite and Zeolite Catalysis. *Acc. Chem. Res.* **2021**, *54* (13), 2894–2904. https://doi.org/10.1021/acs.accounts.1c00274.

(67) Busca, G. Acidity and Basicity of Zeolites: A Fundamental Approach. *Microporous Mesoporous Mater.* **2017**, *254*, 3–16. https://doi.org/10.1016/j.micromeso.2017.04.007.
(68) Shamzhy, M.; Opanasenko, M.; Concepción, P.; Martínez, A. New Trends in Tailoring Active Sites in Zeolite-Based Catalysts. *Chem. Soc. Rev.* **2019**, *48* (4), 1095–1149. https://doi.org/10.1039/C8CS00887F.
(69) Martínez, C.; Corma, A. 5.05 - Zeolites. In *Comprehensive Inorganic Chemistry II (Second Edition)*; Reedijk, J., Poeppelmeier, K., Eds.; Elsevier: Amsterdam, 2013; pp 103–131. https://doi.org/10.1016/B978-0-08-097774-4.00506-4.
(70) Gounder, R.; Iglesia, E. The Catalytic Diversity of Zeolites: Confinement and Solvation Effects within Voids of Molecular Dimensions. *Chem. Commun.* **2013**, *49* (34), 3491–3509. https://doi.org/10.1039/C3CC40731D.
(71) *Database of Zeolite Structures*. http://www.iza-structure.org/databases/ (accessed 2023-07-06).
(72) Coombs, D. S.; Alberti, A.; Armbruster, T.; Artioli, G.; Colella, C.; Galli, E.; Grice, J. D.; Liebau, F.; Mandarino, J. A.; Minato, H.; Nickel, E. H.; Passaglia, E.; Peacor, D. R.; Quartieri, S.; Rinaldi, R.; Ross, M.; Sheppard, R. A.; Tillmanns, E.; Vezzalini, G. Recommended Nomenclature for Zeolite Minerals: Report of the Subcommittee on Zeolites of the International Mineralogical Association, Commission on New Minerals and Mineral Names. *Mineral. Mag.* **1998**, *62* (4), 533–571. https://doi.org/10.1180/002646198547800.
(73) Moshoeshoe, M.; Nadiye-Tabbiruka, M. S.; Obuseng, V. A Review of the Chemistry, Structure, Properties and Applications of Zeolites. *Am. J. Mater. Sci.* **2017**, *7* (5), 196–221.
(74) Tahraoui, Z.; Nouali, H.; Marichal, C.; Forler, P.; Klein, J.; Daou, T. J. Influence of the Compensating Cation Nature on the Water Adsorption Properties of Zeolites. *Molecules* **2020**, *25* (4), 944. https://doi.org/10.3390/molecules25040944.
(75) Peters, S.; Pillai, R. S.; Jasra, R. V. Significance of Extra-Framework Monovalent and Divalent Cation Motion upon CO2 and N2 Sorption in Zeolite X. *Mater. Today Proc.* **2022**, *68*, 85–92. https://doi.org/10.1016/j.matpr.2022.06.105.
(76) Pidko, E. A.; Hensen, E. J. M.; van Santen, R. A. Self-Organization of Extraframework Cations in Zeolites. *Proc. R. Soc. Math. Phys. Eng. Sci.* **2012**, *468* (2143), 2070–2086. https://doi.org/10.1098/rspa.2012.0057.

(77) Li, G.; Pidko, E. A. The Nature and Catalytic Function of Cation Sites in Zeolites: A Computational Perspective. *ChemCatChem* **2019**, *11* (1), 134–156. https://doi.org/10.1002/cctc.201801493.
(78) Zhang, Q.; Yu, J.; Corma, A. Applications of Zeolites to C1 Chemistry: Recent Advances, Challenges, and Opportunities. *Adv. Mater.* **2020**, *32* (44), 2002927. https://doi.org/10.1002/adma.202002927.
(79) Davis, M. E.; Lobo, R. F. Zeolite and Molecular Sieve Synthesis. *Chem. Mater.* **1992**, *4* (4), 756–768. https://doi.org/10.1021/cm00022a005.
(80) Cundy, C. S.; Cox, P. A. The Hydrothermal Synthesis of Zeolites: History and Development from the Earliest Days to the Present Time. *Chem. Rev.* **2003**, *103* (3), 663–702. https://doi.org/10.1021/cr020060i.
(81) Cundy, C. S.; Cox, P. A. The Hydrothermal Synthesis of Zeolites: Precursors, Intermediates and Reaction Mechanism. *Microporous Mesoporous Mater.* **2005**, *82* (1), 1–78. https://doi.org/10.1016/j.micromeso.2005.02.016.
(82) Moliner, M.; Martínez, C.; Corma, A. Synthesis Strategies for Preparing Useful Small Pore Zeolites and Zeotypes for Gas Separations and Catalysis. *Chem. Mater.* **2014**, *26* (1), 246–258. https://doi.org/10.1021/cm4015095.
(83) Li, J.; Corma, A.; Yu, J. Synthesis of New Zeolite Structures. *Chem. Soc. Rev.* **2015**, *44* (20), 7112–7127. https://doi.org/10.1039/C5CS00023H.
(84) Derbe, T.; Temesgen, S.; Bitew, M. A Short Review on Synthesis, Characterization, and Applications of Zeolites. *Adv. Mater. Sci. Eng.* **2021**, *2021*, e6637898. https://doi.org/10.1155/2021/6637898.
(85) Loewenstein, W. The Distribution of Aluminum in the Tetrahedra of Silicates and Aluminates. *Am. Mineral.* **1954**, *39* (1–2), 92–96.
(86) Larin, A. V. The Loewenstein Rule: The Increase in Electron Kinetic Energy as the Reason for Instability of Al–O–Al Linkage in Aluminosilicate Zeolites. *Phys. Chem. Miner.* **2013**, *40* (10), 771–780. https://doi.org/10.1007/s00269-013-0611-7.
(87) Fletcher, R. E.; Ling, S.; Slater, B. Violations of Löwenstein's Rule in Zeolites. *Chem. Sci.* **2017**, *8* (11), 7483–7491. https://doi.org/10.1039/C7SC02531A.
(88) Fant, M.; Ångqvist, M.; Hellman, A.; Erhart, P. To Every Rule There Is an Exception: A Rational Extension of Loewenstein's Rule. *Angew. Chem. Int. Ed.* **2021**, *60* (10), 5132–5135. https://doi.org/10.1002/anie.202013256.

(89) McCusker, L. B.; Liebau, F.; Engelhardt, G. Nomenclature of Structural and Compositional Characteristics of Ordered Microporous and Mesoporous Materials with Inorganic Hosts(IUPAC Recommendations 2001). *Pure Appl. Chem.* **2001**, *73* (2), 381–394. https://doi.org/10.1351/pac200173020381.
(90) Van Koningsveld, H. *Compendium of Zeolite Framework Types: Building Schemes and Type Characteristics*; Elsevier, 2007.
(91) Li, Y.; Yu, J. New Stories of Zeolite Structures: Their Descriptions, Determinations, Predictions, and Evaluations. *Chem. Rev.* **2014**, *114* (14), 7268–7316. https://doi.org/10.1021/cr500010r.
(92) *IZA Structure Commission*. http://www.iza-structure.org/ (accessed 2022-11-25).
(93) *Atlas of Zeolite Framework Types*; Elsevier, 2007. https://doi.org/10.1016/B978-0-444-53064-6.X5186-X.
(94) Ramos, F. S. O.; Pietre, M. K. de; Pastore, H. O. Lamellar Zeolites: An Oxymoron? *RSC Adv.* **2013**, *3* (7), 2084–2111. https://doi.org/10.1039/C2RA21573J.
(95) Roth, W. J.; Nachtigall, P.; Morris, R. E.; Čejka, J. Two-Dimensional Zeolites: Current Status and Perspectives. *Chem. Rev.* **2014**, *114* (9), 4807–4837. https://doi.org/10.1021/cr400600f.
(96) Díaz, U.; Corma, A. Layered Zeolitic Materials: An Approach to Designing Versatile Functional Solids. *Dalton Trans.* **2014**, *43* (27), 10292–10316. https://doi.org/10.1039/C3DT53181C.
(97) Roth, W. J.; Čejka, J. Two-Dimensional Zeolites: Dream or Reality? *Catal. Sci. Technol.* **2011**, *1* (1), 43–53. https://doi.org/10.1039/C0CY00027B.
(98) Tsapatsis, M. 2-Dimensional Zeolites. *AIChE J.* **2014**, *60* (7), 2374–2381. https://doi.org/10.1002/aic.14462.
(99) Liu, P.; Hou, J.; Zhang, Y.; Li, L.; Lu, X.; Tang, Z. Two-Dimensional Material Membranes for Critical Separations. *Inorg. Chem. Front.* **2020**, *7* (13), 2560–2581. https://doi.org/10.1039/D0QI00307G.
(100) Antúnez-García, J.; Galván, D. H.; Petranovskii, V.; Murrieta-Rico, F. N.; Yocupicio-Gaxiola, R. I.; Fuentes-Moyado, S. Theoretical Study of the Effect of Isomorphous Substitution by $$\hbox {Al}^{3+}$$ and/or $$\hbox {Fe}^{3+}$$ Cations to Tetrahedral Positions in the Framework of a Zeolite with Erionite Topology. *J. Mater. Sci.* **2019**, *54* (20), 13190–13199. https://doi.org/10.1007/s10853-019-03845-6.

(101) Yabushita, M.; Osuga, R.; Muramatsu, A. Control of Location and Distribution of Heteroatoms Substituted Isomorphously in Framework of Zeolites and Zeotype Materials. *CrystEngComm* **2021**, *23* (36), 6226–6233. https://doi.org/10.1039/D1CE00912E.
(102) Zhang, Q.; Gao, S.; Yu, J. Metal Sites in Zeolites: Synthesis, Characterization, and Catalysis. *Chem. Rev.* **2023**, *123* (9), 6039–6106. https://doi.org/10.1021/acs.chemrev.2c00315.
(103) Colella, C.; Wise, W. S. The IZA Handbook of Natural Zeolites: A Tool of Knowledge on the Most Important Family of Porous Minerals. *Microporous Mesoporous Mater.* **2014**, *189*, 4–10. https://doi.org/10.1016/j.micromeso.2013.08.028.
(104) Wilson, S. T.; Lok, B. M.; Messina, C. A.; Cannan, T. R.; Flanigen, E. M. Aluminophosphate Molecular Sieves: A New Class of Microporous Crystalline Inorganic Solids. *J. Am. Chem. Soc.* **1982**, *104* (4), 1146–1147. https://doi.org/10.1021/ja00368a062.
(105) Corà, F.; Alfredsson, M.; Barker, C. M.; Bell, R. G.; Foster, M. D.; Saadoune, I.; Simperler, A.; Catlow, C. R. A. Modeling the Framework Stability and Catalytic Activity of Pure and Transition Metal-Doped Zeotypes. *J. Solid State Chem.* **2003**, *176* (2), 496–529. https://doi.org/10.1016/S0022-4596(03)00275-5.
(106) Lok, B. M.; Messina, C. A.; Patton, R. L.; Gajek, R. T.; Cannan, T. R.; Flanigen, E. M. Silicoaluminophosphate Molecular Sieves: Another New Class of Microporous Crystalline Inorganic Solids. *J. Am. Chem. Soc.* **1984**, *106* (20), 6092–6093. https://doi.org/10.1021/ja00332a063.
(107) Potter, M. E. Down the Microporous Rabbit Hole of Silicoaluminophosphates: Recent Developments on Synthesis, Characterization, and Catalytic Applications. *ACS Catal.* **2020**, *10* (17), 9758–9789. https://doi.org/10.1021/acscatal.0c02278.
(108) Agliullin, M. R.; Kutepov, B. I.; Ostroumova, V. A.; Maximov, A. L. Silicoaluminophosphate Molecular Sieves SAPO-11 and SAPO-41: Synthesis, Properties, and Applications for Hydroisomerization of C16+ n-Paraffins. Part 1: Current State of Research on SAPO-11 and SAPO-41 Synthesis (A Review). *Pet. Chem.* **2021**, *61* (8), 836–851. https://doi.org/10.1134/S0965544121080028.
(109) Yu, W.; Wu, X.; Cheng, B.; Tao, T.; Min, X.; Mi, R.; Huang, Z.; Fang, M.; Liu, Y. Synthesis and Applications of SAPO-34 Molecular Sieves. *Chem. – Eur. J.* **2022**, *28* (11), e202102787. https://doi.org/10.1002/chem.202102787.

(110) Flanigen, E. M.; Lok, B. M.; Patton, R. L.; Wilson, S. T. Aluminophosphate Molecular Sieves and the Periodic Table. *Pure Appl. Chem.* **1986**, *58* (10), 1351–1358. https://doi.org/10.1351/pac198658101351.

(111) Hartmann, M.; Kevan, L. Transition-Metal Ions in Aluminophosphate and Silicoaluminophosphate Molecular Sieves: Location, Interaction with Adsorbates and Catalytic Properties. *Chem. Rev.* **1999**, *99* (3), 635–664. https://doi.org/10.1021/cr9600971.

(112) Thomas, J. M. Design, Synthesis, and In Situ Characterization of New Solid Catalysts. *Angew. Chem. Int. Ed.* **1999**, *38* (24), 3588–3628. https://doi.org/10.1002/(SICI)1521-3773(19991216)38:24<3588::AID-ANIE3588>3.0.CO;2-4.

(113) Thomas, J. M.; Raja, R.; Sankar, G.; Bell, R. G. Molecular Sieve Catalysts for the Regioselective and Shape- Selective Oxyfunctionalization of Alkanes in Air. *Acc. Chem. Res.* **2001**, *34* (3), 191–200. https://doi.org/10.1021/ar970020e.

(114) Harris, J. W.; Bates, J. S.; Bukowski, B. C.; Greeley, J.; Gounder, R. Opportunities in Catalysis over Metal-Zeotypes Enabled by Descriptions of Active Centers Beyond Their Binding Site. *ACS Catal.* **2020**, *10* (16), 9476–9495. https://doi.org/10.1021/acscatal.0c02102.

(115) Parlitz, B.; Lohse, U.; Schreier, E. Hydrolysis of □P□O□Al□ Bonds in AlPO4 and SAPO Molecular Sieves. *Microporous Mater.* **1994**, *2* (3), 223–228. https://doi.org/10.1016/0927-6513(93)E0054-K.

(116) Yu, J.; Xu, R. Insight into the Construction of Open-Framework Aluminophosphates. *Chem. Soc. Rev.* **2006**, *35* (7), 593–604. https://doi.org/10.1039/B505856M.

(117) Zhang, D.; Li, W.; Liu, Z.; Xu, R. Molecular Simulation of Methane Adsorption in Aluminophosphate Molecular Sieve AlPO4-11. *J. Mol. Struct. THEOCHEM* **2007**, *804* (1), 89–94. https://doi.org/10.1016/j.theochem.2006.09.032.

(118) Rouquerol, J.; Llewellyn, P.; Sing, K. 12 - Adsorption by Clays, Pillared Clays, Zeolites and Aluminophosphates. In *Adsorption by Powders and Porous Solids (Second Edition)*; Rouquerol, F., Rouquerol, J., Sing, K. S. W., Llewellyn, P., Maurin, G., Eds.; Academic Press: Oxford, 2014; pp 467–527. https://doi.org/10.1016/B978-0-08-097035-6.00012-7.

(119) Yu, Y.; Li, X.; Krishna, R.; Liu, Y.; Cui, Y.; Du, J.; Liang, Z.; Song, X.; Yu, J. Enhancing CO2 Adsorption and Separation Properties of Aluminophosphate Zeolites by Isomorphous

Heteroatom Substitutions. *ACS Appl. Mater. Interfaces* **2018**, *10* (50), 43570–43577. https://doi.org/10.1021/acsami.8b11235.

(120) Nagashima, H.; Martineau-Corcos, C.; Tricot, G.; Trébosc, J.; Pourpoint, F.; Amoureux, J.-P.; Lafon, O. Chapter Four - Recent Developments in NMR Studies of Aluminophosphates. In *Annual Reports on NMR Spectroscopy*; Webb, G. A., Ed.; Academic Press, 2018; Vol. 94, pp 113–185. https://doi.org/10.1016/bs.arnmr.2017.12.004.

(121) Kornatowski, J.; Finger, G.; Jancke, K.; Richter-Mendau, J.; Schultze, D.; Joswig, W.; Baur, W. H. Group Behaviour of SAPO-11 Molecular Sieves Containing Various Metals (Mg, Zn, Mn or Cd, Ni, Cr). *J. Chem. Soc. Faraday Trans.* **1994**, *90* (14), 2141–2146. https://doi.org/10.1039/FT9949002141.

(122) Kang, M. Methanol Conversion on Metal-Incorporated SAPO-34s (MeAPSO-34s). *J. Mol. Catal. Chem.* **2000**, *160* (2), 437–444. https://doi.org/10.1016/S1381-1169(00)00281-8.

(123) Salmasi, M.; Fatemi, S.; Taheri Najafabadi, A. Improvement of Light Olefins Selectivity and Catalyst Lifetime in MTO Reaction; Using Ni and Mg-Modified SAPO-34 Synthesized by Combination of Two Templates. *J. Ind. Eng. Chem.* **2011**, *17* (4), 755–761. https://doi.org/10.1016/j.jiec.2011.05.031.

(124) Sena, F. C.; de Souza, B. F.; de Almeida, N. C.; Cardoso, J. S.; Fernandes, L. D. Influence of Framework Composition over SAPO-34 and MeAPSO-34 Acidity. *Appl. Catal. Gen.* **2011**, *406* (1), 59–62. https://doi.org/10.1016/j.apcata.2011.08.010.

(125) Li, D.; Xing, B.; Wang, B.; Li, R. Theoretical Study of Zirconium Isomorphous Substitution into Zeolite Frameworks. *Molecules* **2019**, *24* (24), 4466. https://doi.org/10.3390/molecules24244466.

(126) Wang, T.; Yang, C.; Li, S.; Yu, G.; Liu, Z.; Wang, H.; Gao, P.; Sun, Y. Solvent-Free Synthesis of Mg-Incorporated Nanocrystalline SAPO-34 Zeolites via Natural Clay for Chloromethane-to-Olefin Conversion. *ACS Sustain. Chem. Eng.* **2020**, *8* (10), 4185–4193. https://doi.org/10.1021/acssuschemeng.9b07129.

(127) Dubois, D. R.; Obrzut, D. L.; Liu, J.; Thundimadathil, J.; Adekkanattu, P. M.; Guin, J. A.; Punnoose, A.; Seehra, M. S. Conversion of Methanol to Olefins over Cobalt-, Manganese- and Nickel-Incorporated SAPO-34 Molecular Sieves. *Fuel Process. Technol.* **2003**, *83* (1), 203–218. https://doi.org/10.1016/S0378-3820(03)00069-9.

(128) Blasco, T.; Chica, A.; Corma, A.; Murphy, W. J.; Agúndez-Rodríguez, J.; Pérez-Pariente, J. Changing the Si Distribution in SAPO-11 by Synthesis with Surfactants Improves the Hydroisomerization/Dewaxing Properties. *J. Catal.* **2006**, *242* (1), 153–161. https://doi.org/10.1016/j.jcat.2006.05.027.

(129) Zanjanchi, M. A.; Ghanadzadeh, A.; Khadem-Nahvi, F. Incorporation of Silicon into AlPO-5 Framework Sites: Higher Thermal Stability and Lower Extra-Framework Aluminum Concentration. *J. Incl. Phenom. Macrocycl. Chem.* **2002**, *42* (3), 295–299. https://doi.org/10.1023/A:1016015210310.

(130) Sánchez-Sánchez, M.; Sankar, G.; Gómez-Hortiguela, L. NMR Evidence of Different Conformations of Structure-Directing Cyclohexylamine in High-Doped AlPO4-44 Materials. *Microporous Mesoporous Mater.* **2008**, *114* (1), 485–494. https://doi.org/10.1016/j.micromeso.2008.01.036.

(131) Man, P. P.; Briend, M.; Peltre, M. J.; Lamy, A.; Beaunier, P.; Barthomeuf, D. A Topological Model for the Silicon Incorporation in SAPO-37 Molecular Sieves: Correlations with Acidity and Catalysis. *Zeolites* **1991**, *11* (6), 563–572. https://doi.org/10.1016/S0144-2449(05)80006-5.

(132) Murthy, K. V. V. S. B. S. R.; Kulkarni, S. J.; Khaja Masthan, S. Sorption Properties of Modified Silicoaluminophosphate(SAPO)-5 and SAPO-11 Molecular Sieves. *Microporous Mesoporous Mater.* **2001**, *43* (2), 201–209. https://doi.org/10.1016/S1387-1811(00)00364-4.

(133) Usman, M. Recent Progress of SAPO-34 Zeolite Membranes for CO2 Separation: A Review. *Membranes* **2022**, *12* (5), 507. https://doi.org/10.3390/membranes12050507.

(134) ghavipour, M.; Behbahani, R. M.; Rostami, R. B.; Lemraski, A. S. Methanol/Dimethyl Ether to Light Olefins over SAPO-34: Comprehensive Comparison of the Products Distribution and Catalyst Performance. *J. Nat. Gas Sci. Eng.* **2014**, *21*, 532–539. https://doi.org/10.1016/j.jngse.2014.09.015.

(135) Yadav, R.; Sakthivel, A. Silicoaluminophosphate Molecular Sieves as Potential Catalysts for Hydroisomerization of Alkanes and Alkenes. *Appl. Catal. Gen.* **2014**, *481*, 143–160. https://doi.org/10.1016/j.apcata.2014.05.010.

(136) Wulfers, M. J.; Teketel, S.; Ipek, B.; Lobo, R. F. Conversion of Methane to Methanol on Copper-Containing Small-Pore Zeolites and Zeotypes. *Chem. Commun.* **2015**, *51* (21), 4447–4450. https://doi.org/10.1039/C4CC09645B.

(137) Guan, B.; Jiang, H.; Peng, X.; Wei, Y.; Liu, Z.; Chen, T.; Lin, H.; Huang, Z. Promotional Effect and Mechanism of the Modification of Ce on the Enhanced NH3-SCR Efficiency and the Low Temperature Hydrothermal Stability over Cu/SAPO-34 Catalysts. *Appl. Catal. Gen.* **2021**, *617*, 118110. https://doi.org/10.1016/j.apcata.2021.118110.

(138) Rimaz, S.; Kosari, M.; Zarinejad, M.; Ramakrishna, S. A Comprehensive Review on Sustainability-Motivated Applications of SAPO-34 Molecular Sieve. *J. Mater. Sci.* **2022**, *57* (2), 848–886. https://doi.org/10.1007/s10853-021-06643-1.

(139) Elanany, M.; Vercauteren, D. P.; Kubo, M.; Miyamoto, A. The Acidic Properties of H-MeAlPO-5 (Me=Si, Ti, or Zr): A Periodic Density Functional Study. *J. Mol. Catal. Chem.* **2006**, *248* (1), 181–184. https://doi.org/10.1016/j.molcata.2005.12.026.

(140) Chatterjee, A. A Reactivity Index Study to Rationalize the Effect of Dopants on Brönsted and Lewis Acidity Occurring in MeAlPOs. *J. Mol. Graph. Model.* **2006**, *24* (4), 262–270. https://doi.org/10.1016/j.jmgm.2005.09.003.

(141) Modén, B.; Zhan, B.-Z.; Dakka, J.; Santiesteban, J. G.; Iglesia, E. Kinetics and Mechanism of Cyclohexane Oxidation on MnAPO-5 Catalysts. *J. Catal.* **2006**, *239* (2), 390–401. https://doi.org/10.1016/j.jcat.2006.02.006.

(142) Maurelli, S.; Vishnuvarthan, M.; Chiesa, M.; Berlier, G.; Van Doorslaer, S. Elucidating the Nature and Reactivity of Ti Ions Incorporated in the Framework of AlPO-5 Molecular Sieves. New Evidence from 31P HYSCORE Spectroscopy. *J. Am. Chem. Soc.* **2011**, *133* (19), 7340–7343. https://doi.org/10.1021/ja202210g.

(143) Potter, M. E.; Paterson, A. J.; Mishra, B.; Kelly, S. D.; Bare, S. R.; Corà, F.; Levy, A. B.; Raja, R. Spectroscopic and Computational Insights on Catalytic Synergy in Bimetallic Aluminophosphate Catalysts. *J. Am. Chem. Soc.* **2015**, *137* (26), 8534–8540. https://doi.org/10.1021/jacs.5b03734.

(144) Faraday, M. The Bakerian Lecture: Experimental Relations of Gold (and Other Metals) to Light. *Philos. Trans. R. Soc. Lond.* **1857**, *147*, 145–181.

(145) Ruivo, A.; Gomes, C.; Lima, A.; Botelho, M. L.; Melo, R.; Belchior, A.; Matos, A. P. de. Gold Nanoparticles in Ancient and Contemporary Ruby Glass. *J. Cult. Herit.* **2008**, *9*, e134.

(146) Cardell, C.; Guerra, I. Natural Corrosion-Induced Gold Nanoparticles Yield Purple Color of Alhambra Palaces Decoration. *Sci. Adv.* **2022**, *8* (36), eabn2541. https://doi.org/10.1126/sciadv.abn2541.

(147) Piening, H. Gold to Purple Violet Traces on Antique Marble. **2013**.
(148) Mapes, J. E.; Eischens, R. P. The Infrared Spectra of Ammonia Chemisorbed on Cracking Catalysts. *J. Phys. Chem.* **1954**, *58* (12), 1059–1062. https://doi.org/10.1021/j150522a002.
(149) Eischens, R. P.; Pliskin, W. A. The Infrared Spectra of Adsorbed Molecules. In *Advances in Catalysis*; Eley, D. D., Frankenburg, W. G., Komarewsky, V. I., Weisz, P. B., Eds.; Academic Press, 1958; Vol. 10, pp 1–56. https://doi.org/10.1016/S0360-0564(08)60403-4.
(150) Cotton, F. A. Metal Atom Clusters in Oxide Systems. *Inorg. Chem.* **1964**, *3* (9), 1217–1220. https://doi.org/10.1021/ic50019a003.
(151) Becker, E. W.; Bier, K.; Henkes, W. Strahlen aus kondensierten Atomen und Molekeln im Hochvakuum. *Z. Für Phys.* **1956**, *146* (3), 333–338. https://doi.org/10.1007/BF01330428.
(152) Bentley, P. G. Polymers of Carbon Dioxide. *Nature* **1961**, *190* (4774), 432–433. https://doi.org/10.1038/190432b0.
(153) Kantrowitz, A.; Grey, J. A High Intensity Source for the Molecular Beam. Part I. Theoretical. *Rev. Sci. Instrum.* **2004**, *22* (5), 328–332. https://doi.org/10.1063/1.1745921.
(154) Kistiakowsky, G. B.; Slichter, W. P. A High Intensity Source for the Molecular Beam. Part II. Experimental. *Rev. Sci. Instrum.* **2004**, *22* (5), 333–337. https://doi.org/10.1063/1.1745922.
(155) Hintenberger, H.; Franzen, J.; Schuy, K. D. Notizen: Die Periodizitäten in Den Häufigkeitsverteilungen Der Positiv Und Negativ Geladenen Vielatomigen Kohlenstoffmolekülionen Cn+ Und Cn- Im Hochfrequenzfunken Zwischen Graphitelektroden. *Z. Für Naturforschung A* **1963**, *18* (11), 1236–1237. https://doi.org/10.1515/zna-1963-1113.
(156) Cotton, F. A. Transition-Metal Compounds Containing Clusters of Metal Atoms. *Q. Rev. Chem. Soc.* **1966**, *20* (3), 389–401. https://doi.org/10.1039/QR9662000389.
(157) Robbins, E. J.; Leckenby, R. E.; Willis, P. The Ionization Potentials of Clustered Sodium Atoms. *Adv. Phys.* **1967**, *16* (64), 739–744. https://doi.org/10.1080/00018736700101865.
(158) Johnson, B. F. G.; Lewis, J.; Williams, I. G.; Wilson, J. M. Mass Spectra of Inorganic Molecules. Part I. Some Bridged Nitrosyl Complexes of Iron and Cobalt. *J. Chem. Soc. Inorg. Phys. Theor.* **1967**, No. 0, 338–341. https://doi.org/10.1039/J19670000338.

(159) CARON, L. G.; PRATT, G. W. Correlation and Magnetic Effects in Narrow Energy Bands. II. *Rev. Mod. Phys.* **1968**, *40* (4), 802–806. https://doi.org/10.1103/RevModPhys.40.802.
(160) Hortig, G.; Müller, M. Multiatomic Clusters Emerging from a Metal Surface under Ion Bombardment. *Z. Für Phys. Hadrons Nucl.* **1969**, *221* (2), 119–121. https://doi.org/10.1007/BF01392136.
(161) Castleman, A. W. Jr.; Khanna, S. N. Clusters, Superatoms, and Building Blocks of New Materials. *J. Phys. Chem. C* **2009**, *113* (7), 2664–2675. https://doi.org/10.1021/jp806850h.
(162) Luo, Z.; Castleman, A. W. Special and General Superatoms. *Acc. Chem. Res.* **2014**, *47* (10), 2931–2940. https://doi.org/10.1021/ar5001583.
(163) Somorjai, G. A.; Carrazza, J. Structure Sensitivity of Catalytic Reactions. *Ind. Eng. Chem. Fundam.* **1986**, *25* (1), 63–69. https://doi.org/10.1021/i100021a009.
(164) Ryali, S. B.; Fenn, J. B. Clustering in Free Jets — Aggregation by Dispersion. *Berichte Bunsenges. Für Phys. Chem.* **1984**, *88* (3), 245–253. https://doi.org/10.1002/bbpc.19840880315.
(165) Castleman, A. W.; Bowen, K. H. Clusters: Structure, Energetics, and Dynamics of Intermediate States of Matter. *J. Phys. Chem.* **1996**, *100* (31), 12911–12944. https://doi.org/10.1021/jp961030k.
(166) Binnig, G.; Rohrer, H.; Gerber, Ch.; Weibel, E. Tunneling through a Controllable Vacuum Gap. *Appl. Phys. Lett.* **1982**, *40* (2), 178–180. https://doi.org/10.1063/1.92999.
(167) Binnig, G.; Rohrer, H.; Gerber, Ch.; Weibel, E. Surface Studies by Scanning Tunneling Microscopy. *Phys. Rev. Lett.* **1982**, *49* (1), 57–61. https://doi.org/10.1103/PhysRevLett.49.57.
(168) Binnig, G.; Quate, C. F.; Gerber, Ch. Atomic Force Microscope. *Phys. Rev. Lett.* **1986**, *56* (9), 930–933. https://doi.org/10.1103/PhysRevLett.56.930.
(169) Bian, K.; Gerber, C.; Heinrich, A. J.; Müller, D. J.; Scheuring, S.; Jiang, Y. Scanning Probe Microscopy. *Nat. Rev. Methods Primer* **2021**, *1* (1), 1–29. https://doi.org/10.1038/s43586-021-00033-2.
(170) Knight, W. D.; Clemenger, K.; de Heer, W. A.; Saunders, W. A.; Chou, M. Y.; Cohen, M. L. Electronic Shell Structure and Abundances of Sodium Clusters. *Phys. Rev. Lett.* **1984**, *52* (24), 2141–2143. https://doi.org/10.1103/PhysRevLett.52.2141.

(171) Boudart, M. Heterogeneous Catalysis by Metals. *J. Mol. Catal.* **1985**, *30* (1), 27–38. https://doi.org/10.1016/0304-5102(85)80014-6.
(172) Kroto, H. W.; Heath, J. R.; O'Brien, S. C.; Curl, R. F.; Smalley, R. E. C60: Buckminsterfullerene. *Nature* **1985**, *318* (6042), 162–163. https://doi.org/10.1038/318162a0.
(173) Trevor, D. J.; Whetten, R. L.; Cox, D. M.; Kaldor, A. Gas Phase Platinum Cluster Reactions with Benzene and Several Hexanes: Evidence of Extensive Dehydrogenation and Size-Dependent Chemisorption. *J. Am. Chem. Soc.* **1985**, *107* (2), 518–519. https://doi.org/10.1021/ja00288a049.
(174) *Metal Clusters in Catalysis*; Gates, B. C., Guczi, L., Knözinger, H., Eds.; Studies in surface science and catalysis; Elsevier ; Distributors for the U.S.A. and Canada, Elsevier Science Pub. Co: Amsterdam ; New York : New York, NY, U.S.A, 1986.
(175) McElvany, S. W.; Creasy, W. R.; O'Keefe, A. Ion–Molecule Reaction Studies of Mass Selected Carbon Cluster Ions Formed by Laser Vaporization. *J. Chem. Phys.* **1986**, *85* (1), 632–633. https://doi.org/10.1063/1.451589.
(176) Kondow, Tamotsu. Ionization of Clusters in Collision with High-Rydberg Rare Gas Atoms. *J. Phys. Chem.* **1987**, *91* (6), 1307–1316. https://doi.org/10.1021/j100290a009.
(177) Haruta, M.; Kobayashi, T.; Sano, H.; Yamada, N. Novel Gold Catalysts for the Oxidation of Carbon Monoxide at a Temperature Far Below 0 °C. *Chem. Lett.* **1987**, *16* (2), 405–408. https://doi.org/10.1246/cl.1987.405.
(178) Bell, A. T. The Impact of Nanoscience on Heterogeneous Catalysis. *Science* **2003**, *299* (5613), 1688–1691. https://doi.org/10.1126/science.1083671.
(179) Murzin, D. Y.; Parmon, V. N. Quantification of Cluster Size Effect (Structure Sensitivity) in Heterogeneous Catalysis. **2011**. https://doi.org/10.1039/9781849732772-00179.
(180) Murzin, D. Yu. On Cluster Size Dependent Activity and Selectivity in Heterogeneous Catalysis. *Catal. Lett.* **2012**, *142* (11), 1279–1285. https://doi.org/10.1007/s10562-012-0896-z.
(181) Luo, Z.; Castleman, A. W. Jr.; Khanna, S. N. Reactivity of Metal Clusters. *Chem. Rev.* **2016**, *116* (23), 14456–14492. https://doi.org/10.1021/acs.chemrev.6b00230.
(182) Liu, L.; Corma, A. Metal Catalysts for Heterogeneous Catalysis: From Single Atoms to Nanoclusters and Nanoparticles.

Chem. Rev. **2018**, *118* (10), 4981–5079. https://doi.org/10.1021/acs.chemrev.7b00776.
(183) Liu, L.; Corma, A. Evolution of Isolated Atoms and Clusters in Catalysis. *Trends Chem.* **2020**, *2* (4), 383–400. https://doi.org/10.1016/j.trechm.2020.02.003.
(184) Cui, W.-G.; Hu, T.-L. Incorporation of Active Metal Species in Crystalline Porous Materials for Highly Efficient Synergetic Catalysis. *Small* **2021**, *17* (22), 2003971. https://doi.org/10.1002/smll.202003971.
(185) *The IUPAC Compendium of Chemical Terminology: The Gold Book*, 4th ed.; Gold, V., Ed.; International Union of Pure and Applied Chemistry (IUPAC): Research Triangle Park, NC, 2019. https://doi.org/10.1351/goldbook.
(186) Che, M.; Bennett, C. O. The Influence of Particle Size on the Catalytic Properties of Supported Metals. In *Advances in Catalysis*; Eley, D. D., Pines, H., Weisz, P. B., Eds.; Academic Press, 1989; Vol. 36, pp 55–172. https://doi.org/10.1016/S0360-0564(08)60017-6.
(187) Alonso, J. A. Electronic and Atomic Structure, and Magnetism of Transition-Metal Clusters. *Chem. Rev.* **2000**, *100* (2), 637–678. https://doi.org/10.1021/cr980391o.
(188) *Zeolites and Catalysis: Synthesis, Reactions and Applications*, 1st ed.; Čejka, J., Corma, A., Zones, S., Eds.; Wiley, 2010. https://doi.org/10.1002/9783527630295.
(189) Lu, Y.; Chen, W. Sub-Nanometre Sized Metal Clusters: From Synthetic Challenges to the Unique Property Discoveries. *Chem. Soc. Rev.* **2012**, *41* (9), 3594–3623. https://doi.org/10.1039/C2CS15325D.
(190) Goswami, N.; Li, J.; Xie, J. Chapter 11 - Functionalization and Application. In *Frontiers of Nanoscience*; Tsukuda, T., Häkkinen, H., Eds.; Protected Metal Clusters; Elsevier, 2015; Vol. 9, pp 297–345. https://doi.org/10.1016/B978-0-08-100086-1.00011-7.
(191) Park, H.; Shin, D. J.; Yu, J. Categorization of Quantum Dots, Clusters, Nanoclusters, and Nanodots. *J. Chem. Educ.* **2021**, *98* (3), 703–709. https://doi.org/10.1021/acs.jchemed.0c01403.
(192) Schmid, G.; Fenske, D. Metal Clusters and Nanoparticles. *Philos. Trans. R. Soc. Math. Phys. Eng. Sci.* **2010**, *368* (1915), 1207–1210. https://doi.org/10.1098/rsta.2009.0281.
(193) Chakraborty, I.; Pradeep, T. Atomically Precise Clusters of Noble Metals: Emerging Link between Atoms and Nanoparticles.

Chem. Rev. **2017**, *117* (12), 8208–8271. https://doi.org/10.1021/acs.chemrev.6b00769.
(194) Murray, R. W. Nanoelectrochemistry: Metal Nanoparticles, Nanoelectrodes, and Nanopores. *Chem. Rev.* **2008**, *108* (7), 2688–2720. https://doi.org/10.1021/cr068077e.
(195) Pelton, M.; Bryant, G. W. *Introduction to Metal-Nanoparticle Plasmonics*; A Wiley-Science Wise Co-Publication; Wiley, 2013.
(196) Wang, Y.; Herron, N. Nanometer-Sized Semiconductor Clusters: Materials Synthesis, Quantum Size Effects, and Photophysical Properties. *J. Phys. Chem.* **1991**, *95* (2), 525–532. https://doi.org/10.1021/j100155a009.
(197) Kang, X.; Zhu, M. Tailoring the Photoluminescence of Atomically Precise Nanoclusters. *Chem. Soc. Rev.* **2019**, *48* (8), 2422–2457. https://doi.org/10.1039/C8CS00800K.
(198) Sabarinathan, D.; Sharma, A. S.; Murugavelu, M.; Kirubasankar, B.; Balusamy, I.; Han, Z.; Li, H.; Chen, Q. Recent Advances in the Biomolecules Mediated Synthesis of Nanoclusters for Food Safety Analysis. *Heliyon* **2023**, *9* (5), e15655. https://doi.org/10.1016/j.heliyon.2023.e15655.
(199) Yang, Y.; Han, A.; Li, R.; Fang, G.; Liu, J.; Wang, S. Synthesis of Highly Fluorescent Gold Nanoclusters and Their Use in Sensitive Analysis of Metal Ions. *Analyst* **2017**, *142* (23), 4486–4493. https://doi.org/10.1039/C7AN01348E.
(200) Baghdasaryan, A.; Bürgi, T. Copper Nanoclusters: Designed Synthesis, Structural Diversity, and Multiplatform Applications. *Nanoscale* **2021**, *13* (13), 6283–6340. https://doi.org/10.1039/D0NR08489A.
(201) Chatterjee, S.; Lou, X.-Y.; Liang, F.; Yang, Y.-W. Surface-Functionalized Gold and Silver Nanoparticles for Colorimetric and Fluorescent Sensing of Metal Ions and Biomolecules. *Coord. Chem. Rev.* **2022**, *459*, 214461. https://doi.org/10.1016/j.ccr.2022.214461.
(202) Echt, O.; Sattler, K.; Recknagel, E. Magic Numbers for Sphere Packings: Experimental Verification in Free Xenon Clusters. *Phys. Rev. Lett.* **1981**, *47* (16), 1121–1124. https://doi.org/10.1103/PhysRevLett.47.1121.
(203) de Heer, W. A.; Knight, W. D.; Chou, M. Y.; Cohen, M. L. Electronic Shell Structure and Metal Clusters. In *Solid State Physics*; Ehrenreich, H., Turnbull, D., Eds.; Academic Press, 1987; Vol. 40, pp 93–181. https://doi.org/10.1016/S0081-1947(08)60691-8.

(204) Baletto, F.; Ferrando, R. Structural Properties of Nanoclusters: Energetic, Thermodynamic, and Kinetic Effects. *Rev. Mod. Phys.* **2005**, *77* (1), 371–423. https://doi.org/10.1103/RevModPhys.77.371.
(205) Khanna, S. N.; Jena, P. Designing Ionic Solids from Metallic Clusters. *Chem. Phys. Lett.* **1994**, *219* (5), 479–483. https://doi.org/10.1016/0009-2614(94)00097-2.
(206) Bergeron, D. E.; Castleman, A. W.; Morisato, T.; Khanna, S. N. Formation of Al13I-: Evidence for the Superhalogen Character of Al13. *Science* **2004**, *304* (5667), 84–87. https://doi.org/10.1126/science.1093902.
(207) Bergeron, D. E.; Roach, P. J.; Castleman, A. W.; Jones, N. O.; Khanna, S. N. Al Cluster Superatoms as Halogens in Polyhalides and as Alkaline Earths in Iodide Salts. *Science* **2005**, *307* (5707), 231–235. https://doi.org/10.1126/science.1105820.
(208) Khanna, S. N.; Jena, P. Atomic Clusters: Building Blocks for a Class of Solids. *Phys. Rev. B* **1995**, *51* (19), 13705–13716. https://doi.org/10.1103/PhysRevB.51.13705.
(209) Claridge, S. A.; Castleman, A. W. Jr.; Khanna, S. N.; Murray, C. B.; Sen, A.; Weiss, P. S. Cluster-Assembled Materials. *ACS Nano* **2009**, *3* (2), 244–255. https://doi.org/10.1021/nn800820e.
(210) Vilar-Vidal, N.; Rivas, J.; López-Quintela, M. A. Size Dependent Catalytic Activity of Reusable Subnanometer Copper(0) Clusters. *ACS Catal.* **2012**, *2* (8), 1693–1697. https://doi.org/10.1021/cs300355n.
(211) Qian, H.; Jiang, D.; Li, G.; Gayathri, C.; Das, A.; Gil, R. R.; Jin, R. Monoplatinum Doping of Gold Nanoclusters and Catalytic Application. *J. Am. Chem. Soc.* **2012**, *134* (39), 16159–16162. https://doi.org/10.1021/ja307657a.
(212) Rong, W.; Zou, H.; Zang, W.; Xi, S.; Wei, S.; Long, B.; Hu, J.; Ji, Y.; Duan, L. Size-Dependent Activity and Selectivity of Atomic-Level Copper Nanoclusters during CO/CO2 Electroreduction. *Angew. Chem. Int. Ed.* **2021**, *60* (1), 466–472. https://doi.org/10.1002/anie.202011836.
(213) Das, A.; Das, U.; Das, A. K. Relativistic Effects on the Chemical Bonding Properties of the Heavier Elements and Their Compounds. *Coord. Chem. Rev.* **2023**, *479*, 215000. https://doi.org/10.1016/j.ccr.2022.215000.
(214) Pyykkö, P. Relativistic Effects in Chemistry: More Common Than You Thought. *Annu. Rev. Phys. Chem.* **2012**, *63* (1), 45–64. https://doi.org/10.1146/annurev-physchem-032511-143755.

(215) Lee, H. M.; Kim, K. S. Observable Structures of Small Neutral and Anionic Gold Clusters. *Chem. – Eur. J.* **2012**, *18* (41), 13203–13207. https://doi.org/10.1002/chem.201200771.
(216) Chaves, A. S.; Rondina, G. G.; Piotrowski, M. J.; Tereshchuk, P.; Da Silva, J. L. F. The Role of Charge States in the Atomic Structure of Cun and Ptn (n = 2–14 Atoms) Clusters: A DFT Investigation. *J. Phys. Chem. A* **2014**, *118* (45), 10813–10821. https://doi.org/10.1021/jp508220h.
(217) Fernández, E.; Boronat, M.; Corma, A. Trends in the Reactivity of Molecular O2 with Copper Clusters: Influence of Size and Shape. *J. Phys. Chem. C* **2015**, *119* (34), 19832–19846. https://doi.org/10.1021/acs.jpcc.5b05023.
(218) Chen, B.; He, K.; Dai, W.; Gutsev, G. L.; Lu, C. Geometric and Electronic Diversity of Metal Doped Boron Clusters. *J. Phys. Condens. Matter* **2023**, *35* (18), 183002. https://doi.org/10.1088/1361-648X/acbf18.
(219) Fernández, E.; Boronat, M. Sub Nanometer Clusters in Catalysis. *J. Phys. Condens. Matter* **2018**, *31* (1), 013002. https://doi.org/10.1088/1361-648X/aaed84.
(220) Zhai, H.; Alexandrova, A. N. Fluxionality of Catalytic Clusters: When It Matters and How to Address It. *ACS Catal.* **2017**, *7* (3), 1905–1911. https://doi.org/10.1021/acscatal.6b03243.
(221) Fung, V.; Jiang, D. Exploring Structural Diversity and Fluxionality of Ptn (n = 10–13) Clusters from First-Principles. *J. Phys. Chem. C* **2017**, *121* (20), 10796–10802. https://doi.org/10.1021/acs.jpcc.6b11968.
(222) Mondal, U.; Ghosh, P. Role of Geometry, Charge and Fluxionality of Clusters in CO2 Activation on Supported Sub-Nanometer Metal Clusters: The Case of Cu Tetramers on Pristine and O-Terminated MXene. *Catal. Today* **2021**, *370*, 93–103. https://doi.org/10.1016/j.cattod.2020.09.002.
(223) Kulkarni, A.; Lobo-Lapidus, R. J.; Gates, B. C. Metal Clusters on Supports: Synthesis, Structure, Reactivity, and Catalytic Properties. *Chem. Commun.* **2010**, *46* (33), 5997–6015. https://doi.org/10.1039/C002707N.
(224) Mukherji, A.; Thorne, P.; Cheung, W. W. L.; Connors, S. L.; Garschagen, M.; Geden, O.; Hayward, B.; Simpson, N. P.; Totin, E.; Blok, K.; Eriksen, S.; Fischer, E.; Garner, G.; Guivarch, C.; Haasnoot, M.; Hermans, T.; Ley, D.; Lewis, J.; Nicholls, Z.; Niamir, L.; Szopa, S.; Trewin, B.; Howden, M.; Méndez, C.; Pereira, J.; Pichs, R.; Rose, S. K.; Saheb, Y.; Sánchez, R.; Xiao,

C.; Yassaa, N. SYNTHESIS REPORT OF THE IPCC SIXTH ASSESSMENT REPORT (AR6). **2023**.

(225) Lan, X.; Nisbet, E. G.; Dlugokencky, E. J.; Michel, S. E. What Do We Know about the Global Methane Budget? Results from Four Decades of Atmospheric CH4 Observations and the Way Forward. *Philos. Trans. R. Soc. Math. Phys. Eng. Sci.* **2021**, *379* (2210), 20200440. https://doi.org/10.1098/rsta.2020.0440.

(226) Offermanns, H.; Schulz, K.; Brandes, E.; Schendler, T. Substance Properties of Methanol. In *Methanol: The Basic Chemical and Energy Feedstock of the Future: Asinger's Vision Today*; Bertau, M., Offermanns, H., Plass, L., Schmidt, F., Wernicke, H.-J., Eds.; Springer: Berlin, Heidelberg, 2014; pp 303–325. https://doi.org/10.1007/978-3-642-39709-7_5.

(227) Simon Araya, S.; Liso, V.; Cui, X.; Li, N.; Zhu, J.; Sahlin, S. L.; Jensen, S. H.; Nielsen, M. P.; Kær, S. K. A Review of The Methanol Economy: The Fuel Cell Route. *Energies* **2020**, *13* (3), 596. https://doi.org/10.3390/en13030596.

(228) Bennett, R. K.; Steinberg, L. M.; Chen, W.; Papoutsakis, E. T. Engineering the Bioconversion of Methane and Methanol to Fuels and Chemicals in Native and Synthetic Methylotrophs. *Curr. Opin. Biotechnol.* **2018**, *50*, 81–93. https://doi.org/10.1016/j.copbio.2017.11.010.

(229) Molino, A.; Larocca, V.; Chianese, S.; Musmarra, D. Biofuels Production by Biomass Gasification: A Review. *Energies* **2018**, *11* (4), 811. https://doi.org/10.3390/en11040811.

(230) Liaquat, A. M.; Kalam, M. A.; Masjuki, H. H.; Jayed, M. H. Potential Emissions Reduction in Road Transport Sector Using Biofuel in Developing Countries. *Atmos. Environ.* **2010**, *44* (32), 3869–3877. https://doi.org/10.1016/j.atmosenv.2010.07.003.

(231) Shojae, K.; Mahdavian, M. Environmental Effects of Using Methanol as a Biofuel into the Combustion Chamber of a Heavy-Duty Diesel Engine. *Adv. Environ. Technol.* **2016**, *2* (1), 1–10. https://doi.org/10.22104/aet.2016.328.

(232) Alberico, E.; Nielsen, M. Towards a Methanol Economy Based on Homogeneous Catalysis: Methanol to H2 and CO2 to Methanol. *Chem. Commun.* **2015**, *51* (31), 6714–6725. https://doi.org/10.1039/C4CC09471A.

(233) Bertau, M.; Wernicke, H. J.; Schmidt, F.; Standt, U.-D.; Seyfried, F.; Buchholz, S.; Busch, G.; Winterberg, M.; Reichelt, L.; Pätzold, C.; Pohl, S.; Plass, L.; Roes, J.; Steffen, M.; Sandstede, G.; Heinzel, A.; Hippmann, S.; Holtmann, D.; Sonntag, F.; Veith, T.; Schrader, J. Methanol Utilisation

Technologies. In *Methanol: The Basic Chemical and Energy Feedstock of the Future: Asinger's Vision Today*; Bertau, M., Offermanns, H., Plass, L., Schmidt, F., Wernicke, H.-J., Eds.; Springer: Berlin, Heidelberg, 2014; pp 327–601. https://doi.org/10.1007/978-3-642-39709-7_6.

(234) Younas, M.; Shafique, S.; Hafeez, A.; Javed, F.; Rehman, F. An Overview of Hydrogen Production: Current Status, Potential, and Challenges. *Fuel* **2022**, *316*, 123317. https://doi.org/10.1016/j.fuel.2022.123317.

(235) Capurso, T.; Stefanizzi, M.; Torresi, M.; Camporeale, S. M. Perspective of the Role of Hydrogen in the 21st Century Energy Transition. *Energy Convers. Manag.* **2022**, *251*, 114898. https://doi.org/10.1016/j.enconman.2021.114898.

(236) Choudhary, T. V.; Choudhary, V. R. Energy-Efficient Syngas Production through Catalytic Oxy-Methane Reforming Reactions. *Angew. Chem. Int. Ed.* **2008**, *47* (10), 1828–1847. https://doi.org/10.1002/anie.200701237.

(237) Tang, P.; Zhu, Q.; Wu, Z.; Ma, D. Methane Activation: The Past and Future. *Energy Environ. Sci.* **2014**, *7* (8), 2580–2591. https://doi.org/10.1039/C4EE00604F.

(238) Karakaya, C.; Kee, R. J. Progress in the Direct Catalytic Conversion of Methane to Fuels and Chemicals. *Prog. Energy Combust. Sci.* **2016**, *55*, 60–97. https://doi.org/10.1016/j.pecs.2016.04.003.

(239) Li, D.; Xu, R.; Gu, Z.; Zhu, X.; Qing, S.; Li, K. Chemical-Looping Conversion of Methane: A Review. *Energy Technol.* **2020**, *8* (8), 1900925. https://doi.org/10.1002/ente.201900925.

(240) Liu, Y.; Deng, D.; Bao, X. Catalysis for Selected C1 Chemistry. *Chem* **2020**, *6* (10), 2497–2514. https://doi.org/10.1016/j.chempr.2020.08.026.

(241) Tang, Y.; Li, Y.; Tao, F. (Feng). Activation and Catalytic Transformation of Methane under Mild Conditions. *Chem. Soc. Rev.* **2022**, *51* (1), 376–423. https://doi.org/10.1039/D1CS00783A.

(242) Jabbour, K. Tuning Combined Steam and Dry Reforming of Methane for "Metgas" Production: A Thermodynamic Approach and State-of-the-Art Catalysts. *J. Energy Chem.* **2020**, *48*, 54–91. https://doi.org/10.1016/j.jechem.2019.12.017.

(243) Zhang, H.; Sun, Z.; Hu, Y. H. Steam Reforming of Methane: Current States of Catalyst Design and Process Upgrading. *Renew. Sustain. Energy Rev.* **2021**, *149*, 111330. https://doi.org/10.1016/j.rser.2021.111330.

(244) Fan, L.; Li, C.; van Biert, L.; Zhou, S.-H.; Tabish, A. N.; Mokhov, A.; Aravind, P. V.; Cai, W. Advances on Methane Reforming in Solid Oxide Fuel Cells. *Renew. Sustain. Energy Rev.* **2022**, *166*, 112646. https://doi.org/10.1016/j.rser.2022.112646.

(245) Torimoto, M.; Sekine, Y. Effects of Alloying for Steam or Dry Reforming of Methane: A Review of Recent Studies. *Catal. Sci. Technol.* **2022**, *12* (11), 3387–3411. https://doi.org/10.1039/D2CY00066K.

(246) Wang, S.; Nabavi, S. A.; Clough, P. T. A Review on Bi/Polymetallic Catalysts for Steam Methane Reforming. *Int. J. Hydrog. Energy* **2023**. https://doi.org/10.1016/j.ijhydene.2023.01.034.

(247) Pakhare, D.; Spivey, J. A Review of Dry (CO2) Reforming of Methane over Noble Metal Catalysts. *Chem. Soc. Rev.* **2014**, *43* (22), 7813–7837. https://doi.org/10.1039/C3CS60395D.

(248) Abdullah, B.; Abd Ghani, N. A.; Vo, D.-V. N. Recent Advances in Dry Reforming of Methane over Ni-Based Catalysts. *J. Clean. Prod.* **2017**, *162*, 170–185. https://doi.org/10.1016/j.jclepro.2017.05.176.

(249) Chen, Y.; deGlee, B.; Tang, Y.; Wang, Z.; Zhao, B.; Wei, Y.; Zhang, L.; Yoo, S.; Pei, K.; Kim, J. H.; Ding, Y.; Hu, P.; Tao, F. F.; Liu, M. A Robust Fuel Cell Operated on Nearly Dry Methane at 500 °C Enabled by Synergistic Thermal Catalysis and Electrocatalysis. *Nat. Energy* **2018**, *3* (12), 1042–1050. https://doi.org/10.1038/s41560-018-0262-5.

(250) Abdulrasheed, A.; Jalil, A. A.; Gambo, Y.; Ibrahim, M.; Hambali, H. U.; Shahul Hamid, M. Y. A Review on Catalyst Development for Dry Reforming of Methane to Syngas: Recent Advances. *Renew. Sustain. Energy Rev.* **2019**, *108*, 175–193. https://doi.org/10.1016/j.rser.2019.03.054.

(251) Yentekakis, I. V.; Panagiotopoulou, P.; Artemakis, G. A Review of Recent Efforts to Promote Dry Reforming of Methane (DRM) to Syngas Production via Bimetallic Catalyst Formulations. *Appl. Catal. B Environ.* **2021**, *296*, 120210. https://doi.org/10.1016/j.apcatb.2021.120210.

(252) Yoon, Y.; You, H. M.; Kim, H. J.; Curnan, M. T.; Kim, K.; Han, J. W. Computational Catalyst Design for Dry Reforming of Methane: A Review. *Energy Fuels* **2022**, *36* (17), 9844–9865. https://doi.org/10.1021/acs.energyfuels.2c01776.

(253) Malik, M. I.; Achouri, I. E.; Abatzoglou, N.; Gitzhofer, F. Intensified Performance of Methane Dry Reforming Based on

Non-Thermal Plasma Technology: Recent Progress and Key Challenges. *Fuel Process. Technol.* **2023**, *245*, 107748. https://doi.org/10.1016/j.fuproc.2023.107748.

(254) Christian Enger, B.; Lødeng, R.; Holmen, A. A Review of Catalytic Partial Oxidation of Methane to Synthesis Gas with Emphasis on Reaction Mechanisms over Transition Metal Catalysts. *Appl. Catal. Gen.* **2008**, *346* (1), 1–27. https://doi.org/10.1016/j.apcata.2008.05.018.

(255) Tang, M.; Xu, L.; Fan, M. Progress in Oxygen Carrier Development of Methane-Based Chemical-Looping Reforming: A Review. *Appl. Energy* **2015**, *151*, 143–156. https://doi.org/10.1016/j.apenergy.2015.04.017.

(256) Arku, P.; Regmi, B.; Dutta, A. A Review of Catalytic Partial Oxidation of Fossil Fuels and Biofuels: Recent Advances in Catalyst Development and Kinetic Modelling. *Chem. Eng. Res. Des.* **2018**, *136*, 385–402. https://doi.org/10.1016/j.cherd.2018.05.044.

(257) Jin, Z.; Wang, L.; Zuidema, E.; Mondal, K.; Zhang, M.; Zhang, J.; Wang, C.; Meng, X.; Yang, H.; Mesters, C.; Xiao, F.-S. Hydrophobic Zeolite Modification for in Situ Peroxide Formation in Methane Oxidation to Methanol. *Science* **2020**, *367* (6474), 193–197. https://doi.org/10.1126/science.aaw1108.

(258) Shi, S.; Sun, Z.; Bao, C.; Gao, T.; Hu, Y. H. The Special Route toward Conversion of Methane to Methanol on a Fluffy Metal-Free Carbon Nitride Photocatalyst in the Presence of H2O2. *Int. J. Energy Res.* **2020**, *44* (4), 2740–2753. https://doi.org/10.1002/er.5088.

(259) Tanios, C.; Labaki, M. Chapter 5 - Catalytic Reforming: A Sustainable Technology for Hydrogen Production. In *Recent Advances in Renewable Energy Technologies*; Jeguirim, M., Ed.; Academic Press, 2022; pp 199–247. https://doi.org/10.1016/B978-0-12-823532-4.00008-2.

(260) Soleimani, S.; Lehner, M. Tri-Reforming of Methane: Thermodynamics, Operating Conditions, Reactor Technology and Efficiency Evaluation—A Review. *Energies* **2022**, *15* (19), 7159. https://doi.org/10.3390/en15197159.

(261) Narsimhan, K.; Iyoki, K.; Dinh, K.; Román-Leshkov, Y. Catalytic Oxidation of Methane into Methanol over Copper-Exchanged Zeolites with Oxygen at Low Temperature. *ACS Cent. Sci.* **2016**, *2* (6), 424–429. https://doi.org/10.1021/acscentsci.6b00139.

(262) Latimer, A. A.; Kakekhani, A.; Kulkarni, A. R.; Nørskov, J. K. Direct Methane to Methanol: The Selectivity–Conversion Limit and Design Strategies. *ACS Catal.* **2018**, *8* (8), 6894–6907. https://doi.org/10.1021/acscatal.8b00220.

(263) Dinh, K. T.; Sullivan, M. M.; Narsimhan, K.; Serna, P.; Meyer, R. J.; Dincă, M.; Román-Leshkov, Y. Continuous Partial Oxidation of Methane to Methanol Catalyzed by Diffusion-Paired Copper Dimers in Copper-Exchanged Zeolites. *J. Am. Chem. Soc.* **2019**, *141* (29), 11641–11650. https://doi.org/10.1021/jacs.9b04906.

(264) Lange, J.-P.; Sushkevich, V. L.; Knorpp, A. J.; van Bokhoven, J. A. Methane-to-Methanol via Chemical Looping: Economic Potential and Guidance for Future Research. *Ind. Eng. Chem. Res.* **2019**, *58* (20), 8674–8680. https://doi.org/10.1021/acs.iecr.9b01407.

(265) Zakaria, Z.; Kamarudin, S. K. Direct Conversion Technologies of Methane to Methanol: An Overview. *Renew. Sustain. Energy Rev.* **2016**, *65*, 250–261. https://doi.org/10.1016/j.rser.2016.05.082.

(266) Ravi, M.; Ranocchiari, M.; van Bokhoven, J. A. The Direct Catalytic Oxidation of Methane to Methanol—A Critical Assessment. *Angew. Chem. Int. Ed.* **2017**, *56* (52), 16464–16483. https://doi.org/10.1002/anie.201702550.

(267) Ravi, M.; Sushkevich, V. L.; Knorpp, A. J.; Newton, M. A.; Palagin, D.; Pinar, A. B.; Ranocchiari, M.; van Bokhoven, J. A. Misconceptions and Challenges in Methane-to-Methanol over Transition-Metal-Exchanged Zeolites. *Nat. Catal.* **2019**, *2* (6), 485–494. https://doi.org/10.1038/s41929-019-0273-z.

(268) Jovanovic, Z. R.; Lange, J.-P.; Ravi, M.; Knorpp, A. J.; Sushkevich, V. L.; Newton, M. A.; Palagin, D.; van Bokhoven, J. A. Oxidation of Methane to Methanol over Cu-Exchanged Zeolites: Scientia Gratia Scientiae or Paradigm Shift in Natural Gas Valorization? *J. Catal.* **2020**, *385*, 238–245. https://doi.org/10.1016/j.jcat.2020.02.001.

(269) Wang, Y.; Hu, P.; Yang, J.; Zhu, Y.-A.; Chen, D. C–H Bond Activation in Light Alkanes: A Theoretical Perspective. *Chem. Soc. Rev.* **2021**, *50* (7), 4299–4358. https://doi.org/10.1039/D0CS01262A.

(270) Sushkevich, V. L.; van Bokhoven, J. A. Methane-to-Methanol: Activity Descriptors in Copper-Exchanged Zeolites for the Rational Design of Materials. *ACS Catal.* **2019**, *9* (7), 6293–6304. https://doi.org/10.1021/acscatal.9b01534.

(271) Sushkevich, V. L.; Palagin, D.; Ranocchiari, M.; van Bokhoven, J. A. Selective Anaerobic Oxidation of Methane Enables Direct Synthesis of Methanol. *Science* **2017**, *356* (6337), 523–527. https://doi.org/10.1126/science.aam9035.
(272) Sushkevich, V. L.; Bokhoven, J. A. van. Effect of Brønsted Acid Sites on the Direct Conversion of Methane into Methanol over Copper-Exchanged Mordenite. *Catal. Sci. Technol.* **2018**, *8* (16), 4141–4150. https://doi.org/10.1039/C8CY01055B.
(273) Sushkevich, V. L.; Bokhoven, J. A. van. Kinetic Study and Effect of Water on Methane Oxidation to Methanol over Copper-Exchanged Mordenite. *Catal. Sci. Technol.* **2020**, *10* (2), 382–390. https://doi.org/10.1039/C9CY01711A.
(274) Sushkevich, V. L.; Verel, R.; van Bokhoven, J. A. Pathways of Methane Transformation over Copper-Exchanged Mordenite as Revealed by In Situ NMR and IR Spectroscopy. *Angew. Chem.* **2020**, *132* (2), 920–928. https://doi.org/10.1002/ange.201912668.
(275) Artsiusheuski, M. A.; Verel, R.; van Bokhoven, J. A.; Sushkevich, V. L. Mechanism of Hydrocarbon Formation in Methane and Methanol Conversion over Copper-Containing Mordenite. *ACS Catal.* **2023**, *13* (9), 5864–5875. https://doi.org/10.1021/acscatal.2c06312.
(276) Zhao, G.; Yan, P.; Procter, K.; Adesina, A.; Jin, Y.; Kennedy, E.; Stockenhuber, M. Effect of Desilication on the Catalytic Activity of Fe-FER for Direct, Selective, Partial Oxidation of Methane. *J. Catal.* **2023**, *417*, 140–152. https://doi.org/10.1016/j.jcat.2022.11.030.
(277) Gabrienko, A. A.; Yashnik, S. A.; Kolganov, A. A.; Sheveleva, A. M.; Arzumanov, S. S.; Fedin, M. V.; Tuna, F.; Stepanov, A. G. Methane Activation on H-ZSM-5 Zeolite with Low Copper Loading. The Nature of Active Sites and Intermediates Identified with the Combination of Spectroscopic Methods. *Inorg. Chem.* **2020**, *59* (3), 2037–2050. https://doi.org/10.1021/acs.inorgchem.9b03462.
(278) Zheng, J.; Lee, I.; Khramenkova, E.; Wang, M.; Peng, B.; Gutiérrez, O. Y.; Fulton, J. L.; Camaioni, D. M.; Khare, R.; Jentys, A.; Haller, G. L.; Pidko, E. A.; Sanchez-Sanchez, M.; Lercher, J. A. Importance of Methane Chemical Potential for Its Conversion to Methanol on Cu-Exchanged Mordenite. *Chem. – Eur. J.* **2020**, *26* (34), 7563–7567. https://doi.org/10.1002/chem.202000772.
(279) Wu, J.-F.; Gao, X.-D.; Wu, L.-M.; Wang, W. D.; Yu, S.-M.; Bai, S. Mechanistic Insights on the Direct Conversion of Methane

into Methanol over Cu/Na–ZSM-5 Zeolite: Evidence from EPR and Solid-State NMR. *ACS Catal.* **2019**, *9* (9), 8677–8681. https://doi.org/10.1021/acscatal.9b02898.

(280) Lin, R.; Amrute, A. P.; Pérez-Ramírez, J. Halogen-Mediated Conversion of Hydrocarbons to Commodities. *Chem. Rev.* **2017**, *117* (5), 4182–4247. https://doi.org/10.1021/acs.chemrev.6b00551.

(281) Schwartz, N. A.; Boaz, N. C.; Kalman, S. E.; Zhuang, T.; Goldberg, J. M.; Fu, R.; Nielsen, R. J.; Goddard, W. A. I.; Groves, J. T.; Gunnoe, T. B. Mechanism of Hydrocarbon Functionalization by an Iodate/Chloride System: The Role of Ester Protection. *ACS Catal.* **2018**, *8* (4), 3138–3149. https://doi.org/10.1021/acscatal.7b04397.

(282) Periana, R. A.; Taube, D. J.; Evitt, E. R.; Löffler, D. G.; Wentrcek, P. R.; Voss, G.; Masuda, T. A Mercury-Catalyzed, High-Yield System for the Oxidation of Methane to Methanol. *Science* **1993**, *259* (5093), 340–343. https://doi.org/10.1126/science.259.5093.340.

(283) Periana, R. A.; Taube, D. J.; Gamble, S.; Taube, H.; Satoh, T.; Fujii, H. Platinum Catalysts for the High-Yield Oxidation of Methane to a Methanol Derivative. *Science* **1998**, *280* (5363), 560–564. https://doi.org/10.1126/science.280.5363.560.

(284) Michalkiewicz, B. Methane Conversion to Methanol in Condensed Phase. *Kinet. Catal.* **2003**, *44* (6), 801–805. https://doi.org/10.1023/B:KICA.0000009057.79026.0b.

(285) Periana, R. A.; Bhalla, G.; Tenn, W. J.; Young, K. J. H.; Liu, X. Y.; Mironov, O.; Jones, C.; Ziatdinov, V. R. Perspectives on Some Challenges and Approaches for Developing the next Generation of Selective, Low Temperature, Oxidation Catalysts for Alkane Hydroxylation Based on the CH Activation Reaction. *J. Mol. Catal. Chem.* **2004**, *220* (1), 7–25. https://doi.org/10.1016/j.molcata.2004.05.036.

(286) Davico, G. E. The Conversion of Methane to Methanol: A Reaction Catalyzed by I+ or I2+? *J. Phys. Chem. A* **2005**, *109* (15), 3433–3437. https://doi.org/10.1021/jp050046k.

(287) Kao, L. C.; Hutson, A. C.; Sen, A. Low-Temperature, Palladium(II)-Catalyzed, Solution-Phase Oxidation of Methane to Methanol Derivative. *J. Am. Chem. Soc.* **1991**, *113* (2), 700–701. https://doi.org/10.1021/ja00002a063.

(288) Muehlhofer, M.; Strassner, T.; Herrmann, W. A. New Catalyst Systems for the Catalytic Conversion of Methane into Methanol. *Angew. Chem. Int. Ed.* **2002**, *41* (10), 1745–1747.

https://doi.org/10.1002/1521-3773(20020517)41:10<1745::AID-ANIE1745>3.0.CO;2-E.

(289) Prakash, G. K. S. *Selective Bromination of Methane over Solid Acid Catalysts and Poly (4-Vinyl Pyridine) Catalyzed Hydrolysis and Methanolysis of Methyl Bromide*; 2011.

(290) Vargaftik, M. N.; Stolarov, I. P.; Moiseev, I. I. Highly Selective Partial Oxidation of Methane to Methyl Trifluoroacetate. *J. Chem. Soc. Chem. Commun.* **1990**, No. 15, 1049–1050. https://doi.org/10.1039/C39900001049.

(291) Strassner, T.; Muehlhofer, M.; Zeller, A.; Herdtweck, E.; Herrmann, W. A. The Counterion Influence on the CH-Activation of Methane by Palladium(II) Biscarbene Complexes – Structures, Reactivity and DFT Calculations. *J. Organomet. Chem.* **2004**, *689* (8), 1418–1424. https://doi.org/10.1016/j.jorganchem.2004.02.013.

(292) Yuan, J.; Wang, L.; Wang, Y. Direct Oxidation of Methane to a Methanol Derivative Using Molecular Oxygen. *Ind. Eng. Chem. Res.* **2011**, *50* (10), 6513–6516. https://doi.org/10.1021/ie1018113.

(293) Zhang, Y.; Zhang, M.; Han, Z.; Huang, S.; Yuan, D.; Su, W. Atmosphere-Pressure Methane Oxidation to Methyl Trifluoroacetate Enabled by a Porous Organic Polymer-Supported Single-Site Palladium Catalyst. *ACS Catal.* **2021**, *11* (3), 1008–1013. https://doi.org/10.1021/acscatal.0c05205.

(294) An, Z.; Pan, X.; Liu, X.; Han, X.; Bao, X. Combined Redox Couples for Catalytic Oxidation of Methane by Dioxygen at Low Temperatures. *J. Am. Chem. Soc.* **2006**, *128* (50), 16028–16029. https://doi.org/10.1021/ja0647912.

(295) Li, T.; Wang, S. J.; Yu, C. S.; Ma, Y. C.; Li, K. L.; Lin, L. W. Direct Conversion of Methane to Methanol over Nano-[Au/SiO2] in [Bmim]Cl Ionic Liquid. *Appl. Catal. Gen.* **2011**, *398* (1), 150–154. https://doi.org/10.1016/j.apcata.2011.03.028.

(296) Coutard, N.; Musgrave, C. B. I.; Moon, J.; Liebov, N. S.; Nielsen, R. M.; Goldberg, J. M.; Li, M.; Jia, X.; Lee, S.; Dickie, D. A.; Schinski, W. L.; Wu, Z.; Groves, J. T.; Goddard, W. A. I.; Gunnoe, T. B. Manganese Catalyzed Partial Oxidation of Light Alkanes. *ACS Catal.* **2022**, *12* (9), 5356–5370. https://doi.org/10.1021/acscatal.2c00982.

(297) Ma, J.; Zhu, C.; Mao, K.; Jiang, W.; Low, J.; Duan, D.; Ju, H.; Liu, D.; Wang, K.; Zang, Y.; Chen, S.; Zhang, H.; Qi, Z.; Long, R.; Liu, Z.; Song, L.; Xiong, Y. Sustainable Methane Utilization Technology via Photocatalytic Halogenation with Alkali Halides.

Nat. Commun. **2023**, *14* (1), 1410. https://doi.org/10.1038/s41467-023-36977-0.

(298) Ji, Y.; Blankenship, A. N.; van Bokhoven, J. A. Heterogeneous Mn-Based Catalysts for the Aerobic Conversion of Methane-to-Methyl Trifluoroacetate. *ACS Catal.* **2023**, *13* (6), 3896–3901. https://doi.org/10.1021/acscatal.2c06292.

(299) Yang, J.; Chang, Y.; Dai, W.; Wu, G.; Guan, N.; Li, L. Ru-In/H-SSZ-13 for the Selective Reduction of Nitric Oxide by Methane: Insights from Temperature-Programmed Desorption Studies. *Appl. Catal. B Environ.* **2018**, *236*, 404–412. https://doi.org/10.1016/j.apcatb.2018.05.048.

(300) Göltl, F.; Bhandari, S.; Mavrikakis, M. Thermodynamics Perspective on the Stepwise Conversion of Methane to Methanol over Cu-Exchanged SSZ-13. *ACS Catal.* **2021**, *11* (13), 7719–7734. https://doi.org/10.1021/acscatal.1c00691.

(301) Ruscic, B. Active Thermochemical Tables: Sequential Bond Dissociation Enthalpies of Methane, Ethane, and Methanol and the Related Thermochemistry. *J. Phys. Chem. A* **2015**, *119* (28), 7810–7837. https://doi.org/10.1021/acs.jpca.5b01346.

(302) Nkinahamira, F.; Yang, R.; Zhu, R.; Zhang, J.; Ren, Z.; Sun, S.; Xiong, H.; Zeng, Z. Current Progress on Methods and Technologies for Catalytic Methane Activation at Low Temperatures. *Adv. Sci.* **2023**, *10* (5), 2204566. https://doi.org/10.1002/advs.202204566.

(303) Palkovits, R.; von Malotki, C.; Baumgarten, M.; Müllen, K.; Baltes, C.; Antonietti, M.; Kuhn, P.; Weber, J.; Thomas, A.; Schüth, F. Development of Molecular and Solid Catalysts for the Direct Low-Temperature Oxidation of Methane to Methanol. *ChemSusChem* **2010**, *3* (2), 277–282. https://doi.org/10.1002/cssc.200900123.

(304) Gunsalus, N. J.; Koppaka, A.; Park, S. H.; Bischof, S. M.; Hashiguchi, B. G.; Periana, R. A. Homogeneous Functionalization of Methane. *Chem. Rev.* **2017**, *117* (13), 8521–8573. https://doi.org/10.1021/acs.chemrev.6b00739.

(305) Fersht, A. *Structure and Mechanism in Protein Science: A Guide to Enzyme Catalysis and Protein Folding*; W.H. Freeman: New York, 1999.

(306) Sirajuddin, S.; Barupala, D.; Helling, S.; Marcus, K.; Stemmler, T. L.; Rosenzweig, A. C. Effects of Zinc on Particulate Methane Monooxygenase Activity and Structure*. *J. Biol. Chem.* **2014**, *289* (31), 21782–21794. https://doi.org/10.1074/jbc.M114.581363.

(307) Wang, V. C.-C.; Maji, S.; Chen, P. P.-Y.; Lee, H. K.; Yu, S. S.-F.; Chan, S. I. Alkane Oxidation: Methane Monooxygenases, Related Enzymes, and Their Biomimetics. *Chem. Rev.* **2017**, *117* (13), 8574–8621. https://doi.org/10.1021/acs.chemrev.6b00624.
(308) Zhang, S.; Karthikeyan, R.; Fernando, S. D. Low-Temperature Biological Activation of Methane: Structure, Function and Molecular Interactions of Soluble and Particulate Methane Monooxygenases. *Rev. Environ. Sci. Biotechnol.* **2017**, *16* (4), 611–623. https://doi.org/10.1007/s11157-017-9447-9.
(309) Pham, D. N.; Nguyen, A. D.; Lee, E. Y. Outlook on Engineering Methylotrophs for One-Carbon-Based Industrial Biotechnology. *Chem. Eng. J.* **2022**, *449*, 137769. https://doi.org/10.1016/j.cej.2022.137769.
(310) Sheets, J. P.; Ge, X.; Li, Y.-F.; Yu, Z.; Li, Y. Biological Conversion of Biogas to Methanol Using Methanotrophs Isolated from Solid-State Anaerobic Digestate. *Bioresour. Technol.* **2016**, *201*, 50–57. https://doi.org/10.1016/j.biortech.2015.11.035.
(311) Park, S.; Kim, C. Application and Development of Methanotrophs in Environmental Engineering. *J. Mater. Cycles Waste Manag.* **2019**, *21* (3), 415–422. https://doi.org/10.1007/s10163-018-00826-w.
(312) Dinh, K. T.; Sullivan, M. M.; Serna, P.; Meyer, R. J.; Dincă, M.; Román-Leshkov, Y. Viewpoint on the Partial Oxidation of Methane to Methanol Using Cu- and Fe-Exchanged Zeolites. *ACS Catal.* **2018**, *8* (9), 8306–8313. https://doi.org/10.1021/acscatal.8b01180.
(313) Martínez, C.; Corma, A. Inorganic Molecular Sieves: Preparation, Modification and Industrial Application in Catalytic Processes. *Coord. Chem. Rev.* **2011**, *255* (13), 1558–1580. https://doi.org/10.1016/j.ccr.2011.03.014.
(314) Snyder, B. E. R.; Bols, M. L.; Schoonheydt, R. A.; Sels, B. F.; Solomon, E. I. Iron and Copper Active Sites in Zeolites and Their Correlation to Metalloenzymes. *Chem. Rev.* **2018**, *118* (5), 2718–2768. https://doi.org/10.1021/acs.chemrev.7b00344.
(315) Roduner, E.; Kaim, W.; Sarkar, B.; Urlacher, V. B.; Pleiss, J.; Gläser, R.; Einicke, W.-D.; Sprenger, G. A.; Beifuß, U.; Klemm, E.; Liebner, C.; Hieronymus, H.; Hsu, S.-F.; Plietker, B.; Laschat, S. Selective Catalytic Oxidation of C□H Bonds with Molecular Oxygen. *ChemCatChem* **2013**, *5* (1), 82–112. https://doi.org/10.1002/cctc.201200266.
(316) Hone, C. A.; Kappe, C. O. The Use of Molecular Oxygen for Liquid Phase Aerobic Oxidations in Continuous Flow. *Top. Curr.*

Chem. **2018**, *377* (1), 2. https://doi.org/10.1007/s41061-018-0226-z.

(317) Tsai, M.-L.; Hadt, R. G.; Vanelderen, P.; Sels, B. F.; Schoonheydt, R. A.; Solomon, E. I. [Cu2O]2+ Active Site Formation in Cu–ZSM-5: Geometric and Electronic Structure Requirements for N2O Activation. *J. Am. Chem. Soc.* **2014**, *136* (9), 3522–3529. https://doi.org/10.1021/ja4113808.

(318) Ipek, B.; Lobo, R. F. Catalytic Conversion of Methane to Methanol on Cu-SSZ-13 Using N2O as Oxidant. *Chem. Commun.* **2016**, *52* (91), 13401–13404. https://doi.org/10.1039/C6CC07893A.

(319) Simons, M. C.; Prinslow, S. D.; Babucci, M.; Hoffman, A. S.; Hong, J.; Vitillo, J. G.; Bare, S. R.; Gates, B. C.; Lu, C. C.; Gagliardi, L.; Bhan, A. Beyond Radical Rebound: Methane Oxidation to Methanol Catalyzed by Iron Species in Metal–Organic Framework Nodes. *J. Am. Chem. Soc.* **2021**, *143* (31), 12165–12174. https://doi.org/10.1021/jacs.1c04766.

(320) Fang, G.; Lin, J.; Wang, X. Low-Temperature Conversion of Methane to Oxygenates by Supported Metal Catalysts: From Nanoparticles to Single Atoms. *Chin. J. Chem. Eng.* **2021**, *38*, 18–29. https://doi.org/10.1016/j.cjche.2021.04.034.

(321) Hammond, C.; Forde, M. M.; Ab Rahim, M. H.; Thetford, A.; He, Q.; Jenkins, R. L.; Dimitratos, N.; Lopez-Sanchez, J. A.; Dummer, N. F.; Murphy, D. M.; Carley, A. F.; Taylor, S. H.; Willock, D. J.; Stangland, E. E.; Kang, J.; Hagen, H.; Kiely, C. J.; Hutchings, G. J. Direct Catalytic Conversion of Methane to Methanol in an Aqueous Medium by Using Copper-Promoted Fe-ZSM-5. *Angew. Chem. Int. Ed.* **2012**, *51* (21), 5129–5133. https://doi.org/10.1002/anie.201108706.

(322) Liu, Y.; Wang, L.; Xiao, F.-S. Selective Oxidation of Methane into Methanol Under Mild Conditions. *Chem. Res. Chin. Univ.* **2022**, *38* (3), 671–676. https://doi.org/10.1007/s40242-022-1428-z.

(323) Koishybay, A.; Shantz, D. F. Water Is the Oxygen Source for Methanol Produced in Partial Oxidation of Methane in a Flow Reactor over Cu-SSZ-13. *J. Am. Chem. Soc.* **2020**, *142* (28), 11962–11966. https://doi.org/10.1021/jacs.0c03283.

(324) Panov, G. I.; Uriarte, A. K.; Rodkin, M. A.; Sobolev, V. I. Generation of Active Oxygen Species on Solid Surfaces. Opportunity for Novel Oxidation Technologies over Zeolites. *Catal. Today* **1998**, *41* (4), 365–385. https://doi.org/10.1016/S0920-5861(98)00026-1.

(325) Uzunova, E. L. Cation Pair Formation in Copper and Palladium Exchanged MFI Zeolite Frameworks – a Theoretical Study. *Phys. Chem. Chem. Phys.* **2019**, *21* (27), 14786–14798. https://doi.org/10.1039/C9CP02088H.
(326) Wang, G.; Chen, W.; Huang, L.; Liu, Z.; Sun, X.; Zheng, A. Reactivity Descriptors of Diverse Copper-Oxo Species on ZSM-5 Zeolite towards Methane Activation. *Catal. Today* **2019**, *338*, 108–116. https://doi.org/10.1016/j.cattod.2019.05.007.
(327) Wang, L.; Li, Z.; Wang, Z.; Chen, X.; Song, W.; Zhao, Z.; Wei, Y.; Zhang, X. Hetero-Metallic Active Sites in Omega (MAZ) Zeolite-Catalyzed Methane Partial Oxidation: A DFT Study. *Ind. Eng. Chem. Res.* **2021**, *60* (6), 2400–2409. https://doi.org/10.1021/acs.iecr.0c05457.
(328) Guo, J.; Ding, C.; Ma, Z.; Ma, L.; Wang, J.; Shangguan, J.; Yuan, Q.; Zhao, M.; Li, Y.; Wang, M.; Zhang, K. Highly Dispersed and Stable Pt Clusters Encapsulated within ZSM-5 with Aid of Sodium Ion for Partial Oxidation of Methane. *Fuel* **2021**, *289*, 119839. https://doi.org/10.1016/j.fuel.2020.119839.
(329) Mahyuddin, M. H.; Tanaka, S.; Kitagawa, R.; Maulana, A. L.; Saputro, A. G.; Agusta, M. K.; Yudistira, H. T.; Dipojono, H. K.; Yoshizawa, K. Distinct Behaviors of Cu- and Ni-ZSM-5 Zeolites toward the Post-Activation Reactions of Methane. *J. Phys. Chem. C* **2021**, *125* (35), 19333–19344. https://doi.org/10.1021/acs.jpcc.1c06400.
(330) Xue, Z.; Liu, P.; Li, N.; Ling, L.; Liu, P.; Shen, X.; Zhang, R.; Wang, B. Effect of ZSM–5 with Different Active Centers on Methane Partial Oxidation. *Mol. Catal.* **2022**, *524*, 112308. https://doi.org/10.1016/j.mcat.2022.112308.
(331) Liu, L.; Chen, D.; Tan, K.; Wu, A.; Lu, X. Mechanism Investigation on Direct Conversion of Methane over a Mononuclear Rh-ZSM-5 Catalyst: Multiple Roles of CO. *J. Phys. Chem. C* **2023**, *127* (10), 4887–4895. https://doi.org/10.1021/acs.jpcc.2c07627.
(332) Tomkins, P.; Ranocchiari, M.; van Bokhoven, J. A. Direct Conversion of Methane to Methanol under Mild Conditions over Cu-Zeolites and Beyond. *Acc. Chem. Res.* **2017**, *50* (2), 418–425. https://doi.org/10.1021/acs.accounts.6b00534.
(333) Tabor, E.; Lemishka, M.; Sobalik, Z.; Mlekodaj, K.; Andrikopoulos, P. C.; Dedecek, J.; Sklenak, S. Low-Temperature Selective Oxidation of Methane over Distant Binuclear Cationic Centers in Zeolites. *Commun. Chem.* **2019**, *2* (1), 1–9. https://doi.org/10.1038/s42004-019-0173-9.

(334) Zeng, R.; Li, L.; Shimizu, T.; Kim, H. J. Direct Conversion of Methane to Methanol over Copper-Exchanged Zeolite under Mild Conditions. *J. Energy Eng.* **2020**, *146* (6), 04020061. https://doi.org/10.1061/(ASCE)EY.1943-7897.0000712.
(335) Wu, L.; Fan, W.; Wang, X.; Lin, H.; Tao, J.; Liu, Y.; Deng, J.; Jing, L.; Dai, H. Methane Oxidation over the Zeolites-Based Catalysts. *Catalysts* **2023**, *13* (3), 604. https://doi.org/10.3390/catal13030604.
(336) Moteki, T.; Tominaga, N.; Ogura, M. CO-Assisted Direct Methane Conversion into C1 and C2 Oxygenates over ZSM-5 Supported Transition and Platinum Group Metal Catalysts Using Oxygen as an Oxidant. *ChemCatChem* **2020**, *12* (11), 2957–2961. https://doi.org/10.1002/cctc.202000168.
(337) Moteki, T.; Tominaga, N.; Tsunoji, N.; Yokoi, T.; Ogura, M. Impact of the Zeolite Cage Structure on Product Selectivity in CO-Assisted Direct Partial Oxidation of Methane over Rh Supported AEI-, CHA-, and AFX-Type Zeolites. *Chem. Lett.* **2021**, *50* (8), 1597–1600. https://doi.org/10.1246/cl.210250.
(338) Burnett, L.; Rysakova, M.; Wang, K.; González-Carballo, J.; Tooze, R. P.; García-García, F. R. Isothermal Cyclic Conversion of Methane to Methanol Using Copper-Exchanged ZSM-5 Zeolite Materials under Mild Conditions. *Appl. Catal. Gen.* **2019**, *587*, 117272. https://doi.org/10.1016/j.apcata.2019.117272.
(339) Mahyuddin, M. H.; Shiota, Y.; Yoshizawa, K. Methane Selective Oxidation to Methanol by Metal-Exchanged Zeolites: A Review of Active Sites and Their Reactivity. *Catal. Sci. Technol.* **2019**, *9* (8), 1744–1768. https://doi.org/10.1039/C8CY02414F.
(340) Park, M. B.; Park, E. D.; Ahn, W.-S. Recent Progress in Direct Conversion of Methane to Methanol Over Copper-Exchanged Zeolites. *Front. Chem.* **2019**, *7*.
(341) Xu, J.; Armstrong, R. D.; Shaw, G.; Dummer, N. F.; Freakley, S. J.; Taylor, S. H.; Hutchings, G. J. Continuous Selective Oxidation of Methane to Methanol over Cu- and Fe-Modified ZSM-5 Catalysts in a Flow Reactor. *Catal. Today* **2016**, *270*, 93–100. https://doi.org/10.1016/j.cattod.2015.09.011.
(342) Pokhrel, J.; Shantz, D. F. Continuous Partial Oxidation of Methane to Methanol over Cu-SSZ-39 Catalysts. *J. Catal.* **2023**, *421*, 300–308. https://doi.org/10.1016/j.jcat.2023.03.021.
(343) Groothaert, M. H.; Smeets, P. J.; Sels, B. F.; Jacobs, P. A.; Schoonheydt, R. A. Selective Oxidation of Methane by the Bis(μ-Oxo)Dicopper Core Stabilized on ZSM-5 and Mordenite Zeolites.

J. Am. Chem. Soc. **2005**, *127* (5), 1394–1395. https://doi.org/10.1021/ja047158u.

(344) Hammond, C.; Jenkins, R. L.; Dimitratos, N.; Lopez-Sanchez, J. A.; ab Rahim, M. H.; Forde, M. M.; Thetford, A.; Murphy, D. M.; Hagen, H.; Stangland, E. E.; Moulijn, J. M.; Taylor, S. H.; Willock, D. J.; Hutchings, G. J. Catalytic and Mechanistic Insights of the Low-Temperature Selective Oxidation of Methane over Cu-Promoted Fe-ZSM-5. *Chem. – Eur. J.* **2012**, *18* (49), 15735–15745. https://doi.org/10.1002/chem.201202802.

(345) Hammond, C.; Dimitratos, N.; Jenkins, R. L.; Lopez-Sanchez, J. A.; Kondrat, S. A.; Hasbi ab Rahim, M.; Forde, M. M.; Thetford, A.; Taylor, S. H.; Hagen, H.; Stangland, E. E.; Kang, J. H.; Moulijn, J. M.; Willock, D. J.; Hutchings, G. J. Elucidation and Evolution of the Active Component within Cu/Fe/ZSM-5 for Catalytic Methane Oxidation: From Synthesis to Catalysis. *ACS Catal.* **2013**, *3* (4), 689–699. https://doi.org/10.1021/cs3007999.

(346) Forde, M. M.; Armstrong, R. D.; McVicker, R.; Wells, P. P.; Dimitratos, N.; He, Q.; Lu, L.; Jenkins, R. L.; Hammond, C.; Lopez-Sanchez, J. A.; Kiely, C. J.; Hutchings, G. J. Light Alkane Oxidation Using Catalysts Prepared by Chemical Vapour Impregnation: Tuning Alcohol Selectivity through Catalyst Pre-Treatment. *Chem. Sci.* **2014**, *5* (9), 3603–3616. https://doi.org/10.1039/C4SC00545G.

(347) A. Newton, M.; J. Knorpp, A.; L. Sushkevich, V.; Palagin, D.; Bokhoven, J. A. van. Active Sites and Mechanisms in the Direct Conversion of Methane to Methanol Using Cu in Zeolitic Hosts: A Critical Examination. *Chem. Soc. Rev.* **2020**, *49* (5), 1449–1486. https://doi.org/10.1039/C7CS00709D.

(348) Kulkarni, A. R.; Zhao, Z.-J.; Siahrostami, S.; Nørskov, J. K.; Studt, F. Monocopper Active Site for Partial Methane Oxidation in Cu-Exchanged 8MR Zeolites. *ACS Catal.* **2016**, *6* (10), 6531–6536. https://doi.org/10.1021/acscatal.6b01895.

(349) Heyer, A. J.; Plessers, D.; Braun, A.; Rhoda, H. M.; Bols, M. L.; Hedman, B.; Hodgson, K. O.; Schoonheydt, R. A.; Sels, B. F.; Solomon, E. I. Methane Activation by a Mononuclear Copper Active Site in the Zeolite Mordenite: Effect of Metal Nuclearity on Reactivity. *J. Am. Chem. Soc.* **2022**, *144* (42), 19305–19316. https://doi.org/10.1021/jacs.2c06269.

(350) Plessers, D.; Heyer, A. J.; Rhoda, H. M.; Bols, M. L.; Solomon, E. I.; Schoonheydt, R. A.; Sels, B. F. Tuning Copper Active Site Composition in Cu-MOR through Co-Cation

Modification for Methane Activation. *ACS Catal.* **2023**, *13* (3), 1906–1915. https://doi.org/10.1021/acscatal.2c05271.

(351) Le, H. V.; Ho, P. H.; Trunschke, A.; Schomäcker, R.; Thomas, A. Stepwise Conversion of Methane to Methanol on Cu and Fe/Zeolites Prepared in Solid State: The Effect of Zeolite Type and Activation Temperature. *J. Chem. Technol. Biotechnol. n/a* (n/a). https://doi.org/10.1002/jctb.7342.

(352) Smeets, P. J.; Groothaert, M. H.; Schoonheydt, R. A. Cu Based Zeolites: A UV–Vis Study of the Active Site in the Selective Methane Oxidation at Low Temperatures. *Catal. Today* **2005**, *110* (3), 303–309. https://doi.org/10.1016/j.cattod.2005.09.028.

(353) Ipek, B.; Wulfers, M. J.; Kim, H.; Göltl, F.; Hermans, I.; Smith, J. P.; Booksh, K. S.; Brown, C. M.; Lobo, R. F. Formation of [Cu2O2]2+ and [Cu2O]2+ toward C-H Bond Activation in Cu-SSZ-13 and Cu-SSZ-39. *ACS Catal.* **2017**, *7* (7), 4291–4303. https://doi.org/10.1021/acscatal.6b03005.

(354) Woertink, J. S.; Smeets, P. J.; Groothaert, M. H.; Vance, M. A.; Sels, B. F.; Schoonheydt, R. A.; Solomon, E. I. A [Cu2O]2+core in Cu-ZSM-5, the Active Site in the Oxidation of Methane to Methanol. *Proc. Natl. Acad. Sci.* **2009**, *106* (45), 18908. https://doi.org/10.1073/pnas.0910461106.

(355) Liu, X.; Zhang, J.; Huang, C.; Sun, X. Density Functional Theory Study of Cu-ZSM-5-Catalyzed C–H Bond Activation: The Importance of Active Centers. *J. Phys. Chem. C* **2018**, *122* (50), 28645–28651. https://doi.org/10.1021/acs.jpcc.8b08137.

(356) Panthi, D.; Adeyiga, O.; Odoh, S. O. DFT Analysis of Methane C−H Activation and Over-Oxidation by [Cu2O]2+ and [Cu2O2]2+ Sites in Zeolite Mordenite: Intra- versus Inter-Site Over-Oxidation. *ChemPhysChem* **2021**, *22* (24), 2517–2525. https://doi.org/10.1002/cphc.202100580.

(357) Engedahl, U.; Arvidsson, A. A.; Grönbeck, H.; Hellman, A. Reaction Mechanism for Methane-to-Methanol in Cu-SSZ-13: First-Principles Study of the Z2[Cu2O] and Z2[Cu2OH] Motifs. *Catalysts* **2021**, *11* (1), 17. https://doi.org/10.3390/catal11010017.

(358) Brezicki, G.; Zheng, J.; Paolucci, C.; Schlögl, R.; Davis, R. J. Effect of the Co-Cation on Cu Speciation in Cu-Exchanged Mordenite and ZSM-5 Catalysts for the Oxidation of Methane to Methanol. *ACS Catal.* **2021**, *11* (9), 4973–4987. https://doi.org/10.1021/acscatal.1c00543.

(359) Grundner, S.; Markovits, M. A. C.; Li, G.; Tromp, M.; Pidko, E. A.; Hensen, E. J. M.; Jentys, A.; Sanchez-Sanchez, M.;

Lercher, J. A. Single-Site Trinuclear Copper Oxygen Clusters in Mordenite for Selective Conversion of Methane to Methanol. *Nat. Commun.* **2015**, *6* (1), 7546. https://doi.org/10.1038/ncomms8546.

(360) Grundner, S.; Luo, W.; Sanchez-Sanchez, M.; Lercher, J. A. Synthesis of Single-Site Copper Catalysts for Methane Partial Oxidation. *Chem. Commun.* **2016**, *52* (12), 2553–2556. https://doi.org/10.1039/C5CC08371K.

(361) Palagin, D.; Knorpp, A. J.; Pinar, A. B.; Ranocchiari, M.; Bokhoven, J. A. van. Assessing the Relative Stability of Copper Oxide Clusters as Active Sites of a CuMOR Zeolite for Methane to Methanol Conversion: Size Matters? *Nanoscale* **2017**, *9* (3), 1144–1153. https://doi.org/10.1039/C6NR07723D.

(362) Dandu, N. K.; Reed, J. A.; Odoh, S. O. Performance of Density Functional Theory for Predicting Methane-to-Methanol Conversion by a Tri-Copper Complex. *J. Phys. Chem. C* **2018**, *122* (2), 1024–1036. https://doi.org/10.1021/acs.jpcc.7b09284.

(363) Suleiman, O.; Panthi, D.; Adeyiga, O.; Odoh, S. O. Methane C–H Activation by [Cu2O]2+ and [Cu3O3]2+ in Copper-Exchanged Zeolites: Computational Analysis of Redox Chemistry and X-Ray Absorption Spectroscopy. *Inorg. Chem.* **2021**, *60* (9), 6218–6227. https://doi.org/10.1021/acs.inorgchem.0c03693.

(364) Li, G.; Vassilev, P.; Sanchez-Sanchez, M.; Lercher, J. A.; Hensen, E. J. M.; Pidko, E. A. Stability and Reactivity of Copper Oxo-Clusters in ZSM-5 Zeolite for Selective Methane Oxidation to Methanol. *J. Catal.* **2016**, *338*, 305–312. https://doi.org/10.1016/j.jcat.2016.03.014.

(365) Zhao, Z.-J.; Kulkarni, A.; Vilella, L.; Nørskov, J. K.; Studt, F. Theoretical Insights into the Selective Oxidation of Methane to Methanol in Copper-Exchanged Mordenite. *ACS Catal.* **2016**, *6* (6), 3760–3766. https://doi.org/10.1021/acscatal.6b00440.

(366) Suleiman, O.; Adeyiga, O.; Panthi, D.; Odoh, S. O. Copper-Oxo Active Sites in the 8MR of Zeolite Mordenite: DFT Investigation of the Impact of Acid Sites on Methanol Yield and Selectivity. *J. Phys. Chem. C* **2021**, *125* (12), 6684–6693. https://doi.org/10.1021/acs.jpcc.1c00561.

(367) Artiglia, L.; Sushkevich, V. L.; Palagin, D.; Knorpp, A. J.; Roy, K.; van Bokhoven, J. A. In Situ X-Ray Photoelectron Spectroscopy Detects Multiple Active Sites Involved in the Selective Anaerobic Oxidation of Methane in Copper-Exchanged Zeolites. *ACS Catal.* **2019**, *9* (8), 6728–6737. https://doi.org/10.1021/acscatal.9b01223.

(368) Lee, I.; Lee, M.-S.; Tao, L.; Ikuno, T.; Khare, R.; Jentys, A.; Huthwelker, T.; Borca, C. N.; Kalinko, A.; Gutiérrez, O. Y.; Govind, N.; Fulton, J. L.; Hu, J. Z.; Glezakou, V.-A.; Rousseau, R.; Sanchez-Sanchez, M.; Lercher, J. A. Activity of Cu–Al–Oxo Extra-Framework Clusters for Selective Methane Oxidation on Cu-Exchanged Zeolites. *JACS Au* **2021**, *1* (9), 1412–1421. https://doi.org/10.1021/jacsau.1c00196.

(369) Newton, M. A.; Knorpp, A. J.; Pinar, A. B.; Sushkevich, V. L.; Palagin, D.; van Bokhoven, J. A. On the Mechanism Underlying the Direct Conversion of Methane to Methanol by Copper Hosted in Zeolites; Braiding Cu K-Edge XANES and Reactivity Studies. *J. Am. Chem. Soc.* **2018**, *140* (32), 10090–10093. https://doi.org/10.1021/jacs.8b05139.

(370) Tomkins, P.; Mansouri, A.; Bozbag, S. E.; Krumeich, F.; Park, M. B.; Alayon, E. M. C.; Ranocchiari, M.; van Bokhoven, J. A. Isothermal Cyclic Conversion of Methane into Methanol over Copper-Exchanged Zeolite at Low Temperature. *Angew. Chem. Int. Ed.* **2016**, *55* (18), 5467–5471. https://doi.org/10.1002/anie.201511065.

(371) Mahyuddin, M. H.; Shiota, Y.; Staykov, A.; Yoshizawa, K. Theoretical Overview of Methane Hydroxylation by Copper–Oxygen Species in Enzymatic and Zeolitic Catalysts. *Acc. Chem. Res.* **2018**, *51* (10), 2382–2390. https://doi.org/10.1021/acs.accounts.8b00236.

(372) Yeh, C.-H.; Yu, S. S.-F.; Chan, S. I.; Jiang, J.-C. Quantum Chemical Studies of Methane Oxidation to Methanol on a Biomimetic Tricopper Complex: Mechanistic Insights. *ChemistrySelect* **2018**, *3* (18), 5113–5122. https://doi.org/10.1002/slct.201800550.

(373) Mao, Y.; Hu, P. Identification of the Active Sites and Mechanism for Partial Methane Oxidation to Methanol over Copper-Exchanged CHA Zeolites. *Sci. China Chem.* **2020**, *63* (6), 850–859. https://doi.org/10.1007/s11426-019-9695-9.

(374) Mousavian, P.; Esrafili, M. D. Methane Oxidation into Methanol Catalyzed by TM-Anchored C24N24 Nanoclusters (TM = Fe, Co and Ni): A DFT Study. *Inorg. Chem. Commun.* **2020**, *122*, 108317. https://doi.org/10.1016/j.inoche.2020.108317.

(375) Xi, Y.; Heyden, A. Selective Activation of Methane CH Bond in the Presence of Methanol. *J. Catal.* **2020**, *386*, 12–18. https://doi.org/10.1016/j.jcat.2020.03.036.

(376) Tao, L.; Lee, I.; Sanchez-Sanchez, M. Cu Oxo Nanoclusters for Direct Oxidation of Methane to Methanol: Formation,

Structure and Catalytic Performance. *Catal. Sci. Technol.* **2020**, *10* (21), 7124–7141. https://doi.org/10.1039/D0CY01325K.
(377) Nunthakitgoson, W.; Thivasasith, A.; Maihom, T.; Wattanakit, C. Effects of Single and Double Active Sites of Cu Oxide Clusters over the MFI Zeolite for Direct Conversion of Methane to Methanol: DFT Calculations. *Phys. Chem. Chem. Phys.* **2021**, *23* (3), 2500–2510. https://doi.org/10.1039/D0CP05435F.
(378) Yumura, T.; Hirose, Y.; Wakasugi, T.; Kuroda, Y.; Kobayashi, H. Roles of Water Molecules in Modulating the Reactivity of Dioxygen-Bound Cu-ZSM-5 toward Methane: A Theoretical Prediction. *ACS Catal.* **2016**, *6* (4), 2487–2495. https://doi.org/10.1021/acscatal.5b02477.
(379) Sun, L.; Wang, Y.; Wang, C.; Xie, Z.; Guan, N.; Li, L. Water-Involved Methane-Selective Catalytic Oxidation by Dioxygen over Copper Zeolites. *Chem* **2021**, *7* (6), 1557–1568. https://doi.org/10.1016/j.chempr.2021.02.026.
(380) Hirayama, A.; Tsuchimura, Y.; Yoshida, H.; Machida, M.; Nishimura, S.; Kato, K.; Takahashi, K.; Ohyama, J. Catalytic Oxidation of Methane to Methanol over Cu-CHA with Molecular Oxygen. *Catal. Sci. Technol.* **2021**, *11* (18), 6217–6224. https://doi.org/10.1039/D1CY00676B.
(381) Mizuno, S. C. M.; Dulnee, S.; Pereira, T. C. P.; Passini, R. J.; Urquieta-Gonzalez, E. A.; Gallo, J. M. R.; Santos, J. B. O.; Bueno, J. M. C. Stepwise Methane to Methanol Conversion: Effect of Copper Loading on the Formation of Active Species in Copper-Exchanged Mordenite. *Catal. Today* **2021**, *381*, 13–25. https://doi.org/10.1016/j.cattod.2020.11.027.
(382) Engedahl, U.; Boje, A.; Ström, H.; Grönbeck, H.; Hellman, A. Complete Reaction Cycle for Methane-to-Methanol Conversion over Cu-SSZ-13: First-Principles Calculations and Microkinetic Modeling. *J. Phys. Chem. C* **2021**, *125* (27), 14681–14688. https://doi.org/10.1021/acs.jpcc.1c04062.
(383) Vora, B.; Chen, J. Q.; Bozzano, A.; Glover, B.; Barger, P. Various Routes to Methane Utilization—SAPO-34 Catalysis Offers the Best Option. *Catal. Today* **2009**, *141* (1), 77–83. https://doi.org/10.1016/j.cattod.2008.05.038.
(384) Sun, Q.; Xie, Z.; Yu, J. The State-of-the-Art Synthetic Strategies for SAPO-34 Zeolite Catalysts in Methanol-to-Olefin Conversion. *Natl. Sci. Rev.* **2018**, *5* (4), 542–558. https://doi.org/10.1093/nsr/nwx103.

(385) Kvande, K.; Pappas, D. K.; Dyballa, M.; Buono, C.; Signorile, M.; Borfecchia, E.; Lomachenko, K. A.; Arstad, B.; Bordiga, S.; Berlier, G.; Olsbye, U.; Beato, P.; Svelle, S. Comparing the Nature of Active Sites in Cu-Loaded SAPO-34 and SSZ-13 for the Direct Conversion of Methane to Methanol. *Catalysts* **2020**, *10* (2), 191. https://doi.org/10.3390/catal10020191.

(386) Sankar, G.; Sánchez-Sánchez, M. Metal-Substituted Microporous Aluminophosphates. In *Structure and Reactivity of Metals in Zeolite Materials*; Pérez Pariente, J., Sánchez-Sánchez, M., Eds.; Structure and Bonding; Springer International Publishing: Cham, 2018; pp 251–303. https://doi.org/10.1007/430_2018_25.

(387) Sader, S.; Miliordos, E. Methane to Methanol Conversion Facilitated by Anionic Transition Metal Centers: The Case of Fe, Ni, Pd, and Pt. *J. Phys. Chem. A* **2021**, *125* (11), 2364–2373. https://doi.org/10.1021/acs.jpca.0c10577.

(388) Liu, G.; Zhu, Z.; Ciborowski, S. M.; Ariyarathna, I. R.; Miliordos, E.; Bowen, K. H. Selective Activation of the C−H Bond in Methane by Single Platinum Atomic Anions. *Angew. Chem. Int. Ed.* **2019**, *58* (23), 7773–7777. https://doi.org/10.1002/anie.201903252.

(389) Perera, M.; Metz, R. B.; Kostko, O.; Ahmed, M. Vacuum Ultraviolet Photoionization Studies of PtCH2 and H-Pt-CH3: A Potential Energy Surface for the Pt+CH4 Reaction. *Angew. Chem. Int. Ed.* **2013**, *52* (3), 888–891. https://doi.org/10.1002/anie.201207931.

(390) Shavi, R.; Hiremath, V.; Seo, J. G. Radical-Initiated Oxidative Conversion of Methane to Methanol over Metallic Iron and Copper Catalysts. *Mol. Catal.* **2018**, *445*, 232–239. https://doi.org/10.1016/j.mcat.2017.12.001.

(391) Golovanova, S. A.; Sadkov, A. P.; Shestakov, A. F. Effect of Oxygen on the Oxidation of Methane with Hydrogen Peroxide to Methanol in the Presence of Glutathione-Stabilized Gold Nanoclusters. *Kinet. Catal.* **2020**, *61* (5), 740–749. https://doi.org/10.1134/S0023158420040060.

(392) Li, H.; Shen, Y.; Xiao, X.; Jiang, H.; Gu, Q.; Zhang, Y.; Lin, L.; Luo, W.; Zhou, S.; Zhao, J.; Wang, A.; Zhang, T.; Yang, B. Controlled-Release Mechanism Regulates Rhodium Migration and Size Redistribution Boosting Catalytic Methane Conversion. *ACS Catal.* **2023**, *13* (2), 1197–1206. https://doi.org/10.1021/acscatal.2c05463.

(393) Heisenberg, W. Über quantentheoretische Umdeutung kinematischer und mechanischer Beziehungen. *Z. Für Phys.* **1925**, *33* (1), 879–893. https://doi.org/10.1007/BF01328377.
(394) Schrödinger, E. Quantisierung Als Eigenwertproblem. *Ann. Phys.* **1926**, *384* (4), 361–376. https://doi.org/10.1002/andp.19263840404.
(395) Born, M. Zur Quantenmechanik der Stoßvorgänge. *Z. Für Phys.* **1926**, *37* (12), 863–867. https://doi.org/10.1007/BF01397477.
(396) National Research Council. *Mathematical Challenges from Theoretical/Computational Chemistry*; The National Academies Press: Washington, DC, 1995. https://doi.org/10.17226/4886.
(397) Defranceschi, M.; Le Bris, C. *Mathematical Models and Methods for Ab Initio Quantum Chemistry*; Berthier, G., Fischer, H., Fukui, K., Hall, G. G., Hinze, J., Jortner, J., Kutzelnigg, W., Ruedenberg, K., Tomasi, J., Series Eds.; Lecture Notes in Chemistry; Springer: Berlin, Heidelberg, 2000; Vol. 74. https://doi.org/10.1007/978-3-642-57237-1.
(398) Friesner, R. A. Ab Initio Quantum Chemistry: Methodology and Applications. *Proc. Natl. Acad. Sci.* **2005**, *102* (19), 6648–6653. https://doi.org/10.1073/pnas.0408036102.
(399) Thiel, W. Semiempirical Quantum–Chemical Methods. *WIREs Comput. Mol. Sci.* **2014**, *4* (2), 145–157. https://doi.org/10.1002/wcms.1161.
(400) Christensen, A. S.; Kubař, T.; Cui, Q.; Elstner, M. Semiempirical Quantum Mechanical Methods for Noncovalent Interactions for Chemical and Biochemical Applications. *Chem. Rev.* **2016**, *116* (9), 5301–5337. https://doi.org/10.1021/acs.chemrev.5b00584.
(401) Rossi, M. Progress and Challenges in Ab Initio Simulations of Quantum Nuclei in Weakly Bonded Systems. *J. Chem. Phys.* **2021**, *154* (17), 170902. https://doi.org/10.1063/5.0042572.
(402) Aspuru-Guzik, A. Neither Physics nor Chemistry: A History of Quantum Chemistry. *Phys. Today* **2012**, *65* (8), 52–54. https://doi.org/10.1063/PT.3.1683.
(403) *Philosophical Perspectives in Quantum Chemistry*; Lombardi, O., Martínez González, J. C., Fortin, S., Eds.; Synthese Library; Springer International Publishing: Cham, 2022; Vol. 461. https://doi.org/10.1007/978-3-030-98373-4.
(404) Born, M.; Oppenheimer, R. Zur Quantentheorie Der Molekeln. *Ann. Phys.* **1927**, *389* (20), 457–484. https://doi.org/10.1002/andp.19273892002.

(405) Hartree, D. R. The Wave Mechanics of an Atom with a Non-Coulomb Central Field. Part I. Theory and Methods. *Math. Proc. Camb. Philos. Soc.* **1928**, *24* (1), 89–110. https://doi.org/10.1017/S0305004100011919.
(406) Fock, V. Näherungsmethode zur Lösung des quantenmechanischen Mehrkörperproblems. *Z. Für Phys.* **1930**, *61* (1), 126–148. https://doi.org/10.1007/BF01340294.
(407) Pauli, W. Über den Zusammenhang des Abschlusses der Elektronengruppen im Atom mit der Komplexstruktur der Spektren. *Z. Für Phys.* **1925**, *31* (1), 765–783. https://doi.org/10.1007/BF02980631.
(408) Møller, Chr.; Plesset, M. S. Note on an Approximation Treatment for Many-Electron Systems. *Phys. Rev.* **1934**, *46* (7), 618–622. https://doi.org/10.1103/PhysRev.46.618.
(409) Bartlett, R. J.; Stanton, J. F. Applications of Post-Hartree—Fock Methods: A Tutorial. In *Reviews in Computational Chemistry*; John Wiley & Sons, Ltd, 1994; pp 65–169. https://doi.org/10.1002/9780470125823.ch2.
(410) Zlatar, M.; Gruden, M. Chapter 2 - Introduction to Ligand Field Theory and Computational Chemistry. In *Practical Approaches to Biological Inorganic Chemistry (Second Edition)*; Crichton, R. R., Louro, R. O., Eds.; Elsevier, 2020; pp 17–67. https://doi.org/10.1016/B978-0-444-64225-7.00002-X.
(411) Shikano, Y.; Watanabe, H. C.; Nakanishi, K. M.; Ohnishi, Y. Post-Hartree-Fock Method in Quantum Chemistry for Quantum Computer. *Eur. Phys. J. Spec. Top.* **2021**, *230* (4), 1037–1051. https://doi.org/10.1140/epjs/s11734-021-00087-z.
(412) Thomas, L. H. The Calculation of Atomic Fields. *Math. Proc. Camb. Philos. Soc.* **1927**, *23* (5), 542–548. https://doi.org/10.1017/S0305004100011683.
(413) Fermi, E. Statistical Method to Determine Some Properties of Atoms. *Rendiconti Lincei* **1927**, No. 6, 602–607.
(414) Fermi, E. Eine statistische Methode zur Bestimmung einiger Eigenschaften des Atoms und ihre Anwendung auf die Theorie des periodischen Systems der Elemente. *Z. Für Phys.* **1928**, *48* (1), 73–79. https://doi.org/10.1007/BF01351576.
(415) Gill, P. M. W. Density Functional Theory (DFT), Hartree–Fock (HF), and the Self-Consistent Field. In *Encyclopedia of Computational Chemistry*; John Wiley & Sons, Ltd, 2002. https://doi.org/10.1002/0470845015.cda011.

(416) Hohenberg, P.; Kohn, W. Inhomogeneous Electron Gas. *Phys. Rev.* **1964**, *136* (3B), B864–B871. https://doi.org/10.1103/PhysRev.136.B864.
(417) Levy, M. Universal Variational Functionals of Electron Densities, First-Order Density Matrices, and Natural Spin-Orbitals and Solution of the v-Representability Problem. *Proc. Natl. Acad. Sci. U. S. A.* **1979**, *76* (12), 6062–6065. https://doi.org/10.1073/pnas.76.12.6062.
(418) Vignale, G.; Rasolt, M. Density-Functional Theory in Strong Magnetic Fields. *Phys. Rev. Lett.* **1987**, *59* (20), 2360–2363. https://doi.org/10.1103/PhysRevLett.59.2360.
(419) Levy, M. Electron Densities in Search of Hamiltonians. *Phys. Rev. A* **1982**, *26* (3), 1200–1208. https://doi.org/10.1103/PhysRevA.26.1200.
(420) Baerends, E. J. Chemical Potential, Derivative Discontinuity, Fractional Electrons, Jump of the Kohn–Sham Potential, Atoms as Thermodynamic Open Systems, and Other (Mis)Conceptions of the Density Functional Theory of Electrons in Molecules. *Phys. Chem. Chem. Phys.* **2022**, *24* (21), 12745–12766. https://doi.org/10.1039/D2CP01585D.
(421) Koch, W.; Holthausen, M. C. *A Chemist's Guide to Density Functional Theory*, 1st ed.; Wiley, 2001. https://doi.org/10.1002/3527600043.
(422) Kohn, W.; Sham, L. J. Self-Consistent Equations Including Exchange and Correlation Effects. *Phys. Rev.* **1965**, *140* (4A), A1133–A1138. https://doi.org/10.1103/PhysRev.140.A1133.
(423) Stowasser, R.; Hoffmann, R. What Do the Kohn−Sham Orbitals and Eigenvalues Mean? *J. Am. Chem. Soc.* **1999**, *121* (14), 3414–3420. https://doi.org/10.1021/ja9826892.
(424) van Meer, R.; Gritsenko, O. V.; Baerends, E. J. Physical Meaning of Virtual Kohn–Sham Orbitals and Orbital Energies: An Ideal Basis for the Description of Molecular Excitations. *J. Chem. Theory Comput.* **2014**, *10* (10), 4432–4441. https://doi.org/10.1021/ct500727c.
(425) Perdew, J. P.; Schmidt, K. Jacob's Ladder of Density Functional Approximations for the Exchange-Correlation Energy. *AIP Conf. Proc.* **2001**, *577* (1), 1–20. https://doi.org/10.1063/1.1390175.
(426) Dirac, P. a. M. Note on Exchange Phenomena in the Thomas Atom. *Math. Proc. Camb. Philos. Soc.* **1930**, *26* (3), 376–385. https://doi.org/10.1017/S0305004100016108.

(427) Ceperley, D. M.; Alder, B. J. Ground State of the Electron Gas by a Stochastic Method. *Phys. Rev. Lett.* **1980**, *45* (7), 566–569. https://doi.org/10.1103/PhysRevLett.45.566.
(428) Perdew, J. P.; Zunger, A. Self-Interaction Correction to Density-Functional Approximations for Many-Electron Systems. *Phys. Rev. B* **1981**, *23* (10), 5048–5079. https://doi.org/10.1103/PhysRevB.23.5048.
(429) Perdew, J. P. Accurate Density Functional for the Energy: Real-Space Cutoff of the Gradient Expansion for the Exchange Hole. *Phys. Rev. Lett.* **1985**, *55* (16), 1665–1668. https://doi.org/10.1103/PhysRevLett.55.1665.
(430) Jones, R. O.; Gunnarsson, O. The Density Functional Formalism, Its Applications and Prospects. *Rev. Mod. Phys.* **1989**, *61* (3), 689–746. https://doi.org/10.1103/RevModPhys.61.689.
(431) Barth, U. von; Hedin, L. A Local Exchange-Correlation Potential for the Spin Polarized Case. i. *J. Phys. C Solid State Phys.* **1972**, *5* (13), 1629. https://doi.org/10.1088/0022-3719/5/13/012.
(432) Langreth, D. C.; Perdew, J. P. Theory of Nonuniform Electronic Systems. I. Analysis of the Gradient Approximation and a Generalization That Works. *Phys. Rev. B* **1980**, *21* (12), 5469–5493. https://doi.org/10.1103/PhysRevB.21.5469.
(433) Perdew, J. P.; Yue, W. Accurate and Simple Density Functional for the Electronic Exchange Energy: Generalized Gradient Approximation. *Phys. Rev. B* **1986**, *33* (12), 8800–8802. https://doi.org/10.1103/PhysRevB.33.8800.
(434) Lee, C.; Yang, W.; Parr, R. G. Development of the Colle-Salvetti Correlation-Energy Formula into a Functional of the Electron Density. *Phys. Rev. B* **1988**, *37* (2), 785–789. https://doi.org/10.1103/PhysRevB.37.785.
(435) Becke, A. D. Density-functional Thermochemistry. III. The Role of Exact Exchange. *J. Chem. Phys.* **1993**, *98* (7), 5648–5652. https://doi.org/10.1063/1.464913.
(436) Perdew, J. P.; Chevary, J. A.; Vosko, S. H.; Jackson, K. A.; Pederson, M. R.; Singh, D. J.; Fiolhais, C. Atoms, Molecules, Solids, and Surfaces: Applications of the Generalized Gradient Approximation for Exchange and Correlation. *Phys. Rev. B* **1992**, *46* (11), 6671–6687. https://doi.org/10.1103/PhysRevB.46.6671.
(437) Perdew, J. P.; Burke, K.; Ernzerhof, M. Generalized Gradient Approximation Made Simple. *Phys. Rev. Lett.* **1996**, *77* (18), 3865–3868. https://doi.org/10.1103/PhysRevLett.77.3865.

(438) Tao, J.; Perdew, J. P.; Staroverov, V. N.; Scuseria, G. E. Climbing the Density Functional Ladder: Nonempirical Meta--Generalized Gradient Approximation Designed for Molecules and Solids. *Phys. Rev. Lett.* **2003**, *91* (14), 146401. https://doi.org/10.1103/PhysRevLett.91.146401.
(439) Zhao, Y.; Truhlar, D. G. A New Local Density Functional for Main-Group Thermochemistry, Transition Metal Bonding, Thermochemical Kinetics, and Noncovalent Interactions. *J. Chem. Phys.* **2006**, *125* (19), 194101. https://doi.org/10.1063/1.2370993.
(440) Vosko, S. H.; Wilk, L.; Nusair, M. Accurate Spin-Dependent Electron Liquid Correlation Energies for Local Spin Density Calculations: A Critical Analysis. *Can. J. Phys.* **1980**, *58* (8), 1200–1211. https://doi.org/10.1139/p80-159.
(441) Stephens, P. J.; Devlin, F. J.; Chabalowski, C. F.; Frisch, M. J. Ab Initio Calculation of Vibrational Absorption and Circular Dichroism Spectra Using Density Functional Force Fields. *J. Phys. Chem.* **1994**, *98* (45), 11623–11627. https://doi.org/10.1021/j100096a001.
(442) Heyd, J.; Scuseria, G. E.; Ernzerhof, M. Hybrid Functionals Based on a Screened Coulomb Potential. *J. Chem. Phys.* **2003**, *118* (18), 8207–8215. https://doi.org/10.1063/1.1564060.
(443) Heyd, J.; Scuseria, G. E.; Ernzerhof, M. Erratum: “Hybrid Functionals Based on a Screened Coulomb Potential” [J. Chem. Phys. 118, 8207 (2003)]. *J. Chem. Phys.* **2006**, *124* (21), 219906. https://doi.org/10.1063/1.2204597.
(444) Grimme, S. Accurate description of van der Waals complexes by density functional theory including empirical corrections. *J. Comput. Chem.* **2004**, *25* (12), 1463–1473. https://doi.org/10.1002/jcc.20078.
(445) Grimme, S. Semiempirical GGA-type density functional constructed with a long-range dispersion correction. *J. Comput. Chem.* **2006**, *27* (15), 1787–1799. https://doi.org/10.1002/jcc.20495.
(446) Grimme, S.; Antony, J.; Ehrlich, S.; Krieg, H. A Consistent and Accurate Ab Initio Parametrization of Density Functional Dispersion Correction (DFT-D) for the 94 Elements H-Pu. *J. Chem. Phys.* **2010**, *132* (15), 154104. https://doi.org/10.1063/1.3382344.
(447) Becke, A. D. Density-Functional Thermochemistry. V. Systematic Optimization of Exchange-Correlation Functionals. *J.*

Chem. Phys. **1997**, *107* (20), 8554–8560. https://doi.org/10.1063/1.475007.
(448) Slater, J. C. Atomic Shielding Constants. *Phys. Rev.* **1930**, *36* (1), 57–64. https://doi.org/10.1103/PhysRev.36.57.
(449) Boys, S. F. Electronic Wave Functions - I. A General Method of Calculation for the Stationary States of Any Molecular System. *Proc. R. Soc. Lond. Ser. Math. Phys. Sci.* **1950**, *200* (1063), 542–554. https://doi.org/10.1098/rspa.1950.0036.
(450) Magalhães, A. L. Gaussian-Type Orbitals versus Slater-Type Orbitals: A Comparison. *J. Chem. Educ.* **2014**, *91* (12), 2124–2127. https://doi.org/10.1021/ed500437a.
(451) Hehre, W. J.; Stewart, R. F.; Pople, J. A. Self-Consistent Molecular-Orbital Methods. I. Use of Gaussian Expansions of Slater-Type Atomic Orbitals. *J. Chem. Phys.* **1969**, *51* (6), 2657–2664. https://doi.org/10.1063/1.1672392.
(452) Gordon, M. S.; Binkley, J. S.; Pople, J. A.; Pietro, W. J.; Hehre, W. J. Self-Consistent Molecular-Orbital Methods. 22. Small Split-Valence Basis Sets for Second-Row Elements. *J. Am. Chem. Soc.* **1982**, *104* (10), 2797–2803. https://doi.org/10.1021/ja00374a017.
(453) Kaufmann, K.; Baumeister, W.; Jungen, M. Universal Gaussian Basis Sets for an Optimum Representation of Rydberg and Continuum Wavefunctions. *J. Phys. B At. Mol. Opt. Phys.* **1989**, *22* (14), 2223. https://doi.org/10.1088/0953-4075/22/14/007.
(454) Dunning, T. H., Jr. Gaussian Basis Sets for Use in Correlated Molecular Calculations. I. The Atoms Boron through Neon and Hydrogen. *J. Chem. Phys.* **1989**, *90* (2), 1007–1023. https://doi.org/10.1063/1.456153.
(455) Ditchfield, R.; Hehre, W. J.; Pople, J. A. Self-Consistent Molecular-Orbital Methods. IX. An Extended Gaussian-Type Basis for Molecular-Orbital Studies of Organic Molecules. *J. Chem. Phys.* **2003**, *54* (2), 724–728. https://doi.org/10.1063/1.1674902.
(456) Weigend, F.; Ahlrichs, R. Balanced Basis Sets of Split Valence, Triple Zeta Valence and Quadruple Zeta Valence Quality for H to Rn: Design and Assessment of Accuracy. *Phys. Chem. Chem. Phys.* **2005**, *7* (18), 3297–3305. https://doi.org/10.1039/B508541A.
(457) Jensen, F. Atomic Orbital Basis Sets. *WIREs Comput. Mol. Sci.* **2013**, *3* (3), 273–295. https://doi.org/10.1002/wcms.1123.

(458) Gibbs, J. W. *Elements of Vector Analysis: Arranged for the Use of Students in Physics - Primary Source Edition*; Creative Media Partners, LLC, 2014.
(459) Bloch, F. Über die Quantenmechanik der Elektronen in Kristallgittern. *Z. Für Phys.* **1929**, *52* (7), 555–600. https://doi.org/10.1007/BF01339455.
(460) Alase, A.; Cobanera, E.; Ortiz, G.; Viola, L. Generalization of Bloch's Theorem for Arbitrary Boundary Conditions: Theory. *Phys. Rev. B* **2017**, *96* (19), 195133. https://doi.org/10.1103/PhysRevB.96.195133.
(461) *The VASP Manual - KPOINTS*. https://www.vasp.at/wiki/index.php/KPOINTS (accessed 2023-09-05).
(462) Payne, M. C.; Teter, M. P.; Allan, D. C.; Arias, T. A.; Joannopoulos, J. D. Iterative Minimization Techniques for Ab Initio Total-Energy Calculations: Molecular Dynamics and Conjugate Gradients. *Rev. Mod. Phys.* **1992**, *64* (4), 1045–1097. https://doi.org/10.1103/RevModPhys.64.1045.
(463) Hafner, J. Ab-Initio Simulations of Materials Using VASP: Density-Functional Theory and Beyond. *J. Comput. Chem.* **2008**, *29* (13), 2044–2078. https://doi.org/10.1002/jcc.21057.
(464) Hellmann, H. A New Approximation Method in the Problem of Many Electrons. *J. Chem. Phys.* **1935**, *3* (1), 61. https://doi.org/10.1063/1.1749559.
(465) Hamann, D. R.; Schlüter, M.; Chiang, C. Norm-Conserving Pseudopotentials. *Phys. Rev. Lett.* **1979**, *43* (20), 1494–1497. https://doi.org/10.1103/PhysRevLett.43.1494.
(466) Kleinman, L.; Bylander, D. M. Efficacious Form for Model Pseudopotentials. *Phys. Rev. Lett.* **1982**, *48* (20), 1425–1428. https://doi.org/10.1103/PhysRevLett.48.1425.
(467) Schwerdtfeger, P. The Pseudopotential Approximation in Electronic Structure Theory. *ChemPhysChem* **2011**, *12* (17), 3143–3155. https://doi.org/10.1002/cphc.201100387.
(468) *Energy-consistent Pseudopotentials of the Stuttgart/Cologne Group*. https://www.tc.uni-koeln.de/PP/clickpse.en.html (accessed 2023-09-06).
(469) Troullier, N.; Martins, J. L. Efficient Pseudopotentials for Plane-Wave Calculations. *Phys. Rev. B* **1991**, *43* (3), 1993–2006. https://doi.org/10.1103/PhysRevB.43.1993.
(470) Vanderbilt, D. Soft Self-Consistent Pseudopotentials in a Generalized Eigenvalue Formalism. *Phys. Rev. B* **1990**, *41* (11), 7892–7895. https://doi.org/10.1103/PhysRevB.41.7892.

(471) Kresse, G.; Hafner, J. Norm-Conserving and Ultrasoft Pseudopotentials for First-Row and Transition Elements. *J. Phys. Condens. Matter* **1994**, *6* (40), 8245. https://doi.org/10.1088/0953-8984/6/40/015.
(472) Corso, A. D.; Conte, A. M. Spin-Orbit Coupling with Ultrasoft Pseudopotentials: Application to Au and Pt. *Phys. Rev. B* **2005**, *71* (11), 115106. https://doi.org/10.1103/PhysRevB.71.115106.
(473) Blöchl, P. E. Projector Augmented-Wave Method. *Phys. Rev. B* **1994**, *50* (24), 17953–17979. https://doi.org/10.1103/PhysRevB.50.17953.
(474) Hobbs, D.; Kresse, G.; Hafner, J. Fully Unconstrained Noncollinear Magnetism within the Projector Augmented-Wave Method. *Phys. Rev. B* **2000**, *62* (17), 11556–11570. https://doi.org/10.1103/PhysRevB.62.11556.
(475) Kresse, G.; Joubert, D. From Ultrasoft Pseudopotentials to the Projector Augmented-Wave Method. *Phys. Rev. B* **1999**, *59* (3), 1758–1775. https://doi.org/10.1103/PhysRevB.59.1758.
(476) Andersen, O. K. Linear Methods in Band Theory. *Phys. Rev. B* **1975**, *12* (8), 3060–3083. https://doi.org/10.1103/PhysRevB.12.3060.
(477) Singh, D. J. *Planewaves, Pseudopotentials and the LAPW Method*; Springer US: Boston, MA, 1994. https://doi.org/10.1007/978-1-4757-2312-0.
(478) Kresse, G.; Furthmüller, J. Efficient Iterative Schemes for Ab Initio Total-Energy Calculations Using a Plane-Wave Basis Set. *Phys. Rev. B* **1996**, *54* (16), 11169–11186. https://doi.org/10.1103/PhysRevB.54.11169.
(479) Nocedal, J. Updating Quasi-Newton Matrices with Limited Storage. *Math. Comput.* **1980**, *35* (151), 773–782. https://doi.org/10.1090/S0025-5718-1980-0572855-7.
(480) Sheppard, D.; Terrell, R.; Henkelman, G. Optimization Methods for Finding Minimum Energy Paths. *J. Chem. Phys.* **2008**, *128* (13), 134106. https://doi.org/10.1063/1.2841941.
(481) *FORCE BASED OPTIMIZERS — Transition State Tools for VASP*. https://theory.cm.utexas.edu/vtsttools/optimizers.html (accessed 2023-09-12).
(482) Henkelman, G.; Jónsson, H. A Dimer Method for Finding Saddle Points on High Dimensional Potential Surfaces Using Only First Derivatives. *J. Chem. Phys.* **1999**, *111* (15), 7010–7022. https://doi.org/10.1063/1.480097.

(483) Heyden, A.; Bell, A. T.; Keil, F. J. Efficient Methods for Finding Transition States in Chemical Reactions: Comparison of Improved Dimer Method and Partitioned Rational Function Optimization Method. *J. Chem. Phys.* **2005**, *123* (22), 224101. https://doi.org/10.1063/1.2104507.
(484) Baker, J.; Gill, P. M. W. An Algorithm for the Location of Branching Points on Reaction Paths. *J. Comput. Chem.* **1988**, *9* (5), 465–475. https://doi.org/10.1002/jcc.540090505.
(485) Wales, D. J. Finding Saddle Points for Clusters. *J. Chem. Phys.* **1989**, *91* (11), 7002–7010. https://doi.org/10.1063/1.457316.
(486) Tsai, C. J.; Jordan, K. D. Use of an Eigenmode Method to Locate the Stationary Points on the Potential Energy Surfaces of Selected Argon and Water Clusters. *J. Phys. Chem.* **1993**, *97* (43), 11227–11237. https://doi.org/10.1021/j100145a019.
(487) Baroni, S.; de Gironcoli, S.; Dal Corso, A.; Giannozzi, P. Phonons and Related Crystal Properties from Density-Functional Perturbation Theory. *Rev. Mod. Phys.* **2001**, *73* (2), 515–562. https://doi.org/10.1103/RevModPhys.73.515.
(488) *Phonons from density-functional-perturbation theory*. https://www.vasp.at/wiki/index.php/Phonons_from_density-functional-perturbation_theory.
(489) Baxter, R. J. *Exactly Solved Models in Statistical Mechanics*; Academic Press: London ; New York, 1982.
(490) Cramer, C. J. *Essentials of Computational Chemistry: Theories and Models*, 2nd ed.; Wiley: Chichester, West Sussex, England ; Hoboken, NJ, 2004.
(491) Zain, S. *Thermodynamics and Statistical Mechanics: An Introduction for Physicists and Engineers*; IOP Publishing, 2021.
(492) Bader, R. F. W. Atoms in Molecules. *Acc. Chem. Res.* **1985**, *18* (1), 9–15. https://doi.org/10.1021/ar00109a003.
(493) Matta, C. F.; Boyd, R. J. An Introduction to the Quantum Theory of Atoms in Molecules. In *The Quantum Theory of Atoms in Molecules*; John Wiley & Sons, Ltd, 2007; pp 1–34. https://doi.org/10.1002/9783527610709.ch1.
(494) KUMAR, P. S. V.; RAGHAVENDRA, V.; SUBRAMANIAN, V. Bader's Theory of Atoms in Molecules (AIM) and Its Applications to Chemical Bonding. *J. Chem. Sci.* **2016**, *128* (10), 1527–1536. https://doi.org/10.1007/s12039-016-1172-3.

(495) Esser, S. The Quantum Theory of Atoms in Molecules and the Interactive Conception of Chemical Bonding. *Philos. Sci.* **2019**, *86* (5), 1307–1317. https://doi.org/10.1086/705448.
(496) Hellmann, H. Einführung in die Quantenchemie. In *Hans Hellmann: Einführung in die Quantenchemie: Mit biografischen Notizen von Hans Hellmann jr.*; Andrae, D., Ed.; Springer: Berlin, Heidelberg, 2015; pp 19–376. https://doi.org/10.1007/978-3-662-45967-6_2.
(497) Feynman, R. P. Forces in Molecules. *Phys. Rev.* **1939**, *56* (4), 340–343. https://doi.org/10.1103/PhysRev.56.340.
(498) Clausius, R. XVI. On a Mechanical Theorem Applicable to Heat. *Lond. Edinb. Dublin Philos. Mag. J. Sci.* **1870**, *40* (265), 122–127. https://doi.org/10.1080/14786447008640370.
(499) Henkelman, G.; Arnaldsson, A.; Jónsson, H. A Fast and Robust Algorithm for Bader Decomposition of Charge Density. *Comput. Mater. Sci.* **2006**, *36* (3), 354–360. https://doi.org/10.1016/j.commatsci.2005.04.010.
(500) Manz, T. A.; Sholl, D. S. Improved Atoms-in-Molecule Charge Partitioning Functional for Simultaneously Reproducing the Electrostatic Potential and Chemical States in Periodic and Nonperiodic Materials. *J. Chem. Theory Comput.* **2012**, *8* (8), 2844–2867. https://doi.org/10.1021/ct3002199.
(501) Manz, T. A.; Limas, N. G. Introducing DDEC6 Atomic Population Analysis: Part 1. Charge Partitioning Theory and Methodology. *RSC Adv.* **2016**, *6* (53), 47771–47801. https://doi.org/10.1039/C6RA04656H.
(502) Gallego, M.; Corma, A.; Boronat, M. Sub-Nanometer Copper Clusters as Alternative Catalysts for the Selective Oxidation of Methane to Methanol with Molecular O2. *J. Phys. Chem. A* **2022**. https://doi.org/10.1021/acs.jpca.2c02895.
(503) Guo, D.; Wang, G.-C. Partial Oxidation of Methane on Anatase and Rutile Defective TiO2 Supported Rh4 Cluster: A Density Functional Theory Study. *J. Phys. Chem. C* **2017**, *121* (47), 26308–26320. https://doi.org/10.1021/acs.jpcc.7b07489.
(504) Tang, Y.; Fung, V.; Zhang, X.; Li, Y.; Nguyen, L.; Sakata, T.; Higashi, K.; Jiang, D.; Tao, F. F. Single-Atom High-Temperature Catalysis on a Rh1O5 Cluster for Production of Syngas from Methane. *J. Am. Chem. Soc.* **2021**, *143* (40), 16566–16579. https://doi.org/10.1021/jacs.1c06432.
(505) Xiao, L.; Wang, L. Methane Activation on Pt and Pt4: A Density Functional Theory Study. *J. Phys. Chem. B* **2007**, *111* (7), 1657–1663. https://doi.org/10.1021/jp065288e.

(506) Hirabayashi, S.; Ichihashi, M. Dehydrogenation of Methane by Partially Oxidized Tungsten Cluster Cations: High Reactivity Comparable to That of Platinum Cluster Cations. *J. Phys. Chem. A* **2019**, *123* (32), 6840–6847. https://doi.org/10.1021/acs.jpca.9b04606.

(507) Sirijaraensre, J.; Limtrakul, J. Modification of the Catalytic Properties of the Au4 Nanocluster for the Conversion of Methane-to-Methanol: Synergistic Effects of Metallic Adatoms and a Defective Graphene Support. *Phys. Chem. Chem. Phys.* **2015**, *17* (15), 9706–9715. https://doi.org/10.1039/c4cp05131a.

(508) Cai, X.; Saranya, G.; Shen, K.; Chen, M.; Si, R.; Ding, W.; Zhu, Y. Reversible Switching of Catalytic Activity by Shuttling an Atom into and out of Gold Nanoclusters. *Angew. Chem. Int. Ed.* **2019**, *58* (29), 9964–9968. https://doi.org/10.1002/anie.201903853.

(509) Hu, W.; Sun, Y.; Li, S.; Cheng, X.; Cai, X.; Chen, M.; Zhu, Y. Visible-Light-Driven Methane Conversion with Oxygen Enabled by Atomically Precise Nickel Catalyst. *CCS Chem.* **2021**, *3* (9), 2509–2519. https://doi.org/10.31635/ccschem.020.202000521.

(510) Lustemberg, P. G.; Senanayake, S. D.; Rodriguez, J. A.; Ganduglia-Pirovano, M. V. Tuning Selectivity in the Direct Conversion of Methane to Methanol: Bimetallic Synergistic Effects on the Cleavage of C–H and O–H Bonds over NiCu/CeO2 Catalysts. *J. Phys. Chem. Lett.* **2022**, *13* (24), 5589–5596. https://doi.org/10.1021/acs.jpclett.2c00885.

(511) Pappas, D. K.; Martini, A.; Dyballa, M.; Kvande, K.; Teketel, S.; Lomachenko, K. A.; Baran, R.; Glatzel, P.; Arstad, B.; Berlier, G.; Lamberti, C.; Bordiga, S.; Olsbye, U.; Svelle, S.; Beato, P.; Borfecchia, E. The Nuclearity of the Active Site for Methane to Methanol Conversion in Cu-Mordenite: A Quantitative Assessment. *J. Am. Chem. Soc.* **2018**, *140* (45), 15270–15278. https://doi.org/10.1021/jacs.8b08071.

(512) Srivastava, R. K.; Sarangi, P. K.; Bhatia, L.; Singh, A. K.; Shadangi, K. P. Conversion of Methane to Methanol: Technologies and Future Challenges. *Biomass Convers. Biorefinery* **2022**, *12* (5), 1851–1875. https://doi.org/10.1007/s13399-021-01872-5.

(513) Chen, G.; Waterhouse, G. I. N.; Shi, R.; Zhao, J.; Li, Z.; Wu, L.-Z.; Tung, C.-H.; Zhang, T. From Solar Energy to Fuels: Recent Advances in Light-Driven C1 Chemistry. *Angew. Chem. Int. Ed.* **2019**, *58* (49), 17528–17551. https://doi.org/10.1002/anie.201814313.

(514) Yuan, S.; Li, Y.; Peng, J.; Questell-Santiago, Y. M.; Akkiraju, K.; Giordano, L.; Zheng, D. J.; Bagi, S.; Román-Leshkov, Y.; Shao-Horn, Y. Conversion of Methane into Liquid Fuels—Bridging Thermal Catalysis with Electrocatalysis. *Adv. Energy Mater.* **2020**, *10* (40), 2002154. https://doi.org/10.1002/aenm.202002154.

(515) Kalassov, N.; Dzhonova, D.; Tsibranska, I.; Panyovska, S.; Manatbayev, R. APPLICATION OF INTEGRATED MEMBRANE BIOREACTORS IN RENEWABLE ENERGY INDUSTRY. *J. Chem. Technol. Metall.* **2020**, *55* (2), 314–323.

(516) Freakley, S. J.; Dimitratos, N.; Willock, D. J.; Taylor, S. H.; Kiely, C. J.; Hutchings, G. J. Methane Oxidation to Methanol in Water. *Acc. Chem. Res.* **2021**, *54* (11), 2614–2623. https://doi.org/10.1021/acs.accounts.1c00129.

(517) Feng, N.; Lin, H.; Song, H.; Yang, L.; Tang, D.; Deng, F.; Ye, J. Efficient and Selective Photocatalytic CH4 Conversion to CH3OH with O2 by Controlling Overoxidation on TiO2. *Nat. Commun.* **2021**, *12* (1), 4652. https://doi.org/10.1038/s41467-021-24912-0.

(518) Cao, Y.; Yang, Y.; Yu, W.; Li, G.; Rao, Z.; Huang, Z.; Wang, F.; Yuan, C.; Zhou, Y. Regulating the Spin State of Single Noble Metal Atoms by Hydroxyl for Selective Dehydrogenation of CH4 Direct Conversion to CH3OH. *ACS Appl. Mater. Interfaces* **2022**, *14* (11), 13344–13351. https://doi.org/10.1021/acsami.1c25203.

(519) Florez, E.; Tiznado, W.; Mondragón, F.; Fuentealba, P. Theoretical Study of the Interaction of Molecular Oxygen with Copper Clusters. *J. Phys. Chem. A* **2005**, *109* (34), 7815–7821. https://doi.org/10.1021/jp052245+.

(520) Concepción, P.; Boronat, M.; García-García, S.; Fernández, E.; Corma, A. Enhanced Stability of Cu Clusters of Low Atomicity against Oxidation. Effect on the Catalytic Redox Process. *ACS Catal.* **2017**, *7* (5), 3560–3568. https://doi.org/10.1021/acscatal.7b00778.

(521) Zanchet, A.; López-Caballero, P.; Mitrushchenkov, A. O.; Buceta, D.; López-Quintela, M. A.; Hauser, A. W.; Pilar de Lara-Castells, M. On the Stability of Cu5 Catalysts in Air Using Multireference Perturbation Theory. *J. Phys. Chem. C* **2019**, *123* (44), 27064–27072. https://doi.org/10.1021/acs.jpcc.9b08378.

(522) Mitrushchenkov, A. O.; Zanchet, A.; Hauser, A. W.; de Lara-Castells, M. P. Nonadiabatic Effects in the Molecular Oxidation of Subnanometric Cu5 Clusters. *J. Phys. Chem. A* **2021**, *125* (41), 9143–9150. https://doi.org/10.1021/acs.jpca.1c07271.

(523) Schröder, D.; Shaik, S.; Schwarz, H. Two-State Reactivity as a New Concept in Organometallic Chemistry. *Acc. Chem. Res.* **2000**, *33* (3), 139–145. https://doi.org/10.1021/ar990028j.
(524) Mahyuddin, M. H.; Staykov, A.; Shiota, Y.; Miyanishi, M.; Yoshizawa, K. Roles of Zeolite Confinement and Cu–O–Cu Angle on the Direct Conversion of Methane to Methanol by [Cu2(μ-O)]2+-Exchanged AEI, CHA, AFX, and MFI Zeolites. *ACS Catal.* **2017**, *7* (6), 3741–3751. https://doi.org/10.1021/acscatal.7b00588.
(525) Lezcano-Gonzalez, I.; Deka, U.; Arstad, B.; Deyne, A. V. Y.-D.; Hemelsoet, K.; Waroquier, M.; Speybroeck, V. V.; Weckhuysen, B. M.; Beale, A. M. Determining the Storage, Availability and Reactivity of NH3 within Cu-Chabazite-Based Ammonia Selective Catalytic Reduction Systems. *Phys. Chem. Chem. Phys.* **2013**, *16* (4), 1639–1650. https://doi.org/10.1039/C3CP54132K.
(526) Bates, S. A.; Verma, A. A.; Paolucci, C.; Parekh, A. A.; Anggara, T.; Yezerets, A.; Schneider, W. F.; Miller, J. T.; Delgass, W. N.; Ribeiro, F. H. Identification of the Active Cu Site in Standard Selective Catalytic Reduction with Ammonia on Cu-SSZ-13. *J. Catal.* **2014**, *312*, 87–97. https://doi.org/10.1016/j.jcat.2014.01.004.
(527) Crandell, D. W.; Zhu, H.; Yang, X.; Hochmuth, J.; Baik, M.-H. Computational and Spectroscopic Characterization of Key Intermediates of the Selective Catalytic Reduction Cycle of NO on Zeolite-Supported Cu Catalyst. *Inorganica Chim. Acta* **2015**, *430*, 132–143. https://doi.org/10.1016/j.ica.2015.02.021.
(528) Paolucci, C.; Di Iorio, J. R.; Ribeiro, F. H.; Gounder, R.; Schneider, W. F. Chapter One - Catalysis Science of NOx Selective Catalytic Reduction With Ammonia Over Cu-SSZ-13 and Cu-SAPO-34. In *Advances in Catalysis*; Song, C., Ed.; Academic Press, 2016; Vol. 59, pp 1–107. https://doi.org/10.1016/bs.acat.2016.10.002.
(529) Dahl, I. M.; Mostad, H.; Akporiaye, D.; Wendelbo, R. Structural and Chemical Influences on the MTO Reaction: A Comparison of Chabazite and SAPO-34 as MTO Catalysts. *Microporous Mesoporous Mater.* **1999**, *29* (1), 185–190. https://doi.org/10.1016/S1387-1811(98)00330-8.
(530) Van Speybroeck, V.; Hemelsoet, K.; De Wispelaere, K.; Qian, Q.; Van der Mynsbrugge, J.; De Sterck, B.; Weckhuysen, B. M.; Waroquier, M. Mechanistic Studies on Chabazite-Type Methanol-to-Olefin Catalysts: Insights from Time-Resolved UV/Vis

Microspectroscopy Combined with Theoretical Simulations. *ChemCatChem* **2013**, *5* (1), 173–184. https://doi.org/10.1002/cctc.201200580.

(531) Wu, L.; Degirmenci, V.; Magusin, P. C. M. M.; Lousberg, N. J. H. G. M.; Hensen, E. J. M. Mesoporous SSZ-13 Zeolite Prepared by a Dual-Template Method with Improved Performance in the Methanol-to-Olefins Reaction. *J. Catal.* **2013**, *298*, 27–40. https://doi.org/10.1016/j.jcat.2012.10.029.

(532) Zhu, X.; Hofmann, J. P.; Mezari, B.; Kosinov, N.; Wu, L.; Qian, Q.; Weckhuysen, B. M.; Asahina, S.; Ruiz-Martínez, J.; Hensen, E. J. M. Trimodal Porous Hierarchical SSZ-13 Zeolite with Improved Catalytic Performance in the Methanol-to-Olefins Reaction. *ACS Catal.* **2016**, *6* (4), 2163–2177. https://doi.org/10.1021/acscatal.5b02480.

(533) Gallego, M.; Corma, A.; Boronat, M. Influence of the Zeolite Support on the Catalytic Properties of Confined Metal Clusters: A Periodic DFT Study of O2 Dissociation on Cun Clusters in CHA. *Phys. Chem. Chem. Phys.* **2022**, *24* (48), 30044–30050. https://doi.org/10.1039/D2CP04915E.

(534) Gallego, M.; Corma, A.; Boronat, M. An Alternative Catalytic Cycle for Selective Methane Oxidation to Methanol with Cu Clusters in Zeolites. *Phys. Chem. Chem. Phys.* **2024**. https://doi.org/10.1039/D3CP05802F.

(535) Stamires, D. N.; Turkevich, John. Electron Spin Resonance of Molecules Adsorbed on Synthetic Zeolites. *J. Am. Chem. Soc.* **1964**, *86* (5), 749–757. https://doi.org/10.1021/ja01059a001.

(536) Vinek, H.; Noller, H.; Ebel, M.; Schwarz, K. X-Ray Photoelectron Spectroscopy and Heterogeneous Catalysis, with Elimination Reactions as an Example. *J. Chem. Soc. Faraday Trans. 1 Phys. Chem. Condens. Phases* **1977**, *73* (0), 734–746. https://doi.org/10.1039/F19777300734.

(537) Xu, X.; Wang, J.; Long, Y. Zeolite-Based Materials for Gas Sensors. *Sensors* **2006**, *6* (12), 1751–1764. https://doi.org/10.3390/s6121751.

(538) Ribeiro, L. E. B.; de ALCÂNTARA, G. P.; Andrade, C. M. G.; Fruett, F. Analysis of the Planar Electrode Morphology Applied to Zeolite Based Chemical Sensors. **2015**, *193* (10), 6.

(539) Bandura, L.; Franus, M.; Józefaciuk, G.; Franus, W. Synthetic Zeolites from Fly Ash as Effective Mineral Sorbents for Land-Based Petroleum Spills Cleanup. *Fuel* **2015**, *147*, 100–107. https://doi.org/10.1016/j.fuel.2015.01.067.

(540) Calabrese, L. Anticorrosion Behavior of Zeolite Coatings Obtained by In Situ Crystallization: A Critical Review. *Materials* **2019**, *12* (1), 59. https://doi.org/10.3390/ma12010059.
(541) Bacakova, L.; Vandrovcova, M.; Kopova, I.; Jirka, I. Applications of Zeolites in Biotechnology and Medicine – a Review. *Biomater. Sci.* **2018**, *6* (5), 974–989. https://doi.org/10.1039/C8BM00028J.
(542) Mahdavi Far, R.; Van der Bruggen, B.; Verliefde, A.; Cornelissen, E. A Review of Zeolite Materials Used in Membranes for Water Purification: History, Applications, Challenges and Future Trends. *J. Chem. Technol. Biotechnol.* **2022**, *97* (3), 575–596. https://doi.org/10.1002/jctb.6963.
(543) Punniakodi, B. M. S.; Senthil, R. Recent Developments in Nano-Enhanced Phase Change Materials for Solar Thermal Storage. *Sol. Energy Mater. Sol. Cells* **2022**, *238*, 111629. https://doi.org/10.1016/j.solmat.2022.111629.
(544) Zhu, Q.; Kondo, J. N.; Ohnuma, R.; Kubota, Y.; Yamaguchi, M.; Tatsumi, T. The Study of Methanol-to-Olefin over Proton Type Aluminosilicate CHA Zeolites. *Microporous Mesoporous Mater.* **2008**, *112* (1), 153–161. https://doi.org/10.1016/j.micromeso.2007.09.026.
(545) Izumi, Y. Recent Advances in the Photocatalytic Conversion of Carbon Dioxide to Fuels with Water and/or Hydrogen Using Solar Energy and Beyond. *Coord. Chem. Rev.* **2013**, *257* (1), 171–186. https://doi.org/10.1016/j.ccr.2012.04.018.
(546) Kistler, J. D.; Chotigkrai, N.; Xu, P.; Enderle, B.; Praserthdam, P.; Chen, C.-Y.; Browning, N. D.; Gates, B. C. A Single-Site Platinum CO Oxidation Catalyst in Zeolite KLTL: Microscopic and Spectroscopic Determination of the Locations of the Platinum Atoms. *Angew. Chem. Int. Ed.* **2014**, *53* (34), 8904–8907. https://doi.org/10.1002/anie.201403353.
(547) Goodarzi, F.; Kang, L.; Wang, F. R.; Joensen, F.; Kegnæs, S.; Mielby, J. Methanation of Carbon Dioxide over Zeolite-Encapsulated Nickel Nanoparticles. *ChemCatChem* **2018**, *10* (7), 1566–1570. https://doi.org/10.1002/cctc.201701946.
(548) Ojelade, O. A.; Zaman, S. F. A Review on CO2hydrogenation to Lower Olefins: Understanding the Structure-Property Relationships in Heterogeneous Catalytic Systems. *J. CO2 Util.* **2021**, *47*. https://doi.org/10.1016/j.jcou.2021.101506.
(549) Sajith, P. K.; Shiota, Y.; Yoshizawa, K. Role of Acidic Proton in the Decomposition of NO over Dimeric Cu(I) Active Sites in

Cu-ZSM-5 Catalyst: A QM/MM Study. *ACS Catal.* **2014**, *4* (6), 2075–2085. https://doi.org/10.1021/cs500223z.

(550) Boroń, P.; Rutkowska, M.; Gil, B.; Marszałek, B.; Chmielarz, L.; Dzwigaj, S. Experimental Evidence of the Mechanism of Selective Catalytic Reduction of NO with NH3 over Fe-Containing BEA Zeolites. *ChemSusChem* **2019**, *12* (3), 692–705. https://doi.org/10.1002/cssc.201801883.

(551) Ippolito, J. A.; Tarkalson, D. D.; Lehrsch, G. A. Zeolite Soil Application Method Affects Inorganic Nitrogen, Moisture, and Corn Growth. *Soil Sci.* **2011**, *176* (3), 136–142. https://doi.org/10.1097/SS.0b013e31820e4063.

(552) Reháková, M.; Čuvanová, S.; Dzivák, M.; Rimár, J.; Gaval'ová, Z. Agricultural and Agrochemical Uses of Natural Zeolite of the Clinoptilolite Type. *Curr. Opin. Solid State Mater. Sci.* **2004**, *8* (6), 397–404. https://doi.org/10.1016/j.cossms.2005.04.004.

(553) Evans, J. D.; Coudert, F.-X. Predicting the Mechanical Properties of Zeolite Frameworks by Machine Learning. *Chem. Mater.* **2017**, *29* (18), 7833–7839. https://doi.org/10.1021/acs.chemmater.7b02532.

(554) Jensen, Z.; Kim, E.; Kwon, S.; Gani, T. Z. H.; Román-Leshkov, Y.; Moliner, M.; Corma, A.; Olivetti, E. A Machine Learning Approach to Zeolite Synthesis Enabled by Automatic Literature Data Extraction. *ACS Cent. Sci.* **2019**, *5* (5), 892–899. https://doi.org/10.1021/acscentsci.9b00193.

(555) Nandy, A.; Adamji, H.; Kastner, D. W.; Vennelakanti, V.; Nazemi, A.; Liu, M.; Kulik, H. J. Using Computational Chemistry To Reveal Nature's Blueprints for Single-Site Catalysis of C–H Activation. *ACS Catal.* **2022**, *12* (15), 9281–9306. https://doi.org/10.1021/acscatal.2c02096.

(556) Tariq, R.; Abatal, M.; Bassam, A. Computational Intelligence for Empirical Modeling and Optimization of Methylene Blue Adsorption Phenomena Using Available Local Zeolites and Clay of Morocco. *J. Clean. Prod.* **2022**, *370*, 133517. https://doi.org/10.1016/j.jclepro.2022.133517.

(557) Kulkarni, A. R.; Zhao, Z.-J.; Siahrostami, S.; Nørskov, J. K.; Studt, F. Cation-Exchanged Zeolites for the Selective Oxidation of Methane to Methanol. *Catal. Sci. Technol.* **2018**, *8* (1), 114–123. https://doi.org/10.1039/C7CY01229B.

(558) Pappas, D. K.; Kvande, K.; Kalyva, M.; Dyballa, M.; Lomachenko, K. A.; Arstad, B.; Borfecchia, E.; Bordiga, S.; Olsbye, U.; Beato, P.; Svelle, S. Influence of Cu-Speciation in

Mordenite on Direct Methane to Methanol Conversion: Multi-Technique Characterization and Comparison with NH3 Selective Catalytic Reduction of NOx. *Catal. Today* **2021**, *369*, 105–111. https://doi.org/10.1016/j.cattod.2020.06.050.

(559) Fernández, E.; Boronat, M.; Corma, A. The Crucial Role of Cluster Morphology on the Epoxidation of Propene Catalyzed by Cu5: A DFT Study. *J. Phys. Chem. C* **2020**, *124* (39), 21549–21558. https://doi.org/10.1021/acs.jpcc.0c06295.

(560) Fernández, E.; Boronat, M.; Corma, A. The 2D or 3D Morphology of Sub-Nanometer Cu5 and Cu8 Clusters Changes the Mechanism of CO Oxidation. *Phys. Chem. Chem. Phys.* **2022**, *24* (7), 4504–4514. https://doi.org/10.1039/D1CP05166K.

(561) Borfecchia, E.; Beato, P.; Svelle, S.; Olsbye, U.; Lamberti, C.; Bordiga, S. Cu-CHA – a Model System for Applied Selective Redox Catalysis. *Chem. Soc. Rev.* **2018**, *47* (22), 8097–8133. https://doi.org/10.1039/C8CS00373D.

(562) Pappas, D. K.; Borfecchia, E.; Dyballa, M.; Pankin, I. A.; Lomachenko, K. A.; Martini, A.; Signorile, M.; Teketel, S.; Arstad, B.; Berlier, G.; Lamberti, C.; Bordiga, S.; Olsbye, U.; Lillerud, K. P.; Svelle, S.; Beato, P. Methane to Methanol: Structure–Activity Relationships for Cu-CHA. *J. Am. Chem. Soc.* **2017**, *139* (42), 14961–14975. https://doi.org/10.1021/jacs.7b06472.

(563) Engedahl, U.; Grönbeck, H.; Hellman, A. First-Principles Study of Oxidation State and Coordination of Cu-Dimers in Cu-SSZ-13 during Methane-to-Methanol Reaction Conditions. *J. Phys. Chem. C* **2019**, *123* (43), 26145–26150. https://doi.org/10.1021/acs.jpcc.9b07954.

(564) Zhou, C.; Li, S.; He, S.; Zhao, Z.; Jiao, Y.; Zhang, H. Temperature-Dependant Active Sites for Methane Continuous Conversion to Methanol over Cu-Zeolite Catalysts Using Water as the Oxidant. *Fuel* **2022**, *329*, 125483. https://doi.org/10.1016/j.fuel.2022.125483.

(565) Campbell, A. N.; Stahl, S. S. Overcoming the "Oxidant Problem": Strategies to Use O2 as the Oxidant in Organometallic C–H Oxidation Reactions Catalyzed by Pd (and Cu). *Acc. Chem. Res.* **2012**, *45* (6), 851–863. https://doi.org/10.1021/ar2002045.

(566) Jones, A. B.; Wang, J.; Hamme II, A. T.; Han, W. Oxygen. In *Encyclopedia of Reagents for Organic Synthesis*; John Wiley & Sons, Ltd, 2013. https://doi.org/10.1002/047084289X.ro028.pub3.

(567) Liang, Y.-F.; Jiao, N. Oxygenation via C–H/C–C Bond Activation with Molecular Oxygen. *Acc. Chem. Res.* **2017**, *50* (7), 1640–1653. https://doi.org/10.1021/acs.accounts.7b00108.
(568) Bryliakov, K. P. Catalytic Asymmetric Oxygenations with the Environmentally Benign Oxidants H2O2 and O2. *Chem. Rev.* **2017**, *117* (17), 11406–11459. https://doi.org/10.1021/acs.chemrev.7b00167.
(569) Hu, M.; Wu, W.; Jiang, H. Palladium-Catalyzed Oxidation Reactions of Alkenes with Green Oxidants. *ChemSusChem* **2019**, *12* (13), 2911–2935. https://doi.org/10.1002/cssc.201900397.
(570) Bryliakov, K. *Environmentally Sustainable Catalytic Asymmetric Oxidations*; CRC Press: Boca Raton, 2014. https://doi.org/10.1201/b17422.
(571) Gawande, M. B.; Goswami, A.; Felpin, F.-X.; Asefa, T.; Huang, X.; Silva, R.; Zou, X.; Zboril, R.; Varma, R. S. Cu and Cu-Based Nanoparticles: Synthesis and Applications in Catalysis. *Chem. Rev.* **2016**, *116* (6), 3722–3811. https://doi.org/10.1021/acs.chemrev.5b00482.
(572) Azizi, Z.; Rezaeimanesh, M.; Tohidian, T.; Rahimpour, M. R. Dimethyl Ether: A Review of Technologies and Production Challenges. *Chem. Eng. Process. Process Intensif.* **2014**, *82*, 150–172. https://doi.org/10.1016/j.cep.2014.06.007.
(573) Catizzone, E.; Freda, C.; Braccio, G.; Frusteri, F.; Bonura, G. Dimethyl Ether as Circular Hydrogen Carrier: Catalytic Aspects of Hydrogenation/Dehydrogenation Steps. *J. Energy Chem.* **2021**, *58*, 55–77. https://doi.org/10.1016/j.jechem.2020.09.040.
(574) Pawelczyk, E.; Łukasik, N.; Wysocka, I.; Rogala, A.; Gębicki, J. Recent Progress on Hydrogen Storage and Production Using Chemical Hydrogen Carriers. *Energies* **2022**, *15* (14), 4964. https://doi.org/10.3390/en15144964.
(575) Millar, G. J.; Collins, M. Industrial Production of Formaldehyde Using Polycrystalline Silver Catalyst. *Ind. Eng. Chem. Res.* **2017**, *56* (33), 9247–9265. https://doi.org/10.1021/acs.iecr.7b02388.
(576) Mahdi, H. I.; Ramlee, N. N.; Santos, D. H. da S.; Giannakoudakis, D. A.; de Oliveira, L. H.; Selvasembian, R.; Azelee, N. I. W.; Bazargan, A.; Meili, L. Formaldehyde Production Using Methanol and Heterogeneous Solid Catalysts: A Comprehensive Review. *Mol. Catal.* **2023**, *537*, 112944. https://doi.org/10.1016/j.mcat.2023.112944.
(577) Advani, J. H.; Kumar, A.; Srivastava, R. Tailoring the Porosity and Active Sites in Silicoaluminophosphate Zeolites and

Their Catalytic Applications. In *Catalysis in Confined Frameworks*; John Wiley & Sons, Ltd, 2024; pp 363–396. https://doi.org/10.1002/9783527839278.ch11.

(578) Ristić, A.; Tušar, N. N.; Arčon, I.; Thibault-Starzyk, F.; Hanžel, D.; Czyzniewska, J.; Kaučič, V. Synthesis and Characterization of Triclinic MeAPO-34 (Me=Zn, Fe) Molecular Sieves. *Microporous Mesoporous Mater.* **2002**, *56* (3), 303–315. https://doi.org/10.1016/S1387-1811(02)00504-8.

(579) Pliego, J. A.; Ruíz, M. G.; Álvarez, C. M.; Casas, M. G.; Andrés, E. S. de. MTO Synthesis and Characterization of ZnAPO-34 and SAPO-34: Effect of Zn on the Acidity and Catalytic Activity in the MTO Reaction. *J. Mex. Chem. Soc.* **2021**, *65* (1). https://doi.org/10.29356/jmcs.v65i1.1261.

(580) Usman, M.; Ghanem, A. S.; Niaz Ali Shah, S.; Garba, M. D.; Yusuf Khan, M.; Khan, S.; Humayun, M.; Laeeq Khan, A. A Review on SAPO-34 Zeolite Materials for CO2 Capture and Conversion. *Chem. Rec.* **2022**, *22* (7), e202200039. https://doi.org/10.1002/tcr.202200039.

(581) Lee, S.-O.; Raja, R.; Harris, K. D. M.; Thomas, J. M.; Johnson, B. F. G.; Sankar, G. Mechanistic Insights into the Conversion of Cyclohexene to Adipic Acid by H2O2 in the Presence of a TAPO-5 Catalyst. *Angew. Chem. Int. Ed.* **2003**, *42* (13), 1520–1523. https://doi.org/10.1002/anie.200250351.

(582) Raboin, L.; Yano, J.; Tilley, T. D. Epoxidation Catalysts Derived from Introduction of Titanium Centers onto the Surface of Mesoporous Aluminophosphate: Comparisons with Analogous Catalysts Based on Mesoporous Silica. *J. Catal.* **2012**, *285* (1), 168–176. https://doi.org/10.1016/j.jcat.2011.09.023.

(583) Chatterjee, S.; Shyamal, S.; Chandra, D.; Hara, M.; Bhaumik, A. Ti(IV)-Containing Aluminophosphate Material TAPO-25 for Photoelectrochemical Water Oxidation. *Mol. Catal.* **2020**, *486*, 110876. https://doi.org/10.1016/j.mcat.2020.110876.

(584) Mehravar, M.; Mirjalili, B. B. F.; Babaei, E.; Bamoniri, A. Efficient Solvent Free Synthesis of Tetrahydrobenzo[a]Xanthene-11-One Derivatives Using Nano-AlPO4/Ti (IV) as a Green, Heterogeneous and Reusable Catalyst. *Inorg. Nano-Met. Chem.* **2022**, *52* (2), 241–252. https://doi.org/10.1080/24701556.2021.1891429.